ASME
SETTING THE STANDARD

Transactions of the ASME, Journal of Fluids Engineering (ISSN 0098-2202) is published monthly by The American Society of Mechanical Engineers, Three Park Avenue, New York, NY 10016. Periodicals postage paid at New York, NY and additional mailing offices.
POSTMASTER: Send address changes to Transactions of the ASME, Journal of Fluids Engineering, c/o THE AMERICAN SOCIETY OF MECHANICAL ENGINEERS, 22 Law Drive, Box 2300, Fairfield, NJ 07007-2300.
CHANGES OF ADDRESS must be received at Society headquarters seven weeks before they are to be effective. Please send old label and new address.
STATEMENT from By-Laws. The Society shall not be responsible for statements or opinions advanced in papers or ... printed in its publications (B7.1, Par. 3).

Journal of Fluids Engineering

Published Monthly by ASME

VOLUME 129 • NUMBER 11 • NOVEMBER 2007

TECHNICAL PAPERS

(Contents continued on inside back cover)

This journal is printed on acid-free paper, which exceeds the ANSI Z39.48-1992 specification for permanence of paper and library materials. ♾™
♻ 85% recycled content, including 10% post-consumer fibers.

The ASME Journal of Fluids Engineering is abstracted and indexed in the following:

Applied Science & Technology Index, Chemical Abstracts, Chemical Engineering and Biotechnology Abstracts (Electronic equivalent of Process and Chemical Engineering), Civil Engineering Abstracts, Computer & Information Systems Abstracts, Corrosion Abstracts, Current Contents, Ei EncompassLit, Electronics & Communications Abstracts, Engineered Materials Abstracts, Engineering Index, Environmental Engineering Abstracts, Environmental Science and Pollution Management, Excerpta Medica, Fluidex, Index to Scientific Reviews, INSPEC, International Building Services Abstracts, Mechanical & Transportation Engineering Abstracts, Mechanical Engineering Abstracts, METADEX (The electronic equivalent of Metals Abstracts and Alloys Index), Petroleum Abstracts, Process and Chemical Engineering, Referativnyi Zhurnal, Science Citation Index, SciSearch (The electronic equivalent of Science Citation Index), Shock and Vibration Digest, Solid State and Superconductivity Abstracts, Theoretical Chemical Engineering

Numerical Simulations of Peristaltic Mixing

Saurabh Kumar

Ho Jun Kim

Ali Beskok[1]
e-mail: abeskok@odu.edu

Aerospace Engineering Department,
Old Dominion University,
Norfolk, VA 23529-0247

Numerical simulations of two-dimensional flow and species transport in a peristaltically driven closed mixer are performed as a function of the Reynolds number ($\mathrm{Re} \leqslant 6288$) *and the normalized traveling wave amplitude* ($\varepsilon \leqslant 0.3$) *at low to moderate Schmidt number* ($\mathrm{Sc} \leqslant 10$) *conditions. The mixer consists of a rectangular box with a traveling wave motion induced on its bottom surface. Flow and species mixing are produced by the surface motion. The numerical algorithm, based on an arbitrary Lagrangian–Eulerian spectral element formulation, is verified using the asymptotic solutions for small wave amplitude cases. Kinematics of large-deformation conditions are studied as a function of the Reynolds number. Species mixing is simulated at various* Re *and* Sc *conditions. Mixing index inverse* (M^{-1}) *is utilized to characterize the mixing efficiency, where* $M^{-1} \propto \exp(\mathrm{Pe}^{-\alpha} t)$ *is observed as the long-time behavior. Simulation data are utilized to determine the exponent* α *at various* Re *and* Sc *conditions. For all simulations,* $0.28 \leqslant \alpha \leqslant 0.35$*, typical of partially chaotic flows, have been observed. The effect of flow kinematics and species diffusion on mixing is interpreted.* [DOI: 10.1115/1.2786480]

Keywords: peristaltic mixing, chaotic stirring, mixing efficiency, spectral element methods, ALE simulations

1 Introduction

There is a growing need to efficiently manipulate small volumes of fluids in biological and chemical analysis, environmental sampling, DNA sequencing, drug delivery, and other biotechnology applications [1,2]. Successful implementations of these new technologies require design and fabrication of miniaturized devices, which can carry out all fluid handling functions, such as pumping, mixing, and filtering in a small volume. Especially for biomedical applications, the desired functions need to be performed without causing drastic changes in the properties of the fluid being handled. Particularly, blood, cell cultures, enzymes, proteins, etc., are highly sensitive to the shear rates and temperature changes. Peristaltic pumping induces significantly lower shear stresses on the fluid, and it is suitable for multiphase flows. Hence, it is preferred over other pumping techniques for biomedical and industrial applications [3–6]. With the advent of the microsystem technologies, several research groups developed miniaturized peristaltic pumps for microfluidic [7–11] and drug delivery applications [12,13].

In addition to pumping, peristalsis also induces mixing of two fluids. Perhaps, the best example for a peristaltic pump/mixer is the human gastrointestinal system, where the small and large intestines efficiently pump and mix their constituents using peristalsis [14]. Early theoretical studies on peristaltic pumping were based on the lubrication theory, and they were valid for low Reynolds number flows with small wave amplitude motion [15]. Comparisons between the theoretical results and experiments were given in Ref. [16]. Fauci simulated solid particle transport by peristalsis in a two-dimensional channel with sinusoidal waves using the immersed boundary technique [17]. This work also included fluid-particle interactions. Selverov and Stone investigated transport in long rectangular cavities, with small amplitude peristaltic motion, and presented asymptotic solutions for the velocity field, valid for both high- and low-frequency motions [18]. Yi et al. presented comparisons between the asymptotic and numerical solutions of the velocity field for low and intermediate wave amplitudes at various frequencies [19]. They also performed interface tracking simulations, and have shown enhanced fluid stirring. In a later study, Yi et al. presented asymptotic solutions for peristaltically induced flow in a closed cavity with two vibrating walls [20]. Most recently, Carlsson et al. presented fluid mixing induced by vibrating walls, where they first developed analytical solutions for the velocity field, and then utilized this to obtain dispersion of passive scalar particles [21].

Species mixing is characterized as a function of the Peclet number, which is the ratio of the species diffusion and convection time scales. Species convection is determined by the flow kinematics that is characterized by the Reynolds number, while diffusion is determined by the species mass diffusivity that is characterized by the Schmidt number. Therefore, the Peclet number is based on both the Reynolds and Schmidt numbers (i.e., $\mathrm{Pe} = \mathrm{Sc} \times \mathrm{Re}$). Mixers operating at $\mathrm{Re} > 1$ conditions experience Reynolds number dependent flow fields. Hence, convective-diffusive transport in such cases cannot be solely characterized as a function of the Pe, and one has to consider the flow dynamics (Re) and the species transport (Pe) effects separately. Recognizing the importance of fluid motion in peristaltic mixing, Yi et al. investigated mixing via interface tracking methods using the asymptotically and numerically predicted velocity fields at various Re values [19]. However, asymptotic solutions of the velocity field are strictly valid for small amplitude motion, and numerical solutions become increasingly challenging for large amplitude deformations of the flow domain.

The mixing time (t_m) for laminar convective/diffusive transport typically scales as $t_m \propto \mathrm{Pe}^{0.5}$ [22,23]. It is possible to reduce the mixing time drastically by inducing *chaotic advection* [24–26]. Exponential growth of the interface between the two fluids in chaotically stirred flows results in small striation thickness, followed by mixing due to diffusion. At fixed kinematic conditions (i.e., fixed Re values), the mixing time varies as $t_m \propto \ln(\mathrm{Pe})$ for fully chaotic [2], and $t_m \propto \mathrm{Pe}^{\alpha}$ (with $\alpha \leqslant 0.25$) for partially chaotic flows [27]. Either case results in significant gains over laminar flow mixing for large Pe values. Two-dimensional time-periodic flows, such as in the case of the peristaltic mixer, may exhibit chaotic stirring [22]. Therefore, mixing by peristalsis is of interest for both scientists and engineers.

[1]Corresponding author.

Contributed by the Fluids Engineering Division of ASME for publication in the JOURNAL OF FLUIDS ENGINEERING. Manuscript received December 28, 2005; final manuscript received June 6, 2007. Review conducted by Kenneth Breuer.

In this paper, we investigate the fluid flow and species transport in a peristaltically driven mixer under large amplitude deformations ($\varepsilon \leqslant 0.3$) and a wide range of Reynolds numbers ($\mathrm{Re} \leqslant 6288$). Since the peristaltic motion has substantial inertial effects ($\mathrm{Re} \leqslant 6288$), mixing is characterized as a function of both the Reynolds and Schmidt numbers. Although the Reynolds number is determined by selecting the mixer dimensions and traveling wave speed, the Schmidt number is a fluid property, which can vary from 0.1 for gases [28] to 1.0×10^5 for large particles and biomolecules [2]. In this paper, we are interested in the convective-diffusive transport and species mixing under inertial effects. Considering the wide range of Re reported in this paper, numerical simulations at large Sc result in Pe values that are beyond our current computational capabilities. Therefore, simulations were restricted to the $1 \leqslant \mathrm{Sc} \leqslant 10$ range. Typical Schmidt number values for dilute binary mixtures can be found in Ref. [28]. Although the mixing simulations were limited to low Sc values, the Peclet numbers are large enough to exhibit predominantly convection dominated transport. Numerical simulations are performed using spectral element arbitrary Lagrangian–Eulerian (ALE) formulation, which enables high-order accurate solutions for moving domain problems. The *objectives* of this paper are as follows:

1. Investigation of flow dynamics for large amplitude traveling wave motion in a wide Re range, where the numerical results enable exploration of flow physics beyond the capabilities of perturbation expansion solutions.
2. Quantification of mixing efficiency as functions of the Re, Sc, and Pe. For this purpose, the inverse of mixing index M^{-1}, which is a measure based on the standard deviation of species concentration from a perfect mix, is utilized. Study of temporal growth of M^{-1} enables investigation of how fast homogenizations of concentration values are achieved at various Re, Sc, and Pe conditions.

This paper is organized as follows. We first present the mathematical modeling and governing equations. Then, we present the numerical simulation methodology and code validation using asymptotic solutions valid for small-deformation cases. This is followed by the study of flow and mixing under large amplitude motion as a function of the Re and Sc. Finally, we summarize our findings and conclude.

2 Mathematical Formulation and Governing Equations

In this section, we summarize the previous research on mathematical modeling of peristaltically driven flows. Results from the literature will be utilized for validation of our numerical solutions in the next section. Following Yi et al. [19,20], we consider a closed rectangular domain with length L^* and height h^*, as shown in Fig. 1. The bottom surface of the domain deforms in the form of a traveling wave, which can be generally written as

$$a^* f(x^*, t^*) \tag{1}$$

where a^* is the amplitude of deformation and $f(x^*, t^*)$ is its shape. The streamwise position and time are denoted by x^* and t^*, respectively. A traveling wave motion can be generated by simply choosing

$$f(x^*, t^*) = \cos(k^* x^* - \omega^* t^*) \tag{2}$$

where k^* is the wave number and ω^* is the wave angular velocity. We normalize the length and time scales using the height of the domain h^*, and ω^*, respectively. This results in the following nondimensional parameters:

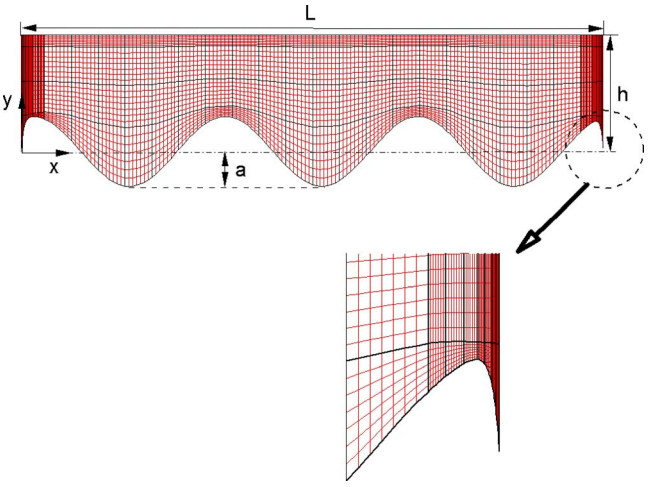

Fig. 1 Top: Schematic view of the peristaltic mixer with its relevant length scales, and seventh-order spectral element discretization for $\varepsilon = a/h = 0.3$. The thick lines show the element boundaries, while the thin lines correspond to the internal degrees of freedom used for each element. Bottom: Zoomed view of the right bottom corner of the domain that exhibits exponential variations in the *x* direction, as given by Eq. (4).

$$\varepsilon = \frac{a^*}{h^*} \quad L = \frac{L^*}{h^*} \quad t = t^* \omega^* \quad \mathbf{u} = \frac{\mathbf{u}^*}{\omega^* h^*} \quad k = k^* h^* \quad x = \frac{x^*}{h^*} \tag{3}$$

where t, k, ε, and $\mathbf{u}$ are the normalized time, wave number, wave amplitude, and the velocity vector, respectively. The corresponding nondimensional quantities are shown without an asterisk. The velocity vector is defined in the Cartesian coordinate system $\mathbf{u} = u\mathbf{e}_x + v\mathbf{e}_y$, where $\mathbf{e}_x$ and $\mathbf{e}_y$ are the unit vectors along the x and y directions, respectively. Due to the lack of a prescribed velocity in the problem, the velocity vector is normalized by the wave angular velocity and the channel height, $\omega^* h^*$.

Following Yi et al. [19,20], we specified the membrane deformation shape as

$$f(x,t) = Re\left\{ \exp[i(kx - t)] \left[1 - \exp\left(-\frac{x}{m} \right) \right] \left[1 - \exp\left(-\frac{L - x}{m} \right) \right] \right\} \tag{4}$$

where m is a small number obtained by the condition that the box is closed and the fluid is incompressible. Hence, the membrane deformation must preserve volume. The first term on the right hand side of Eq. (4) shows a traveling wave motion, while the exponential terms are used to annihilate the traveling wave closer to the side boundaries of the mixer. A snapshot of the membrane at $t = 0$ is shown in Fig. 1 for the $\varepsilon = 0.3$ deformation case. In order to compare our numerical results with the results of Yi et al. [19], we selected identical conditions of $L = 5$ and $k = 3.8$ and $m = 0.02$. This value of m is sufficiently small so that traveling wave motion with three wavelengths is sustained in the mixing domain. As shown in Fig. 1, the wave decays exponentially at both ends of the closed domain. Although such conditions cannot be easily imposed in experiments, it is important to utilize this to limit the mixing domain size.

Incompressible Newtonian fluid flow is governed by the Navier–Stokes equations

$$\frac{\partial \mathbf{u}}{\partial t} + (\mathbf{u} \cdot \nabla)\mathbf{u} = -\nabla p + \frac{1}{\mathrm{Re}} \nabla^2 \mathbf{u} \tag{5}$$

where p is the pressure normalized by the dynamic head and Re is the Reynolds number. Incompressibility is imposed by the continuity equation

Table 1 Summary of the equations used to determine the leading-order velocity field

Velocity component	$\beta \leq 50$	$\beta \geq 50$
$u_{0,1}(x,y,t)$	Eqs. (A3) and (A7)	Eqs. (A3) and (A15)
$u_{0,2}(y,t)$	Eqs. (A3) and (A5)	Eqs. (A3) and (A6)
$v_0(x,y,t)$	Eqs. (A4) and (A7)	Eqs. (A4) and (A16)

$$\nabla \cdot \mathbf{u} = 0 \tag{6}$$

Since the flow is driven by the boundary motion and the characteristic velocity is chosen as $\omega^* h^*$, the Reynolds number in Eq. (5) is defined as

$$\mathrm{Re} = \beta^2 = (\omega^* h^*) h^* / \nu^* \tag{7}$$

where ν^* is the kinematic viscosity of the fluid. This definition of the Reynolds number is *identical* to the square of the Womersley number (β) often used in pulsatile flows, which can be interpreted either as the ratio of pulsatile to viscous forces or the ratio of viscous to pulsatile time scales. Equations (5) and (6) are subject to the no-slip boundary conditions on all surfaces.

Using perturbation expansions in ε, Yi et al. [19,20] obtained asymptotic solutions for the velocity field. For convenience, we included a brief summary of their analytical work along with the leading-order solutions for the velocity field in Appendix A. Equations utilized for code verification are listed in Table 1. We must state that all equations in Table 1 were obtained as the leading-order solution to the problem, given by $\mathbf{u}_0$ in Eq. (A1), and for $m \to 0$ conditions. In addition, $U_{0,2}$ is independent of x far away from the lateral walls (Eqs. (A3) and (A4)), while $u_{0,1}$ and v_0 are periodic in x (Eqs. (A15) and (A16)). These are somewhat nonrealistic conditions due to the closed-box nature of the peristaltic mixer. Therefore, our code validation efforts in the next section will be limited to very small ε values. Even these cases will give considerable deviations near lateral boundaries.

The $\beta \geq 50$ cases correspond to $\mathrm{Re} \geq 2500$. Due to the large Reynolds number, flow may become three dimensional and/or turbulent. Such conditions are *neglected* in the analytical solutions, and cannot be properly modeled using two-dimensional numerical simulations presented in this paper. Although we cannot comment on the onset of three-dimensionality effects and possible transition to turbulence, we must remind the reader that the characteristic velocity used in the definition of Re is based on the wave angular velocity ω^* and channel height h^*, and it is given as $\omega^* h^*$. Time dependent velocity profiles that will be shown in the next section have considerably smaller magnitudes than $\omega^* h^*$ for most of the membrane period. In addition, velocity magnitudes decay rapidly with the distance from the membrane. We expect about an order of magnitude reduction in the Reynolds number, if we utilized a characteristic velocity based on the average velocity obtained as a result of the peristaltic motion. Therefore, similar to the previous theoretical and numerical studies [18–21,29], onset of three dimensionality and turbulence are neglected in the present work.

Results in this paper are obtained for $\mathrm{Re} \leq 6288$ and $\varepsilon \leq 0.3$ conditions. Dimensional parameters for experiments that would correspond to the simulation parameter range used in this paper can be determined by choosing the characteristic length scale (h^*) of the mixer. For example, choosing $h^* = 1$ cm results in a mixing chamber that is $L^* = 5$ cm long, which is in the same size range of the experimental studies reported in Refs. [12,30,31]. Depending on the ε value, the amplitude of deformation can be found as $\varepsilon h^* \leq 3$ mm, which can be induced by an elastic membrane. The Reynolds number range and kinematic viscosity of fluid determine the actuation frequency as $\omega^* = \nu \mathrm{Re}/(h^*)^2$. Assuming water with $\nu^* = 10^{-6}$ m^2/s and $\mathrm{Re} \leq 6288$, we obtain $\omega^* \leq 63$ Hz. An order of magnitude of change in h^* results in two orders of magnitude change in ω^*. For example, choosing $h^* = 10$ cm results in $\omega^* \leq 0.63$ Hz, while choosing $h^* = 1$ mm requires $\omega^* \leq 6300$ Hz. The latter example can be considered a microelectromechanical (MEMS) device, where actuation frequencies over 1 MHz can be achieved [32]. Therefore, we expect the simulation parameter range used in this paper to be applicable for a characteristic length scale (h^*) varying from 1 mm to 10 cm for mixing aqueous solutions.

3 Numerical Simulation Methodology and Code Verification

Numerical simulations of flow and species transport in a peristaltic mixer require long-time integration of the scalar transport equation and the incompressible Navier–Stokes equations in a closed moving domain. Proper resolution of the flow and scalar transport requires robust numerical algorithms that minimize the dispersion and diffusion errors. Furthermore, peristaltic motion in the closed mixing chamber needs to be accurately modeled to avoid divergence errors, since numerical inaccuracies will result in violation of the incompressibility condition. These numerical challenges become even more cumbersome for large membrane deformation cases. In addition, exponential variations in the membrane shape near the two lateral boundaries, imposed to maintain traveling wave motion with three wave lengths, need to be properly resolved (see Eq. (4) and Fig. 1). Simulations for a *continuous* flow mixer would have required manyfold increase in the computational domain size due to the spatially nonperiodic nature of the species transport, which requires longer mixing lengths for increased Pe. Therefore, closed mixer simulations are computationally more feasible than the continuous mixer simulations, and preferred in this study.

In order to address these computational challenges, we employed *hp* spectral element discretization of the Navier–Stokes and species transport equations using an ALE formulation [33]. Our algorithm discretizes the domain into large elements, where each element utilizes *N*th-order modal expansions per direction. For example, the thick lines in Fig. 1 show 136 rectangular spectral elements used to discretize the mixer domain, while eighth-order modal expansions per direction are "represented" in the figure at the cross section of the thin lines. We must note that the modal expansions do not use collocation points. Hence, they cannot be properly shown on the elemental mesh unless these modal functions ($8 \times 8 = 64$ of them for this case) are separately plotted on the master element (see Fig. 3.1 and Chap. 3 in Ref. [34] for further details).

Spectral element methods use *hp* refinement techniques. Specifically, further resolution of a problem can be achieved by increasing the number of elements in the domain, known as the *h* refinement. This is similar to the finite element or finite volume methods, and for an *N*th-order discretization, this results in *N*th-order algebraic convergence [34]. The second alternative is to progressively increase the elemental/modal expansion of each element, similar to the spectral methods. This latter approach results in exponential decay of the discretization errors for problems that yield smooth (C^∞) solutions [34].

In Ref. [33], we presented verification of our spectral element ALE algorithm in moving domains. In addition to the usual advantages of spectral methods, such as exponential error reduction with *p*-type refinements, we have shown that the algorithm is robust and maintains its spatial accuracy for large mesh deformation cases. Third-order stiffly stable time integration schemes are used to solve the time-periodic flow and transient species transport in the mixer. Due to the mesh motion, ALE algorithm requires calculation of the element size, shape, and the isoparametric mapping variables at every time step. Hence, the ALE simulations are considerably more expensive than the Eulerian simulations.

Peristaltic mixer simulations require proper initial deformation of the bottom surface. Since our mesh generation capabilities did

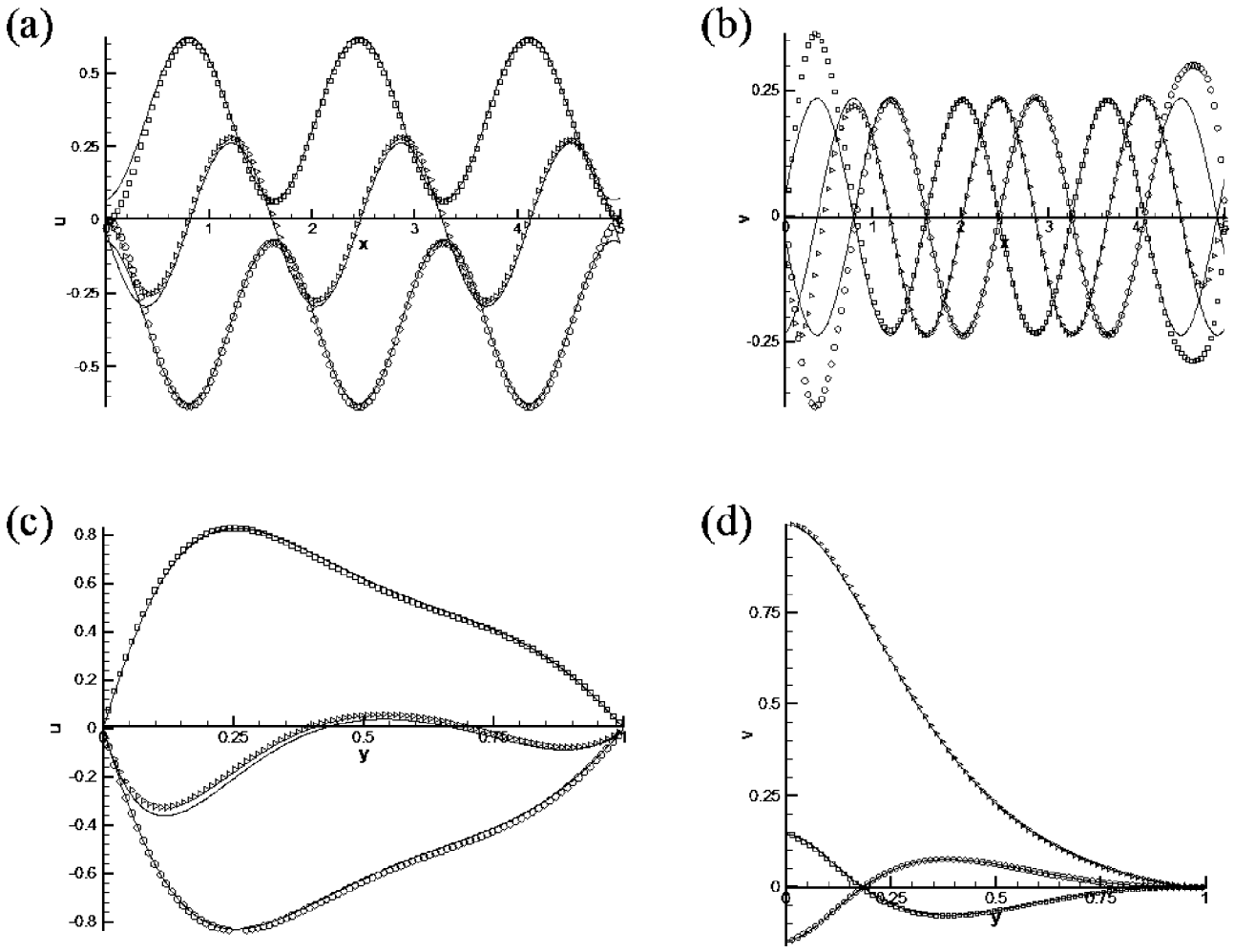

Fig. 2 Velocity profiles for $\varepsilon=0.01$ and Re=63 at various times during a cycle. (*a*), (*b*), (*c*), and (*d*) show variation of $u(x,0.5,t)$, $v(x,0.5,t)$, $u(L/2,y,t)$, and $v(L/2,y,t)$, respectively. Symbols show the numerical solutions and the solid lines represent the leading-order asymptotic solution. Squares, triangles, and circles represent numerical snapshots at $t=0$, $T/4$, and $T/2$, respectively.

not allow creation of a mesh with a prescribed initial deformation in the form of Eq. (1), we used appropriate moving boundary conditions on the membrane to obtain the desired initial deformation. Most of the initial deformation cases are done using eighth-order modal expansions. This resolution was satisfactory, since there is no flow during this stage. Once the initial mesh deformation is obtained, the grid is refined by *p*-type refinements whenever deemed necessary. Numerically computed velocities are inspected for time periodicity. Synchronization between the numerical and leading-order asymptotic results is obtained by matching the instant, when the streamwise velocity at the mixer center $(L/2, h/2)$ attained its maximum value during the cycle.

In order to verify our code, we first performed numerical simulations for $\varepsilon=0.01$. The results for this case are compared with the leading-order asymptotic solutions (herein referred to as "analytical solution"). In Figs. 2 and 3, we present comparisons of our numerical solutions with analytical solutions for Re=63 and Re =6288 flows, respectively. We particularly chose these parameters to further verify our results with Yi et al. [19]. The analytical solution for Re=63 flow is obtained using Eqs. (A3)–(A5) and (A7), and the analytical solution for Re=6288 flow is based on Eqs. (A3), (A4), (A6), (A15), and (A16). Both components of the velocity vector are periodic in time. Since the analytical solution is invalid near the lateral walls, we observe deviations between the numerical and analytical results near the boundaries. These deviations increase with increasing the Reynolds number. For the large Re case, Fig. 3(*b*) exhibits a boundary layer in the v velocity near the lateral walls (at $x=0$ and $x=L$). In addition, Fig. 3(*c*) exhibits boundary layer in the streamwise velocity near the top and bottom walls (at $y=1$ and $y=0$). The velocity profiles are symmetric about the ordinate, and they match the leading-order asymptotic results reasonably well.

4 Kinematics of Large Amplitude Deformation

Once the numerical approach is verified using small amplitude deformation cases, we now present results for the large amplitude traveling wave cases, which involve amplitudes as large as 30% of the cavity height. Large-deformation cases present problems for low-order discretization methods, due to mesh tangling problems. Spectral element method does not experience this problem, since it utilizes elements larger than the low-order discretization methods. Furthermore, spectral element methods are tolerant to skew meshes, and they can maintain their accuracy under very large deformations [33].

In this section, we present results for the $\varepsilon=0.3$ case with Re =63 and Re=400. Since the bottom wall is subjected to large deformations, the y coordinate in the results is scaled using

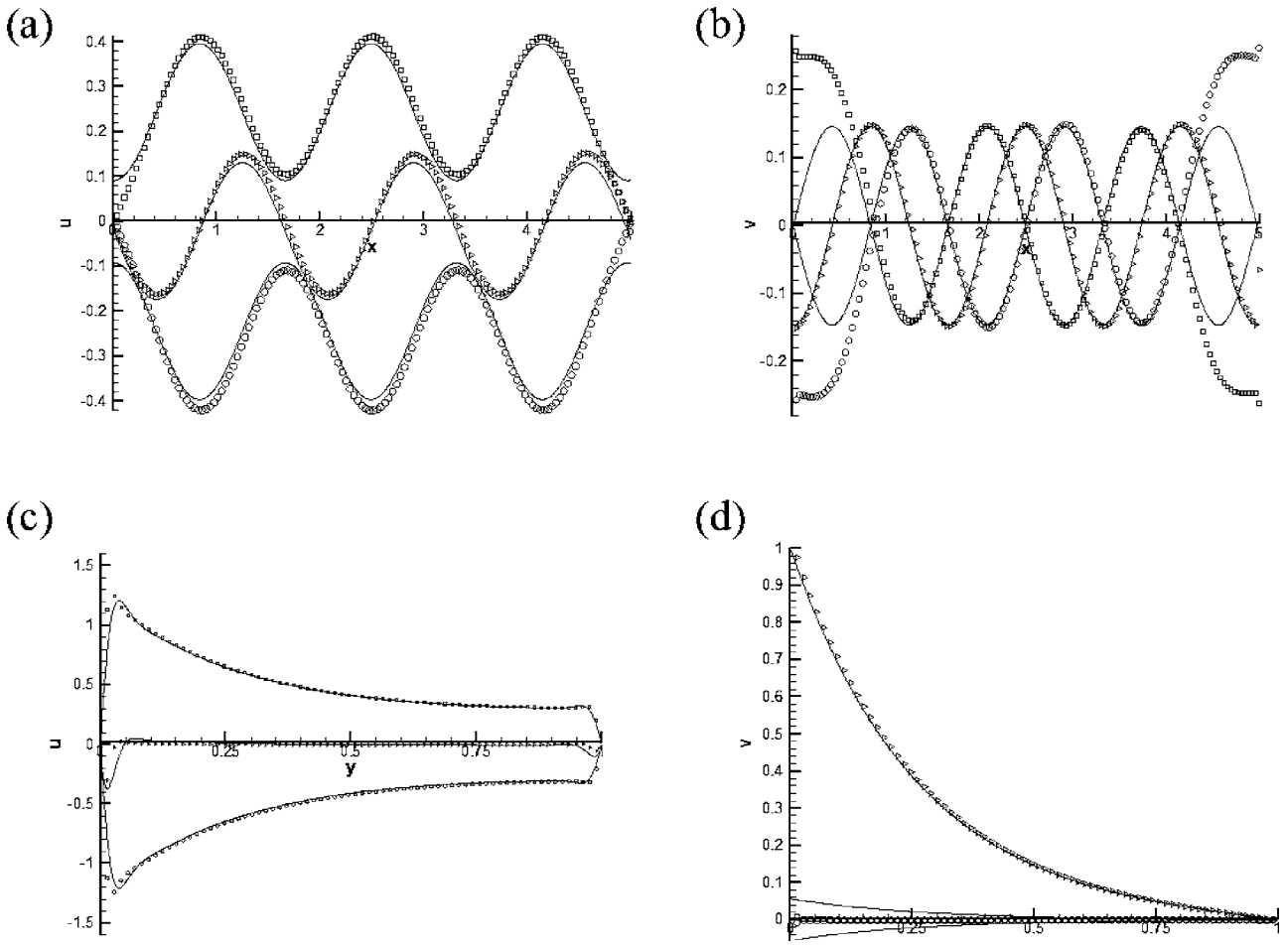

Fig. 3 Velocity profiles for $\varepsilon=0.01$ and Re=6288 at various times during a cycle. (*a*), (*b*), (*c*), and (*d*) show variation of $u(x,0.5,t)$, $v(x,0.5,t)$, $u(L/2,y,t)$, and $v(L/2,y,t)$, respectively. Symbols show the numerical solutions and the solid lines represent the leading-order asymptotic solution. Squares, triangles, and circles represent numerical snapshots at $t=0$, $T/4$, and $T/2$, respectively.

$$y' = \frac{y - \varepsilon f(x,t)}{1 - \varepsilon f(x,t)} \tag{8}$$

where $0 \leqslant y' \leqslant 1$. For convenience, we denoted y' as y in the figures. For the 30% deformation case ($\varepsilon=0.3$), we used a grid with 136 quadrilateral elements, similar to the grid shown in Fig. 1. The initial condition is obtained using an eighth-order simulation. The elements are concentrated near the lateral walls, where large gradients occur. Largest elements are placed near the moving surface and their height is equal to the amplitude of the traveling wave. The simulation results for Re=63 and Re=400 flows are shown in Figs. 4 and 5, respectively. The corresponding leading-order asymptotic solutions for both cases were obtained using Eqs. (A3)–(A5) and (A7). The numerical results were checked for grid independence by increasing the modal expansion order used in the simulations. For Re=63 flow, the computed velocities are qualitatively the same with the leading-order asymptotic results. However, there are some deviations between these two results. These deviations are attributed to the fact that the analytical solutions are based on an asymptotic expansion in ε, where the leading-order solution valid for $\varepsilon \equiv 0$ is plotted in the figures. For large ε values, the first- and higher-order terms in ε also play an important role, and these terms are neglected in our comparisons, but they were given in the works of Selverov and Stone [18] and Yi et al. [20]. For Re=400 flow, u velocity profile at time $t=T/4$ in Fig. 7(*c*) is completely different from the predictions of the leading-order analytical solution. This velocity profile shows that the fluid away from the bottom wall moves in the opposite direction to the traveling wave. We expect this behavior to further enhance mixing. Time-periodic flow was achieved for the streamwise and transverse velocity components at both Reynolds number values. Symmetry of the velocity profiles around the ordinate, observed in low amplitude simulations (Figs. 2 and 3), no longer exists for large-deformation cases. This can be explained by formation of a preferred flow direction for large amplitude motion, resulting in peristaltic pumping.

As can be seen from these figures, the velocity profiles are significantly different from those predicted by the asymptotic solution. For example, in Fig. 5, the numerically obtained streamwise and transverse velocities at $t=T/4$ are substantially different from the corresponding asymptotic predictions. This behavior is expected, due to the limitations of the asymptotic solution presented in the Appendix. We have also observed a time lag between the bottom wall motion and the bulk response of the fluid in the cavity at high Re conditions. Further comparisons between the asymptotic solution and the numerical results can be found in Ref. [35].

5 Mixing

In the previous section, we have shown the Reynolds number dependence of flow dynamics. In this section, we present the spe-

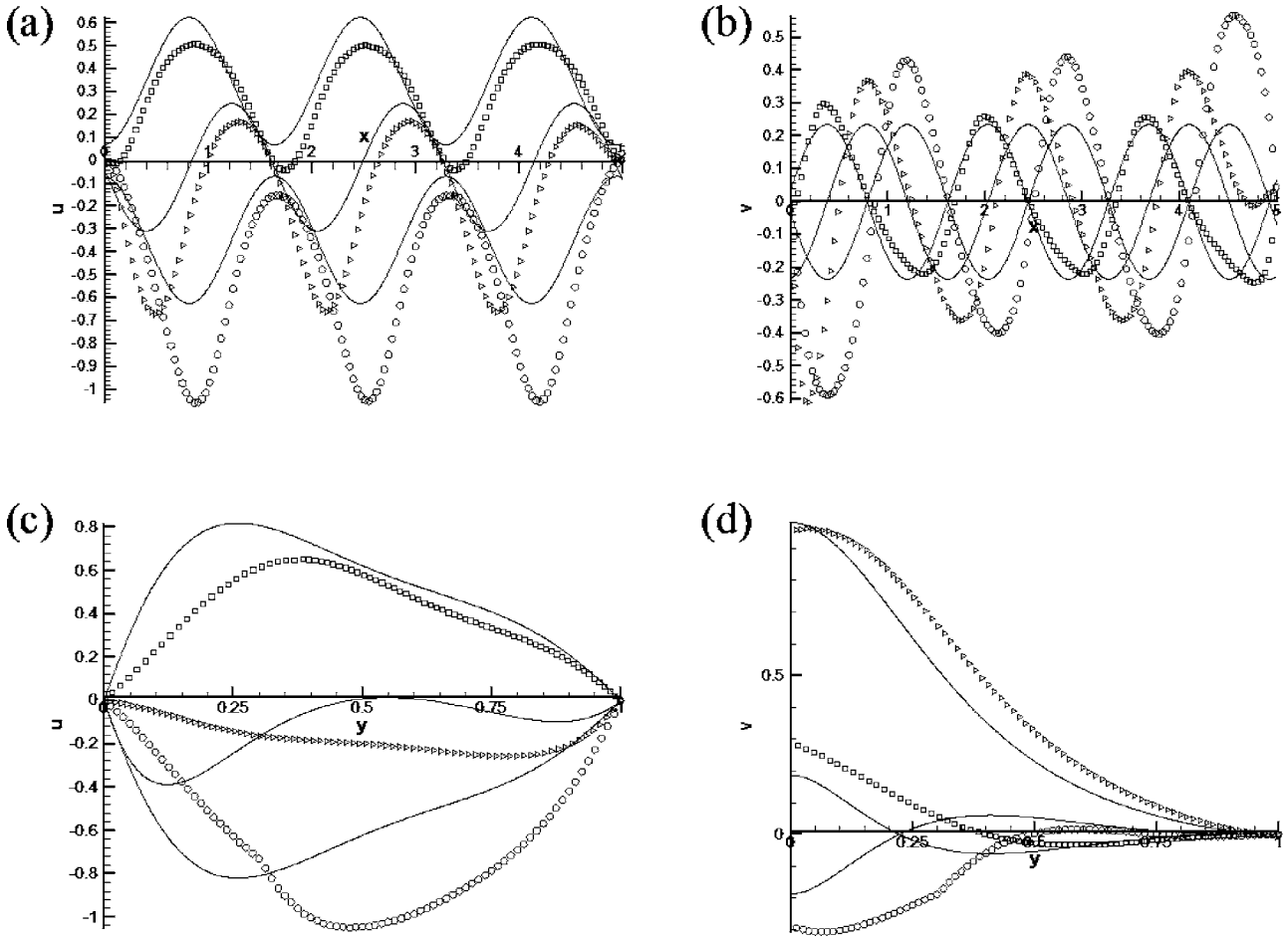

Fig. 4 Velocity profiles for $\varepsilon=0.3$ and Re=63 at various times during a cycle. (*a*), (*b*), (*c*), and (*d*) show variation of $u(x,0.5,t)$, $v(x,0.5,t)$, $u(L/2,y,t)$, and $v(L/2,y,t)$, respectively. Symbols show the numerical solutions and the solid lines represent the leading-order asymptotic solution. Squares, triangles, and circles represent numerical snapshots at $t=0$, $T/4$, and $T/2$, respectively.

cies mixing results for laminar flows. Numerical simulation of mixing requires solution of the Navier–Stokes (5) and (6) and the species transport equations given by

$$\frac{\partial\theta}{\partial t}+(\mathbf{u}\cdot\nabla)\theta=\frac{1}{\mathrm{Pe}}\nabla^2\theta \tag{9}$$

where θ is the species concentration and Pe is the Peclet number defined as

$$\mathrm{Pe}=\omega^* h^{*2}/D^* \tag{10}$$

where D^* is the mass diffusivity. The Peclet number is based on both the Reynolds and Schmidt numbers (i.e., $\mathrm{Pe}=\mathrm{Sc}\times\mathrm{Re}$), where the Schmidt number is given as

$$\mathrm{Sc}=D^*/\nu^* \tag{11}$$

We performed a series of mixing simulations for the high deformation case of $\varepsilon=0.3$. All simulations were performed for mixing of a scalar marker that has concentration of $\theta=1$ and $\theta=0$ in the upper and lower halves of the initially rectangular mixing domain, respectively. Therefore, the initial interface between the $\theta=1$ and $\theta=0$ conditions was at $y=0.5$, and a perfect mix would reach $\theta_0=0.5$ everywhere in the domain. In all simulations, the membrane is deformed and then moved in the form of a traveling wave motion, while the velocity field is developed from quiescent initial conditions.

In Fig. 6, we present evolution of the species concentration contours at various times. The results are obtained at Pe=6000 and Re=6000 conditions. Although the velocity and pressure fields are time periodic, species transport is transient. Since we start simulations from the quiescent initial conditions, transport is diffusion dominated for $t<4T$. At later times, we observe strong convective mixing, as shown in the contour plots. We qualitatively claim "convection enhanced mixing" for this flow, since the green colored contours, corresponding to $\theta_0\approx0.5$ conditions of a perfect mix, dominate the plot at later times. In the next section, we will quantify the mixing efficiency using the mixing index inverse (M^{-1}). Following this "rapid" mixing trend, we observe entrapment of higher-concentration fluid ($\theta>0.5$) at top left corner of the mixer for $t>20T$. The entrapped fluid mixes slowly and reduces the mixing efficiency.

We must emphasize that numerical resolution of the species concentration field becomes increasingly challenging for increased Pe. For example, the mixing results presented in Fig. 6 were obtained using the 136 element mesh shown in Fig. 1. However, each element utilized 15th-order modal expansions per direction, during both the initial membrane dilation and mixing simulations. Simulation of higher Pe values requires further increase in the elemental expansion orders, and makes numerical simulations impractical. Interface tracking methods may also become impractical for chaotically stirred flows, since the interface stretches and folds quite rapidly, and after a while it looses its coherence [36].

5.1 Mixing Quantification. In order to verify the mixing ef-

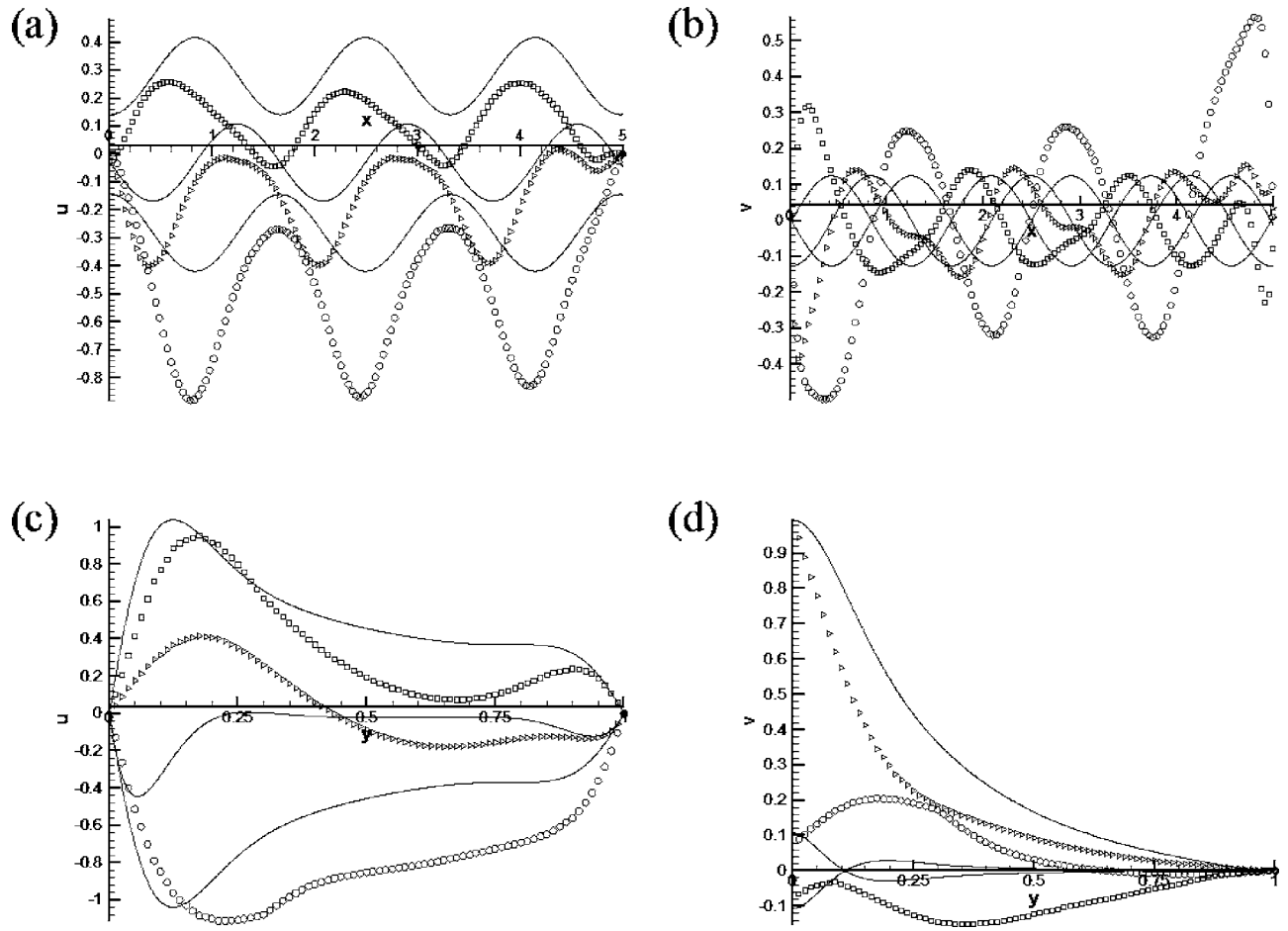

Fig. 5 Velocity profiles for $\varepsilon=0.3$ and Re=400 at various times during a cycle. (*a*), (*b*), (*c*), and (*d*) show variation of $u(x,0.5,t)$, $v(x,0.5,t)$, $u(L/2,y,t)$, and $v(L/2,y,t)$, respectively. Symbols show the numerical solutions and the solid lines represent the leading-order asymptotic solution. Squares, triangles, and circles represent numerical snapshots at $t=0, T/4$, and $T/2$, respectively.

ficiency, we used mixing index (M), which is based on the statistical distribution of concentration values in the domain. The mixing index is defined as

$$M = \frac{\sigma}{\theta_0} = \frac{1}{\theta_0}\sqrt{\langle\theta^2\rangle - \langle\theta\rangle^2} = \sqrt{\frac{1}{N}\sum_{i=1}^{N}\left(\frac{\theta_i}{\theta_0} - 1\right)^2} \qquad (12)$$

where θ_i is the average concentration inside the ith section of a total of N interrogation areas and σ is the standard deviation. The $\langle\cdots\rangle$ symbol denotes averaging over the area of the mixer. Based on the initial distribution of the species in our problem, a perfect mix would reach $\theta_0=0.5$. Most experimental studies on mixing utilize the mixing index based on the standard deviation of fluorescence intensity values from a perfect mix. We decided on the total number of interrogation areas (N) by subdividing each spectral element into $K\times K$ subsections. In the following, we used $K=30$, resulting in $N=122,400$. We checked the sensitivity of mixing index to N, and we have observed that further increase in N does not yield significant changes in the mixing index value (sensitivity of mixing index evolution as a function of N can be found in Ref. [35]). According to the definition in Eq. (12), a perfect mix results in $M=0$. Hence, smaller values of M show better mixing. For the closed mixer considered here, the mixing index varies as a function of time, and it can be used as a metric to assess the mixing efficiency. Better comparisons between various cases are possible using the *mixing index inverse* (M^{-1}). Since $M^{-1}\to\infty$, while $M\to 0$, therefore in the following, we present variation of M^{-1} as a function of time. One can associate the M^{-1} values with the concentration range ($\theta_0\pm\sigma$) using Eq. (12). For example, $M^{-1}=20$ corresponds to $\sigma=0.025$. This gives 95% mixing, if we define the mixing percentage as $(1-\sigma/\theta_0)\times 100\%$. Similarly, $M^{-1}=10$ corresponds to 90% mixing.

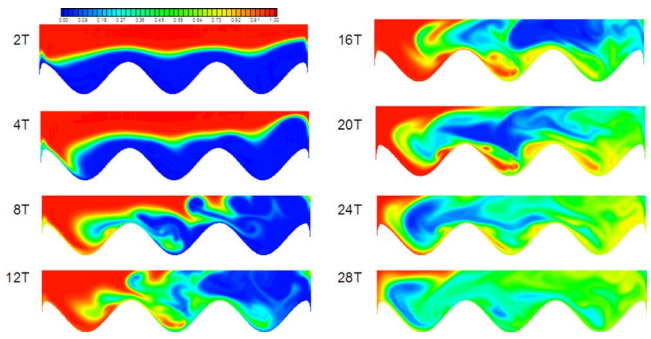

Fig. 6 Time evolution of species concentration contours at Re=6000 and Pe=6000 conditions for the $\varepsilon=0.3$ case

For convective-diffusive transport, long-time ($t\to\infty$) behavior of M^{-1} at large Peclet numbers (Pe$\to\infty$) is given as [22,23,27]

$$M^{-1} \propto \exp(\mathrm{Pe}^{-\alpha}t) \qquad (13)$$

where α is a positive exponent less than unity and t is the time normalized using convective time scales. The value of α depends

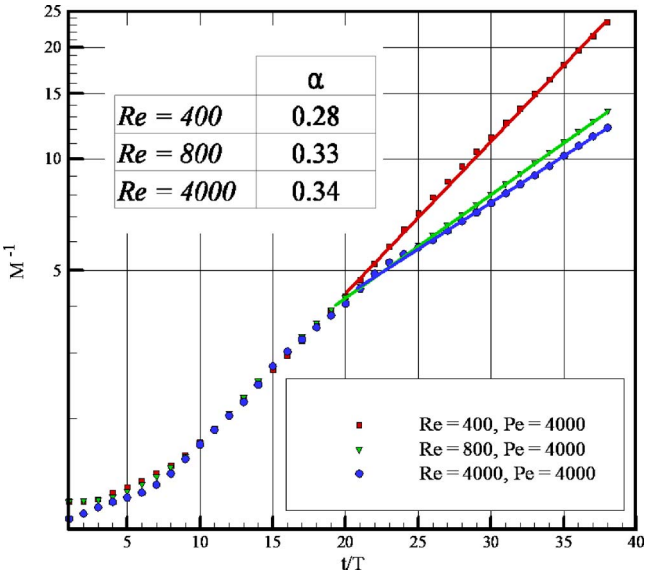

Fig. 7 Mixing index inverse variation as a function of the number of time periods (T) for three different flow conditions at Pe=4000. Time periods for all three cases are different from each other.

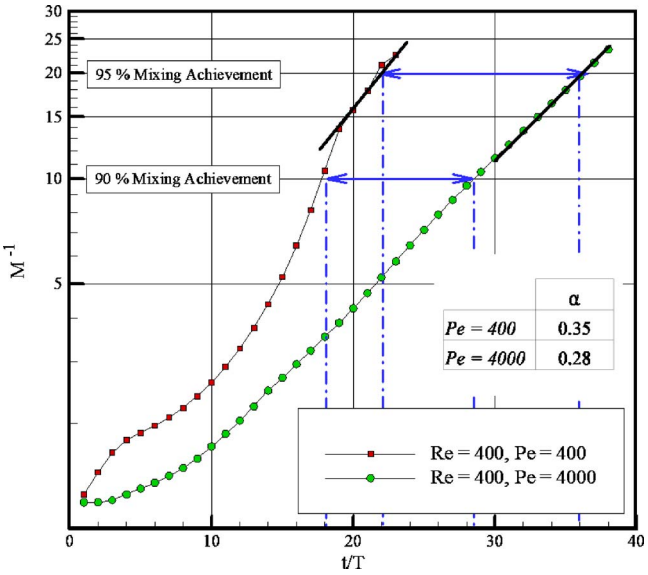

Fig. 8 Mixing index inverse variation as a function of the number of time period (T) for Re=400 flow at Sc=1 and Sc=10 conditions

on the flow conditions. For pure diffusion, $\alpha=1$ is observed, when the mixing time is normalized using a typical convective time scale so that Pe can still be defined. For several spatially periodic and unidirectional flows, $\alpha=1/2$ has been reported [22,23,27]. Theoretical estimates for α in globally chaotic flows give $\alpha\to 0$, while locally chaotic flows result in $\alpha<1/2$ for $\mathrm{Pe}\gg 1$ [27]. We must note that $\alpha=0$ is a singular limit, since it implies physical diffusion for $\mathrm{Pe}\to\infty$. Therefore, it is impossible to have $\alpha=0$ in an actual fully chaotic flow. Similarly, $\alpha<0$ implies faster mixing for increased Pe values at fixed kinematic conditions (i.e., Re), which is physically impossible for $\mathrm{Pe}\gg 1$.

In Fig. 7, we present the M^{-1} variation as a function of the number of time periods (T) for $\varepsilon=0.3$ and Pe=4000. Since the Pe is fixed while Re is varied, the Sc decreases with increasing Re. Comparison of mixing efficiency for all three cases can be done in several different ways depending on the size (h^*) and operation conditions (ω^*) of the device. For practical comparisons, let us assume that we fix the mixer size (h^*) and alter the Re simply by varying the wave speed (ω^*). The abscissa shows the number of time periods for each case. However, the time periods for all three cases are different, and can be obtained using $T_i^*=2\pi/\omega_i^*$. For example, $T^*_{\mathrm{Re}=400}=10\times T^*_{\mathrm{Re}=4000}$ and $T^*_{\mathrm{Re}=400}=2\times T^*_{\mathrm{Re}=800}$. This shows faster mixing with increased Re using dimensional time values. We must note that all simulations started from the same initial concentration distribution and quiescent flow conditions. We observe different trends in the figure, indicating the Re dependence of mixing at fixed Pe. Therefore, flow kinematics affects the species mixing significantly. Using Eq. (13), we observe increase in the α values as we increase Re. This is due to lower Sc values observed in large Re cases. In all cases, we observe three different trends in M^{-1} variation by time. The initial trend is dominated by convection-diffusion in transient flow for $t/T<10$, after which the flow becomes time periodic. The second trend from $t/T=10$ until $t/T=20$ is dominated by convective effects with $\alpha=0.28$ for all three cases. However, for $t/T\geqslant 20$, an asymptotic behavior with $\alpha\approx 1/3$ is observed for lower Sc values, despite the increased Reynolds number. We believe that this is due to the low Sc values, where diffusion effects start to become important in a well stirred flow with small striation thickness [36]. On the other hand, the Re=400 case continues to evolve with $\alpha=0.28$. It is important to note that all α values are below the typical "laminar stirring" limit, which is only possible by *locally chaotic flow* [22].

In Fig. 8, we present the $\varepsilon=0.3$ and Re=400 case at Pe=400 and Pe=4000. The M^{-1} growth for Pe=400 case shows three trends. We first observe diffusive growth for $t/T\leqslant 4$. This is followed by convective-diffusive transport until $t/T=18$, and onset of exponential variation afterward. As the long-time behavior, we observe $\alpha=0.34$ and $\alpha=0.28$ for Pe=400 and Pe=4000 cases, respectively. Since the flow kinematics is fixed, change in the α values at later times is due to the change in the diffusion effects, where lower Sc gives larger α values. By increasing the Schmidt number to 10, we observe that the α value is reduced below 0.35. Hence, we may experience much lower α values if we could have further increased the Schmidt number. This trend is consistent, since α decreases as the Sc is increased at fixed Re conditions [23,27]. Regarding the mixing efficiency, 22 and 36 time periods are required to achieve 95% mixing for the Pe=400 and Pe=4000 flows, respectively, resulting in 1.64 fold increase in the mixing time. This is considerably smaller than the mixing time obtained by typical laminar stirring, which would have scaled as $\mathrm{Pe}^{1/2}$ and resulted in 3.16 fold increase in the mixing time.

Using the mixing efficiency data in Fig. 8, we make a comparison of mixing enhancement due to convective-diffusive transport with that of pure diffusion. We first present the analytical solution of the species diffusion equation in a closed *rectangular domain* of $L\times h$. Due to no flow, the species diffusion equation with zero-flux boundary conditions can be simplified, and given in nondimensional form as

$$\frac{\partial\theta}{\partial t}=D\left(\frac{\partial^2\theta}{\partial y^2}\right) \tag{14}$$

where D $(=D^*t^*/h^{*2})$ is the normalized diffusivity, which can be interpreted as the mass transfer Fourier number [37], and t is the nondimensional time. Analytical solution of Eq. (14) is obtained using separation of variables, and given by [38]

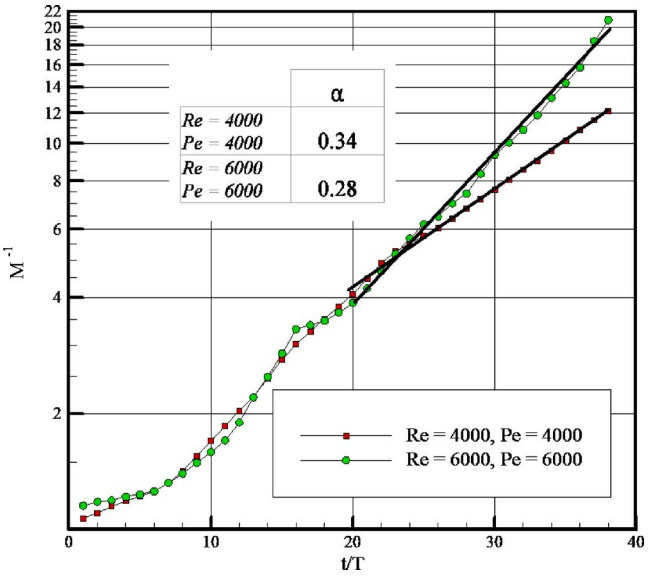

Fig. 9 Mixing index inverse variation as a function of the number of time period (T) for Re=4000 and Re=6000 conditions

$$\theta(y,t) = \frac{1}{\pi}\sum_{n=1}^{\infty} \exp[-\pi^2(2n-1)^2 tD]\sin[\pi(2n-1)y] \times\left\{\frac{1-\cos[\pi(2n-1)]}{2n-1}\right\} \quad (15)$$

If we choose the time scale (t^*) in definition of D as the reference time associated with the convective-diffusive transport cases presented in Fig. 8, we can compare the M^{-1} variation for diffusive and convective-diffusive cases. Our analytical estimates of mixing time for 95% mixing efficiency result in $t/T=120$ and $t/T=1200$ for Sc=1 and Sc=10 cases, respectively. This is 5.5 and 33.3 times slower than the convection enhanced mixing cases for Sc=1 and Sc=10, respectively. Similar gains can also be reported for 90% mixing efficiency.

It is important to give a dimensional example for the mixing times at Re=400 so that the importance of convective-diffusive mixing can be assessed. Let us assume liquid flow with $D^*=10^{-7}$ m^2/s and $\nu^*=10^{-6}$ m^2/s (Sc=10) and a characteristic length scale of $h^*=1$ cm. For Re=400 case, we obtain $T^*=0.25$ s, for which 95% mixing happens in 9 s and 5 min for the convection enhanced and pure diffusion mixing cases, respectively. Further reduction in the length scales results in faster mixing times even using pure diffusion. This is due to the low Sc values used in this study. We expect differences between the time scales of convection enhanced and pure diffusion mixing processes to increase by increasing the Sc. However, Sc numbers utilized in the simulations were limited due to the computational restrictions. Therefore, the current results are most useful for peristaltic mixers with characteristic dimensions on the order of centimeters or larger, where the mixing time can be reduced from minutes to seconds.

In Fig. 9, we present the M^{-1} variation as a function of the number of time periods (T) for $\varepsilon=0.3$ at Re=4000 and Re=6000. Both simulations are performed for Sc=1. For fixed fluid properties and mixer dimensions, we have $T^*_{\mathrm{Re}=4000}=1.5\times T^*_{\mathrm{Re}=6000}$. Hence, we obtain faster mixing at Re=6000 than the Re=4000 case on real time basis. For $t/T\geqslant 20$, we observe $\alpha=0.34$ and $\alpha=0.28$ for Re=4000 and Re=6000 cases, respectively. Although M^{-1} variation at earlier times is similar for both cases, the Re=4000 case exhibits increased α values for $t/T\geqslant 20$, indicating stronger diffusion effects in a well stirred system. Comparison of both cases shows that the α value decreases due to the combined effects of the flow kinematics and increases in the Pe. In addition, the α values for both cases show enhanced mixing beyond the typical laminar stirring limit, which is only possible by locally chaotic flow [22].

6 Conclusions

We studied the two-dimensional flow field, species transport, and mixing in a peristaltic mixer as functions of the Reynolds and Peclet numbers and the traveling wave amplitude. Comparisons between the numerically predicted velocities and the leading-order asymptotic solutions have shown increased deviations for increased Re and ε. This is attributed to the limitations of the *leading-order asymptotic solutions*. In addition, these solutions do not consider the mixer sidewalls, which create additional discrepancies between the two results. Overall, strong dependence of flow kinematics on both the Re and ε is observed.

We simulated species transport in the peristaltic mixer, and quantified the mixing efficiency using time variation of the mixing index inverse M^{-1} at various Re and Sc conditions. From flow kinematics perspective, we expect large amplitude deformations and high Re cases lead to enhanced and faster stirring. However, at a fixed Re, the species transport also experiences diffusion effects characterized by the Sc. Therefore, mixing due to peristalsis needs to be characterized as a function of both the Re and Sc. We observed $M^{-1}\propto\exp(\mathrm{Pe}^{-\alpha}t)$ for $t\geqslant 20T$ in all simulations, and characterized mixing using the exponent α. Smaller values of α show better mixing efficiency. Specifically, we observed $0.28\leqslant\alpha\leqslant 0.35$ in all simulations. In the asymptotic limit of $\mathrm{Pe}\rightarrow\infty$, $\alpha=1/2$ and $\alpha<1/2$ behaviors indicate laminar and partially chaotic stirring cases, respectively [22,27]. Current results obtained at finite Pe conditions indicate $0.28\leqslant\alpha\leqslant 0.34$, which is only possible by locally chaotic flows. Results in Fig. 8 show reduction in α with increased Sc values at fixed kinematic conditions (Re). This indicates importance of the Peclet number in evaluation of the α value. Larger α values are observed at low Sc conditions, where species diffusion becomes dominant. Therefore, we expect to observe further reductions in the α value at fixed Re conditions, with increased Sc values. In Fig. 9, we observed that α values decrease from 0.34 to 0.28, when the Re increased from 4000 to 6000 at fixed Sc conditions. This is due to the effect of change in the flow kinematics and Pe, as a result of increase in the Re. Overall, the simulation results indicate enhanced mixing rates beyond the capabilities of typical laminar flow conditions. We interpreted this as a result of chaotic stirring. However, the presence of chaos and the chaotic strength needs to be further quantified using Lagrangian particle tracking based methods, such as the finite time Lyapunov exponents, Poincaré sections, interface stretching, and box-counting methods [36]. Our future work will include such characterization studies, which require very accurate knowledge of the flow field, and long-time integration of particle paths that will be achieved using high-order numerical formulations.

Acknowledgment

Partial financial support from the TAMU Center for Integrated Microchemical Systems and the National Science Foundation under Grant No. 0306622 is acknowledged.

In Memoriam: This work is dedicated to our colleague and friend, Mr. Saurabh Kumar, who passed away on March 21, 2003 in a car accident. In 1998, Saurabh graduated with honors from the Institute of Technology, Banaras Hindu University, Varanasi, India with a Bachelor of Technology degree in Mechanical Engineering. He worked in India's largest automobile manufacturing company until he started his graduate work in the Mechanical Engineering Department at Texas A&M University in August 2000. He graduated with a Master of Science degree in Mechanical Engineering in August 2002.

Appendix

Using perturbation expansions in ε, Yi et al. [19,20] obtained asymptotic solutions for the velocity field in the following form:

$$\mathbf{u}(x,y,t;\varepsilon) = \mathbf{u}_0(x,y,t) + \varepsilon\mathbf{u}_1(x,y,t) + \varepsilon^2\mathbf{u}_2(x,y,t) + O(\varepsilon^3) \tag{A1}$$

where the subscripts indicate the order of the asymptotic solution. For our studies, we will only consider the leading-order solution ($\mathbf{u}_0$) for convenience. However, solution of the problem including the second-order terms in ε can be found in Refs. [18,20] for the moving bottom-surface and the moving bottom- and top-surface cases, respectively. We must emphasize that the asymptotic analytical solutions presented in this section are valid strictly for $m \to 0$ and $\varepsilon \to 0$. The leading-order solution of Eqs. (5) and (6) is given in the following form:

$$\mathbf{u}_o = u_o\mathbf{e}_x + v_o\mathbf{e}_y \tag{A2}$$

The streamwise velocity is decomposed into two components

$$\begin{aligned} u_0(x,y,t) &= u_{0,1}(x,y,t) + u_{0,2}(y,t) \\ &= Re\{U_{0,1}(y)\exp[i(kx-t)] + U_{0,2}(y)\exp(-it)\} \end{aligned} \tag{A3}$$

while the transverse velocity is given by

$$v_0(x,y,t) = V_0(y)\exp[i(kx-t)] \tag{A4}$$

Here $U_{0,2}$ is independent of x far away from the lateral walls, while $U_{0,1}$ is periodic in x [19]. This makes the solution valid only *far away* from the lateral walls. Following Yi et al. [19],

$$U_{0,2}(y) = \frac{\beta[1 - \cos(\sqrt{i}\beta y) - \tan(1/2\sqrt{i}\beta)\sin(\sqrt{i}\beta y)]}{k[\beta + 2(-1)^{3/4}\tan(1/2\sqrt{i}\beta)]} \tag{A5}$$

This equation is valid for moderate values of β (typically $\beta < 50$). For larger values of β, matched asymptotic expansions are used to approximate (A5) as [19]

$$U_{0,2}(y) \approx \frac{i\sqrt{i}\beta}{k}\frac{\{1 - \exp(i\sqrt{i}\beta y) - \exp[i\sqrt{i}\beta(1-y)]\}}{\{i\sqrt{i}\beta - 2[1 - \exp(i\sqrt{i}\beta)]\}} \tag{A6}$$

The first velocity component $U_{0,1}$ and the transverse velocity V_0 were obtained using a stream function (ψ_0) analysis for a peristaltically pumped channel with open ends. Solution of this problem is given in Ref. [29], and it is valid for all β values.

$$U_{0,1}(y) = \frac{\partial\psi_0}{\partial y} \quad \text{and} \quad V_0(y) = -\frac{\partial\psi_0}{\partial x} \tag{A7}$$

where

$$\psi_0(x,y,t) = Re[k^{-1}e^{i(kx-t)}M(y)] \tag{A8}$$

$$\begin{aligned} M(y) = A\sinh[k(1-y)] + B\cosh[k(1-y)] + C\sinh[\gamma(1-y)] \\ + D\cosh[\gamma(1-y)] \end{aligned} \tag{A9}$$

$$\gamma^2 = k^2 - i\beta^2 \tag{A10}$$

$$A = \frac{[\sinh(k) - (\gamma/k)\sinh(\gamma)]}{F} \tag{A11}$$

$$B = \frac{[\cosh(\gamma) - \cosh(k)]}{F} \tag{A12}$$

$$C = -\frac{k}{\gamma}A \quad D = -B \tag{A13}$$

$$\begin{aligned} F = \left[\sinh(k) - \frac{\gamma}{k}\sinh(\gamma)\right]\left[\sinh(k) - \frac{k}{\gamma}\sinh(\gamma)\right] \\ - [\cosh(k) - \cosh(\gamma)]^2 \end{aligned} \tag{A14}$$

For $\beta > 50$, Eq. (A8) gave large round off and truncation errors that lead to spurious oscillations [19]. For such conditions, Selverov and Stone obtained the following approximate solution [18]:

$$\begin{aligned} u_{0,1}(x,y,t) \\ = Re\left(\exp[i(kx-t)]\right. \\ \left.\times\left\{\frac{\cosh(k)\{\exp(\zeta y) + \exp[\zeta(1-y)]\} - \cosh[k(1-y)]}{\sinh(k)}\right\}\right) \end{aligned} \tag{A15}$$

$$v_0(x,y,t) = \sinh(kx-t)\sinh[k(1-y)]/\sinh(k) \tag{A16}$$

where

$$\zeta = \frac{\beta}{\sqrt{2}}(i-1) \tag{A17}$$

References

[1] Manz, A., Graber, N., and Widmer, H. M., 1990, "Miniaturized Total Chemical Analysis Systems: A Novel Concept for Chemical Sensing," Sens. Actuators B, **1**, pp. 244–248.

[2] Barry, R., and Ivanov, D., 2004, "Microfluidics in Biotechnology," J. Nanobiotechnology, **2**, pp. 2–6.

[3] Natarajan, S., and Dehghan, M., 2000, "Numerical Prediction of Flow in a Model of a (Potential) Soft Acting Peristaltic Blood Pump," Int. J. Numer. Methods Fluids, **32**, pp. 711–724.

[4] Conklin, B., Surowiec, S., Lin, P., and Chen, C., 1999, "A Novel System for Physiologic Pulsatile Perfusion of Intact Vascular Tissue," *Engineering in Medicine and Biology 21st Annual Conference and the 1999 Annual Fall Meeting of the Biomedical Engineering Society*, pp. 123.

[5] Jaouen, P., Vandanjon, L., and Quemeneur, F., 1996, "Shear Stress of Microalgal Cell Suspensions (Tetraselmis Suecica) in Tangential Flow Filtration Systems: The Role of Pumps," Bioresour. Technol., **68**, pp. 149–154

[6] Kieran, P. M., O'Donell, H. J., Malone, D. M., and MacLoughin, P. F., 1995, "Fluid Shear Effects on Suspension Cultures of Morinda Citrifolia," Biotechnol. Bioeng., **45**, pp. 415–425.

[7] Berg, J. M., Anderson, R., Anaya, M., Lahlouh, B., Dallas, T., and Holtz, M., 2003, "A Two-Stage Discrete Peristaltic Micropump," Sens. Actuators, A, **104**, pp. 6–10.

[8] Bu, M., Melvin, T., Ensell, G., Wilkinson, J. S., and Evans, A. G. R., 2003, "Design and Theoretical Evaluation of a Novel Microfluidic Device to be Used for PCR," J. Micromech. Microeng., **13**, pp. S125–S130.

[9] Xie, J., Shih, J., Lin, Q., Yang, B., and Taia, Y., 2004, "Surface Micromachined Electrostatically Actuated Micro Peristaltic Pump," Lab Chip, **4**, pp. 495–501.

[10] Sundararajan, N., Kim, D., and Berlin, A. A., 2005, "Microfluidic Operations Using Deformable Polymer Membranes Fabricated by Single Layer Soft Lithography," Lab Chip, **5**, pp. 350–354.

[11] Goldschmidtböing, F., Doll, A., Heinrichs, M., Woias, P., Schrag, H., and Hopt, U. T., 2005, "A Generic Analytical Model for Micro Diaphragm Pumps With Active Valves," J. Micromech. Microeng., **15**, pp. 673–683.

[12] Cao, L., Mantell, S., and Polla, D., 2000, "Implantable Medical Drug Delivery Systems Using Microelectromechanical Systems Technology," *Proceedings of the first Annual International Conference on Microtechnologies in Medicine and Biology*, pp. 487–490.

[13] Teymoori, M. M., and Abbaspour-Sani, E. A., 2002, "A Novel Electrostatic Micromachined Pump for Drug Delivery Systems," *Semiconductor Electronics, 2002, Proceedings ICSE 2002, IEEE International Conference*, Dec. 19–21, pp. 105–109.

[14] Putz, R., and Pabst, R., 2000, *Sobotta Atlas of Human Anatomy*, 13th ed., Lippincott, Williams and Wilkins, New York, Vol. 2.

[15] Shapiro., A. H., Jaffrin, M. Y., and Weinberg, S. L., 1969, "Peristaltic Pumping With Long Wavelengths at Low Reynolds Numbers," J. Fluid Mech., **97**, pp. 799–825.

[16] Yin, F. C. P., and Fung, Y. C., 1971, "Comparison of Theory and Experiment in Peristaltic Transport," J. Fluid Mech., **47**, pp. 93–112.

[17] Fauci, L. J., 1992, "Peristaltic Pumping of Solid Particles," Comput. Fluids, **21**, pp. 583–598.

[18] Selverov, K. P., and Stone, H. A., 2001, "Peristaltically Driven Channel Flows With Applications Toward Micromixing," Phys. Fluids, **13**, pp. 1837–1859.

[19] Yi, M., Bau, H. H., and Hu, H., 2000, "A Peristaltic Meso-Scale Mixer," *IMECE 2000: Proceedings of the MEMS Symposium*, Orlando, FL, Nov 5–10.

[20] Yi, M., Bau, H. H., and Hu, H., 2002, "Peristaltically Induced Motion in a

Closed Cavity With Two Vibrating Walls," Phys. Fluids, **14**(1), pp. 184–197.
[21] Carlsson, F., Sen, M., and Löfdahl, L., 2005, "Fluid Mixing Induced by Vibrating Walls," Eur. J. Mech. B/Fluids, **24**, pp. 366–378.
[22] Gleeson, J. P., 2005, "Transient Micromixing: Examples of Laminar and Chaotic Stirring," Phys. Fluids, **17**, p. 100614.
[23] Giona, M., Cerbelli, S., and Vitacolonna, V., 2004, "Universality and Imaginary Potentials in Advection-Diffusion Equations in Closed Flows," J. Fluid Mech., **513**, pp. 221–237.
[24] Aref, H., 1984, "Stirring by Chaotic Advection," J. Fluid Mech., **143**, pp. 1–21.
[25] Aref, H., and Balachandar, S., 1986, "Chaotic Advection in Stokes flows," Phys. Fluids, **29**, pp. 3515–3521.
[26] Ottino, J. M., 1989, *The Kinematics of Mixing: Stretching, Chaos, and Transport*, Cambridge University Press, Cambridge.
[27] Giona, M., Cerbelli, S., and Vitacolonna, V., 2004, "Spectral Properties and Transport Mechanisms of Partially Chaotic Bounded Flows in the Presence of Diffusion," Phys. Rev. Lett., **92**(11), p. 114101.
[28] Kays, W. M., and Crawford, M. E., 1980, *Convective Heat and Mass Transfer*, 2nd ed., McGraw-Hill, New York.
[29] Fung, Y. C., and Yih, C. S., 1968, "Peristaltic Transport," ASME Trans. J. Appl. Mech., **35**, pp. 669–675.
[30] Folta, J. A., Raley, N. F., and Hee, E. W., 1992, "Design, Fabrication and Testing of a Miniature Peristaltic Membrane Pump," *Proceedings of IEEE Solid-State Sensor and Actuator Workshop Fifth Technical Digest*, Hilton Head, SC, Jun. 22–25, pp. 186–189.
[31] Tseng, L.-L.-W.-K., Lin, J., Sung, W.-C., Chen, S.-H., and Lee, G.-B., 2006, "Active Micro-Mixers Using Surface Acoustic Waves on Y-Cut 128° $LiNbO_3$," J. Micromech. Microeng., **16**, pp. 539–548.
[32] Gad-el-Hak, M., 2002, *The MEMS Handbook*, CRC, Boca Raton, FL.
[33] Beskok, A., and Warburton, T. C. E., 2001, "An Unstructured hp Finite-Element Scheme for Fluid Flow and Heat Transfer in Moving Domains," J. Comput. Phys., **174**, pp. 492–509.
[34] Karniadakis, G. E., and Sherwin, S. J., 1999, *Spectral hp Element Methods for CFD*, Oxford University Press, Oxford.
[35] Kumar, S., 2002, "*Numerical Simulation of Micro-Fluidic Passive and Active Mixers*," MS thesis, Texas A&M University, College Station, TX.
[36] Kim, H. J., 2004, "*Quantification of Chaotic Mixing in Microfluidic Systems*," MS thesis, Texas A&M University, College Station, TX.
[37] Incorpera, F. P., and DeWitt, D. P., 2002, *Fundamentals of Heat and Mass Transfer*, Wiley, New York.
[38] Holden, M. A., Kumar, S., Castellana, E. T., Beskok, A., and Cremer, P. S., 2003 "Generating Fixed Concentration Arrays in a Microfluidic Device," Sens. Actuators B, **92**, pp. 199–207.

Assessment of Predictive Capabilities of Detached Eddy Simulation to Simulate Flow and Mass Transport Past Open Cavities

Kyoungsik Chang
KAIST,
Daejeon 305-701, South Korea
e-mail: kschang76@kaist.ac.kr

George Constantinescu[1]
Civil and Environmental Engineering Department
and IIHR Hydroscience and Engineering,
The University of Iowa,
Iowa City, IA 52242
e-mail: sconstan@engineering.uiowa.edu

Seung-O Park
KAIST,
Daejeon 305-701, South Korea
e-mail: sopark@kaist.ac.kr

The three-dimensional (3D) incompressible flow past an open cavity in a channel is predicted using the Spalart–Almaras (SA) and the shear-stress-transport model (SST) based versions of detached eddy simulation (DES). The flow upstream of the cavity is fully turbulent. In the baseline case the length to depth (L/D) ratio of the cavity is 2 and the Reynolds number $\mathrm{Re}_D=3360$. *Unsteady RANS (URANS) is performed to better estimate the performance of DES using the same code and meshes employed in DES. The capabilities of DES and URANS to predict the mean flow, velocity spectra, Reynolds stresses, and the temporal decay of the mass of a passive contaminant introduced instantaneously inside the cavity are assessed based on comparisons with results from a well resolved large eddy simulation (LES) simulation of the same flow conducted on a very fine mesh and with experimental data. It is found that the SA-DES simulation with turbulent fluctuations at the inlet gives the best overall predictions for the flow statistics and mass exchange coefficient characterizing the decay of scalar mass inside the cavity. The presence of inflow fluctuations in DES is found to break the large coherence of the vortices shed in the separated shear layer that are present in the simulations with steady inflow conditions and to generate a wider range of 3D eddies inside the cavity, similar to LES. The predictions of the mean velocity field from URANS and DES are similar. However, URANS predictions show poorer agreement with LES and experiment compared to DES for the turbulence quantities. Additionally, simulations with a higher Reynolds number* ($\mathrm{Re}_D=33{,}600$) *and with a larger length to depth ratio* ($L/D=4$) *are conducted to study the changes in the flow and shear-layer characteristics, and their influence on the ejection of the passive contaminant from the cavity.*
[DOI: 10.1115/1.2786529]

Keywords: open cavity, detached eddy simulation, large eddy simulation, mass exchange

1 Introduction

Cavity flows form a special category of separated flows that are relevant for many engineering applications. Two common examples in aerospace and mechanical engineering are the flow over the bomb bay and landing systems of aircrafts or past the sunroof of cars. In these flows, the effect of pressure and velocity oscillations is the generation of aeroacoustic noise and vibrations that can eventually increase the fatigue of the structures. For environmental fluid mechanics applications, the presence of cavity-like geometries in rivers, lakes, or urban canyons may adversely affect the water or air quality when pollutants accumulate in these cavities. Pollutants (e.g., chemical toxic air and contaminated water from groundwater intrusions) infiltrated or introduced inside these cavities can produce stagnant pools, which may be harmful to the environment. The main difference with the cavity flows typically encountered in aerodynamics flows is that the flow is incompressible and fully turbulent upstream of the cavity. This is the regime of interest in the present work. Also, the quantitative characterization of the mass exchange between the cavity and the surrounding is highly important.

Though many experimental and numerical investigations of cavity flows are available, most of them have focused on the compressible case with a developing laminar or turbulent incoming boundary layer. Sorohia [1] measured the minimum cavity length for oscillations to occur in the flow over an axisymmetric cavity. He observed that the frequency of the main oscillations switched to a higher mode as the cavity length was increased. Rockwell [2] used linear stability theory to predict the main oscillatory frequency for incompressible flow over 2D cavities and validated his results with the experimental data of Ethembabaoglu [3]. Pereira and Sousa [4,5] used laser-doppler anemometry (LDA) to measure the mean velocity profiles and Reynolds stresses inside the cavity region and the separated shear layer for the incompressible flow past a 2D rectangular cavity (the cavity Reynolds number was $\mathrm{Re}_D=UD/\nu=3360$, where U is the mean velocity upstream of the cavity, D is the cavity depth, and ν is the molecular viscosity) with an incoming fully turbulent flow. Additionally, they studied the influence of the trailing edge geometry on the flow. Lin and Rockwell [6] performed a similar study for the case in which a relatively thin turbulent boundary layer was present upstream of the cavity at $\mathrm{Re}_D\sim 28{,}000$. They characterized the scaling of the eddies that populate the separated shear layer and found that the jetlike flow, formed because of partial or total injection of shear-layer eddies inside the cavity close to the trailing edge corner, can induce further jittering of the shear layer.

[1]Corresponding author.

Contributed by the Fluids Engineering Division of ASME for publication in the JOURNAL OF FLUIDS ENGINEERING. Manuscript received August 1, 2006; final manuscript received June 5, 2007. Review conducted by Surya P. Vanka.

Grace et al. [7] performed detailed measurements of the mean velocity and Reynolds stresses for 2D shallow cavity flows with a laminar and a turbulent incoming boundary layer at 12,500 $<\mathrm{Re}_D<25{,}000$. In the laminar case, transition to turbulence was observed to take place in the separated shear layer on the top of the cavity. The distribution of the primary Reynolds shear stress was found to be strongly dependent on the characteristics of the incoming boundary layer.

Several studies show that Reynolds averaged Navier-Stokes (RANS) turbulence models predict reasonably well the mean flow past cavitylike geometries but often are not capable of predicting the oscillatory features and higher order statistics. In some cases [8], the unsteady RANS (URANS) simulation was shown to converge to steady state due to excessive values of the eddy viscosity in the regions of high strain rate or near the trailing edge where the shear-layer instabilities originate. Numerical simulations of incompressible cavity flows using eddy-resolving techniques include the 2D direct numerical simulation (DNS) of Ghaddar et al. [9] of the flow in periodically grooved channels and the 2D DNS simulations by Pereira and Sousa [4,5], which focused on the study of the coupling between the shear layer and the recirculation cavity flow. The mesh sizes in these simulations were around 40,000 cells. Recently, Yao et al. [10] used DNS and large eddy simulation (LES) to calculate the flow past a 3D cavity with an incoming laminar boundary layer. At low Reynolds numbers ($\mathrm{Re}_D\sim 5000$), the flow was observed to remain laminar over the cavity. As the Reynolds number was increased to 5×10^4, the disturbances caused by the oscillations of the separated shear layer forced transition to turbulence. The same authors [11] studied the changes in the characteristics of the cavity flow function of the cavity type (deep or shallow) and the incoming boundary layer thickness using DNS. It was observed that for thin boundary layers or higher Reynolds numbers, the large-scale recirculation flow pattern inside the cavity becomes more complex. Chang et al. [12] performed LES of the incompressible flow past an open cavity with a thin laminar and a fully turbulent incoming boundary layer at $\mathrm{Re}_D\sim 3360$.

URANS and detached eddy simulation (DES) simulations of compressible flow past 2D and 3D cavities with $L/D=4.4$ $\mathrm{Re}_D=2\times 10^5$, a Mach number of 0.6, and a turbulent incoming boundary layer were performed by Shieh and Morris [13]. The dominant shear-layer frequencies were found to be in good agreement with Rossiter's formula [14]. For the case of a 2D cavity, the flow was found to oscillate in the wake mode, while for the 3D cavity, the flow was found to oscillate in shear-layer mode. Arunajatesan and Sinha [15] conducted simulations using a hybrid RANS/LES method based on a modified k-ε model. The predicted pressure spectra on the cavity floor were found to be close to experimental results. Chang and Park [16] investigated the physics of deep 3D incompressible cavity flows using the hybrid RANS/LES model of Bush and Mani [17]. The predictions of the oscillatory flow features and vortical structures were found to be close to those measured by Cattafesta [18].

In the present work, the incompressible flow past an open cavity in a channel and the mass exchange between the cavity and the overflow are investigated using 3D URANS and DES simulations. As the characteristics of the separated region in cavity flows are very different compared to the massive separation encountered in flows past bluff bodies for which DES was shown to be very successful, a detailed study of the predictive abilities of DES for this kind of separated flows is important. Regions in which the flow is similar to the one past isolated or series of cavities are present in many complex turbulent flows of interest in engineering in which the Reynolds numbers are too high for LES to be attempted. A question which this study tries to answer is whether or not DES can better capture some aspects of the flow past cavities and associated transport processes compared to URANS. A second question is whether superimposing velocity fluctuations at the inflow section will result in significantly more accurate predictions of the flow and mass transport. Though for the case of flow over bluff bodies the additional jittering was shown not to have a significant effect on the accuracy of the flow predictions, the flow over cavities is more challenging in this respect for DES. Finally, the effects of the Reynolds number and cavity aspect ratio L/D are investigated by performing additional simulations and comparing with the baseline case ($L/D=2$, $\mathrm{Re}_D=3360$) results and with available data from previous numerical simulations and linear stability theory. Recommendations are made on the minimum grid density in the cavity region needed to accurately predict the flow and the mass decay of the contaminant ejected from the cavity.

2 Numerical Method, Computational Domain, Grid Generation, and Flow Conditions

Because of the large computational cost of LES at high Reynolds numbers, several hybrid RANS/LES methods were proposed during the last decade (e.g., see Refs. [19–21]). Maybe the most popular is DES, which uses RANS close to the solid boundaries (most RANS models predict well the flow in the thin attached boundary layers) and LES away from them in a nonzonal approach. DES is well suited for prediction of massively separated flows in which the detached shear-layer instabilities play a more important role than the turbulent structures transported in the attached boundary layers. However, DES has difficulties in predicting flows in which separation does not play an important role (e.g., channel flows).

DES was originally proposed [22] in a formulation based on the Spalart–Almaras (SA) one-equation model that was modified such that it reduces to its RANS formulation near solid surfaces and to a Smagorinsky-like subgrid model away from the solid surfaces. The DES formulation of the SA model is obtained by replacing the turbulence length scale (distance to the nearest wall, l_{SA}, in the SA RANS model) with l_{DES}, which is defined as $l_{\mathrm{DES}}=\min(l_{\mathrm{SA}},C_{\mathrm{DES}}\Delta)$, where the model parameter C_{DES} is equal to 0.65 and Δ is a measure of the local grid size. When the production and destruction terms of the model are balanced, the length scale in the LES regions $l_{\mathrm{DES}}=C_{\mathrm{DES}}\Delta$ becomes proportional to the local grid size and yields an eddy viscosity proportional to the mean rate of strain and Δ^2 as in LES, which allows the energy cascade down to grid size. The eddy viscosity predicted by DES in the LES regions goes to zero if the local grid size decreases to zero as in classical LES.

More recently, Strelets [23] proposed a new DES version based on the shear stress transport (SST) two-equation model. The DES formulation of SST is obtained by redefining the turbulence length scale (l_{SST}) in the dissipation term of the transport equation for the modeled turbulence kinetic energy (tke) as $l_{\mathrm{DES}}=\min(l_{\mathrm{SST}},C_{\mathrm{DES}}\Delta)$. The model parameter C_{DES} is obtained from $C_{\mathrm{DES}}=(1-F_1)C_{\mathrm{DES}}{}^{k\text{-}\varepsilon}+F_1C_{\mathrm{DES}}{}^{k\text{-}\omega}$ using the blending function F_1 proposed by Menter [24]. The values of $C_{\mathrm{DES}}{}^{k\text{-}\varepsilon}$ and $C_{\mathrm{DES}}{}^{k\text{-}\omega}$ are 0.61 and 0.78 respectively.

A general description of the DES/URANS code used in the present work is given in Constantinescu and Squires [25]. The 3D incompressible Navier–Stokes equations are integrated using a fully implicit fractional-step method. The governing equations are transformed to generalized curvilinear coordinates on a nonstaggered grid. Convective terms in DES are discretized using a blend of fifth-order accurate upwind biased scheme and second-order central scheme following Travin et al. [26] to minimize the level of numerical dissipation away from solid boundaries. The blending function σ proposed in Ref. [26] is used. For URANS, the fifth-order upwind scheme is adopted. All other terms in the momentum and pressure-Poisson equations are approximated using second-order central differences. The discrete momentum (predictor step) and turbulence model equations are integrated in pseudotime using the alternate direction implicit (ADI) approximate factorization scheme. Time integration is done using a double time stepping algorithm, and local time stepping is used to

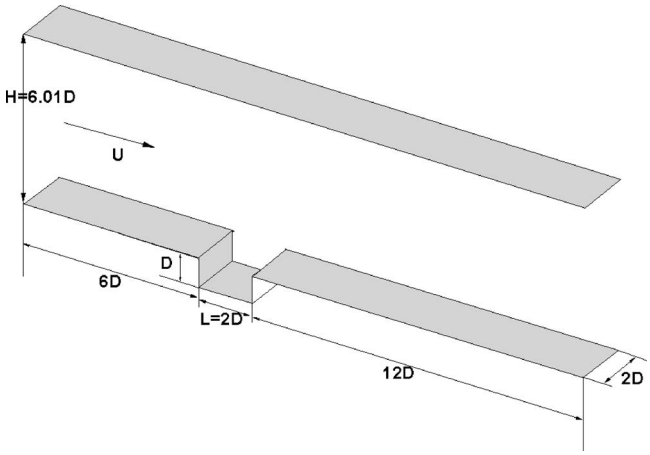

Fig. 1 Computational domain

accelerate the convergence at each physical time step. Source terms in the turbulence model equations are treated implicitly. The time discretization is second order accurate. Grid sensitivity and validation studies for the flow past spheres in the laminar and turbulent (URANS and DES) regimes are described in Refs. [25,27,28].

The SST model is used in the present URANS simulations because the SST model is less dissipative compared to the SA model for RANS simulations, and thus it has a better chance of capturing the large-scale unsteadiness in cavity flows. Both the SA-DES and the SST-DES models in their low-Reynolds-number versions (no wall functions are used) are tested.

Flow conditions and cavity geometry in the main base line case are based on the experiments of Pereira and Sousa [4,5]. The length to depth ratio (L/D) of the cavity is 2 and the Reynolds number Re_D is 3360. A sketch of the computational domain is provided in Fig. 1. The origin of the streamwise axis ($x/D=0$) is at the cavity leading edge. The trailing edge is situated at $x/D=2.0$. The channel height H is equal to $6.01D$. The length of the domain in the spanwise direction is equal to 2D, and periodic boundary conditions are employed in this direction. In the second test case, the Reynolds number is increased to 33,600, while in the third test case, the cavity length is doubled ($L/D=4$, $\mathrm{Re}_D=3360$).

The mass exchange between the cavity and the channel is investigated by considering the ejection of a passive scalar that is introduced instantaneously at a certain time (after the flow becomes statistically steady) inside the cavity domain. An advection-diffusion equation is solved for the conserved scalar. The nondimensional scalar concentration C is initialized as $C=1$ inside the cavity and as $C=0$ outside it at the time at which the mass exchange process between the channel and the cavity starts. The simulations are continued until close to 90% of the scalar is removed from the cavity.

To investigate the sensitivity of the URANS and LES solutions to the presence of velocity fluctuations in the incoming flow, two cases were considered. In the first one, the mean velocity profiles from a precalculated steady RANS solution in a periodic channel were specified at the inflow section. In the second one (HRE), realistic turbulence fluctuations were fed in a time accurate way through the inflow section. The instantaneous velocity fields containing real turbulent fluctuations were obtained from a precalculated LES solution (the mean streamwise velocity profiles from LES and RANS were very close) in a periodic channel of identical section ($H=6.01D$) to the one containing the cavity, at the same channel Reynolds number of 20,450. The same data fields were used to specify the inflow conditions in the well resolved LES simulation in Ref. [12]. The inflow LES data were interpolated in both space and time given the coarser grid and larger time step used in the present DES and URANS simulations.

The particular kind of jittering applied here (from a well resolved LES solution) is an extreme case as it corresponds to realistic turbulence at the same Reynolds number. In most DES simulations, it is too expensive to calculate such a solution, and simpler methods that include generation of synthetic turbulence or just adding random fluctuations are generally used. However, the benefit of using these methods is expected to be lower than the one using the jittering employed in the present work. Thus, the two inflow boundary conditions considered here correspond to two extreme cases: where no fluctuations are present and where realistic turbulent fluctuations are present. The RANS and DES solutions using steady inflow conditions are denoted as SST-URANS-R, SST-DES-R and SA-DES-R. The ones using realistic turbulent fluctuations at the inlet are denoted as SST-URANS-L, SST-DES-L, and SA-DES-L. The higher Reynolds number solutions are denoted as SA-DES-R-HRE and SA-DES-L-HRE.

Simulation results are compared with experimental data [4,5] and results from a recent LES simulation [12] in which the resolution was close to DNS requirements and thus most of the energy was resolved. In the baseline case, the computational domain in DES and URANS consists of close to 500,000 mesh points ($150\times100\times32$) which are more than one order of magnitude less than the mesh used in the LES simulation (14×10^6 mesh points) at the same Reynolds number. In the second test case, there are $175\times120\times32$ mesh points (the mesh density is similar to that in the baseline case; the extra points were added in the wall normal directions to maintain a distance of one wall unit from the solid boundaries), and in the third case ($L/D=4$) there are $180\times100\times32$ mesh points. In all the simulations, the first grid point is located everywhere at about one wall unit away from the walls (assuming fully turbulent flow), and no wall functions are used. The nondimensional time step is $0.02D/U$, which insures that the nondimensional frequencies ($\mathrm{St}=fD/U$, f is the frequency) are well resolved for $\mathrm{St}<10$.

3 Grid Dependency Study

Grid sensitivity was assessed for the SA-DES model for the baseline case in which steady RANS conditions were used at the inflow (SA-DES-R). The mean flow results obtained on the original mesh ($150\times100\times32$ cells of which $51\times41\times32$ cells are inside the cavity) were compared to results (SA-DES-R fine) obtained on a finer mesh ($170\times130\times48$, $61\times51\times48$). The predictions of the mean (spanwise and time-averaged) streamwise velocity profiles at two vertical stations situated just upstream of the cavity and inside the cavity ($x/D=1.0$ and $x/D=1.7$), shown in Fig. 2, confirm the grid independency of the mean solution. The analysis of the vertical velocity spectra (Fig. 3) showed that the dominant frequency associated with the shedding of large-scale vortices in the separated shear layer is $0.34U/D$ in the original mesh simulation and $0.33U/D$ in the fine mesh simulation. The temporal evolution of the mass of contaminant inside the cavity in the two simulations (Fig. 4) is close (within 5–10%) over the entire decay period. Based on these results, one can conclude that the solution obtained using the original mesh is grid independent.

The grid sensitivity study is next extended by considering coarser meshes in the cavity region up to levels of mesh densities for which the flow and especially the contaminant mass decay start being significantly different from the results obtained on the finer (grid independent) meshes. Several meshes were considered. We present in Figs. 2–4 results obtained on a coarser mesh (SA-DES-R C1, $141\times95\times32$ and $42\times36\times32$) for which the solution results, including the contaminant mass decay, remain reasonably close to the fine mesh results. We also include results on an even coarser mesh (SA-DES-R C2, $132\times90\times32$ and $33\times31\times32$) for which the solution is significantly different from that obtained on the fine meshes. The reason for the large drop in the

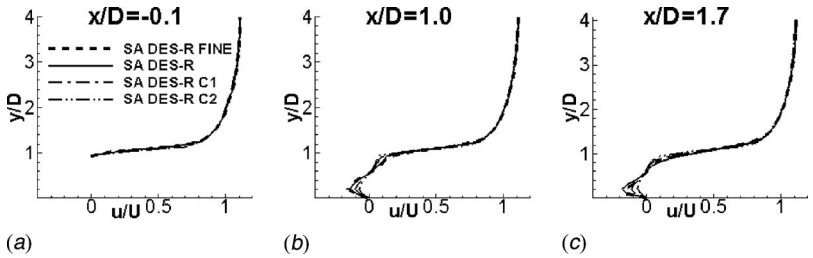

Fig. 2 Mean streamwise velocity profiles for SA DES with different mesh sizes. (*a*) $x/D=-0.1$, (*b*) $x/D=1.0$, and (*c*) $x/D=1.7$.

decay rate of the mass of contaminant in the SA-DES-R C2 simulation is due to the fact that though the value of the fundamental frequency (first mode) of the shear-layer eddies is still correctly predicted ($\mathrm{St}=fD/U\sim 0.37$), the energy associated with this frequency decays significantly compared to the other simulations, including SA-DES-R C1. Thus, one can conclude that the mesh density used in SA-DES-R C1 simulation corresponds to the minimum resolution needed to accurately predict the flow and mass exchange processes using DES at $\mathrm{Re}_D=3360$. A similar grid dependency study was conducted for the second test case ($\mathrm{Re}_D=33,600$). The results showed that roughly the same grid density is required in the cavity region away from the solid boundaries. Of course, at higher Reynolds numbers, one needs some extra grid points in the wall normal direction to resolve the thinner attached boundary layers.

4 Results and Discussion

Comparisons of URANS and DES solutions with no fluctuations at the inlet (URANS-R versus DES-R) serve to investigate whether a hybrid RANS/LES approach such as DES can predict the mean flow quantities, turbulence statistics, and mass transport more accurately than URANS for flows over cavities. The comparison of the DES solutions without fluctuations (DES-R) and with realistic turbulent fluctuations (DES-L) at the inflow serves to evaluate the added benefit of having the solution jittered at the inflow in terms of improving the overall predictions of the mean flow, turbulence statistics, and global mass exchange coefficients. The comparison of SA-DES-L with SST-DES-L and of SA-DES-R with SST-DES-R allows assessing the performances of the SA and SST versions of DES in predicting cavity flows. The effect of the Reynolds number is investigated by comparing the SA-DES-L and SA-DES-L-HRE solutions. The effect of the cavity aspect ratio is studied by comparing the SA-DES-L solutions with $L/D=2$ and $L/D=4$.

The mean flow quantities are calculated by averaging the instantaneous velocity fields in the spanwise direction and in time over a period of $100D/U$. All simulations show that the mean flow inside the cavity in the baseline case is characterized by the presence of two main recirculation eddies (see Fig. 5), with the larger one occupying the whole downstream half of the cavity and part of the top upstream half. The relative size and shape of these main eddies are not exactly the same, with URANS and SA-DES predicting a shallower and more circular eddy on the upstream

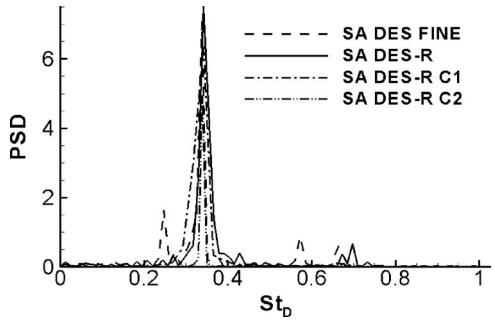

Fig. 3 Power spectra of vertical velocity at a point situated close to the trailing edge corner for SA DES with different mesh sizes

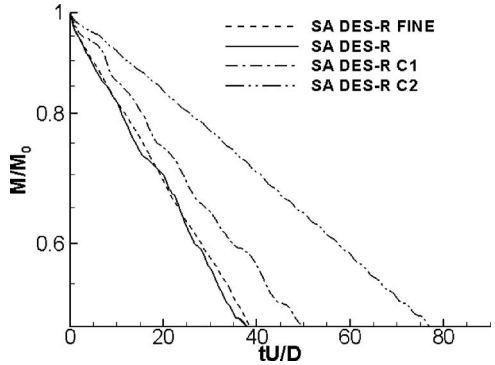

Fig. 4 Decay of scalar mass inside the cavity shown in log-linear scale for SA DES with different mesh sizes

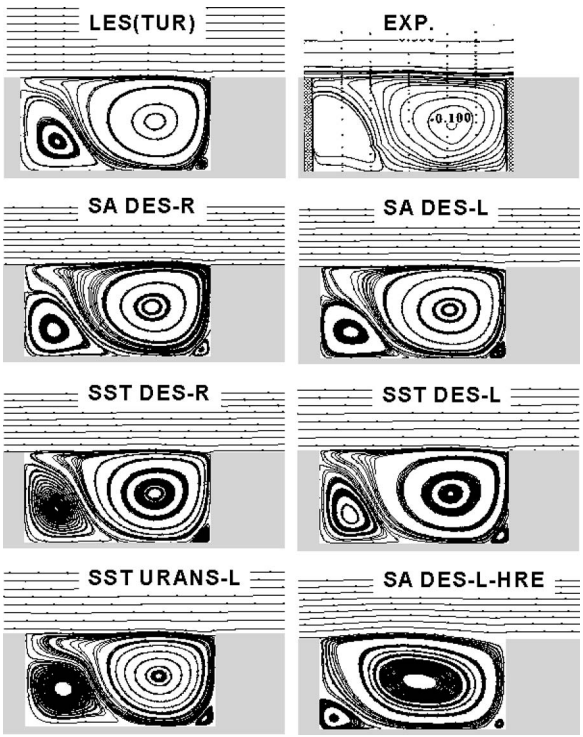

Fig. 5 Mean velocity streamlines. Experimental data are from Pereira and Sousa [4,5].

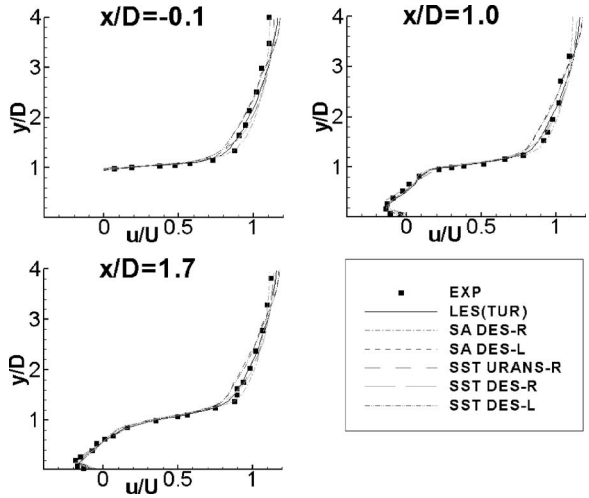

Fig. 6 Mean streamwise velocity profiles at several streamwise stations. Symbols correspond to the experiment of Pereira and Sousa [4,5].

side compared to the LES case. Though the overall agreement is good for all simulations, SST-DES simulations appear to be slightly closer to LES and experimental results. The increase in the Reynolds number greatly reduces the size of the secondary upstream recirculation eddy.

The longitudinal mean velocity profiles for the baseline case are compared with experiment (symbols) in Fig. 6 at a vertical section situated just upstream of the leading edge of the cavity ($x/D=-0.1$) and at two vertical sections cutting through the cavity ($x/D=1.0$ and 1.7). As expected, all the simulations capture accurately the velocity profile corresponding to a fully developed channel flow in the region upstream of the cavity. A very good agreement is also observed for all simulations across the separated shear layer on top of the cavity and inside the cavity ($0<y/D<1$). Some small differences with the experimental data are present in the outer part of the shear layer, above the cavity mouth, in the SA-DES-L and SST-DES-L velocity profiles. However, this small discrepancy starts upstream of the cavity and appears to be related to the presence of velocity fluctuations superimposed on top of the mean velocity profiles at the inflow section.

Figure 7 shows the growth of the mean shear-layer over the cavity for the baseline case. The shear-layer width is defined with the vorticity thickness ($\delta=U/(dU/dy)_{\max}$). Starting at the leading edge, the vorticity thickness increases over most of the cavity and then decreases rapidly as the trailing edge is approached. The vorticity thickness in LES varies linearly between $7\delta_0$ and $13\delta_0$,

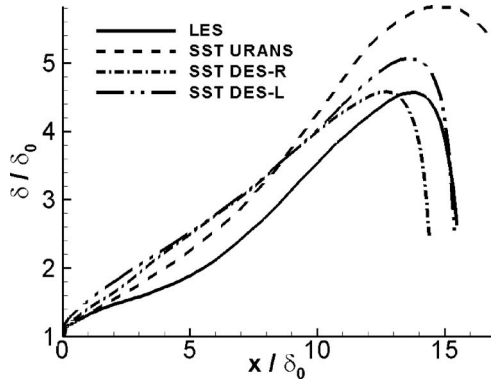

Fig. 7 Variation of shear-layer vorticity thickness (δ) with distance from the leading edge

where δ_0 is the vorticity thickness at the leading edge. The growth rate is close to 0.27 in the linear growth region. In the same region, the growth rates predicted by SST-DES-L and SST-DES-R are approximately equal to 0.26, very close to LES, whereas SST-URANS-L overpredicts the growth rate (0.31). Moreover, near the trailing edge, URANS significantly overpredicts the thickness of the shear layer. Compared to LES, SST-DES-L appears to predict the closest variation of this quantity over the cavity. The SA-DES predictions are close to the corresponding SST-DES predictions.

The total tke (modeled plus resolved, with the exception of SA-DES simulations where only the resolved component is shown) predictions by RANS and DES simulations of the baseline case are shown in Fig. 8 along with the LES results. In LES, the tke increases significantly inside the shear layer and in the vicinity of the upper part of the cavity trailing edge due to the presence of highly energetic vortical structures in the separated shear layer and to their subsequent interaction with the trailing edge (a detailed discussion is given in Ref. [12]), where part of them are convected inside the cavity.

In the SST-URANS-R simulation, the solution is practically steady and the resolved tke component is negligible. The distribution of the modeled component is qualitatively similar to the tke given by LES though the amplification of the tke in the separated shear layer is overpredicted by 50–100% due to the excessive values of the turbulence production predicted by the RANS model. Adding the inflow fluctuations (SST-URANS-L) results in slightly even larger tke levels, as some small resolved fluctuations (see Fig. 8) develop and can be sustained in the unsteady solution. The tke predictions of the DES simulations without fluctuations are poor over the whole length of the separated shear layer. However, once the fluctuations are added, the tke fields predicted by both versions of DES become quite similar to those predicted by LES. SA-DES-L overpredicts by about 50% the total tke within the separated shear layer while SA-DES-L underpredicts by about 20-30% the tke within the same region. Thus, adding velocity fluctuations in DES resulted in a dramatic increase in the accuracy of the tke predictions, with the SST version giving the best agreement. Finally, the larger value of the Reynolds number in the SA-DES-L-HRE simulation (notice the different scale used to plot tke) results in a very significant amplification (by around three times) of the tke inside the shear layer.

The distribution of the resolved turbulence production term is also shown in Fig. 8. Notice the region of negative production near the trailing edge corner present in LES due to the strong interactions between the shear-layer eddies and the cavity trailing edge. Consistent with the small levels of the resolved velocity fluctuations present in the SST-URANS-L simulation, the resolved production term accounts only for a very small fraction of the total turbulence production despite the fact that the total tke is overpredicted by the model compared to LES. In DES, where, regardless of the inflow conditions, most of the energetic eddies are resolved and the modeled part is relatively small, the predictions of the resolved production term are qualitatively similar to the LES distribution. For both versions of the DES model, the presence of the inflow velocity fluctuations results in an increase of the levels of turbulence production and, more importantly, in a considerable increase in the agreement with LES over the whole cavity region. In particular, SA-DES-L and SST-DES-L capture accurately the amplification of the turbulence production associated with the jetlike flow parallel to the trailing edge inside the cavity and the region of negative production around the trailing edge corner. The agreement is excellent for SA-DES-L. Again, the effect of the increase in the Reynolds number is to amplify by two to three times the production term both inside the separated shear layer and in the region around the trailing edge corner. In fact, the magnitude of the production term is significantly larger over the whole cavity region.

Figure 9 shows the distributions of the resolved normal stresses in the streamwise and vertical directions and of the primary shear

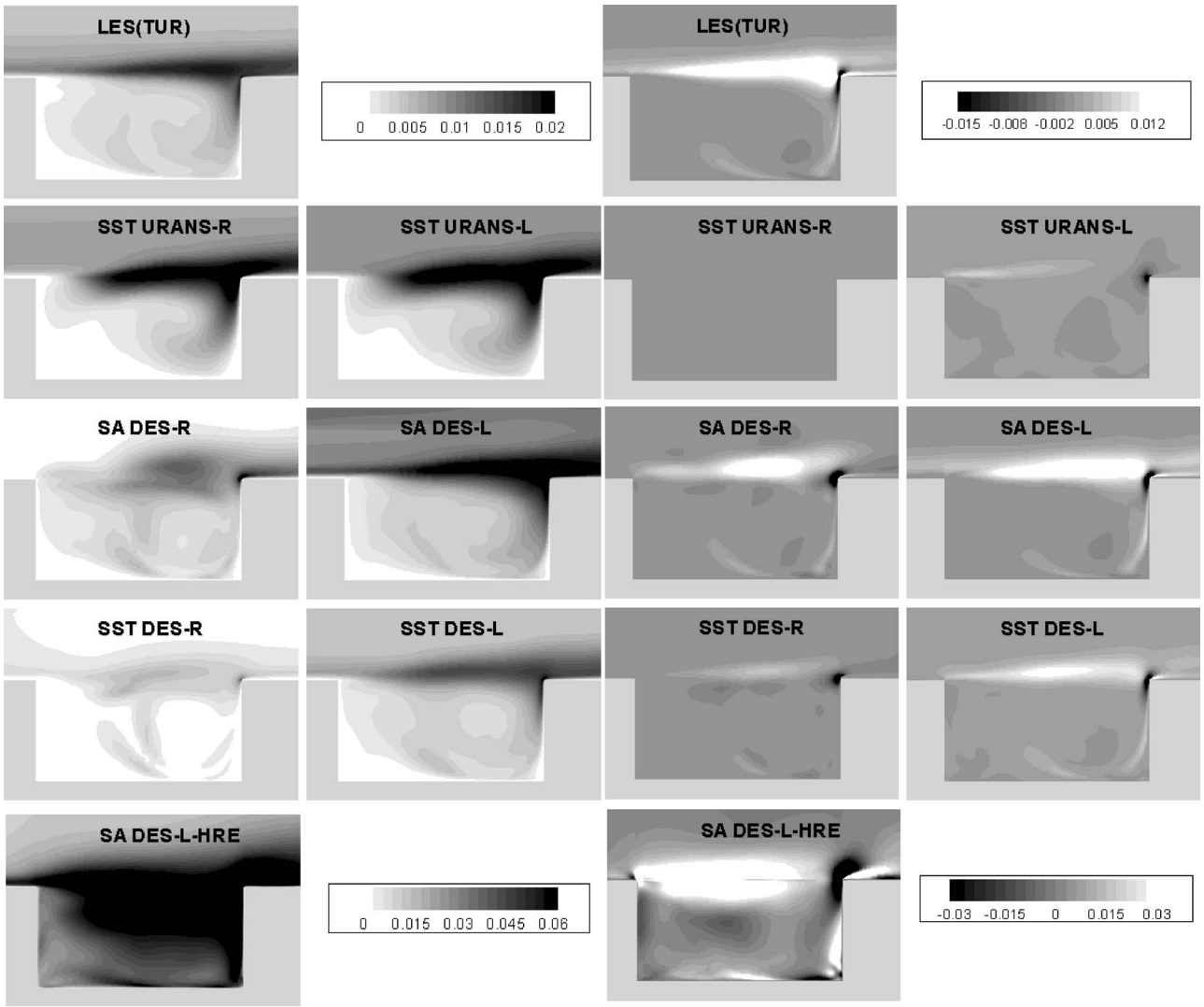

Fig. 8 Distribution of turbulent kinetic energy and turbulence production

stress for the LES, SA-DES-L, SST-DES-L, and SA-DES-R (baseline case) at several streamwise stations. The experimental data from Ref. [5] are shown with symbols. The LES predictions are very close to the experiment at practically all stations. Generally, the width of the narrow region in which these stresses are strongly amplified increases along the cavity mouth consistent with to the growth of the separated shear layer.

For the streamwise normal stress, the SA-DES-L predictions (Fig. 9(*a*)) are in excellent agreement with the experimental data and LES everywhere except over the first half of the cavity length where the decay on the channel side is milder. However, this discrepancy is present even for the profile at $x/D=-0.1$ situated upstream of the cavity and is mainly related to the model performance in a classical channel flow. Qualitatively, the SST-DES-L model also does a good job, though the maximum amplification levels inside the separated shear layer are consistently underpredicted over the cavity by as much as 50%. The absence of turbulent fluctuations is the reason why the incoming flow is practically steady. The resolved fluctuations are negligible over the upstream part of the separated shear layer. Though they are strongly amplified in the downstream part of the separated shear layer, the maximum normal fluctuations are less than half of the experimental values and significantly lower compared to SA-DES-L predictions. No such data were available for the higher Reynolds number simulation.

The predictions of the primary shear stress are compared in Fig. 9(*b*). SA-DES-L predictions are generally in excellent agreement with the experimental data and LES. In particular, the maximum amplification rates along the separated shear layer are very close to LES. SST-DES-L predictions tend to be very accurate outside the separated shear layer, both inside the cavity and on the channel side, but to underpredict the amplification levels within the shear layer. This is true even if the small modeled part of the shear stress is added. When the turbulent fluctuations are not present (DES-R), the values of the resolved shear stress are significantly underpredicted inside the separated shear layer over the first half of the cavity length. However, the predictions are quite close to experiment and the DES-L simulations in the downstream part of the separated shear layer.

The vertical velocity time series in Figs. 10(*a*) and 10(*b*) at a point situated inside the separated shear layer ($x/D=0.2$, $y/D=0.0$), situated just downstream of the leading edge corner, show that when inflow turbulent fluctuations are present the amplitude of these oscillations is comparable in URANS, DES, and LES for the baseline case. Remarkably, this is true even for the DES simulations in which no turbulent fluctuations are added at the inlet (Fig. 10(*b*)). The good agreement in the DES-R simulations is a consequence of the self-sustained jittering of the separated shear layer by the eddies injected near the trailing edge corner and re-

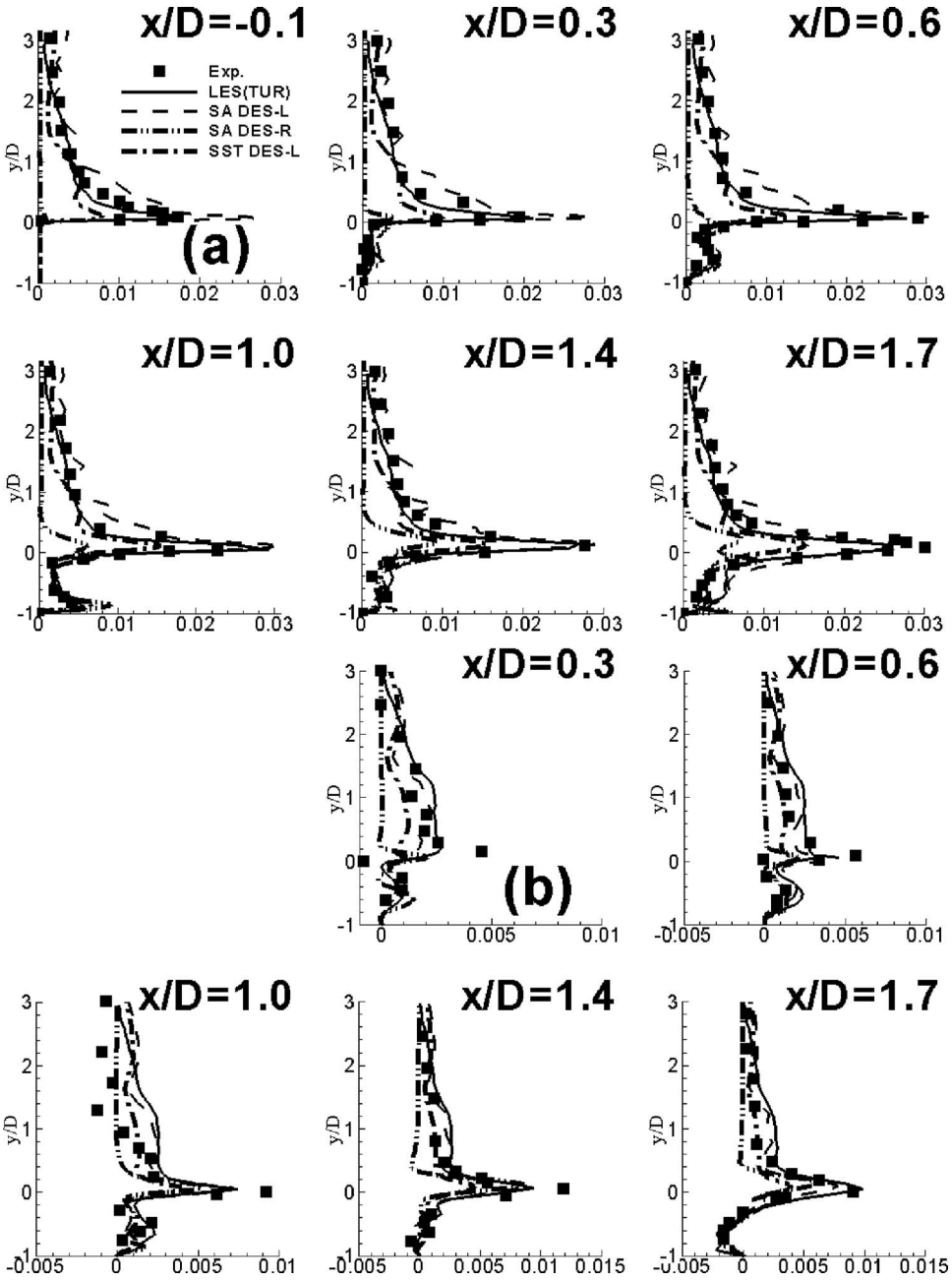

Fig. 9 Resolved Reynolds stresses at different streamwise stations. Symbols correspond to the experiment of Pereira and Sousa [4,5]. (*a*) Normal streamwise stress and (*b*) primary shear stress.

circulated inside the cavity. By comparison, the level of the velocity fluctuations in the URANS simulations with a constant velocity inflow profile (SST-URANS-R in Fig. 10(*a*)) is very weak. The same is true at a point situated close to the trailing edge corner ($x/D=1.8$) for the SST-URANS-R solution. Despite the fact that the SST-URANS-L solution is clearly unsteady, the amplitude of the oscillations inside the separated shear layer is clearly underestimated compared to LES. The agreement becomes worse as one moves along the separated shear layer toward the trailing edge corner. In contrast to that, the mean amplitude of the oscillations predicted at the same point in Fig. 10(*d*) by DES remains high and comparable with that of LES regardless of whether or not turbulence fluctuations were present at the inlet. The SA-DES results were found to be very close to the SST-DES results and were not included.

To describe in a more quantitative way the nature of the velocity fluctuations in the separated shear layers and the differences among the various simulations, the power spectra of the vertical velocity at a point situated at the cavity mouth, close to the trailing edge, are shown in Fig. 11. At this location, the turbulence inside the separated shear layer is strongly amplified compared to the surrounding turbulent flow by the convection of the large-scale shear-layer eddies. Power spectra at the other stations near the cavity mouth over the downstream half of the separated shear layer and downstream of the cavity are similar. As expected, LES (baseline case) predicts the presence of a broad spectrum inside the shear layer. The range of energetic frequencies expressed as a Strouhal number, $St=fD/U$, is between 0.05 and 1, with the most energetic frequency at $St=0.38$ corresponding to the first oscillatory mode predicted by Rockwell's [2] stability theory for cavities

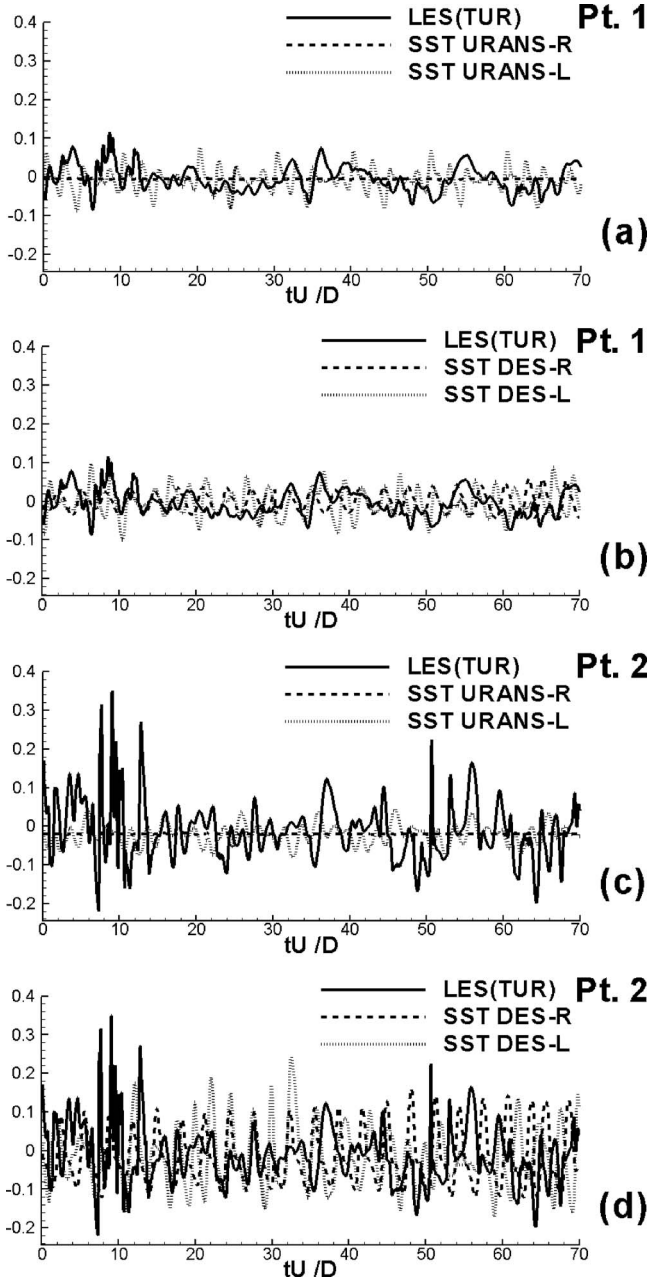

Fig. 10 Vertical velocity time history at point 1 (frames (*a*) and (*b*)) situated close to the leading edge corner and at point 2 (frames (*c*) and (*d*)) situated close to the trailing edge corner

with $L/D=2$. A secondary peak is observed in the spectrum at St=0.51, which corresponds to the second mode predicted by Rockwell [2]. The second mode is the dominant mode in the case in which the incoming boundary layer is laminar and is associated with the quasiregular shedding of the vortex tubes in the detached shear layers [12]. Despite the presence of these two frequencies, the LES flow fields did not show the presence of large coherent spanwise vortices inside the separated layer due to the strong interactions between the shear-layer eddies and the near wall eddies convected from upstream of the cavity.

Consistent with the velocity time series in Fig. 10(*c*), the energy associated with the oscillations present in the downstream part of the separated shear layer in the SST-URANS-L simulation is much smaller compared to LES despite the presence of the inflow fluctuations. The vorticity magnitude contours in an *x*-*y* plane and in a spanwise *y*-*z* plane cutting through the middle of the cavity in Fig. 12(*b*) show that though the instantaneous flow is nonuniform in the spanwise direction, the three-dimensional effects are small and are mainly limited to the presence of some streamwise and spanwise disturbances on the vorticity sheet associated with the separated shear layer. Compared to the steady SST-URANS-R solution (Fig. 12(*a*)) the vorticity distribution in an *x*-*y* plane is very similar, and no additional small scales are present inside the cavity besides the main recirculation eddies observed in the mean flow.

In the SA-DES-R simulation, the spectrum is discrete with most of the energy contained into the oscillation with St$\sim$0.31 (corresponding to the first mode predicted by theory that assumed inviscid flow conditions) and its first harmonic. The energy associated with these discrete frequencies is considerably larger than the one present in the most energetic frequencies in the LES spectrum. This is because in the absence of inflow fluctuations, the perturbations acting on the upstream part of the separated shear layer are fairly regular. This, in turn, makes that large spanwise vortices are shed at the frequency corresponding to the first mode in a fairly regular way (see corresponding vorticity distributions in Fig. 12(*c*)), and the interaction of these vortices with the trailing edge corner results in a partial clipping event. This type of behavior is generally encountered in the case of a thin incoming boundary layer [12]. Inside the cavity, the flow becomes clearly 3D, mainly because of the interaction of the disturbed shear-layer vortices with the trailing edge corner and subsequent momentum exchange between the eddies injected inside the cavity with the main recirculation eddy.

The presence of inflow fluctuations (SA-DES-L) reduces by a factor of 2 the energy associated with the dominant frequency and produces a fuller spectrum with energetic frequencies between St=0.1 and St=0.55. Still, the frequency with St=0.31 is the most energetic. The vorticity sheet is strongly jittered by the incoming velocity fluctuations, and this modifies the nature of the interactions between the large-scale shear-layer eddies and the trailing edge corner. Consequently, the modulations of the jetlike flow inside the cavity are more random, and the recirculating eddies inside the cavity disturb in a more irregular way the vorticity sheet associated with the upstream part of the separated shear layer. The range of eddies present inside the cavity becomes also broader, and the large-scale flow structures in the spanwise direction become less organized, as seen from the comparison of the vorticity distributions in Figs. 12(*c*) and 12(*d*). This mechanism is similar to the one observed in LES, but the range of disturbances and their spectral content is different due to the more dissipative nature of the DES model in the LES mode and also due to the coarser meshes employed. A comparison of SST-DES-L and SST-DES-R simulation results clearly shows that if the spectral content of the flow is relevant for an investigation, adding turbulent fluctuations that mimic as close as possible the real turbulence can help improve the accuracy of the DES predictions. The results obtained using the SA version of DES were qualitatively very similar and are not reproduced here.

Finally, in the test case in which $\mathrm{Re}_D=33{,}600$ and no turbulent fluctuations are introduced, the power spectrum is similar to the one obtained in the corresponding baseline simulation, except the fact that the energy inside the first mode is two to three times larger. In the case where turbulent fluctuations are present (SA-DES-L-HRE), the Strouhal number associated with the first mode is 0.35, which is closer to the value (0.38) predicted by stability analysis, in which the flow was assumed to be inviscid. One would suspect that at higher Reynolds numbers, the DES predictions will be even closer to theory. A comparison of Figs. 12(*d*) and 12(*e*) clearly shows that the effect of the increase in the Reynolds number is the production of a larger content in smaller, but very energetic, three-dimensional eddies. These smaller energetic eddies increase the jittering of the separated shear layer. While in the SA-DES-L simulation these eddies were present mostly in the downstream region occupied by the main recirculation eddy (see

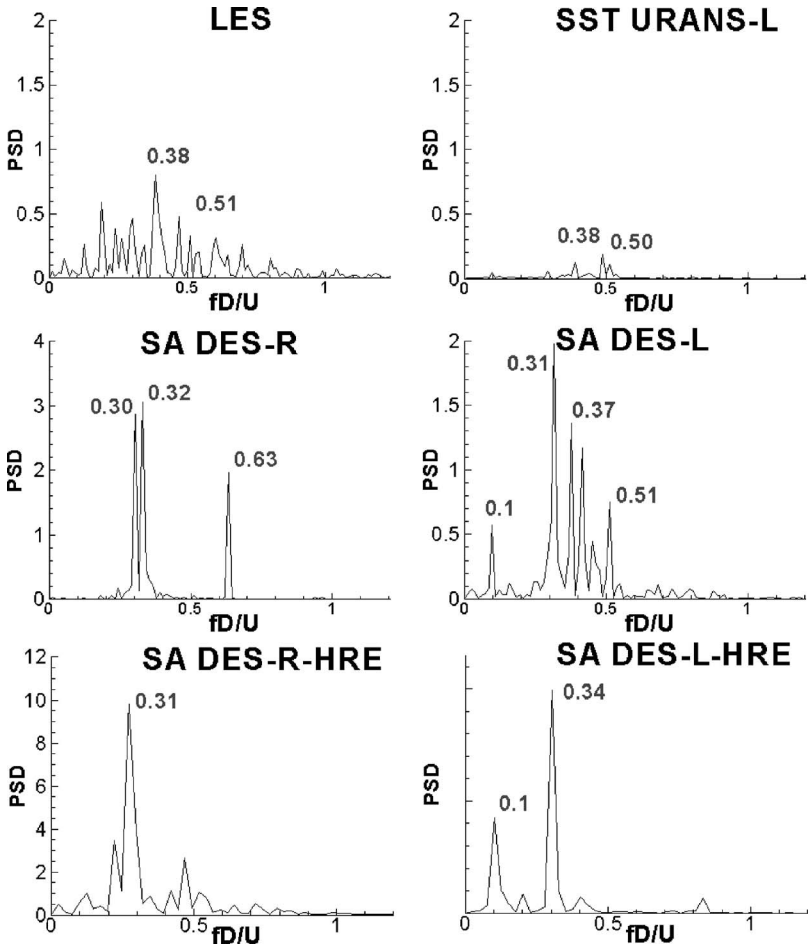

Fig. 11 Power spectra of vertical velocity at a point situated close to the trailing edge corner inside the separated shear layer for simulations with $L/D=2$

Fig. 5), in the SA-DES-L-HRE simulation these turbulent eddies occupy practically the whole cavity region, which is also consistent with the mean streamline patterns in Fig. 5.

Figure 13 shows the temporal variation of the scalar mass (mean concentration) inside the cavity in a log-linear scale. The Schmidt number was equal to 1 in all simulations. In environmental fluid mechanics, simplified models [29] relying on empirical dispersion coefficients are used to describe the mass exchange between the cavity and the main channel. These models simply assume that the local rate of decay of mean concentration inside the cavity is proportional to the mean concentration difference between the channel and cavity. If this law is assumed, then the decay of the mean concentration inside the cavity is exponential, $M/M_0=\exp(-t/T)$, where T is the characteristic time scale and M_0 is the initial mean concentration of the scalar inside the cavity. If one nondimensionalizes T using D and U, one gets the so-called nondimensional exchange coefficient k $(=D/TU)$. A constant value of k corresponds to a linear variation of the mean concentration inside the cavity in time when the mean concentration decay is plotted in a log-linear scale.

The LES simulation results in Ref. [12] are fully consistent with the exponential decay over the whole duration of the scalar ejection process, and the value of k was estimated to be 0.015. The SA-DES-L and SA-DES-R simulations also predict the scalar decay in time to be very close to exponential. In the other simulations, the value of k corresponds to a mean value between the initiation of the scalar ejection process and the time when only 20% of the initial mass of scalar was left inside the cavity. In these simulations, the instantaneous value of the mass exchange coefficient in the exponential decay function slowly decreases as the scalar ejection process advances.

For the baseline case, the SA-DES-L simulation gives by far the best agreement with LES ($k=0.016$). Interestingly, the presence of inflow velocity fluctuations does not make practically any difference in the SST-DES predictions. The underprediction of k by these two simulations is of the same order as the overprediction of k by the SA-DES-R simulation. The absence of inflow velocity fluctuations in the SST-URANS simulation produces a very significant underprediction of the mass exchange coefficient ($k=0.009$). However, when inflow turbulent fluctuations are present, the scalar mass decay is very similar to the one predicted by the SST-DES simulations. The effect of the increase in the Reynolds number is to significantly accelerate the ejection process especially for the case when turbulent fluctuations are present upstream of the cavity. The predicted value of k is 0.047 compared to 0.016 in the corresponding baseline simulation. One suspects that this is due to the presence of smaller highly 3D eddies inside the embayment, which mix very efficiently the flow inside the cavity. The comparison was made for the SA-DES model because for the baseline case, the SA model results were found to be closer to LES than the SST model results.

Finally, Figs. 14–17 summarize the results obtained for the third case ($L/D=4$), for which URANS and SA-DES simulations with and without inflow fluctuations were performed. In contrast to the baseline case (Fig. 5) in which the main recirculation eddy

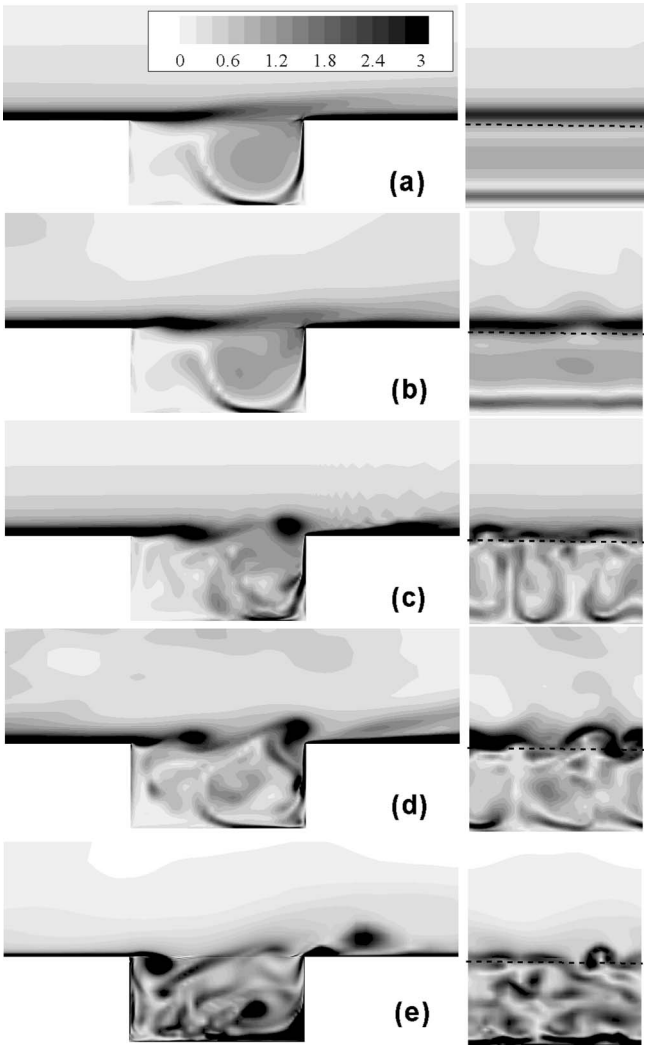

Fig. 12 Instantaneous vorticity magnitude contours in an *x-y* plane (left) and in a spanwise *y-z* plane (right) cutting through the middle of the cavity ($x/D=1.0$) for simulations with $L/D=2$. (*a*) SST-URANS-R, (*b*) SST-URANS-L, (*c*) SA-DES-R, (*d*) SA-DES-L, and (*e*) SA-DES-L-HRE.

was the downstream one, the mean streamline pattern in Fig. 14(*a*) (SA-DES-L) shows that the upstream recirculation region occupies close to three quarters of the cavity length ($L=4D$). The downstream recirculation eddy is much more circular and its center, in the mean flow, is located relatively close to the cavity

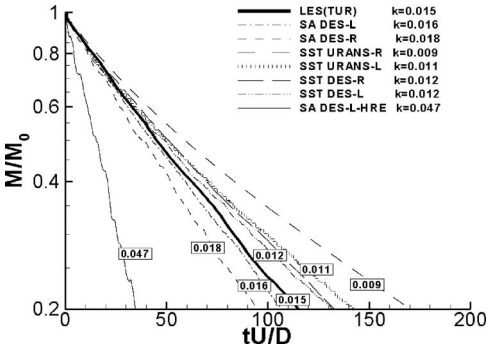

Fig. 13 Decay of scalar mass inside the cavity shown in log-linear scale for simulations with $L/D=2$

bottom. The streamline pattern is quite similar to the one predicted using DES with wall functions (see Fig. 14(*b*)) by Shieh and Morris [13] for the compressible flow (Ma=0.6) past a 2D cavity with $L/D=4.4$ at an even higher Reynolds number ($\mathrm{Re}_D=200{,}000$). Also consistent with their observations, the cavity flow in the $L/D=4$ case is characterized by much larger fluctuations and the presence of large-scale vortices inside the cavity, and resembles more that of a cavity in the wake mode rather than in the shear mode, which is clearly present in the $L/D=2$ simulations. The levels of the tke (Fig. 14(*c*)) and production term (Fig. 14(*d*)) are closer to the ones observed in the higher Reynolds number simulations with $L/D=2$ (see Fig. 8). The comparison of SA-DES-L simulations at $\mathrm{Re}_D=3360$ with $L/D=2$ and $L/D=4$ shows that the region of large tke amplification in the $L/D=4$ case is no longer limited to the downstream part of the separated shear layer but extends deep into the cavity and occupies most of the downstream half of the cavity. However, most of the turbulence production still takes place inside the separated shear layer on both sides of the cavity-channel interface. The magnitude of the production term and the thickness of the region where turbulence production is high are larger compared to those in the $L/D=2$ case.

As the cavity aspect ratio is different, one also expects that the velocity spectra inside the separated layer and cavity will be different. Indeed, the present DES simulation with inflow turbulence shows that the Strouhal numbers associated with the most energetic oscillations are 0.23 and 0.34 (see Fig. 15(*b*) in which the velocity power spectrum at a point located close to the trailing edge corner is shown). They correspond to the second (St=0.24) and third modes (St=0.37) predicted by stability theory. The accurate prediction by DES of these main oscillatory frequencies in the shear layer is of great importance for the prediction of unsteady phenomena such as contaminant removal from the cavity. This is because the mass exchange processes are controlled to a large extent by the shear-layer eddies and their interactions with the trailing edge corner. A third energetic frequency ($\mathrm{St}\sim0.11$) corresponding to the first subharmonic of the second mode is also present in Fig. 15(*b*). By contrast, a URANS simulation with the same turbulent inflow conditions predicts the presence of only the second mode. The energy associated with the second mode in URANS is three to four times smaller compared to DES. The reason is that due to the large viscosity, the growth of the 3D instabilities is much slower and the quasi-2D shear-layer vortices cannot break into smaller three-dimensional scales as they are convected over the cavity interface. These differences between URANS and DES are clearly observed in the instantaneous vorticity magnitude contours shown in Fig. 16. Compared to the corresponding $L/D=2$ simulation (Fig. 12(*d*)), the displacement of the large-scale eddies shed in the shear layer is significantly larger. In fact, this is one of the main reasons why the ejection of the contaminant from the cavity (see Fig. 17) is much faster in the $L/D=4$ case ($k=0.040$) compared to that in the $L/D=2$ case ($k=0.018$) at the same Reynolds number. As expected, the absence of the inflow fluctuations results in a smaller value of the exchange coefficient ($k=0.036$). Finally, the URANS simulations predict once again a considerably slower decay rate of the mass of contaminant ($k=0.018-0.025$).

5 Conclusions

The 3D flow past a rectangular 2D cavity in a channel was investigated using the SST and SA versions of DES and compared with experiments [4], linear stability theory, results from a well-resolved LES simulation [12], and URANS simulations. Though separation is present, cavity flows are more challenging for DES compared to massively separated flows past bluff bodies. DES and URANS simulations without inflow velocity fluctuations and with realistic turbulent fluctuations were performed to investigate to

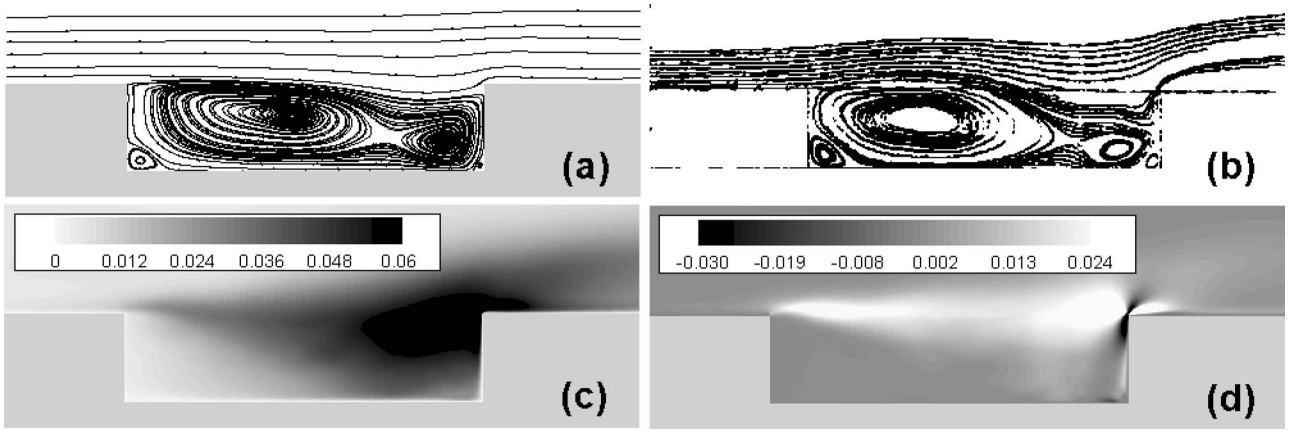

Fig. 14 Statistics for cavity with $L/D=4$ (SA-DES-L). (*a*) 2D streamlines, (*b*) 2D streamlines from Shieh and Morris [13], (*c*) turbulent kinetic energy, and (*d*) turbulence production.

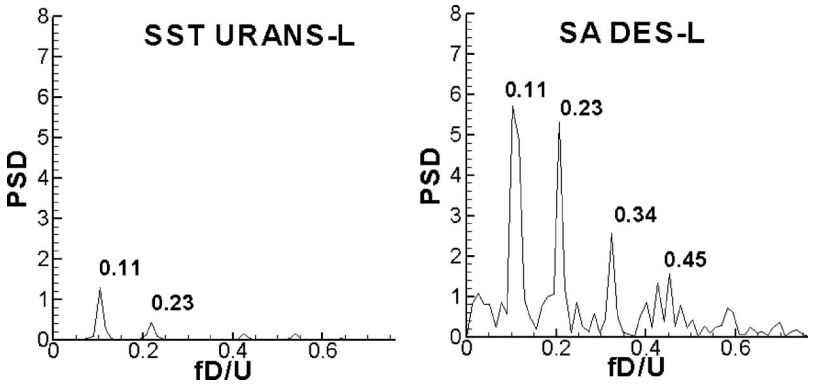

Fig. 15 Power spectra of vertical velocity at a point situated close to the trailing edge corner inside the separated shear layer for simulations with $L/D=4$

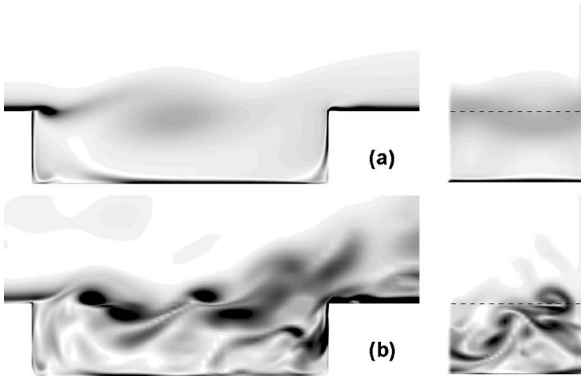

Fig. 16 Instantaneous vorticity magnitude contours in an *x-y* plane (left) and in a spanwise *y-z* plane (right) cutting through the middle of the cavity ($x/D=1.0$) for simulations with $L/D=4$. (*a*) SST-URANS-L and (*b*) SA-DES-L.

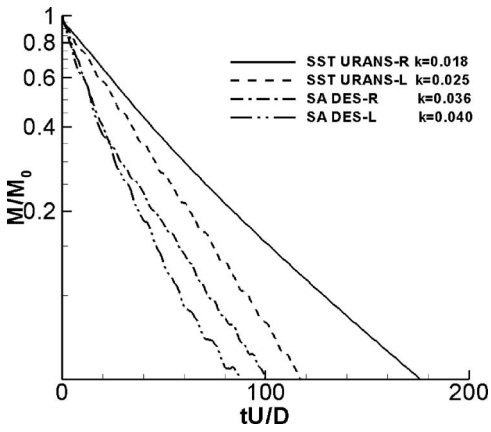

Fig. 17 Decay of scalar mass inside the cavity shown in log-linear scale for simulations with $L/D=4$

what degree the presence of velocity fluctuations in the incoming flow can improve the flow predictions in the cavity region and to study the effect of the model.

Even without any upstream velocity fluctuations, DES was found to produce an unsteady solution with a relatively high content of 3D eddies inside the cavity. The presence of inflow velocity fluctuations increased the range of turbulent eddies present inside the cavity and the jittering of the upstream part of the separating shear layer. For the baseline case ($L/D=2$, $\mathrm{Re}_D=3360$), all URANS and DES simulations successfully predicted the mean velocity field in the cavity region. However, important differences in the prediction of the Reynolds stresses and tke were observed among the various simulations. In the separated flow over the cavity, past the region where the influence of the turbulence content of the incoming channel flow is strong, the Reynolds stresses were fairly accurately predicted by both versions of

DES when turbulent inflow fluctuations were present despite the much coarser meshes used compared to LES. Still, the overall comparison favors the SA version. The spectral content of the separated shear layer away from the leading edge was also found to become much closer to LES once inflow velocity fluctuations were added. The effect of these fluctuations was the breaking of the strong coherence of the vortices shed in the separated shear layer present in the case when the incoming flow contained no oscillations.

Increasing the Reynolds number by one order of magnitude resulted in a change of the recirculatory mean pattern inside the cavity, an amplification of the flow three dimensionality, and, ultimately, a much faster ejection of the contaminant from the cavity compared to the baseline case. The predicted value of the main oscillatory frequency was closer to the first mode oscillatory frequency given by stability theory. This is expected, as the flow is more turbulent and closer to the inviscid flow conditions assumed in stability theory. In the case when the cavity aspect ratio was $L/D=4$, DES was able to accurately capture both the second and third mode frequencies predicted by stability theory. In contrast to this, URANS was able to capture only the presence of the second mode, and the energy associated with this mode was significantly lower compared to DES. As expected, the increase in the Reynolds number and the increase in the cavity aspect ratio resulted in the amplification of the flow three dimensionality in the separated shear layer and inside the cavity. As a consequence, the mixing inside the cavity was stronger and the ejection of the contaminant faster compared to the baseline case.

Regarding the application of DES to simulate mass and heat transfer, the SA-DES simulation containing inflow velocity fluctuations was found to give the best predictions of the scalar mass decay within the cavity. On the other hand, the SST-DES simulations predicted a mass exchange coefficient that was fairly close to LES while being insensitive to the presence of fluctuations in the incoming flow. The degree to which simpler methods to jitter the incoming flow can produce results close to the ones obtained using realistic turbulence fluctuations constitutes an important area of future work.

Acknowledgment

The first author was supported by a BK-21 fellowship awarded by KAIST to work on this study during his visit at IIHR Hydroscience and Engineering, University of Iowa.

References

[1] Sorohia, V., 1997, "Experimental Investigation of Oscillation in Flows Over Shallow Cavities," AIAA J., **15**(7), pp. 984–991.
[2] Rockwell, D., 1977, "Prediction of Oscillation Frequencies for Unstable Flow Past Cavities," ASME J. Fluids Eng., **99**, pp. 294–300.
[3] Ethembabaoglu, S., 1973, Ph.D. thesis, "On the Fluctuating Flow Characteristics in the Vicinity of Gate Slots," Division of Hydraulic Engineering, University of Trondheim, Norwegian Institute of Technology.
[4] Pereira, J. C. F., and Sousa, J. M. M., 1994, "Influence of Impingement Edge Geometry on Cavity Flow Oscillations," AIAA J., **32**(8), pp. 1737–1740.
[5] Pereira, J. C. F., and Sousa, J. M. M., 1995, "Experimental and Numerical Investigation of Flow Oscillations in a Rectangular Cavity," ASME J. Fluids Eng., **117**, pp. 68–73.
[6] Lin, J. C., and Rockwell, D., 2001, "Organized Oscillations of Initially Turbulent Flow Past a Cavity," AIAA J., **39**(6), pp. 1139–1151.
[7] Grace, S. M., Dewar, W. G., and Wroblewski, D. E., 2004, "Experimental Investigation of the Flow Characteristics Within a Shallow Wall Cavity for Both Laminar and Turbulent Upstream Boundary Layer," Exp. Fluids, **36**(5), pp. 791–804.
[8] Sinha, N., Dash, S. M., Chidambaram, N., and Findlay, D., 1998, "A Perspective on the Simulation of Cavity Aeroacoustics," AIAA Paper No. 98-0286.
[9] Ghaddar, N. K., Korczak, K. Z., Mikic, B. B., and Patera, A. T., 1986, "Numerical Investigation of Incompressible Flow in Grooved Channel. Part 1. Stability and Self-Sustained Oscillations," J. Fluid Mech., **163**, pp. 99–127.
[10] Yao, H., Copper, R. K., and Raghunthan, S., 2001, "Large-Eddy Simulation of Laminar-to-Turbulent Transition in Incompressible Flow Past 3-D Rectangular Cavity," AIAA Paper No. 2001-31318.
[11] Yao, H., Cooper, R. K., and Raghunathan, S., 2004, "Numerical Simulations of Incompressible Laminar Flow Over Three-Dimensional Rectangular Cavities," ASME J. Fluids Eng., **126**(6), pp. 919–927.
[12] Chang, K., Constantinescu, S. G., and Park, S., 2006, "Analysis of the Flow and Mass Exchange Processes for the Incompressible Flow Past an Open Cavity With a Laminar and a Fully Turbulent Incoming Boundary Layer," J. Fluid Mech., **561**, pp. 113–145.
[13] Shieh, C. M., and Morris, P. J., 2001, "Comparison of Two and Three-Dimensional Turbulent Shallow Cavity Flows," AIAA Paper No. 2001-0511.
[14] Rossiter, J. E., 1964, "Wind Tunnel Experiments on the Flow Over Rectangular Cavities at Subsonic and Transonic Speeds," RAE Technical Report No. 64037.
[15] Arunajatesan, S., and Sinha, N., 2001, "Unified Unsteady RANS-LES Simulations of Cavity Flowfields," AIAA Paper No. 2001-0516.
[16] Chang, K., and Park, S., 2004, "Hybrid RANS/LES Simulation of Deep Cavity Flow," AIAA Paper No. 2004-53.
[17] Bush, R. H., and Mani, M., 2001, "A Two-Equation Large Eddy Stress Model for High Sub-Grid Shear," AIAA Paper No. 2001-2561.
[18] Cattafesta, L. N., 1997, "Active Control of Flow Induced Cavity Resonance," AIAA Paper No. 1997-1804.
[19] Speziale, C. G., 1998, "Turbulence Modeling for Time-Dependent RANS and VLES: A Review," AIAA J., **36**(2), pp. 173–184.
[20] Batten, P., Goldberg, U., and Chakravarthy, S., 2002, "LNS-An Approach Towards Embedded LES," AIAA Paper No. 2002-0427.
[21] Quéméré, P., and Sagaut, P., 2002, "Zonal Multi-Domain RANS/LES Simulations of Turbulent Flows," Int. J. Numer. Methods Fluids, **40**(7), pp. 903–925.
[22] Spalart, P. R., Jou, W. H., Strelets, M., and Allmaras, S. R., 1997, "Comments on the Feasibility of LES for Wings, and on a Hybrid RANS/LES Approach," *Advances in DNS/LES: First AFOSR International Conference on DNS/LES*, C. Liu and Z. Liu, eds., Greyden, Columbus, OH.
[23] Strelets, M., 2001, "Detached Eddy Simulation of Massively Separated Flows," AIAA Paper No. 2001-16694.
[24] Menter, P. R., 1993, "Zonal Two-Equation k-ω Turbulence Models for Aerodynamic Flows," AIAA Paper No. 1993-2906.
[25] Constantinescu, G., and Squires, K., 2004, "Numerical Investigations of Flow Over a Sphere in the Subcritical and Supercritical Regimes," Phys. Fluids, **16**(5), pp. 1449–1466.
[26] Travin, A., Shur, M., Strelets, M., and Spalart, P. R., 2000, "Physical and Numerical Upgrades in the Detached-Eddy Simulation of Complex Turbulent Flows," *412 EUROMECH Colloquium on LES of Complex Transitional and Turbulent Flows*, Munich, Germany.
[27] Constantinescu, G., and Chapelet, M., and Squires, K., 2003, "Turbulence Modeling Applied to Flow Over a Sphere," AIAA J., **41**(9), pp. 1733–1742.
[28] Constantinescu, G., and Squires, K., 2003, "LES and DES Investigations of Turbulent Flow Over a Sphere at Re=10,000," Flow, Turbul. Combust., **70**, pp. 267–298.
[29] Uijttewaal, W. S. J., Lehmann, D., and van Mazijk, A., 2001, "Exchange Processes Between a River and Its Groyne Fields: Model Experiments," J. Hydraul. Eng., **127**, pp. 928–936.

Annular Extrudate Swell of Newtonian Fluids: Effects of Compressibility and Slip at the Wall

Evan Mitsoulis
Professor
School of Mining Engineering & Metallurgy,
National Technical University of Athens,
Zografou, 15780 Athens, Greece
e-mail: mitsouli@metal.ntua.gr

Numerical simulations have been undertaken for the benchmark problem of annular extrudate swell present in pipe extrusion and parison formation in blow molding. The effects of weak compressibility and slip at the wall are studied through simple linear laws. The finite element method is used to provide numerical results for different inner/outer diameter ratios κ under steady-state conditions for Newtonian fluids. The present results provide the shape of the extrudate, and, in particular, the thickness and diameter swells, as a function of the dimensionless compressibility and slip coefficients, B and B_{sl}, respectively. The pressures from the simulations have been used to compute the excess pressure losses in the flow field (exit correction). Weak compressibility slightly affects the thickness swell (about 1% in the range of simulations $0 \leqslant B \leqslant 0.02$) mainly by a swell reduction, while slip drastically reduces the swelling to 1–2% for obvious slip ($B_{sl} \approx 1$) and to 0 for perfect slip ($B_{sl} > 10$). The exit correction increases with increasing compressibility levels and is highest for the tube ($\kappa=0$) and lowest for the slit ($\kappa=1$). It decreases monotonically to 0 as the dimensionless slip coefficient reaches its asymptotic limit of perfect slip. All results are ordered with the diameter ratio κ, between the limits of tube ($\kappa=0$) and slit ($\kappa=1$). [DOI: 10.1115/1.2786491]

Keywords: annular flow, extrudate swell, exit correction, pipe extrusion, blow molding, Newtonian fluid, weak compressibility, wall slip, linear law

1 Introduction

Annular flow occurs in many processes, such as blow molding and pipe extrusion in polymer processing [1], or in any material flow between two concentric cylinders [2]. The fully developed problem of a Newtonian fluid in an annulus is one of the standard problems in fluid mechanics and transport phenomena textbooks [3]. When considering the exit of the fluid in the atmosphere and the accompanying phenomenon of extrudate swell (Fig. 1), the Newtonian problem has been solved more that 20 years ago for different inner/outer diameter ratios κ by Mitsoulis [4]. Since then, variations of the problem have been studied, including the effect of die design [5], of viscoelasticity [6], of inertia, gravity, surface tension, etc. [7].

On the other hand, the effects of *compressibility* (usually weak) and/or *wall slip* (through some kind of a slip law) have been studied in some key works [8–12]. While the extrudate swell problem for compressible Newtonian fluids has been studied before for tubes ($\kappa=0$) and slits ($\kappa=1$), [8,10], the annular swell problem has not. The same is true for wall slip [9,11]. As more evidenced is accumulated that both effects are present in many polymer and material processes, it is of interest to study these effects first in simple benchmark situations for Newtonian fluids, before embarking on studies for more complicated non-Newtonian viscoplastic and/or viscoelastic materials.

It is, therefore, the purpose of the present paper to undertake a full parametric study of different κ values for Newtonian fluids and provide detailed results both for the free surface location and the associated extrudate swells, as well as the excess pressure losses in the system (exit correction) as a function of a dimensionless compressibility coefficient, B. Then the same is done for Newtonian fluids exhibiting wall slip as a function of a dimensionless slip coefficient, B_{sl}, in a wide parameter range from $B_{sl}=0$ (no slip) to $B_{sl} \to \infty$ (perfect slip). The extreme cases of slits and tubes will also be included for completion.

2 Mathematical Modeling

The problem at hand is shown schematically in Fig. 1, where an incompressible or weakly compressible Newtonian fluid is considered flowing in an annulus under steady-state conditions and exiting in the atmosphere where it acquires a free surface (annular extrudate swell) [4]. The annulus is defined by the inner/outer diameter ratio κ, while the outer radius is R_0 and the annular gap is h_0. The flow is governed by the usual conservation equations of mass and momentum under creeping, isothermal flow conditions. Therefore, the effects of inertia, gravity, and surface tension are neglected, which is a good approximation for all highly viscous fluids.

The conservation of mass for weakly compressible fluids is written as

$$\nabla \cdot (\rho \bar{u}) = 0 \tag{1}$$

where ρ is the density and $\bar{\mathbf{u}}$ is the velocity vector. The conservation of momentum is written as

$$0 = -\nabla p(\rho) + \nabla \cdot \bar{\bar{\tau}} \tag{2}$$

where p is the pressure (a function of density ρ) and τ is the extra stress tensor, which is related to the velocity gradients via the

Contributed by the Fluids Engineering Division of ASME for publication in the JOURNAL OF FLUIDS ENGINEERING. Manuscript received December 14, 2006; final manuscript received June 5, 2007. Review conducted by Dennis Siginer.

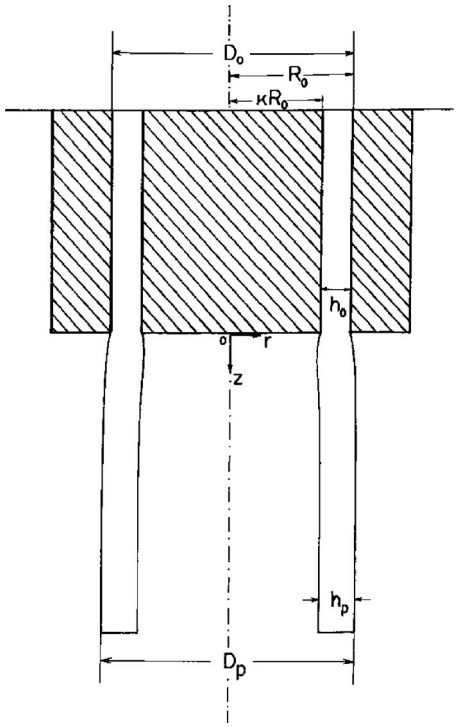

Fig. 1 Schematic representation of extrusion through an annular die and notation for the numerical analysis [2]

Newtonian constitutive equation for compressible fluids [8,10,11]:

$$\bar{\bar{\tau}} = \mu\left[\bar{\bar{\dot{\gamma}}} - \frac{2\Lambda}{3}(\nabla\cdot\bar{u})\bar{\bar{I}}\right] \tag{3}$$

where μ is the constant viscosity, $\bar{\bar{\dot{\gamma}}} = \nabla\bar{\mathbf{u}} + \nabla\bar{\mathbf{u}}^T$ is the rate-of-strain tensor made up by the velocity gradient tensor $\nabla\bar{\mathbf{u}}$ and its transpose $\nabla\bar{\mathbf{u}}^T$, and Λ is a convenient coefficient, which takes the values of 0 for incompressible fluids and 1 for compressible fluids.

For isothermal flows, pressure and density are related as a first approximation via a simple thermodynamic equation of state, the linear form of which is given by [9]

$$\rho = \rho_0(1 + \beta p) \tag{4}$$

where β is the compressibility coefficient (in Pa^{-1} units) defined as

$$\beta = -\frac{1}{V_f}\left(\frac{\partial V_f}{\partial p}\right)_{p_0,T_0} \tag{5}$$

where V_f is the fluid volume at reference pressure p_0 and temperature T_0, also related to reference density ρ_0. For weakly compressible flows, the β values are in the range of 0 (incompressible fluids) to 0.01 MPa^{-1} (weakly compressible fluids) [8–11].

All lengths are scaled with the annular gap width h_0, all velocities with the inlet average velocity V, and all pressures and stresses with $\mu V/h_0$.

The constitutive equation must be solved together with the conservation equations and appropriate boundary conditions. Figure 2 shows the solution domain and boundary conditions. Because of symmetry, only one-half of the flow domain is considered, as was done previously [4,6]. The boundary conditions are therefore as follows:

(a) no slip along the walls AS_1 and DS_2 ($v_z = v_r = 0$);
(b) along the inflow boundary DA, fully developed velocity profile ($v_z(r) = f_1(r)$, $v_r = 0$), corresponding to a given (unit) average velocity (or constant volume flow rate);

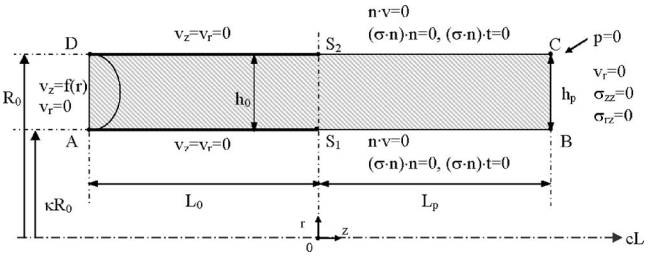

Fig. 2 Schematic diagram of flow domain and boundary conditions

(c) along the outflow boundary BC, zero radial velocity ($v_r = 0$), and vanishing tangential and normal stresses ($(\bar{\bar{\sigma}}\cdot\bar{\mathbf{n}})\cdot\bar{\mathbf{t}} = 0$, $(\bar{\bar{\sigma}}\cdot\bar{\mathbf{n}})\cdot\bar{\mathbf{n}} = 0$), where $\bar{n}$ and $\bar{t}$ are the normal and tangential vectors to the surface and $\bar{\bar{\sigma}} = -p\bar{\bar{I}} + \bar{\bar{\tau}}$ is the total stress;
(d) along the free surfaces S_1B and S_2C, vanishing tangential and normal stresses ($(\bar{\bar{\sigma}}\cdot\bar{\mathbf{n}})\cdot\bar{\mathbf{t}} = 0$, $(\bar{\bar{\sigma}}\cdot\bar{\mathbf{n}})\cdot\bar{\mathbf{n}} = 0$) and no flow through the surface ($\bar{v}\cdot\bar{n} = 0$).

The reference pressure is also set to zero at point C.

In the case of a slip boundary condition on the solid walls, the no-slip boundary condition (a) is relaxed, and the boundary velocities are found as part of the solution as a function of the wall shear stresses. Various slip models have been proposed in the literature [9,11]. The simplest slip model is a linear law, which takes the form

$$u_{\mathrm{sl}} = \beta_{\mathrm{sl}}\tau_w \tag{6}$$

where τ_w is the wall shear stress τ_{rz} (Pa), u_{sl} is the wall slip velocity (m/s), and β_{sl} is a slip coefficient ($\mathrm{m/s\,Pa^{-2}}$) determined experimentally [12,13]. Its tensorial representation becomes

$$\bar{\mathbf{t}}\cdot\bar{\mathbf{u}} = \beta_{\mathrm{sl}}(\bar{\mathbf{t}}\bar{\mathbf{n}}:\bar{\bar{\tau}}) \quad \bar{\mathbf{n}}\cdot\bar{\mathbf{u}} = 0 \tag{7}$$

The introduction of dimensionless quantities leads to two dimensionless numbers in the case of compressibility and the case of slip:

(a) A dimensionless compressibility coefficient B defined by [9,10]

$$B = \frac{\beta\mu V}{h_0} \tag{8}$$

In all cases, the incompressible fluid corresponds to $B = 0$. The range of B values in the simulations is $0 \leqslant B \leqslant 0.02$ [8,10].

(b) A dimensionless slip coefficient B_{sl}, defined by [14]

$$B_{\mathrm{sl}} = \frac{\beta_{\mathrm{sl}}\mu}{h_0} \tag{9}$$

In all cases, the no-slip condition corresponds to $B_{\mathrm{sl}} = 0$. The value of $B_{\mathrm{sl}} = 1$ corresponds to obvious slip, while $B_{\mathrm{sl}} = \infty$ reflects perfect slip. The range of B_{sl} values in the simulations is $0 \leqslant B_{\mathrm{sl}} \leqslant 100$ [14].

In the present simulations, the results are given as a function of these two dimensionless parameters for compressibility and slip effects on Newtonian fluids.

3 Method of Solution

The numerical solution is obtained with the finite element method (FEM), using the in-house program UVPTH, originally developed for multilayer flows [15], which employs as primary variables the two velocities, pressure, temperature, and free surface location (*u-v-p-T-h formulation*). This program was modified in the course of the present work to account for compressibility and slip. It uses nine-node Lagrangian quadrilateral elements with bi-

Table 1 Description of the finite element meshes used for the current computations. For each mesh, the number of elements, nodes, and the unknown degrees of freedom are given.

Mesh	L_0/h_0	L_p/h_0	r nodes	Elements	Nodes	DOF
M1	8:1	8:1	29	560	2349	5,136
M2	8:1	8:1	29	1120	4669	10,362
M3	8:1	8:1	57	2240	9177	20,429

quadratic interpolation for the velocities, temperatures, and free surface location, and bilinear interpolation for the pressures. The free surface is found in a coupled way as part of the solution for the primary variables. All details of the FEM formulation are given in long-hand notation in a thesis [16].

For most of the simulations, we have used three meshes of increasing density. Their characteristics are given in Table 1. Mesh M1 has 560 elements (29 nodes in the r direction and 81 nodes in the z direction), Mesh M2 has 1120 elements and is produced by doubling the elements in the z direction, and Mesh M3 has 2240 elements and is produced by subdividing each M1 element into four subelements. Figure 3 shows M3 (upper half) and M1 (lower half), put together for brevity, for $\kappa=0.5$ as obtained from the Newtonian incompressible solution. More elements are concentrated near the walls and the exit, because of the larger changes expected in these regions. Also, more elements are put near the middle of the gap in anticipation of the plug regions existing in flows with wall slip. In the limiting cases of slit ($\kappa=1$) and tube ($\kappa=0$), the radial distributions of the elements was altered due to the presence of a centerline as the lower boundary.

The entry has been set at $-8h_0$ and the die exit at 0, while the extrudate length is taken as $8h_0$. The entry length $L_0=8h_0$ is in accordance with our previous incompressible simulations [4] and is necessary in order to impose at inlet a fully developed velocity profile, found numerically by solving the 1D problem by the FEM. The entry length L_0 does play a role in compressible flows due to the convective nature of these flows. The adequacy of the exit length L_p was checked by plotting the free surfaces and observing their levelling-off in the extrudate region away from the die. Our meshes are denser than the ones used in our previous works [4,6]. The less dense Mesh M1 with 560 elements was used primarily for preliminary runs to gain experience with compressible annular flows.

The initial mesh configuration was that of a rectangular domain. After an initial solution was obtained in this fixed rectangular domain, the velocities at the free surface were integrated either using Simpson's rule (decoupled approach) or using the Galerkin principle for the h variable in the u-v-p-T-h formulation with comparable results.

The iterative scheme was direct substitution (Picard iterations), and the criteria for termination of the iterative process were for both the norm of the error and the norm of the residuals $<10^{-4}$, and for the maximum free surface change $<10^{-5}$. Due to the two free surfaces present in annular flows, under-relaxation for the movement of the free surface was found helpful, with the under-relaxation factor $\omega_f=0.5$. Around 25 iterations were thus needed to get the incompressible solution ($B=0$), after which continuation in the B values was employed with changes of 0.001. Convergence for the low B values was achieved with very few iterations (4–5), which progressively increased. Problems with convergence started appearing for $B>0.02$, which seems to be the limiting value for the present formulation. Correspondingly, for the wall slip simulations, the number of iterations was always around 25 for all B_{sl} values ($0\leqslant B_{sl}\leqslant 100$).

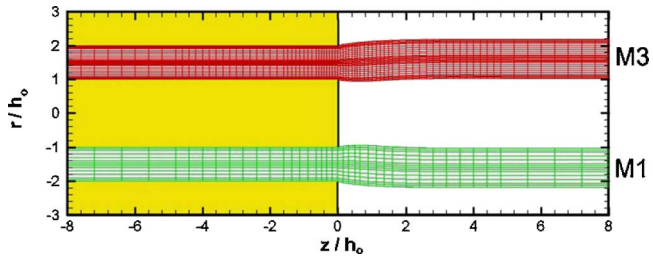

Fig. 3 Finite element meshes used in the computations. The upper half shows Mesh M3 containing 2240 quadrilateral elements, while the lower half shows Mesh M1 containing 560 elements (see also Table 1 for details).

4 Results and Discussion

4.1 Poiseuille Flow of Weakly Compressible Newtonian Fluids. The computer program was first tested against analytical solutions for planar and axisymmetric Poiseuille flows of compressible Newtonian fluids. Following Beverly [17], we consider a parabolic inlet velocity profile with a maximum velocity of 2 at the centerline. Then the average velocity V is 4/3 for planar and 1 for axisymmetric geometries. Assuming a constant mass flow rate $\dot{m}$ at entry and exit in a flow domain of length L, it is easy to show that the inlet pressure p is given by (assuming a zero exit pressure) the following.

In planar geometry,

$$p^2+\left(\frac{2}{\beta}-\frac{6\mu LV}{H^2}\right)p=\frac{6\mu LV}{\beta H^2} \tag{10a}$$

In axisymmetric geometry:

$$p^2+\left(\frac{2}{\beta}-\frac{16\mu LV}{R^2}\right)p=\frac{16\mu LV}{\beta R^2} \tag{10b}$$

where H is the half gap between parallel plates and R the tube radius. Georgiou and Crochet [9] for slits and Georgiou [11] for tubes give the corresponding pressure distributions as a function of $\dot{m}$, and show that the pressure is a quadratic function in the axial direction and the velocity is also quadratic and changes in both directions.

The 2D FEM numerical results were derived in a 5×5 element grid with $r=[0,1]$ and $z=[0,6]$ and with an inlet velocity profile corresponding to $V=4/3$ for planar and 1 for axisymmetric geometries. The use of such a sparse grid is solely for the purpose of showing that the formulation is correct and gives acceptable results when compared with the analytical solutions. Unit values are used for the viscosity μ and half gap H. The numerical solution for the planar case was matching the analytical within 3 Picard iterations for $B=0.0133$, 6 iterations for $B=0.0667$, and 14 iterations for $B=0.1333$, in all cases starting from the incompressible solution and satisfying the aforementioned criteria for convergence. For $B>0.1333$, continuation in the solution was needed and many more iterations were necessary (68 for $B=0.2$), but the solution had already deteriorated. Generally speaking, for *weakly* compressible fluids the equations do not hold for $B>0.15$, and for this reason no simulations have been pursued beyond such a value [11].

The planar results for the centerline axial distributions of pressure P and velocity u_x as a function of the compressibility coefficient B are shown in Figs. 4(a) and 4(b), respectively. Both

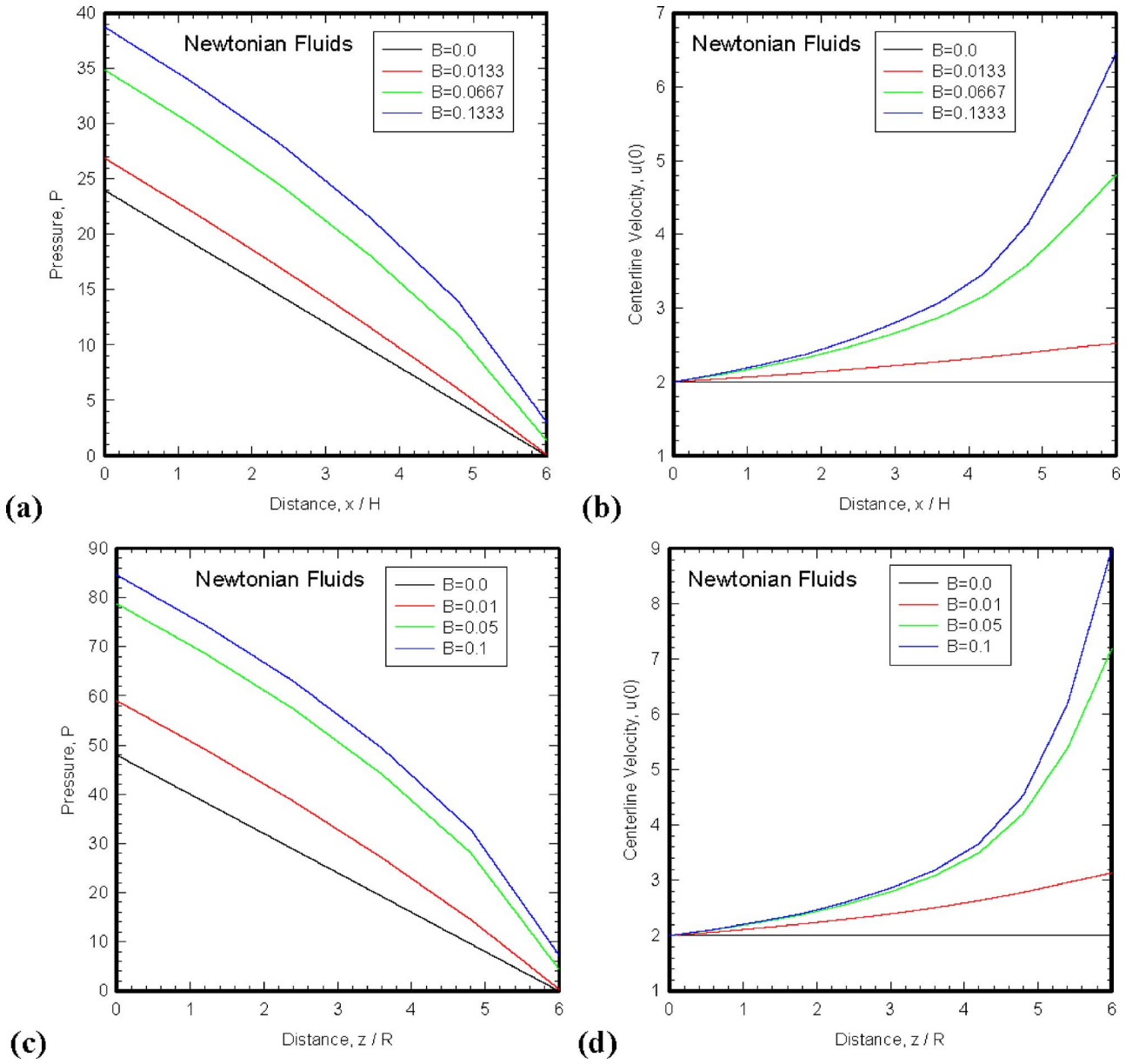

Fig. 4 Poiseuille flow of weakly compressible Newtonian fluids. Axial pressure and velocity distributions along the centerline: (*a*) pressure (planar flow), (*b*) velocity (planar flow), (*c*) pressure (axisymmetric flow), and (*d*) velocity (axisymmetric flow).

variables are parabolic functions of length x. The inlet pressure values for $B=0.0133$ ($\beta=0.01$) are $P=26.91$ at the wall and $P=26.93$ at the symmetry line, while the analytical solution gives $P=26.84$ (Eq. (10*a*)). These results have also been given by Beverly [17] and Beverly and Tanner [8] and validate the present results. The corresponding velocity values are $u_x(0,0)=2$ at inlet and $u_x(0,6)=2.52$ at outlet, while the analytical solution [9] gives $u_x(0,6)=2.54$ at outlet.

The corresponding results for the axisymmetric flow are given in Figs. 4(*c*) and 4(*d*), respectively. Same observations as before are made, but the values now are higher for the same B value. Thus, the pressure values for $B=0.01$ ($\beta=0.01$) are found numerically to be $P=59.04$ at the wall and $P=59.08$ at the symmetry line, while the analytical solution gives $P=58.92$ (Eq. (10*b*)). No such numerical results are found in the literature for direct comparison. The corresponding velocity values are $u_z(0,0)=2$ at inlet and $u_z(0,6)=3.13$ at outlet, while the analytical solution [11]

Table 2 Effect of different meshes on extrudate swell and exit correction for Newtonian fluids in annular flow. Comparison with previous results ($\kappa=0.5$) [4]

Mesh	Dia. swell $B_1(\%)$	Inner dia. swell $B_3(\%)$	Thickness swell $B_2(\%)$	Exit correction n_{ex}
		$B=B_{sl}=0$ (incompressible, no slip)		
M1	9.19	2.33	16.05	0.164
M2	9.14	2.31	15.97	0.165
M3	9.11	2.35	15.87	0.166
[4]	8.87	1.70	16.05	0.171
		$B=0.01$		
M1	8.97	2.02	15.93	0.269
M2	8.54	2.12	14.97	0.269
M3	8.49	2.14	14.84	0.269

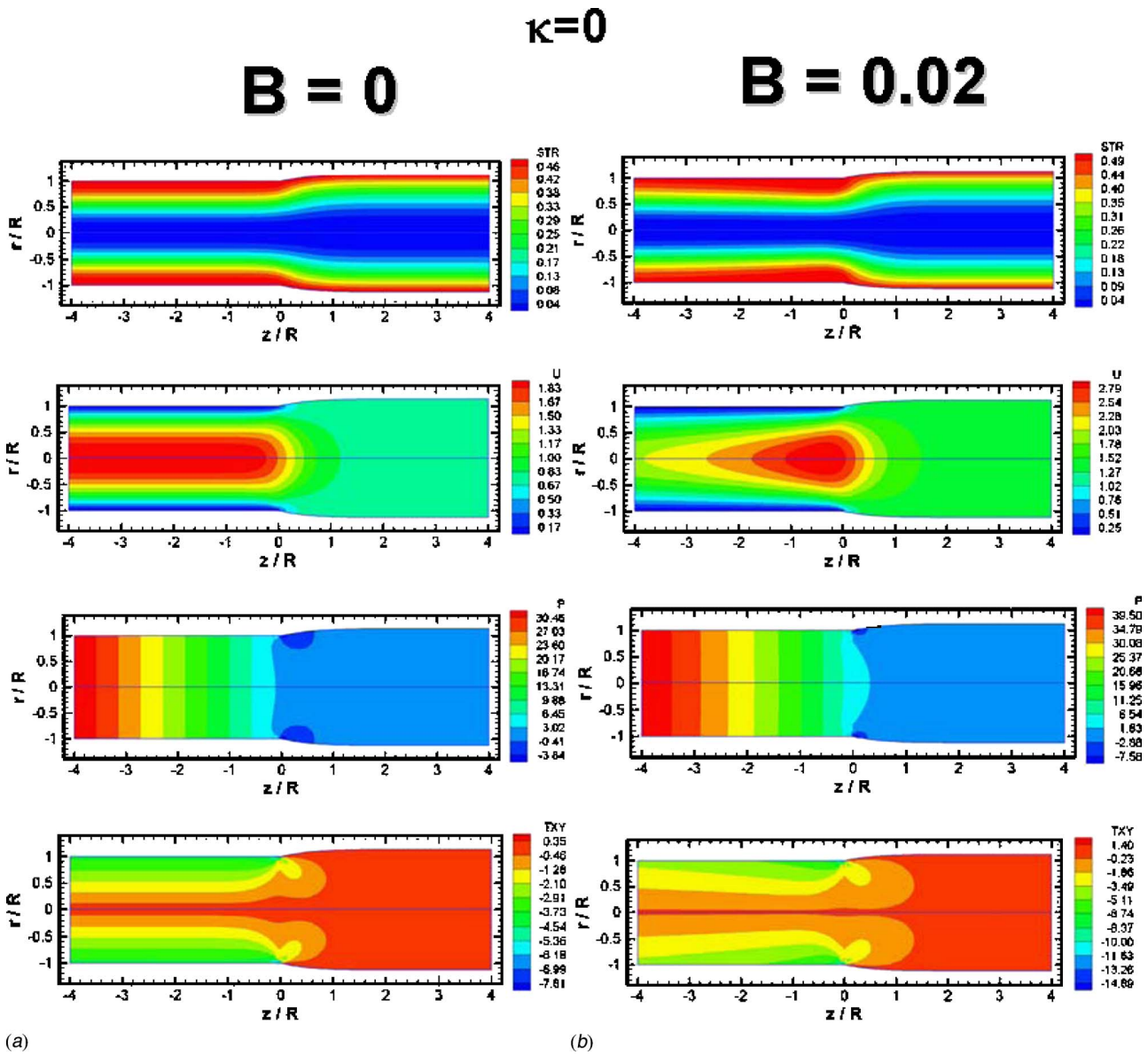

Fig. 5 Extrudate swell of Newtonian fluids for $\kappa=0$ (tube): (*a*) incompressible fluid ($B=0$); (*b*) weakly compressible fluid ($B=0.02$)

gives at the outlet $u_z(0,6)=3.14$ $(=\pi)$. Therefore, even for very sparse grids (25 elements), we observe a very good agreement with the analytical solutions for weakly compressible fluids. In what follows, we apply our numerical scheme to the annular extrudate swell problem employing much denser grids of increasing refinement for the production of accurate numerical results.

4.2 Extrudate Swell of Weakly Compressible Newtonian Fluids. For all cases studied, runs were performed for $\kappa=(0,0.02,0.1,0.25,0.5,0.75,0.9,0.98,1)$ with no slip at the wall assumed as in our previous work for Newtonian fluids [4]. The cases of $\kappa=0$ and $\kappa=1$ correspond to the extreme cases of a round tube and a two-dimensional slit, respectively [3]. The results are given in terms of the three-dimensionless swell ratios, B_i $(i=1,2,3)$ (only two of which are independent), and of the dimensionless change in pressure drop over and above the fully developed values, n_{ex}. These are defined as follows [4,5]:

(i) the (outer) diameter swell B_1 defined by

$$B_1=\frac{D_p}{D_0} \tag{11}$$

where D_p is the extrudate outer diameter and D_0 is the die outer diameter (Fig. 1);

(ii) the thickness swell B_2 defined by

$$B_2=\frac{h_p}{h_0} \tag{12}$$

where h_p is the extrudate (parison) thickness (distance BC, see Fig. 2), and h_0 is the annular gap (distance AD);

(iii) the inner diameter swell B_3 defined by

$$B_3=\frac{D_p-2h_p}{D_0-2h_0} \tag{13}$$

(iv) the exit correction n_{ex} defined by [18,19]

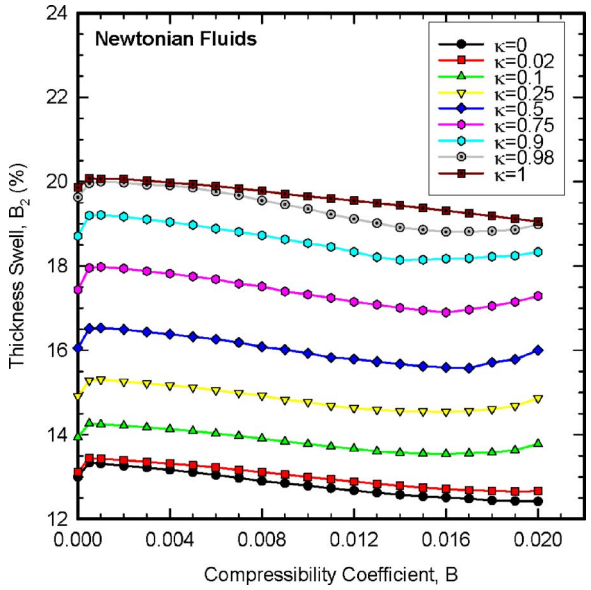

Fig. 6 Thickness swell B_2 as a function of the compressibility coefficient B for Newtonian fluids obeying a linear equation of state (Eq. (4))

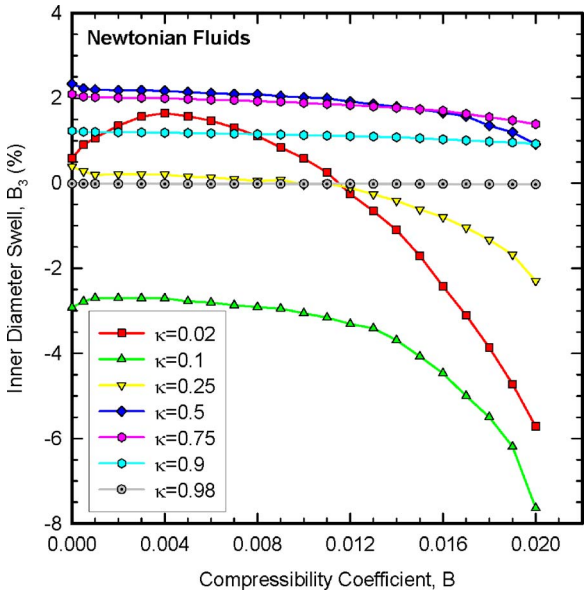

Fig. 8 Inner diameter swell B_3 as a function of the compressibility coefficient B for Newtonian fluids obeying a linear equation of state (Eq. (4))

$$n_{\text{ex}} = \frac{\Delta P - \Delta P_0}{2\tau_{w,o}} \tag{14}$$

where ΔP is the overall pressure drop in the system, ΔP_0 is the pressure drop based on the fully developed flow in the annulus without the extrudate region (distance DS_2 in Fig. 2), and $\tau_{w,o}$ is the shear stress for fully developed flow at the outer annular wall. Results for these quantities have been produced with all three meshes and their variation was at most 1% (compressible fluid with $B=0.01$) (see Table 2).

The calculations are pursued first for weakly compressible fluids in the range of $0 \leqslant B \leqslant 0.02$. Typical results from the simulations are shown in Fig. 5 for $\kappa=0$ (tube) and for $B=0$ and 0.02 (left and right columns, respectively) as contours of various variables. First shown are the streamlines (contours of the stream function ψ or STR). The streamlines have been obtained a posteriori by solving the Poisson equation for the stream function with the known nodal vorticity values. Then shown are the contours for the axial velocity u_z or U, the pressure p or P, and the shear stresses τ_{rz} or TXY. The convective type of compressible flow is evident (due to the convective terms $\bar{u}\cdot\nabla\rho$ in the equation of mass conservation), and for this reason the results depend not only on the compressibility coefficient B but on the die length L_0 as well. Compressibility serves to squeeze the streamlines toward the exit and accelerate the flow there, as evidenced by the increased axial velocities and shear stresses near the exit, and to increase the

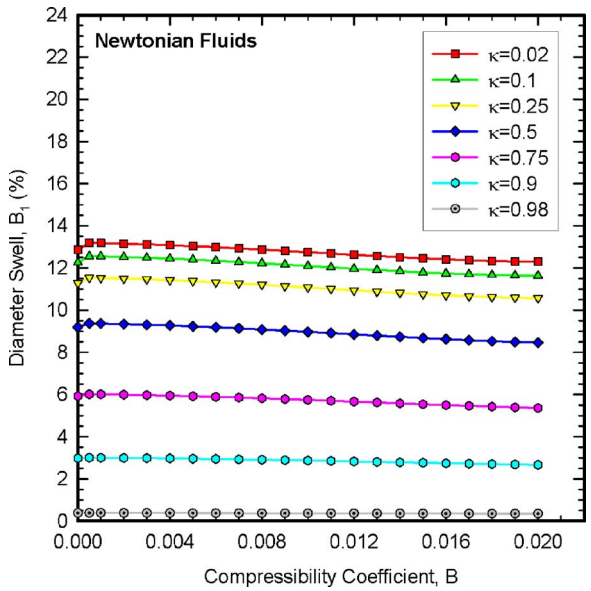

Fig. 7 Diameter swell B_1 as a function of the compressibility coefficient B for Newtonian fluids obeying a linear equation of state (Eq. (4))

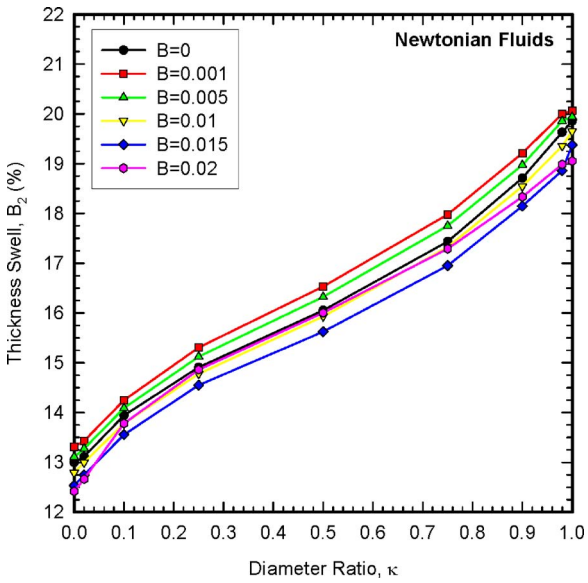

Fig. 9 Thickness swell B_2 as a function of the diameter ratio κ for various values of the compressibility coefficient B for Newtonian fluids obeying a linear equation of state (Eq. (4))

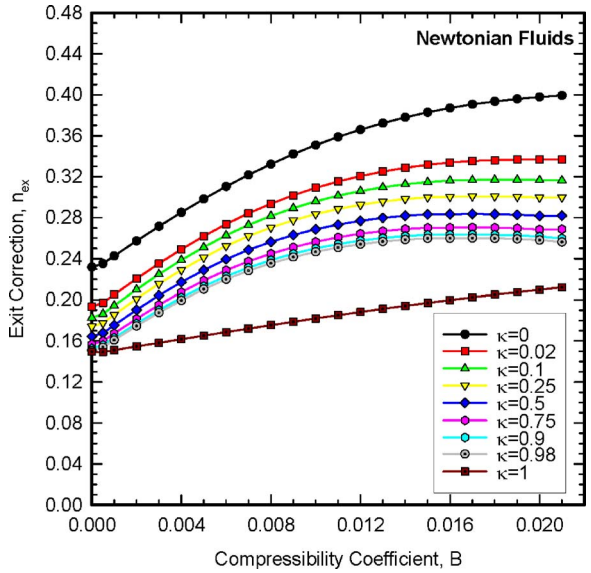

Fig. 10 Exit correction n_{en} as a function of the compressibility coefficient B for Newtonian fluids obeying a linear equation of state (Eq. (4))

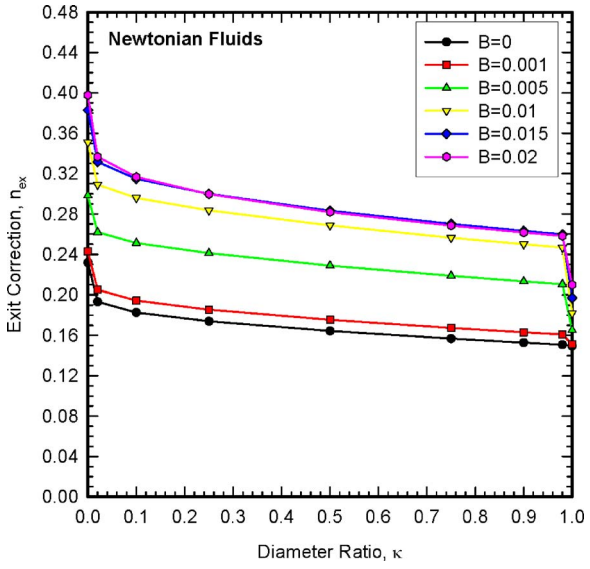

Fig. 11 Exit correction n_{ex} as a function of the diameter ratio κ for various values of the compressibility coefficient B for Newtonian fluids obeying a linear equation of state (Eq. (4))

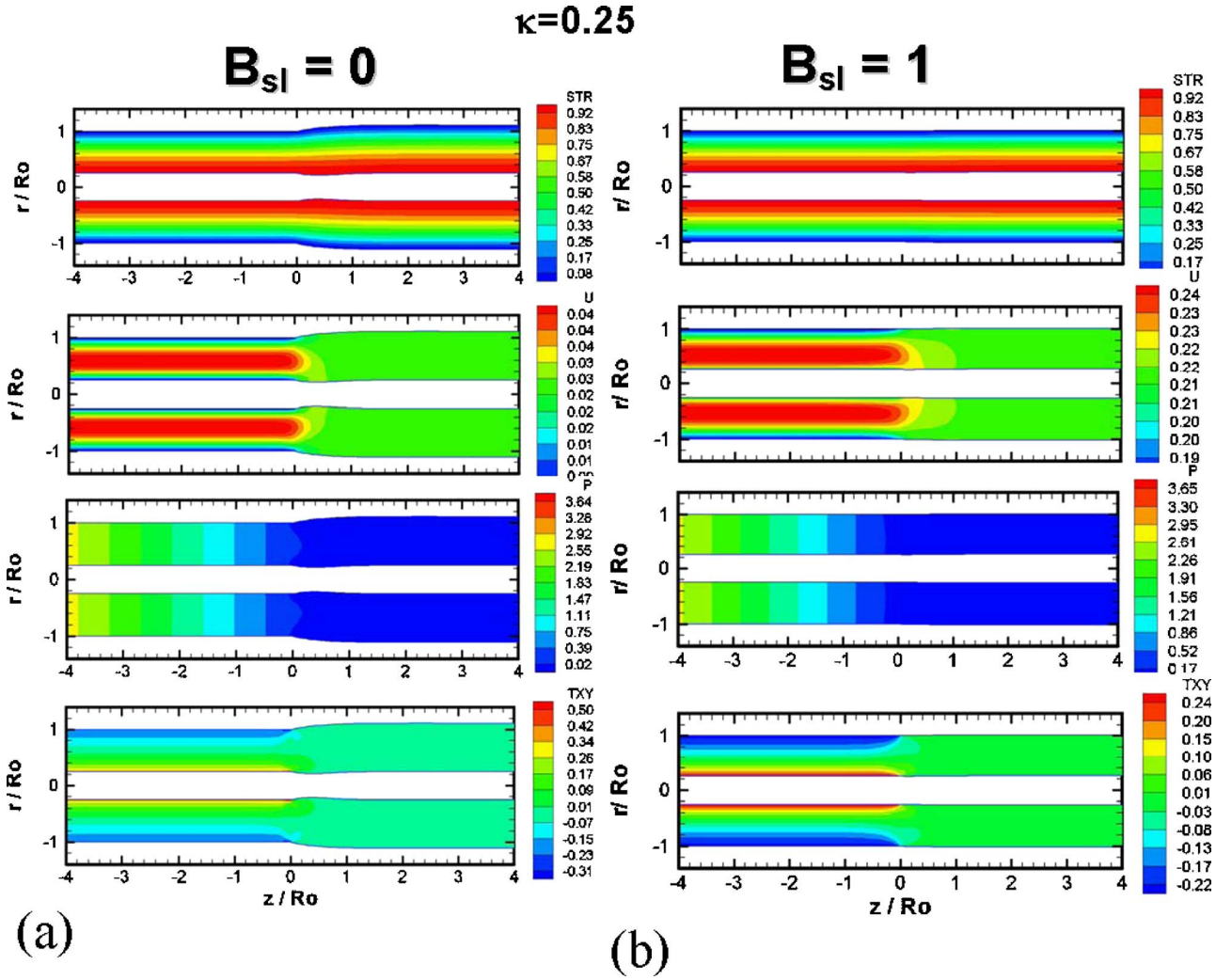

Fig. 12 Annular extrudate swell of Newtonian fluids for κ=0.25: (*a*) B_{sl}=0 (no slip); (*b*) B_{sl}=1 (obvious slip)

pressure drop in the system compared with the incompressible values.

The results for the thickness swell (B_2) as a function of the compressibility coefficient B are given in Fig. 6 for different κ ratios. Interesting trends are observed. Increasing B leads to a nonmonotonic change in the thickness swell, which was also observed by Georgiou [10] for tubes ($\kappa=0$). The initial increase was found to be die-length dependent, i.e., for $L_0=8h_0$ used here, this increase was present, but for $L_0=4h_0$ and $L_0=5h_0$ there was no such initial increase and the results dropped monotonically to a minimum before the upturn. The change in swell is not significant (in the order of 1%), as also found previously for tubes [8,10] and slits [8] in the range of simulations. All results are ordered with κ as they should.

The corresponding results for the diameter swell (B_1) are shown in Fig. 7, while those for the inner diameter swell (B_3) are shown in Fig. 8. Some points to notice are the much smaller change in diameter swell for all B and κ values. The inner diameter swell shows the biggest changes for $\kappa \leqslant 0.25$, to accommodate the upturn in the thickness swell. Also while B_1 follows B_2 in trend, albeit with smaller values, B_3 is not, showing sometimes (for $\kappa < 0.25$) a nonmonotonic behavior for different B values.

If the results for the thickness swell are plotted versus the diameter ratio κ (Fig. 9), we observe a sigmoidal trend, first reported for Newtonian incompressible fluids by Mitsoulis [4]. The curves are not monotonically ordered but are above and below the incompressible case ($B=0$) to reflect the same behavior shown in Fig. 6.

The results for the exit correction (n_{ex}) as a function of the compressibility coefficient B are given in Fig. 10 for different κ ratios. Again, interesting trends are observed. The exit correction is an increasing function of B, but seems to level off at the higher range of B values. The exit correction is highest for the tube ($\kappa=0$) and lowest for the slit ($\kappa=1$), with all other κ values ordered between these two extreme cases.

If the results for the exit correction are plotted versus the diameter ratio κ (Fig. 11), we observe a monotonic decrease, first reported for Newtonian incompressible fluids by Mitsoulis [4]. This trend is somewhat more pronounced for higher B (more compressible fluids). Because of the monotonicity of the results shown in the previous graph, the curves are ordered for different B values, except again at the upper limit of the computations where the results for $B=0.015$ are very close to the ones for $B=0.02$. For the same B value, the effect of increasing κ is to slightly decrease the exit correction, but again the changes are not significant, and they follow those found for the incompressible case ($B=0$).

4.3 Extrudate Swell of Newtonian Fluids With Slip at the Wall. The calculations are then pursued for incompressible Newtonian fluids exhibiting slip at the wall by obeying the linear slip law (Eq. (7) or (8)) in a wide range of the dimensionless slip coefficient B_{sl} ($0 \leqslant B_{sl} \leqslant 100$). The numerical solution was first checked against well-known analytical solutions (see, e.g., Mitsoulis [14] for flow in an annulus) with excellent results. Then the simulations were pursued for annular flows. Typical results from the simulations are shown for $\kappa=0.25$ in Fig. 12(*a*) (no slip, $B_{sl}=0$) and in Fig. 12(*b*) (obvious slip, $B_{sl}=1$). In the latter case, the fluid exits almost as a plug, and the changes relative to the no-slip case are more evident in the axial velocity contours U and the shear stress contours TXY.

The results for the thickness swell (B_2) as a function of the slip coefficient B_{sl} are given in Fig. 13 for different κ ratios. Interesting trends are observed. Increasing B_{sl} decreases substantially the thickness swell, especially in the range $10^{-2} \leqslant B_{sl} \leqslant 1$. For $1 \leqslant B_{sl} \leqslant 10$, the swelling is in the order of 1–2%. For $B_{sl} > 10$, all results approach asymptotically 0 (no distortion, no swell, the fluid exits as a plug) as $B_{sl} \to \infty$. There is no negative swell here for all B_{sl} values. The present results are in full agreement with

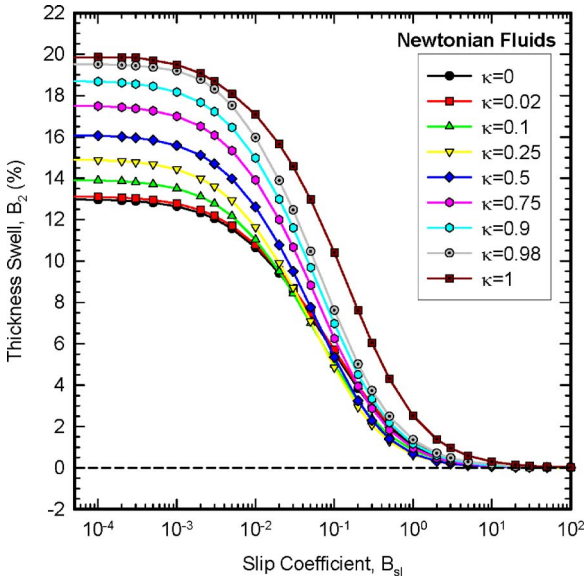

Fig. 13 Thickness swell B_2 as a function of the slip coefficient B_{sl} for Newtonian fluids obeying a linear slip law (Eq. (6))

previous ones for $\kappa=0$ (tube) and $\kappa=1$ (slit) [9,11]. The new results for different κ values are ordered (in the vast majority of cases) between these two extreme cases. However, in some cases of elevated slip values and small κ values, the ordering is not followed, and $\kappa=0$ is not always a lower bound. This apparently is due to the imposition of different boundary conditions for a tube ($\kappa=0$), where there is no inner wall for slip but a symmetry boundary condition is imposed at the centerline, while for an annulus there are both walls where slip is applied.

The corresponding results for the diameter swell (B_1) are shown in Fig. 14, while those for the inner diameter swell (B_3) are shown in Fig. 15. The diameter swell results are ordered with κ for all B_{sl} values. The diameter swell ratios are bounded above by the tube results ($\kappa=0$). The inner diameter results are nonmonotonic, and their maxima and minima reflect the behavior of the thickness

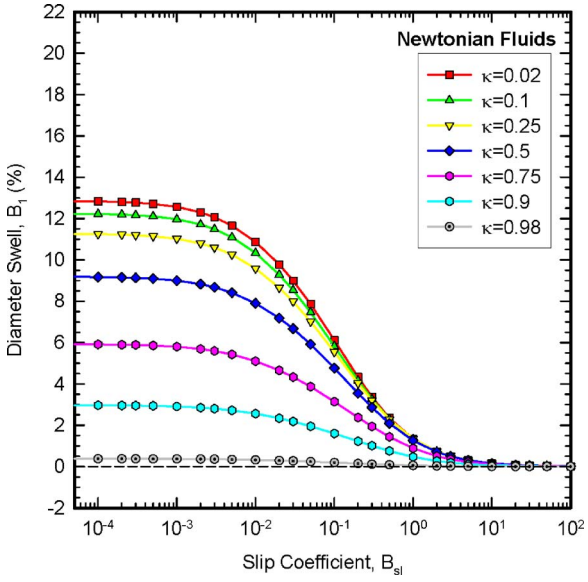

Fig. 14 Diameter swell B_1 as a function of the slip coefficient B_{sl} for Newtonian fluids obeying a linear slip law (Eq. (6))

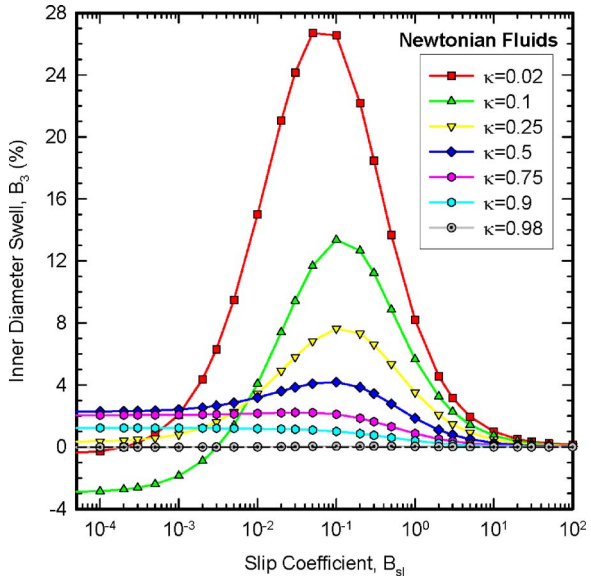

Fig. 15 Inner diameter swell B_3 as a function of the slip coefficient B_{sl} for Newtonian fluids obeying a linear slip law (Eq. (6))

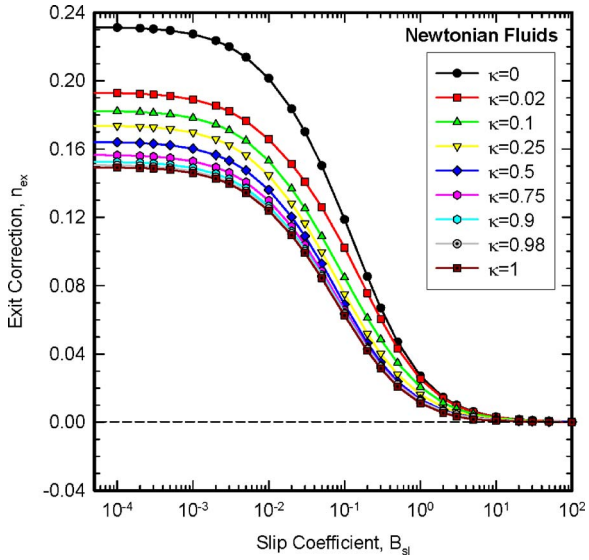

Fig. 17 Exit correction n_{en} as a function of the slip coefficient B_{sl} for Newtonian fluids obeying a linear slip law (Eq. (6))

swell, with its sigmoidal form and the reversal of behavior at middle B_{sl} values for small κ values. This latter behavior is enhanced as $\kappa \to 0$.

If the results for the thickness swell are plotted versus the diameter ratio κ (Fig. 16), we observe that as the B_{sl} increases the influence of κ is not important. The curves are monotonically ordered toward the zero line as B_{sl} increases, which zero line they reach at around $B_{sl} \approx 20$.

The results for the exit correction (n_{ex}) as a function of the slip coefficient B_{sl} are given in Fig. 17 for different κ ratios. Again, interesting trends are observed. The exit correction decreases monotonically in a sigmoidal manner as B_{sl} increases. As was the case with the thickness swell (Fig. 13), most of the drastic drop in n_{ex} occurs in the range $10^{-2} \leq B_{sl} \leq 1$. At the limit of $B_{sl} \to \infty$ (or $B_{sl} \to 100$, plug flow) the results all converge to 0, as they should (no excess pressure losses, since the fluid flows and exits as a plug). The present results are reminiscent of our previous ones on viscoplastic (Bingham) fluids for $\kappa=0$ (tube) and $\kappa=1$ (slit) [20]. The results for different κ values are ordered between these two extreme cases.

If the results for the exit correction are plotted versus the diameter ratio κ (Fig. 18), we observe a monotonic decrease, as with Newtonian fluids without slip [4]. This trend diminishes for higher B_{sl} values (higher slip). Because of the monotonicity of the results shown in the previous graph, the curves are ordered from top to bottom for increasing B_{sl} values. The results do not show significant changes with increasing κ values. As B_{sl} increases, the curves are heading toward the zero line of no excess pressure losses (plug flow throughout the flow field). This is already the case for $B_{sl}=20$.

5 Conclusions

The finite element method has been used to derive numerical solutions for the extrudate swell and exit correction (dimension-

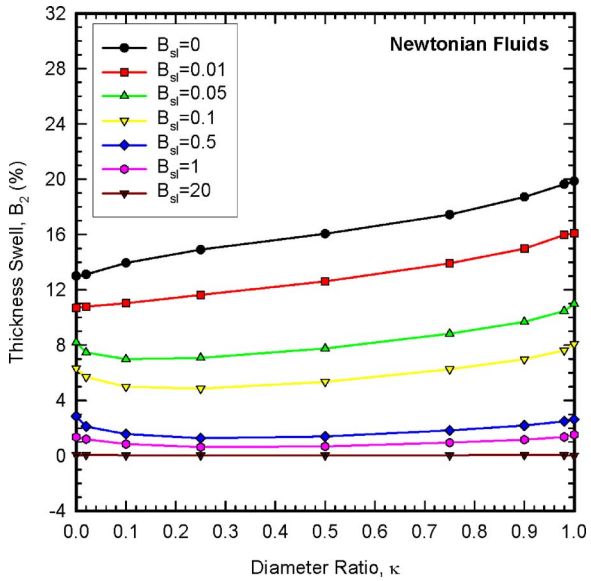

Fig. 16 Thickness swell B_2 as a function of the diameter ratio κ for Newtonian fluids obeying a linear slip law (Eq. (6))

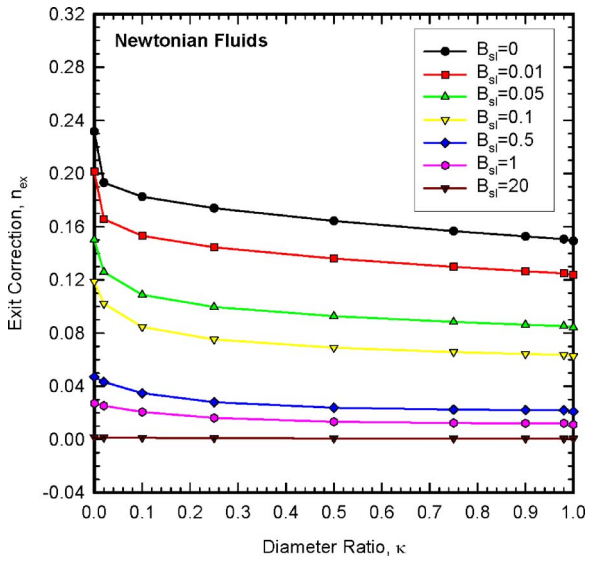

Fig. 18 Exit correction n_{ex} as a function of the diameter ratio κ for Newtonian fluids obeying a linear slip law (Eq. (6))

less excess pressure losses) in annular flow of Newtonian fluids for different diameter ratios κ. The effects of weak compressibility and wall slip have been introduced and studied through simple linear laws.

In the case of weakly compressible fluids, it was found that increasing compressibility has little effect on the extrudate swell, in the order of 1%. However, this influence is not monotonic, showing maxima and minima, which are affected by the die length (due to the convective nature of compressible flows). All thickness swell values range between 13% and 20%, which are the limits for tubular axisymmetric and planar flows, respectively. The exit correction is increased as compressibility increases for all κ values.

The influence of wall slip is to reduce all swells to 0 as slip increases to correspond to a plug profile (or as the slip coefficient $B_{sl} \to \infty$). This decrease to almost no swell is already evident for obvious slip ($B_{sl}=1$). The exit correction also decreases asymptotically to 0 as $B_{sl} \to \infty$. The effect of diameter ratio κ is to reduce slightly the exit correction from the tubular values to the planar ones.

The present results are offered as reference solutions for researchers working with the numerical simulation of pipe extrusion and parison formation in blow molding. They are the prelude for a study of combined effects together with non-Newtonian fluids, exhibiting viscoplasticity and/or viscoelasticity. Such a study is currently under way by the author.

Acknowledgment

Financial support from the European Union's Centres of Excellence consortium under the title of "Polymer Injection Advanced Molding" (PIAM) project (Contract NMP2-CT-2003-505878) is gratefully acknowledged.

References

[1] Tadmor, Z., and Gogos, C. G., 1979, *Principles of Polymer Processing*, SPE Monograph Series, Wiley, New York.
[2] Barnes, H. A., Hutton, J. F., and Walters, K., 1989, *An Introduction to Rheology*, Rheology Series, Elsevier, Amsterdam.
[3] Bird, R. B., Stewart, W. E., and Lightfoot, E. N., 1960, *Transport Phenomena*, Wiley, New York.
[4] Mitsoulis, E., 1986, "Extrudate Swell of Newtonian Fluids From Annular Dies," AIChE J., **32**, pp. 497–500.
[5] Orbey, N., and Dealy, J. M., 1984, "Isothermal Swell of Extrudate From Annular Dies; Effects of Die Geometry, Flow Rate, and Resin Characteristics," Polym. Eng. Sci., **24**, pp. 511–518.
[6] Luo, X.-L., and Mitsoulis, E., 1989, "Memory Phenomena in Extrudate Swell Simulations From Annular Dies," J. Rheol., **33**, pp. 1307–1327.
[7] Housiadas, K., Georgiou, G., and Tsamopoulos, J., 2000, "The Steady Annular Extrusion of a Newtonian Liquid Under Gravity and Surface Tension," Int. J. Numer. Methods Fluids, **33**, pp. 1099–1119.
[8] Beverly, C. R., and Tanner, R. I., 1993, "Compressible Extrudate Swell," Rheol. Acta, **32**, pp. 526–531.
[9] Georgiou, G. C., and Crochet, M. J., 1994, "Compressible Viscous Flow in Slits, With Slip at the Wall," J. Rheol., **38**, pp. 639–654.
[10] Georgiou, G. C., 1995, "The Compressible Newtonian Extrudate Swell Problem," Int. J. Numer. Methods Fluids, **20**, pp. 255–261.
[11] Georgiou, G. C., 2003, "The Time-Dependent, Compressible Poiseuille and Extrudate-Swell Flows of a Carreau Fluid With Slip at the Wall," J. Non-Newtonian Fluid Mech., **109**, pp. 93–114.
[12] Hatzikiriakos, S. G., and Dealy, J. M., 1992,"Wall Slip of Molten High Density Polyethylenes. II. Capillary Rheometer Studies," J. Rheol., **36**, pp. 703–741.
[13] Hatzikiriakos, S. G., and Dealy, J. M., 1992, "Role of Slip and Fracture in the Oscillating Flow of HDPE in a Capillary," J. Rheol., **36**, pp. 845–884.
[14] Mitsoulis, E., 1986, "Finite Element Analysis of Wire Coating," Polym. Eng. Sci., **26**, pp. 171–186.
[15] Hannachi, A., and Mitsoulis, E., 1993, "Sheet Coextrusion of Polymer Solutions and Melts: Comparison Between Simulation and Experiments," Adv. Polym. Technol., **12**, pp. 217–231.
[16] Argyropaidas, I., 2006, "Computational Rheology and its Application to Flows of Polymeric Fluids," Ph.D. Thesis, Department of Mining Engineering and Metallurgy, National Technical University of Athens, Greece.
[17] Beverly, C. R., 1992 "Finite Element Studies of Some Problems in Fluid Mechanics and Rheology," Ph.D. Thesis, Department of Mechanical Engineering, University of Sydney, Sydney, NSW, Australia.
[18] Mitsoulis, E., Vlachopoulos, J., and Mirza, F. A., 1984, "Numerical Simulation of Entry and Exit Flows in Slit Dies," Polym. Eng. Sci., **24**, pp. 707–715.
[19] Tanner, R. I., 2000, *Engineering Rheology*, 2nd ed., Oxford University Press, Oxford, UK.
[20] Abdali, S. S., Mitsoulis, E., and Markatos, N. C., 1992, "Entry and Exit Flows of Bingham Fluids," J. Rheol., **36**, pp. 389–407.

Hybrid Two-Fluid DEM Simulation of Gas-Solid Fluidized Beds

Jin Sun[1]
e-mail: jinsun@iastate.edu

Francine Battaglia

Shankar Subramaniam

Department of Mechanical Engineering,
Iowa State University,
Ames, IA 50011

Simulations of gas-solid fluidized beds have been performed using a hybrid simulation method, which couples the discrete element method (DEM) for particle dynamics with the averaged two-fluid (TF) continuum equations for the gas phase. The coupling between the two phases is modeled using an interphase momentum transfer term. The results of the hybrid TF-DEM simulations are compared to experimental data and TF model simulations. It is found that the TF-DEM simulation is capable of predicting general fluidized bed dynamics, i.e., pressure drop across the bed and bed expansion, which are in agreement with experimental measurements and TF model predictions. Multiparticle contacts and large contact forces distribute in the regions away from bubbles, as demonstrated from the TF-DEM simulation results. The TF-DEM model demonstrates the capability to capture more heterogeneous structural information of the fluidized beds than the TF model alone. The implications to the solid phase constitutive closures for TF models are discussed. However, the TF-DEM simulations depend on the form of the interphase momentum transfer model, which can be computed in terms of averaged or instantaneous particle quantities. Various forms of the interphase momentum transfer model are examined, and simulation results from these models are compared. [DOI: 10.1115/1.2786530]

Keywords: fluidized bed, discrete element method, two-fluid model

Introduction

Gas-solid fluidized beds are widely used in many industrial applications, e.g., fluid catalytic cracking, due to the contact between gas and solid phases, which prompts rapid heat and mass transfer and fast chemical reactions. However, the dynamics of gas-solid fluidized beds need to be better understood in order to improve existing processes and scale up new processes. Reliable simulation tools can provide valuable insights into gas-solid flow processes and, as a result, accelerate the achievement of substantial process improvements [1].

The dynamics of fluidized beds can be described at different levels of detail [2]. At the most fundamental level (atomic or molecular scale is not considered), the motion of the whole system is determined by the Newtonian equations of motion for the translation and rotation of each particle, and the Navier–Stokes and continuity equations. The fluid motion and particle motion are linked by the no-slip condition on each particle boundary. At the second level, the fluid velocity at each point is replaced by its average, taken over a spatial domain large enough to contain many particles but still small compared to the whole region occupied by the flowing mixture. The Newtonian equations of motion are solved for each particle in a Lagrangian framework. The coupling force between fluid and particles is then related to the particle's velocity relative to the locally averaged fluid velocity and to the local concentration of the particle assembly. At a third level, both the fluid velocity and the particle velocity are averaged over local spatial domains. A description at this level of detail is often referred as the two-fluid model (TFM).

The kinetic theory of granular flows (KTGF) has been successfully applied to the TFM for fluidization in the last decade [3]. The KTGF has a basic assumption that particle collisions are instantaneous and binary. However, questions about the validity and capability of KTGF arise because of the microstructures formed in the fluidized beds, e.g., clusters in a riser [4] and "defluidized" zones in a bubbling fluidized bed [5]. In a dense bubbling fluidized bed, the particle pressure around a bubble was experimentally measured and shown to be large in the region far below the bubble where there is no agitation [5]. These facts lead to speculations that lasting multiple contacts in dense fluidized beds limit the application of KTGF. Previous experiments [6] and models [7,8] also showed that diffusion and mixing are dominated by geometry, consistent with long-lasting contacts (but not thermal collisions) in dense granular flows. However, there has not yet been a quantitative analysis to assess multiparticle microstructures under certain fluidization conditions or how the microstructures affect the constitutive behavior of a dense fluidized bed. A good understanding of the spatial distribution and temporal evolution of multiparticle contacts and corresponding particle contact forces is a necessary step toward developing constitutive models that can accurately predict fluidized bed dynamics.

In this paper, a hybrid model at the second level will be employed to improve the understanding of multiparticle contacts in a fluidized bed. The hybrid model couples a TFM to solve the gas phase with the discrete element method (DEM) to solve the particle motion equations. Therefore, the hybrid model can simulate a fluidized bed at particle scales and produce useful information to analyze the microstructures as well as particle dynamics. The computational results from the hybrid model will be compared and validated with experimental and TFM results. A key consideration in the hybrid model is the coupling between the phases, i.e., the fluid-particle interaction force. Different formulations have been used to calculate and transfer the force between phases [9–12]. However, formulations have not been thoroughly analyzed for different flow conditions. In this paper, two different ways to transfer the effective drag force, an important coupling term between gas and particles, will be discussed, and simulation results from these two methods will be compared.

Methodology

Multifluid Model. The multifluid Eulerian model describes the gas phase and solid phases as interpenetrating continua. The particle mixture is divided into a discrete number of phases, each of which can have different physical properties, e.g., particle diam-

[1]Corresponding author.

Contributed by the Fluids Engineering Division of ASME for publication in the JOURNAL OF FLUIDS ENGINEERING. Manuscript received August 28, 2006; final manuscript received June 9, 2007. Review conducted by Ye Zhou. Paper presented at the 2006 ASME International Mechanical Engineering Congress (IMECE2006), Chicago, IL, November 5–10, 2006.

eter. It should be noted that the TFM for a gas phase and single solid phase is a special case, $m=1$, for the general formula presented next. The governing equations for the multifluid model are [13]

Continuity equation for the gas phase:

$$\frac{\partial}{\partial t}(\varepsilon_g \rho_g) + \nabla \cdot (\varepsilon_g \rho_g \mathbf{v}_g) = \sum_{n=1}^{N_g} R_{gn} \tag{1}$$

Continuity equation for the mth solid phase:

$$\frac{\partial}{\partial t}(\varepsilon_{sm} \rho_{sm}) + \nabla \cdot (\varepsilon_{sm} \rho_{sm} \mathbf{v}_{sm}) = \sum_{n=1}^{N_{sm}} R_{smn} \tag{2}$$

Momentum equation for the gas phase:

$$\frac{\partial}{\partial t}(\varepsilon_g \rho_g \mathbf{v}_g) + \nabla \cdot (\varepsilon_g \rho_g \mathbf{v}_g \mathbf{v}_g) = \nabla \cdot \bar{\bar{S}}_g + \varepsilon_g \rho_g \mathbf{g} - \sum_{m=1}^{M} \mathbf{I}_{gm} \tag{3}$$

Momentum equation for the mth solid phase:

$$\frac{\partial}{\partial t}(\varepsilon_{sm} \rho_{sm} \mathbf{v}_{sm}) + \nabla \cdot (\varepsilon_{sm} \rho_{sm} \mathbf{v}_{sm} \mathbf{v}_{sm}) = \nabla \cdot \bar{\bar{S}}_{sm} + \varepsilon_{sm} \rho_{sm} \mathbf{g} + \mathbf{I}_{gm} - \sum_{\substack{l=1 \\ l \neq m}}^{M} \mathbf{I}_{ml} \tag{4}$$

Translational granular temperature equation [4]:

$$\frac{3}{2}\left[\frac{\partial}{\partial t}(\varepsilon_{sm} \rho_{sm} \theta_{sm,t}) + \nabla \cdot (\varepsilon_{sm} \rho_{sm} \theta_{sm,t} \mathbf{v}_{sm})\right] = -\nabla \cdot \mathbf{q}_{sm} - \bar{\bar{S}}_{sm} : \nabla \mathbf{v}_{sm} + \gamma_{sm,\text{slip}} - J_{sm,\text{coll}} - J_{sm,\text{vis}} \tag{5}$$

where the translational granular temperature is defined as

$$\theta_{sm,t} = \frac{1}{3}\langle C_{pi}^2 \rangle \tag{6}$$

The fluctuation in the particle translational velocity shown in Eq. (6) is defined as $\mathbf{C}_{pi}=\mathbf{v}_{pi}-\mathbf{v}_{sm}$, where $\mathbf{v}_{pi}$ is the instantaneous translational particle velocity and the symbol $\langle\ \rangle$ designates the operation of taking average.

The constitutive equations for the solid phases were derived for granular flows [14]. There are two distinct flow regimes in granular flows: a viscous or rapidly shearing regime in which stresses arise due to collisional or translational momentum transfer and a plastic or slowly shearing regime in which stresses arise due to Coulomb friction between grains in close contact. Two different approaches are used for these regimes:

$$\bar{\bar{S}}_{sm} = \begin{cases} -P_{sm}^{p}\bar{\bar{I}} + \bar{\bar{\tau}}_{sm}^{p} & \text{if } \varepsilon_s \geqslant \varepsilon_s^* \\ -P_{sm}^{v}\bar{\bar{I}} + \bar{\bar{\tau}}_{sm}^{v} & \text{if } \varepsilon_s < \varepsilon_s^* \end{cases} \tag{7}$$

where P_{sm}^{p} and $\bar{\bar{\tau}}_{sm}^{p}$ are the pressure and the viscous stress in the mth solid phase for the plastic regime, P_{sm}^{v} and $\bar{\bar{\tau}}_{sm}^{v}$ are the pressure and the viscous stress for the viscous regime, and ε_g^* is a critical packing solid volume fraction, set to 0.58 for the simulations in this paper.

The granular stress equation based on KTGF [15] is applied to the viscous regime. The granular pressure and stresses are given by

$$P_{sm}^{v} = K_{1m}\varepsilon_{sm}^2 \theta_{sm,t} \tag{8}$$

$$\bar{\bar{\tau}}_{sm}^{v} = 2\mu_{sm}^{v}\bar{\bar{D}}_{sm} + \lambda_{sm}^{v}\,\text{tr}(\bar{\bar{D}}_{sm})\bar{\bar{I}} \tag{9}$$

where λ_{sm}^{v} is the second coefficient of viscosity,

$$\lambda_{sm}^{v} = K_{2m}\varepsilon_{sm}\sqrt{\theta_{sm,t}} \tag{10}$$

The shear viscosity factor μ_{sm}^{v} is

$$\mu_{sm}^{v} = K_{3m}\varepsilon_{sm}\sqrt{\theta_{sm,t}} \tag{11}$$

The strain rate tensor $\bar{\bar{D}}_{sm}$ is given by

$$\bar{\bar{D}}_{sm} = \frac{1}{2}[\nabla \mathbf{v}_{sm} + (\nabla \mathbf{v}_{sm})^T] \tag{12}$$

The coefficients K_{1m}, K_{2m}, and K_{3m} are functions of particle density, diameter, restitution coefficient, radial distribution function, and local volume fractions. The solid stress tensor in the viscous regime only takes into account contributions from particle translational momentum flux and binary collisions. In the plastic flow regime, the solid stress tensor was derived based on plastic flow theory [16] and critical state theory [17].

The constitutive equation for the gas phase stress tensor is

$$\bar{\bar{S}}_g = -P_g\bar{\bar{I}} + \bar{\bar{\tau}}_g \tag{13}$$

where P_g is the gas pressure and $\bar{\bar{I}}$ is the identity tensor. The viscous stress tensor $\bar{\bar{\tau}}_g$ is assumed to be of the Newtonian form

$$\bar{\bar{\tau}}_g = 2\mu_g\bar{\bar{D}}_g + \lambda_g \nabla \cdot \mathbf{v}_g \tag{14}$$

where $\bar{\bar{D}}_g$ is the strain rate tensor for the gas phase. The gas-solid momentum transfer ($\mathbf{I}_{gm}$) will be discussed in the subsection on coupling TFM and DEM.

Discrete Element Method. Individual particle motion in a fluidized bed can be described by Newtonian equations of motion, which is a Lagrangian approach. The DEM employs numerical integration of the equations of motion to resolve particle trajectories [18]. The translational and rotational motions of a particle are governed by

$$m_i\frac{d\mathbf{v}_{pi}}{dt} = \mathbf{f}_{ci} + \mathbf{f}_{gpi} + m_i\mathbf{g} \tag{15}$$

$$I_i\frac{d\boldsymbol{\omega}_i}{dt} = \mathbf{T}_i \tag{16}$$

where $\mathbf{f}_{ci}$ is the particle-particle contact force, $\mathbf{f}_{gpi}$ is the fluid-particle interaction force, $m_i\mathbf{g}$ is the gravitational force, $\mathbf{T}_i$ is the torque arising from the tangential components of the contact force, and I_i, $\mathbf{v}_{pi}$, and $\boldsymbol{\omega}_i$ are the moment of inertia, linear velocity, and angular velocity, respectively. The net contact force $\mathbf{f}_{ci}$ and torque $\mathbf{T}_i$ acting on each particle result from a vector summation of the force and torque at each particle-particle contact. A linear spring-dashpot model is employed for the contact force model due to its simplicity and reasonable accuracy [18]. The basic principles of the linear spring-dashpot model are briefly described in the following.

Two contacting particles $\{i,j\}$ are shown in Fig. 1 with radii $\{a_i,a_j\}$ at positions $\{\mathbf{r}_i,\mathbf{r}_j\}$, with velocities $\{\mathbf{v}_i,\mathbf{v}_j\}$ and angular velocities $\{\boldsymbol{\omega}_i,\boldsymbol{\omega}_j\}$. The normal compression δ_{ij}, relative normal velocity $\mathbf{v}_{n_{ij}}$, and relative tangential velocity $\mathbf{v}_{t_{ij}}$ are [19]

$$\delta_{ij} = d - r_{ij} \tag{17}$$

$$\mathbf{v}_{n_{ij}} = (\mathbf{v}_{ij} \cdot \mathbf{n}_{ij})\mathbf{n}_{ij} \tag{18}$$

$$\mathbf{v}_{t_{ij}} = \mathbf{v}_{ij} - \mathbf{v}_{n_{ij}} - (a_i\boldsymbol{\omega}_i + a_j\boldsymbol{\omega}_j) \times \mathbf{n}_{ij} \tag{19}$$

where $d=a_i+a_j$, $\mathbf{r}_{ij}=\mathbf{r}_i-\mathbf{r}_j$, and $\mathbf{n}_{ij}=\mathbf{r}_{ij}/r_{ij}$, with $r_{ij}=|\mathbf{r}_{ij}|$ and $\mathbf{v}_{ij}=\mathbf{v}_i-\mathbf{v}_j$. The rate of change of the elastic tangential displacement $\mathbf{u}_{t_{ij}}$, set to zero at the initiation of a contact, is

$$\frac{d\mathbf{u}_{t_{ij}}}{dt} = \mathbf{v}_{t_{ij}} - \frac{(\mathbf{u}_{t_{ij}} \cdot \mathbf{v}_{ij})\mathbf{r}_{ij}}{r_{ij}^2} \tag{20}$$

The last term in Eq. (20) arises from the rigid body rotation around the contact point and ensures that $\mathbf{u}_{t_{ij}}$ always lies in the

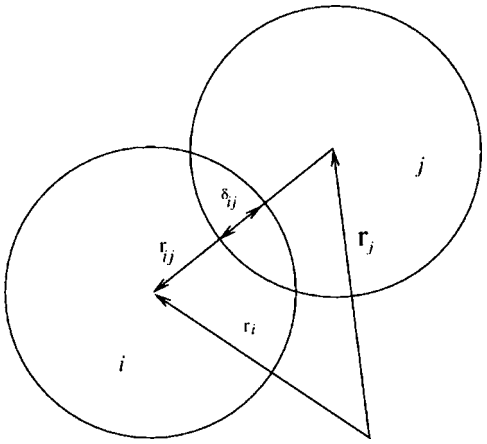

Fig. 1 Schematic of two particles *i* and *j* in contact and position vectors $\mathbf{r}_i$ and $\mathbf{r}_j$, respectively, with overlap δ_{ij}

local tangent plane of contact. Normal and tangential forces acting on particle i are

$$\mathbf{F}_{n_{ij}} = f(\delta_{ij}/d)(k_n \delta_{ij} \mathbf{n}_{ij} - \gamma_n m_{\text{eff}} \mathbf{v}_{n_{ij}}) \tag{21}$$

$$\mathbf{F}_{t_{ij}} = f(\delta_{ij}/d)(-k_t \mathbf{u}_{t_{ij}} - \gamma_t m_{\text{eff}} \mathbf{v}_{t_{ij}}) \tag{22}$$

where $k_{n,t}$ and $\gamma_{n,t}$ are the spring stiffness and viscoelastic constants, respectively, and $m_{\text{eff}}=m_i m_j/(m_i+m_j)$ is the effective mass of the spheres with masses m_i and m_j. The corresponding contact force on particle j is simply given by Newton's third law, i.e., $\mathbf{F}_{ji}=-\mathbf{F}_{ij}$. The function $f(\delta_{ij}/d)=1$ is for the linear spring-dashpot model, and $f(\delta_{ij}/d)=\sqrt{\delta_{ij}/d}$ is for Hertzian contacts with viscoelastic damping between spheres.

Static friction is implemented by keeping track of the elastic shear displacement throughout the lifetime of a contact. The static yield criterion, characterized by a local particle friction coefficient μ, is modeled by truncating the magnitude of $\mathbf{u}_{t_{ij}}$ as necessary to satisfy $|\mathbf{F}_{t_{ij}}| < |\mu \mathbf{F}_{n_{ij}}|$. Thus, the contact surfaces are treated as "sticking" when $|\mathbf{F}_{t_{ij}}| < |\mu \mathbf{F}_{n_{ij}}|$ and as "slipping" when the yield criterion is satisfied. The total contact force and torque acting on particle i are then given by

$$\mathbf{f}_{ci} = \sum_j (\mathbf{F}_{nij} + \mathbf{F}_{tij}) \tag{23}$$

$$\mathbf{T}_i = -\frac{1}{2} \sum_j \mathbf{r}_{ij} \times \mathbf{F}_{tij} \tag{24}$$

The amount of energy lost in collisions, characterized by the inelasticity through the value of the coefficient of restitution e, is defined as the negative ratio of the particle velocity after collision to the velocity before collision. For the linear spring-dashpot model, the coefficient of normal restitution e_n and contact time t_c can be analytically obtained,

$$e_n = \exp(-\gamma_n t_c/2) \tag{25}$$

where the contact time t_c is given by

$$t_c = \pi (k_n/m_{\text{eff}} - \gamma_n^2/4)^{-1/2} \tag{26}$$

The value of the spring constant should be large enough to avoid particle interpenetration, yet not so large as to require an unreasonably small simulation time step δt since an accurate simulation typically requires $\delta t \sim t_c/50$. After the contact force is calculated, the equations of motion, which are ordinary differential equations, can be numerically integrated to get the particle trajectories.

Coupling of the Two-Fluid Model and Discrete Element Method. A hybrid model at the second level is constructed by coupling the TFM for the gas phase with DEM for the particle motion [20]. The coupling term between the equations for gas and particle motion is the gas-particle interaction $\mathbf{I}_{gm}$ in the gas momentum equation and $\mathbf{f}_{gpi}$ in the particle equation of motion. Due to the averaging process in the derivation of momentum equations for the TFM, the fluid-particle interaction force may be written as the sum of a component due to macroscopic variations in the fluid stress tensor and a component representing the effect of variations in the point stress stress tensor as the gas flows around the particle [21]. For the gas force on a particle,

$$\mathbf{f}_{gpi} = V_{pi} \nabla \cdot \bar{\bar{S}}_g + \mathbf{f}'_{gpi} \tag{27}$$

where V_{pi} is the volume of particle i. The first term on the right in Eq. (27) accounts for the macroscopic variation in the fluid stress tensor. The second term on the right in Eq. (27) includes skin friction and drag contributions accounting for the detailed variation in the stress tensor. In general, the term comprises an effective drag force in the direction of the relative velocity between the fluid and particle, and a virtual or added mass force accounting for the resistance of the fluid mass that is moving at the same acceleration as the particle. For gas-solid flows, the virtual mass force may be neglected and $\mathbf{f}'_{gpi}$ reduces to an effective drag force, which should be the product of the local void fraction ε_g and the drag force $\mathbf{f}_{di}$ obtained from experimentally based correlations. Substituting Eq. (13) to Eq. (27),

$$\mathbf{f}_{gpi} = -V_{pi} \nabla P_g + V_{pi} \nabla \cdot \bar{\bar{\tau}}_g + \varepsilon_g \mathbf{f}_{di} \tag{28}$$

The drag force on a single particle of diameter d_{pi} in a multiparticle system can be calculated from the correlation,

$$\mathbf{f}_{di} = \frac{1}{2} C_{Di} \rho_g \frac{\pi d_{pi}^2}{4} \varepsilon_g^2 |\mathbf{v}_g^i - \mathbf{v}_{pi}| (\mathbf{v}_g^i - \mathbf{v}_{pi}) f(\varepsilon_g) = \frac{\pi d_{pi}^3}{6 \varepsilon_g \varepsilon_{sm}} \beta (\mathbf{v}_g^i - \mathbf{v}_{pi}) \tag{29}$$

where $\mathbf{v}_g^i$ is the gas velocity at the location of particle i and $f(\varepsilon_g)$ is a function of the local void fraction. The single particle velocity $\mathbf{v}_{pi}$ is used since the correlations relate the effective drag force to that of a single particle in the absence of other particles. The expressions of β are extended from the work of Ergun [22] and Wen and Yu [23], and were used by Tsuji et al. [9],

$$\beta = \begin{cases} 150 \dfrac{\varepsilon_{sm}^2}{\varepsilon_g d_{pi}^2} \mu_g + 1.75 \varepsilon_{sm} \dfrac{\rho_g}{d_{pi}} |\mathbf{v}_g^i - \mathbf{v}_{pi}| & \text{for } \varepsilon_g \leqslant 0.8 \\ \dfrac{3}{4} C_D \dfrac{\varepsilon_g \varepsilon_{sm}}{d_{pi}} \rho_g |\mathbf{v}_g^i - \mathbf{v}_{pi}| \varepsilon_g^{-2.7} & \text{for } \varepsilon_g > 0.8 \end{cases} \tag{30}$$

The drag coefficient C_{Di} depends on the particle Reynolds number $\text{Re}_{pi}=(d_{pi}\varepsilon_g|\mathbf{v}_g^i-\mathbf{v}_{pi}|\rho_g)/\mu_g$, and is given by

$$C_{Di} = \begin{cases} 24(1 + 0.15 \text{Re}_{pi}^{0.687})/\text{Re}_{pi} & \text{for } \text{Re}_{pi} < 1000 \\ 0.43 & \text{for } \text{Re}_{pi} \geqslant 1000 \end{cases} \tag{31}$$

The fluid-particle interaction force per unit volume of bed, $\mathbf{I}_{gm}$, in the gas momentum equation (refer to Eq. (3)) is obtained by summing the gas forces $\mathbf{f}_{gpi}$ over all the particles in a fluid cell and dividing by the volume of the fluid cell, V_{cell}. Thus,

$$\mathbf{I}_{gm} = \frac{\sum_i^{N_m} \mathbf{f}_{gpi}}{V_{\text{cell}}} = -\varepsilon_{sm} \nabla P_g + \varepsilon_{sm} \nabla \cdot \bar{\bar{\tau}}_g + \sum_i^{N_m} \varepsilon_g \mathbf{f}_{di}/V_{\text{cell}} \tag{32}$$

where N_m is the number of particles of the mth phase in a fluid cell. The last term in Eq. (32) may be calculated approximately using local mean gas and particle velocities,

$$\sum_{i}^{N_m} \varepsilon_g \mathbf{f}_{di} / V_{\text{cell}} = \beta(\mathbf{v}_g - \mathbf{v}_{sm}) \tag{33}$$

where β uses the same form as in Eq. (30), except that the velocity $\mathbf{v}_{pi}$ is replaced by the local mean value in a fluid cell, i.e., $\mathbf{v}_{sm}$.

The solid volume fraction and local mean solid velocities are evaluated in a fluid computational cell,

$$\varepsilon_{sm} = \frac{\sum_{i}^{N_m} V_{pi}}{V_{\text{cell}}} \tag{34}$$

$$\mathbf{v}_{sm} = \frac{\sum_{i}^{N_m} \mathbf{v}_{pi} V_{pi}}{\sum_{i}^{N_m} V_{pi}} \tag{35}$$

The volume of a computational cell, V_{cell}, in two-dimensional (2D) simulations is calculated using the diameter of a spherical particle as the cell thickness in the third dimension.

Based on the previous discussion, it can be seen that the fluid-particle effective drag force can be calculated in two ways to transfer the effects between gas and particle motions. The first method is to calculate the drag force using Eq. (33) in a fluid cell and then assign this mean drag force back to each particle in the cell. This method, with the assumption that particles in a cell with the same diameter have the same drag force, is used for most of the simulations in this paper. The second method is to calculate the drag force on each particle using Eq. (29) and then sum up the particle drag forces in a fluid cell as the total drag force on the fluid according to Newton's third law. This method is employed for one case as a comparison to the results from the first method. However, it should be noted that further assumptions are made in this paper. One assumption is that the total drag force on the gas is calculated using Eq. (33) and is approximately equal in magnitude to that obtained from the summation of each particle's drag force. For the second method, Eq. (33) is also used for calculating the drag force on the gas phase, and the only difference between these methods is the way to obtain the drag force on the particles. Finally, the viscous stress gradient in Eq. (28) is neglected.

Numerical Formulation. A FORTRAN code, multiphase flow with interphase exchanges (MFIX), is used for all simulations in this work. MFIX uses a finite volume approach with a staggered grid for the discretization of the TFM governing equations to reduce numerical instabilities [24]. Scalars such as pressure and volume fraction are stored at the cell centers, and the velocity components are stored at cell surfaces. A second-order discretization is used for spatial derivatives and first-order discretization for temporal derivatives. A modified SIMPLE algorithm is employed to solve the discretized equations [24]. The explicit time integration method is used to solve the translational and rotational motion equations used in the DEM [10,18].

Simulation Conditions

Gas-solid fluidized beds were simulated using the hybrid TFM-DEM model presented in the methodology subsection (for $m=1$). The fluidized beds have very small depths compared to the other two dimensions. Therefore, 2D simulations were performed, which also reduces the computational requirements needed for three dimensional (3D) simulations. The first computational case simulates a fluidized bed experiment with a central air jet flow, presented by Tsuji et al. [9]. This case will be referred to as the central-jet case, hereafter. The computational domain is shown in Fig. 2(*a*), and the simulation parameters are listed in Table 1. Most particle parameters are set to be the same as what were used in the experiment. One important difference between the computational setup and the experimental setup is that there is only one layer of particles in the thin depth direction for computations, while there were about five particle layers in the experiment. A second simulation for a bubbling fluidized bed with a uniform inflow was performed to analyze a different flow situation, where the bed is fluidized by a uniform air inflow. The simulations were based on the experiment of the bubbling fluidized bed by Goldschmidt et al. [25]. This case will be referred to as the uniform

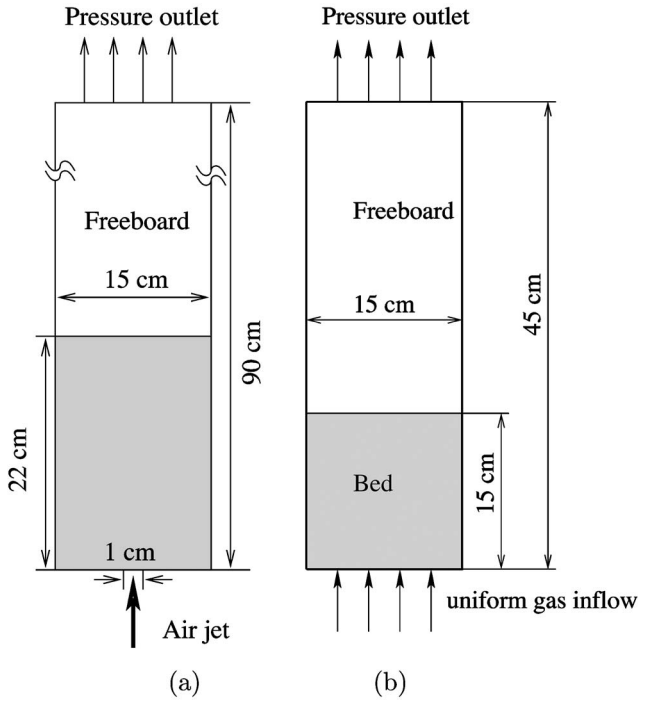

Fig. 2 Schematic showing computational domains for the experiments of (*a*) Tsuji et al. [9] and (*b*) Goldschmidt et al. [25]

Table 1 Computational parameters and general initial and boundary conditions for the experiments of Tsuji et al. [9] and Goldschmidt et al. [25]

	Ref. [9]	Ref. [25]
Geometry		
Height of domain (cm)	90	45
Width of domain (cm)	15	15
Horizontal grid size, Δx (cm)	1	1
Vertical grid size, Δy (cm)	2	1
Particle properties		
Particle diameter (cm)	0.4	0.25
Particle density (g/cm^3)	2.7	2.526
Particle stiffness coefficient (dyn/cm)	8×10^5	8×10^5
Particle damping coefficient (dyn s/cm)	18	1.77
Particle friction coefficient	0.2	0.1
Particle number	2400	4000
Initial conditions		
ε_g	1.0	1.0
$v_g(=U_{\text{mf}})$ (cm/s)	180	128
Initial bed height (cm)	22	15
Boundary conditions		
Central air jet inflow (cm/s)	3900	$1.5U_{\text{mf}}$
Specified pressure at outlet (Pa)	101325	101325
Wall boundary for gas phase	No slip	No slip
Wall stiffness coefficient (dyn/cm)	1.2×10^6	1.2×10^6
Wall damping coefficient (dyn s/cm)	22	3.93

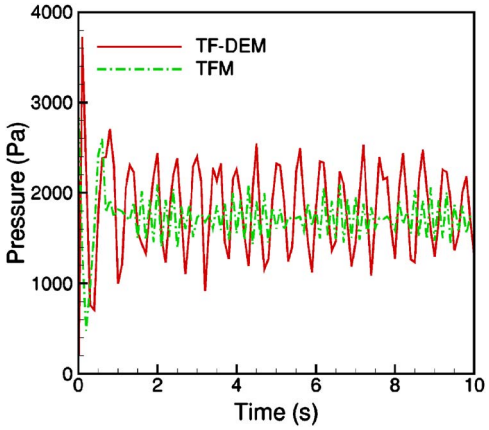

Fig. 3 Pressure drop at 20 cm above the inlet boundary fluctuates with time for the central-jet fluidized bed

inflow case, hereafter. The simulation was set up using the same conditions as in the experiment, except that there is only one layer of particles in the third dimension. The computational domain is shown in Fig. 2(*b*), and parameters are shown in Table 1.

The particle response to the flow fields in these simulations can be analyzed as follows to further elucidate and justify the hybrid method used. The particle Stokes number is defined as

$$\mathrm{St} = \frac{\tau_p}{\tau_g} \tag{36}$$

where $\tau_p = \rho_p d^2/18\mu$ is the particle Stokesian relaxation time and $\tau_g = d/\mathbf{v}_g$ can be deemed as a characteristic time scale for gas momentum convection over one particle diameter. Taking the uniform inflow case as an example, the Stokes number $\mathrm{St} \approx 37{,}422$ and the particle volume fractions are typically greater than 0.1 in the bed. In such a dense particle flow with very high Stokes number, gas turbulence is damped and small scale gas velocity fluctuations do not affect the particle dynamics significantly. Therefore, directly modeling the subgrid gas velocities is not considered in this paper.

Simulations using the TFM for both cases were also carried out using the same grid resolutions corresponding to those listed in Table 1. However, the particle motion is modeled by the solid phase equations in the TFM instead of using DEM directly. All the cases were simulated for 20 s of simulation time. The computational times used by the TFM and the hybrid method for the central-jet case were 5350 s and 6780 s, respectively, on one Opteron 270 (2.0 GHz) processor. Only results for the first 10 s will be presented in the next section since it was found that the fluidized beds reached a quasisteady state after approximately 5 s.

Results and Discussion

Computational results obtained from the simulation of the central-jet case are first presented. The pressure drop at 20 cm above the inlet boundary obtained from the TF-DEM simulation, as shown in Fig. 3, is similar to the computational findings of Tsuji et al.; i.e., the frequency and magnitude of fluctuation are in good agreement with experiments but with a higher mean pressure [9]. The TFM predicts that the pressure drop fluctuates around a similar mean pressure, but with a smaller fluctuating amplitude. This is probably because averaged equations are solved in the TFM. A refined grid with $\Delta x = 1$ cm and $\Delta y = 1$ cm is used to determine the grid dependence of this hybrid method. Statistical error in the particle field estimation becomes larger as the grid is refined due to the grid-cell-based averaging technique used in this paper. The comparison between the temporally averaged solid volume fraction distributions calculated from the coarse and fine grids is shown in Fig. 4. It can be seen that the result from the fine

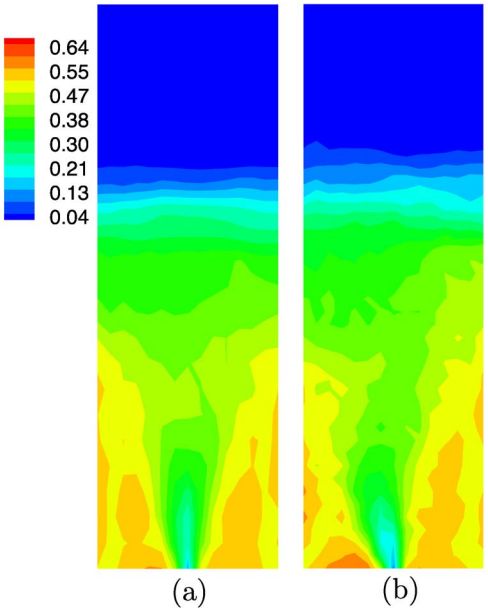

Fig. 4 The averaged (5–10 s) particle volume fractions for the central-jet fluidized bed for (*a*) the coarse grid with $\Delta x = 1$ cm and $\Delta y = 2$ cm and (*b*) the fine grid with $\Delta x = 1$ cm and $\Delta y = 1$ cm. The domain in the figure only shows 45 cm above the inlet.

grid shows a slightly higher bed expansion and a more asymmetric solid distribution with respect to the central jet. A method to address the particle field estimation problem will be discussed in the conclusions. The difference caused by the grid refinement, however, does not alter the comparison between the hybrid method and TFM made in this paper. The coarse grid was also used in previous computational studies [9,11]. The coarse grid results are thus shown in the following. The choice of the grid for the uniform inflow case is based on our grid refinement study for the TFM simulations of the same systems [26]. The logic is that this grid should capture enough details of the gas field and particle field as shown in the TFM simulations. It has been shown that the grid of cell size $\Delta x = 1$ cm and $\Delta y = 1$ cm produced an average error of 1.4% and a maximum error of 3.7% in time-averaged volume fraction, compared to the Richardson extrapolation results, and that further grid refinement had little influence on the results [26].

The bulk coordination number is defined as the average number of contacting neighbors of a particle. The time evolution of bulk coordination number can be used to characterize dynamic responses of granular systems [27]. The bulk coordination number corresponds to the first peak in the isotropic radial distribution function $g(r)$ and is a measure of order in the particle pattern. Thus, it can indirectly give a sense of whether the particle phase is more "gaslike" or "liquidlike." The isotropic radial distribution function $g(r)$ cannot be rigorously defined in the anisotropic configurations used in the simulations and is not presented in the paper. The bulk coordination numbers varying with time for the two simulations are shown in Fig. 5. The bulk coordination number for the central-jet case varies around 1.2, which indicates pair structures or other multicontact structures that exist in the system. In contrast, the bulk coordination number for the uniform inflow case varies around 0.5, which indicates that structures with contacting particles do not prevail. To further elucidate the spatial variation of the particle contacts, we look at local quantities for each particle.

The particle instantaneous positions and velocities are shown in Fig. 6 for the TF-DEM simulation of the central-jet case. The

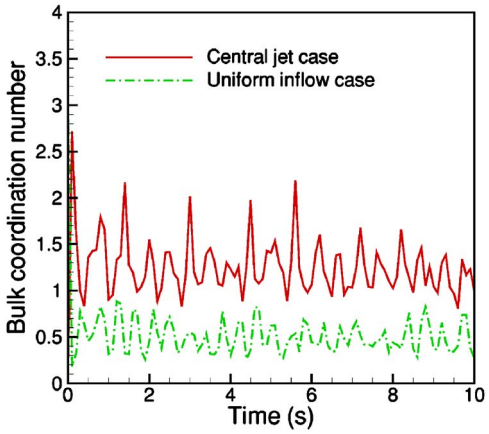

Fig. 5 The bulk coordination numbers as a function of time

particle movements and bed expansion behaviors are also in qualitative agreement with experimental observations. These agreements serve to initially substantiate the practicality of the hybrid TF-DEM model presented here. The number of contacting particles for each particle, N_c, is defined as the number of contacting neighbors of one particle. A direct interpretation of N_c is that a particle is in a binary collision when $N_c=1$, or is in a multicontact when $N_c>1$. The value of N_c for each particle is also presented in Fig. 6. From the results, it is clear that N_c is not distributed homogeneously in space. The value of N_c is low (1–2) in bubble regions but high in other regions (>2), which are mainly near the bottom corners of the bed after the jet penetrates the bed (see Figs. 6(*b*)–6(*d*)). High N_c shows that multicontacts prevail in those regions away from bubbles.

The spatial distributions of particle contact forces, drag forces, and ratios of these forces are shown in Fig. 7 for the central-jet case. The magnitudes of total forces in every computational cell are shown, i.e., the total contact force at a cell center, $\mathbf{f}_{cj}=\Sigma_i^{N_m}\mathbf{f}_{cji}$, and the total drag force at a cell center, $\mathbf{f}'_{gpj}=\Sigma_i^{N_m}\mathbf{f}'_{gpi}$, where i and j are indices of particles and grid nodes, respectively. The force is also scaled by the magnitude of the gravitational force of a particle. It can be seen from the instantaneous distributions (Fig. 7(*a*)) that the contact forces (left frame) are large in the

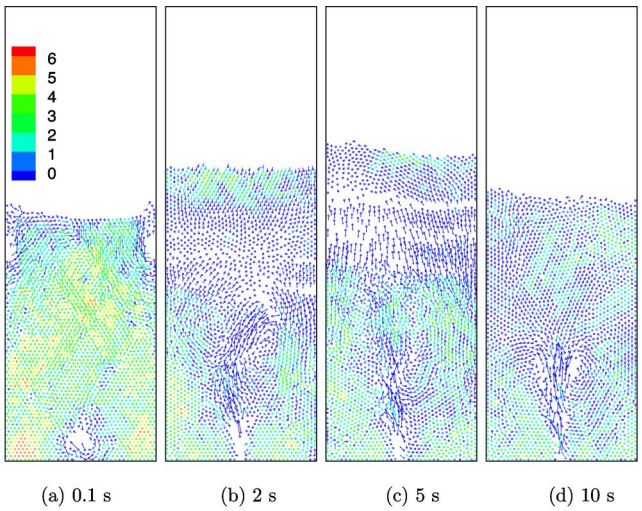

Fig. 6 Instantaneous particle positions and velocities for the central-jet fluidized bed, denoted by points and vectors. The contour levels show the magnitudes of N_c. The domain in the figure only shows 45 cm above the inlet.

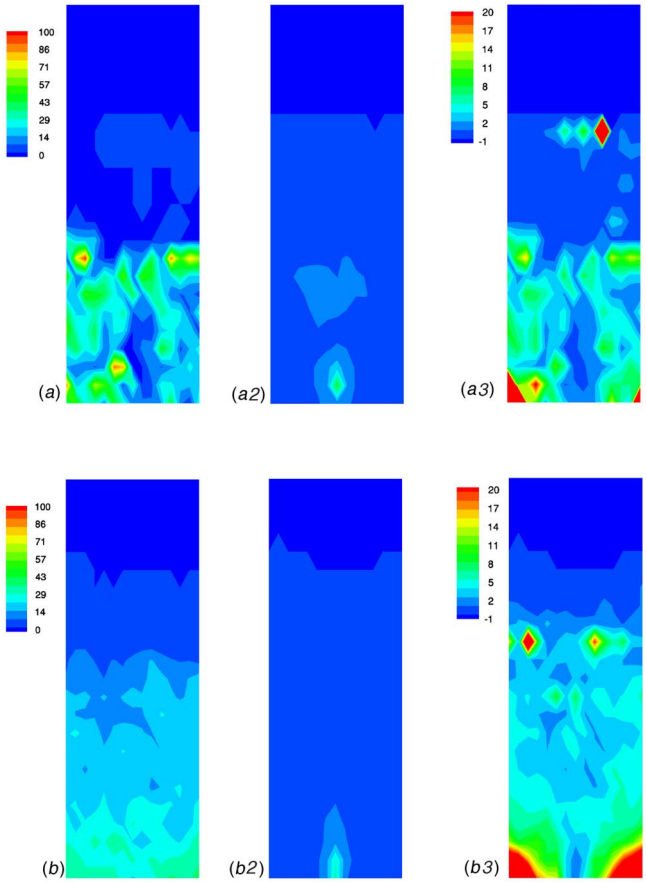

Fig. 7 Particle contact forces, drag forces, and their ratios for the central-jet fluidized bed for (*a*) the instantaneous distribution at 5 s and (*b*) the time-averaged distribution at 5–10 s. The left panels show contact forces, the middle panels show drag forces, and the right panels show the ratios of contact forces to drag forces. The left legends are the magnitudes of forces scaled by the gravitational force of a particle. The right legends are the ratios, where –1 indicates that the drag force is zero at that position. Note that the highest ratio of 100 is not shown in order to distinguish the majority of ratios below 20. The domain in the figure only shows 45 cm above the inlet.

regions away from bubbles, which is consistent with the experimental observation that higher particle pressure is generated under bubbles [5]. The instantaneous drag forces (shown in the middle frame of Fig. 7(*a*)) are large in the jet region. The ratios of contact forces to drag forces vary between 2 and 10 in most of the bed region. However, contact forces may be as high as 100 times that of the drag forces (higher than the maximum contour level shown in Fig. 7) in the corners beside the jet. The high contact force regions could also correspond to the high solid stress regions. The locations of large contact forces and force ratios are correlated with the locations of higher N_c, as compared to the corresponding snapshot at 5 s in Fig. 6. Solid volume fractions in most of these regions are less than the critical solid volume fraction ε_s^* (see the left panels in Fig. 8), and the solid stress is calculated using the KTGF. Since the solid stress calculated using the KTGF does not take into account the contribution from the collisions with $N_c>1$, the solid stresses in these regions are also expected to deviate from the stresses predicted using the KTGF. These observations emphasize the importance of studying particle contacts in the regions away from bubbles in order to understand the constitutive behavior of a fluidized bed. The time-averaged distributions (Fig. 7(*b*)) show similar trends although the forces are distributed more homogeneously.

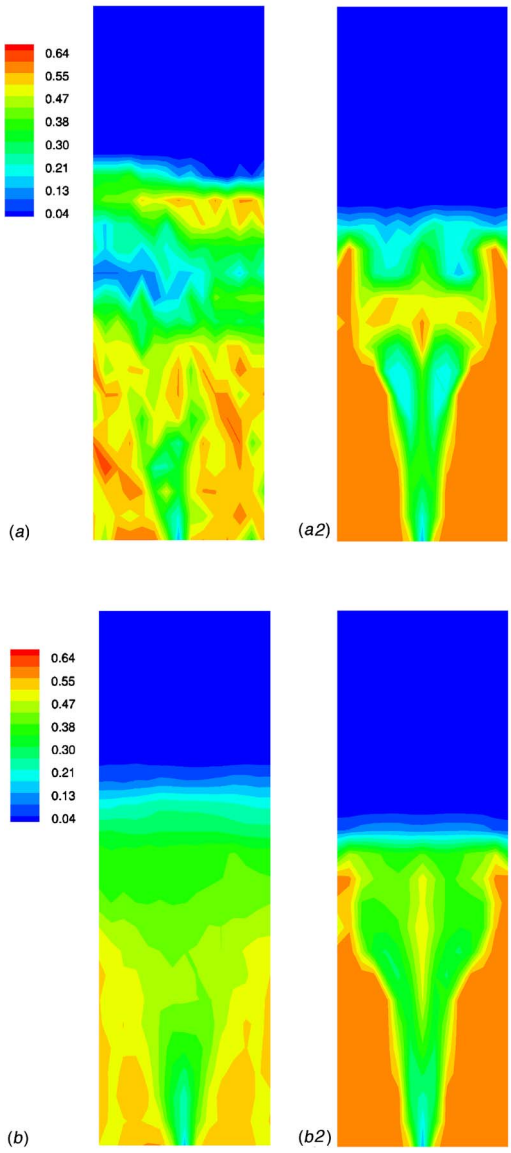

Fig. 8 Particle volume fractions for the central-jet fluidized bed for (*a*) the instantaneous distribution at 5 s and (*b*) the time-averaged distribution at 5–10 s. The left panel shows the TF-DEM simulation and the right panel shows the TFM simulation. The domain in the figure only shows 45 cm above the inlet.

A comparison between the solid volume fractions predicted by the TF-DEM model and those predicted by TFM is also performed. The instantaneous and time-averaged (5–10 s) solid volume fraction distributions for the central-jet case are shown in Figs. 8(*a*) and 8(*b*), respectively. The distributions demonstrate that the TF-DEM model and TFM model predict a similar jet penetration behavior. However, the TFM predicts a more homogeneous and symmetric distribution of solids. The TF-DEM model can capture the concentration difference in the corner regions, as seen in Fig. 8(*b*). The predicted differences reflect the inability of the TFM to capture the structural information although the TFM predicts a similar mean pressure drop as the TF-DEM model does. The inability may also be due to the solid constitutive closures used in the TFM. The closures do not adequately model the stress and energy dissipation caused by multicontacts, which reduces the preferential change in solid volume fractions. A quantitative account of the differences between the stresses and dissipation calculated using the TF-DEM and using the TFM is the subject of a future study [28].

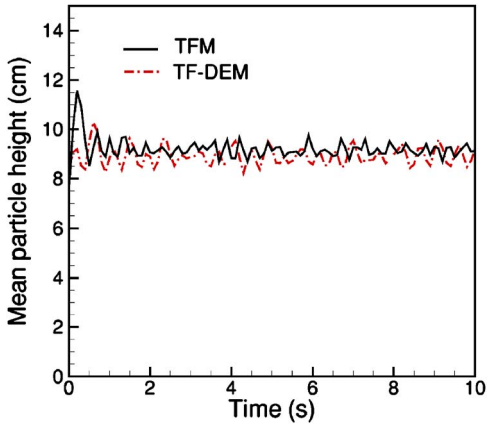

Fig. 9 The mean particle height as a function of time for the uniform inflow fluidized bed calculated from the TF-DEM model and TFM

For the uniform inflow case, bed dynamics were first analyzed by the time evolution of the mean particle height. The mean particle height is defined as the arithmetic mean of the heights of all particles in the bed. It is straightforward to calculate the particle height in the TF-DEM model, and it can also be estimated by a method defined in Ref. [26] for the TFM. The mean particle height as a function of time is shown in Fig. 9. It is found that mean particle heights predicted by both models fluctuate at a similar level. The 5–10 s time-averaged values are 8.9 cm and 9.16 cm for TF-DEM model and TFM, respectively. Both are lower than the experimental value of 11.4 cm [29]. The particles' instantaneous positions, velocities, and N_c are presented in Fig. 10. It can be seen that the bed is uniformly fluidized at the startup stage (Fig. 10(*a*)) with no bubble and zero N_c over almost the whole bed. After bubbles develop, higher N_c appear in regions away from the bubble; however, the ratio of the number of multicontacts over the total number of collisions is small, fluctuating around 0.3, as shown in Fig. 11. This small ratio indicates that the binary collision assumption in the KTGF may still be reasonable under this flow condition. In contrast, the ratio for the central-jet

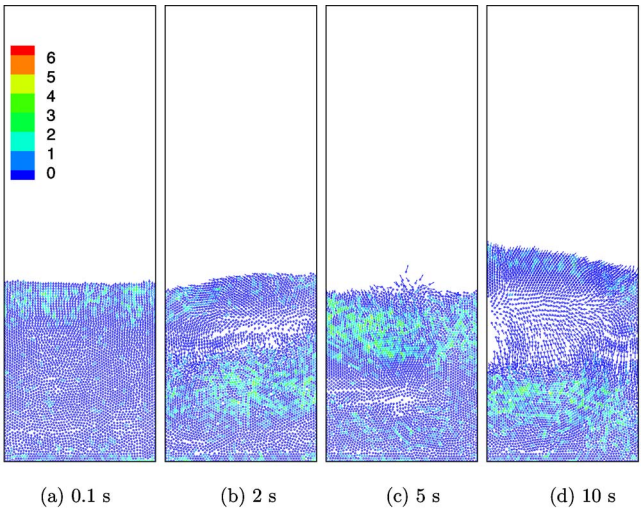

Fig. 10 Instantaneous particle positions and velocities for the uniform inflow fluidized bed denoted by points and vectors. The contour level shows the magnitude of N_c.

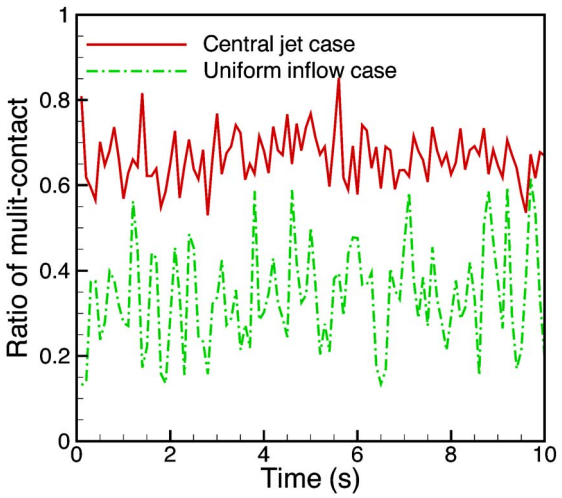

Fig. 11 The ratio of particles in multicontacts to the total number of particles in contact as a function of time

case is higher than 0.6 most of the time, which indicates that the binary collision assumption may deviate from the real particle collision scenario to a larger degree. The spatial distributions of particle contact forces, drag forces, and ratios of these forces for the uniform inflow case are also shown in Fig. 12. Similar observations can be drawn as for the central-jet case. However, there is no region where the contact forces are more than 15 times higher than the drag forces, as observed in the corner regions for the central-jet case.

The two different formulas for computing the effective drag force based on averaged or instantaneous particle velocities were applied to simulate the uniform inflow case. Since the method using the averaged particle velocities produces the same forces on each particle in a fluid cell, it tends to smear the difference between particle movement and results in less vigorous bed dynamics. It is expected that the method using instantaneous particle velocity will predict a higher bed expansion. This effect is actually shown by the time-averaged solid volume fraction in Fig. 13, where the result produced by the second method shows a slightly higher bed expansion. The time-averaged mean particle height predicted by the second method is 9.1 cm, and is higher than that

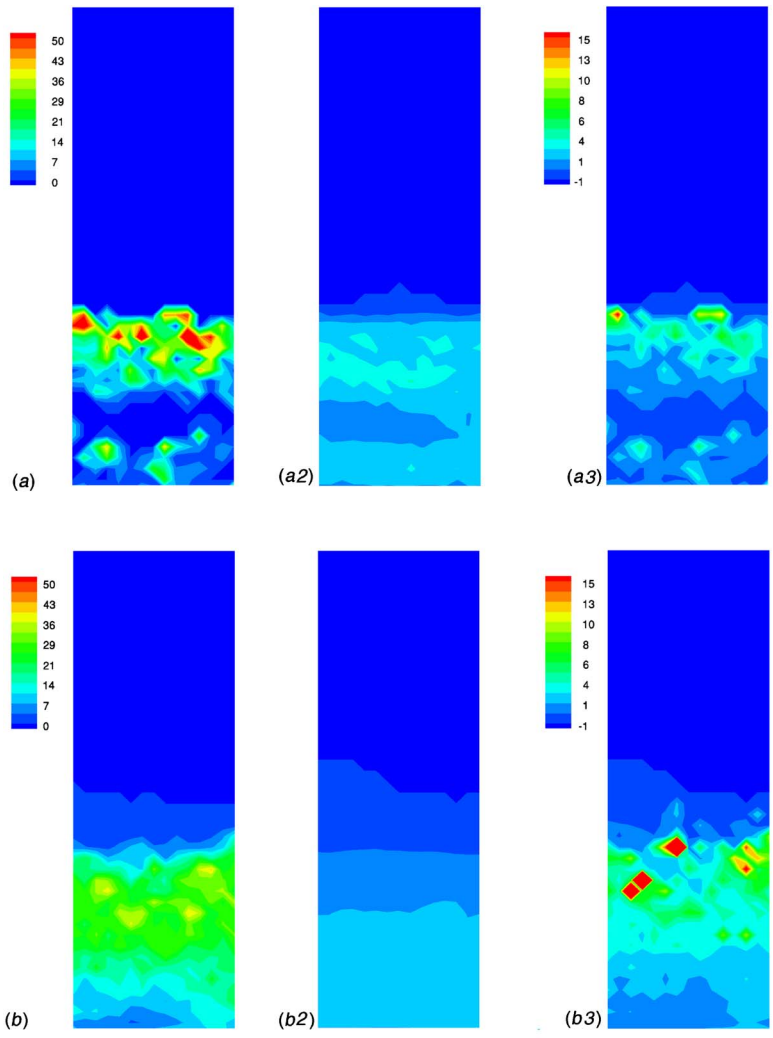

Fig. 12 Particle contact forces, drag forces, and their ratios for the uniform inflow fluidized bed for (*a*) the instantaneous distribution at 5 s and (*b*) the time-averaged distribution at 5–10 s. The left panels show contact forces, the middle panels show drag forces, and the right panels show the ratios of contact forces to drag forces. The left legends are the magnitudes of forces scaled by the gravitational force of a particle. The right legends are the ratios, where –1 indicates that the drag force is zero at that position.

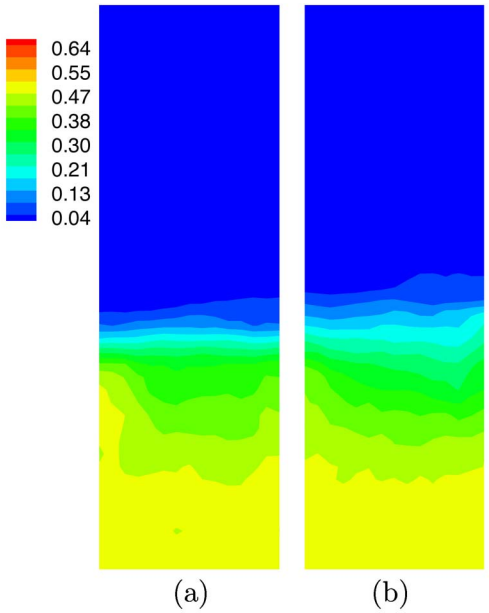

Fig. 13 Time average in the range of 5–10 s of the particle volume fractions for the uniform inflow fluidized bed predicted by the method using (*a*) averaged particle velocities and (*b*) instantaneous particle velocities

predicted by the first method. However, it should be noted that the difference between the mean quantities predicted by the two formulas is not large. Local quantities, such as granular temperature, will be further studied to investigate the effect of the formulas.

Conclusions

A methodology for a hybrid TF-DEM model for gas-solid fluidized beds has been presented. The model couples the DEM for particle dynamics with the TF equations for the gas phase. The coupling between the two phases is modeled by the gas-particle interaction force. Simulations of two types of gas-solid fluidized beds have been carried out using the hybrid simulation method. The results of the hybrid TF-DEM simulations are compared to experimental data and TFM simulations. It is found that the TF-DEM simulation is capable of predicting general fluidized bed dynamics, i.e., pressure drop across the bed and bed expansion, which are in agreement with experimental measurements and TFM predictions. The number of contacting particles N_c is found to be greater than 1 in the regions away from the bubble. The contact forces are much larger than the effective drag forces in the same regions. It is also demonstrated that multicontacts prevail in the central-jet fluidized bed, implying that the binary instantaneous collision assumption in the KTGF may not be applicable in this flow condition. For the uniform inflow fluidized bed, the number of contacting particles are around 1 to 2 so that the binary collision assumption is reasonable in this flow condition. With further research, the particle contact information will hopefully provide guidelines for a constitutive model development and may contribute to the subgrid modeling method proposed by Sundaresan [30]. The relations between the flow conditions and fluidized bed constitutive behaviors and how the multi-interactions should be incorporated into the constitutive modeling clearly need further investigation. It would be instructive to first compare the stresses computed using particle information from the TF-DEM simulations with the stresses computed using the KTGF or using the friction-kinetic model [31]. The stress analysis will be given in a following paper [28].

The effect of computing an effective drag force on a particle in terms of averaged or instantaneous particle velocities was demonstrated. It was shown that the formulation using instantaneous particle velocities better captures the force difference at the particle scale and predicts a higher bed expansion, which is closer to the corresponding experimental results. Furthermore, the statistical error in the estimation of the interphase momentum transfer term becomes high as the grid is refined. This motivates using more sophisticated kernel estimation methods to achieve optimal error control in both statistical error and discretization error [32,33].

Acknowledgment

The authors would like to thank Dr. Sreekanth Pannala and Dr. Dhanunjay Boyalakuntla at Oak Ridge National Laboratory and Dr. Madhava Syamlal at National Energy Technology Laboratory for their useful discussions and help on MFIX. In addition, the computer and technical support by the High Performance Computing Center at Iowa State University is appreciated. This work was supported by the National Energy Technology Laboratory (U.S. Department of Energy) under Contract No. DE-AC02-07CH11358.

Nomenclature

$\mathbf{C}$ = fluctuation in particle translational velocity (cm/s)
d = particle diameter (cm)
e = coefficient of normal restitution
$\mathbf{g}$ = acceleration of gravity (cm/s^2)
I = moment of inertia of a particle (g cm^2)
$\mathbf{I}$ = interphase momentum transfer (dyn/cm^3)
J_{coll} = rate of dissipation of translational fluctuation kinetic energy due to particle collisions (g/cm s^3)
J_{vis} = rate of dissipation of translational fluctuation kinetic energy due to interstitial gas viscous damping (g/cm s^3)
k = stiffness coefficient of a particle (dyn/cm)
m = mass of a particle (g)
$\mathbf{n}$ = unit normal vector from a boundary to particles
N = particle number
N_c = coordination number
N_g = total number of gas phase chemical species
N_{sm} = total number of solid phase (m) chemical species
P = pressure (dyn/cm^2)
$\mathbf{r}$ = position vector (cm)
R = rate of formation (g/cm^3 s)
Re = Reynolds number
$\bar{\bar{S}}$ = stress tensor (dyn/cm^2)
t = time (s)
U = fluidization velocity (cm/s)
$\mathbf{u}$ = tangential displacement (cm)
$\mathbf{v}$ = velocity for gas and solids (cm/s)

Greek Letters

β = coefficient for drag forces (g/cm^3 s)
δ = normal compression in particle collision (cm)
ε = volume fraction
γ = viscous damping coefficient (1/s)
Γ = rate of dissipation of rotational fluctuation kinetic energy (g/cm s^3)
Γ_{slip} = production of translational fluctuation kinetic energy due to gas-particle slip (g/cm s^3)
μ = coefficient of friction in DEM
μ_g = gas shear viscosity (dyn s/cm^2)
μ_{sm} = solid shear viscosity (dyn s/cm^2)
λ_g = gas second coefficient of viscosity (dyn s/cm^2)

λ_{sm} = solid second coefficient viscosity (dyn s/cm^2)
ω = angular velocity(1/s)
ρ = density (g/cm^3)
θ = translational granular temperature (cm^2/s^2)

Superscripts

p = plastic regime in granular flows
v = viscous regime in granular flows

Subscripts

cell = computational cell
coll = collision
g = gas phase
i = index of a particle
l = lth solid phase
m = mth solid phase
n = normal direction in the particle contact frame
t = tangential direction in the particle contact frame
M = number of phases
mf = minimum fluidization
max = maximum value
p = particle
s = solid phase
w = wall boundary

References

[1] Curtis, J. S., and van Wachem, B., 2004, "Modeling Particle-Laden Flows: A Research Outlook," AIChE J., **50**(11), pp. 2638–2645.
[2] Jackson, R., 2000, *The Dynamics of Fluidized Particles*, 1st ed., Cambridge University Press, Cambridge, UK.
[3] Gidaspow, D., Jung, J., and Singh, R. K., 2004, "Hydrodynamics of Fluidization Using Kinetic Theory: An Emerging Paradigm 2002 Flour-Daniel Lecture," Powder Technol., **148**, pp. 123–141.
[4] Agrawal, K., Loezos, P. N., Syamlal, M., and Sundaresan, S., 2001, "The Role of Meso-Scale Structures in Rapid Gas-Solid Flows," J. Fluid Mech., **445**, pp. 151–185.
[5] Rahman, K., and Campbell, C. S., 2002, "Particle Pressures Generated Around Bubbles in Gas-Fluidized Beds," J. Fluid Mech., **455**, pp. 102–127.
[6] Choi, J., Kudrolli, A., Rosales, R. R., and Bazant, M. Z., 2004, "Diffusion and Mixing in Gravity-Driven Dense Granular Flows," Phys. Rev. Lett., **92**(17), p. 174301.
[7] Bazant, M. Z., 2003, "A Theory of Cooperative Diffusion in Dense Granular Flows," Report No. cond-mat/0307379.
[8] Bazant, M. Z., 2006, "The Spot Model for Random-Packing Dynamics," Mech. Mater., **38**(8–10), pp. 717–731.
[9] Tsuji, Y., Kawaguchi, T., and Tanaka, T., 1993, "Discrete Particle Simulation of Two-Dimensional Fluidized Bed," Powder Technol., **77**, pp. 79–87.
[10] Hoomans, B. P., Kuipers, J. A., Briels, W. J., and van Swaaij, W. P., 1996, "Discrete Particle Simulation of Bubble and Slug Formation in a Two-Dimensional Gas-Fluidised Bed: A Hard-Sphere Approach," Chem. Eng. Sci., **51**(1), pp. 99–118.
[11] Xu, B. H., and Yu, A. B., 1997, "Numerical Simulation of the Gas-Solid Flow in a Fluidized Bed by Combining Discrete Particle Method With Computational Fluid Dynamics," Chem. Eng. Sci., **52**(16), pp. 2785–2809.
[12] Kafui, K. D., Thornton, C., and Adams, M. J., 2002, "Discrete Particle-Continuum Fluid Modelling of Gas-Solid Fluidised Beds," Chem. Eng. Sci., **57**, pp. 2395–2410.
[13] Syamlal, M., Rogers, W., and O'Brien, T., 1993, "MFIX Documentation: Theory Guide," National Energy Technology Laboratory, Department of Energy, Technical Note Nos. DOE/METC-95/1013 and NTIS/DE95000031 (see also http://www.mfix.org).
[14] Syamlal, M., 1987. "The Particle-Particle Drag Term in a Multiparticle Model of Fluidization," National Energy Technology Laboratory, Department of Energy, Topical Report Nos. DOE/MC/21353-2373, and NTIS/DE87006500.
[15] Syamlal, M., 1987, "A Review of Granular Stress Constitutive Relations," National Energy Technology Laboratory, Department of Energy, Technical Note Nos. DOE/MC21353-2372 and NTIS/DE87006499.
[16] Jenike, A. W., 1987, "A Theory of Flow of Particulate Solids in Converging and Diverging Channels Based on a Conical Yield Function," Powder Technol., **50**, pp. 229–236.
[17] Schaeffer, D. G., 1987, "Instability in the Evolution Equations Describing Incompressible Granular Flow," J. Differ. Equations, **66**, pp. 19–50.
[18] Cundall, P. A., and Strack, D. L., 1979, "A Discrete Numerical Model for Granular Assemblies," Geotechnique, **29**, pp. 47–65.
[19] Silbert, L. E., Ertas, D., Grest, G. S., Halsey, T. C., Levine, D., and Plimpton, S. J., 2001, "Granular Flow Down an Inclined Plane: Bagnold Scaling and Rheology," Phys. Rev. E, **64**(5), p. 051302.
[20] Boyalakuntla, D., 2003, "Simulation of Granular and Gas-Solid Flows Using Discrete Element Method," Ph.D. thesis, Carnegie Mellon University, Pittsburgh, Pennsylvania.
[21] Anderson, T. B., and Jackson, R., 1967, "A Fluid Mechanical Description of Fluidised Beds," Ind. Eng. Chem. Fundam., **6**, pp. 527–539.
[22] Ergun, S., 1952, "Fluid Flow Through Packed Columns," Chem. Eng. Prog., **48**, pp. 89–94.
[23] Wen, C. Y., and Yu, Y. H., 1966, "Mechanics of Fluidization," *Fluid Particle Technology*, Chemical Engineering Progress Symposium Series Vol. 62, American Institute of Chemical Engineers, New York, pp. 100–111.
[24] Syamlal, M., 1998, "MFIX Documentation: Numerical Technique," National Energy Technology Laboratory, Department of Energy, Technical Note Nos. DOE/MC31346-5824 and NTIS/DE98002029 (see also http://www.mfix.org).
[25] Goldschmidt, M. J., Link, J. M., Mellema, S., and Kuipers, J. A., 2003, "Digital Image Analysis Measurements of Bed Expansion and Segregation Dynamics in Dense Gas-Fluidised Beds," Powder Technol., **138**, pp. 135–159.
[26] Sun, J., and Battaglia, F., 2006, "Hydrodynamic Modeling of Particle Rotation for Segregation in Bubbling Gas-Fluidized Beds," Chem. Eng. Sci., **61**(5), pp. 1470–1479.
[27] Sun, J., Battaglia, F., and Subramaniam, S., 2006, "Dynamics and Structures of Segregation in a Dense, Vibrating Granular Bed," Phys. Rev. E, **74**(6), p. 061307.
[28] Sun, J., and Battaglia, F., 2007, "Analysis of Solid Structures and Stresses in a Gas Fluidized Bed," American Society of Mechanical Engineers, Fluids Engineering Division (Publication), FED Report No. FEDSM2007-37189.
[29] Goldschmidt, M., 2001, "Hydrodynamic Modelling of Fluidised Bed Spray Granulation," Ph.D. thesis, Twente University, Netherlands.
[30] Sundaresan, S., 2000, "Modeling the Hydrodynamics of Multiphase Flow Reactors: Current Status and Challenges," AIChE J., **46**(6), pp. 1102–1105.
[31] Srivastava, A., and Sundaresan, S., 2003, "Analysis of a Frictional-Kinetic Model for Gas-Particle Flow," Powder Technol., **129**, pp. 72–85.
[32] Dreeben, T. D., and Pope, S. B., 1992, "Nonparametric Estimation of Mean Fields With Application to Particle Methods for Turbulent Flows," Sibley School of Mechanical and Aerospace Engineering, Cornell University, Technical Report No. FDA 92-13.
[33] Garg, R., Narayanan, C., Lakehal, D., and Subramaniam, S., 2007, "Accurate Numerical Estimation of Interphase Momentum Transfer in Lagrangian-Eulerian Simulations of Dispersed Two-Phase Flows," Int. J. Multiphase Flow, doi: 10.1016/j.ijmultiphaseflow.2007.06.002

Representing Polydispersed Droplet Behavior in Nucleating Steam Flow

A. G. Gerber
Associate Professor

A. Mousavi
Graduate Student

Department of Mechanical Engineering,
University of New Brunswick,
Fredericton, NB, E3B5A3 Canada

The quadrature method of moments (QMOM) is applied to the particle size distribution (PSD) present in nucleating steam flow, with a particular emphasis on conditions relevant to low-pressure steam turbines. These machines exhibit heterogeneous and homogeneous phase transition in the presence of strong flow discontinuities due to shocks and complex geometry. They offer a particularly difficult two-phase modeling situation. The present work shows that QMOM is a robust and efficient method and, in comparison to current practice of using a monodispersed PSD in computational fluid dynamics (CFD) models, offers promise for dealing with the complex two-phase conditions present in real machines. [DOI: 10.1115/1.2786536]

1 Introduction

This work examines the quadrature method of moments (QMOM) as a computational fluid dynamics (CFD) methodology for representing particle size distributions (PSDs) prevalent in low-pressure (LP) steam turbines. The droplet behavior in steam turbines poses a challenging environment for CFD model development. Presently, CFD is used widely in steam turbine design but with overly simplified representation of the two-phase behavior. In particular, current practice relies on the use of a local monodispersed distribution assumption, even though contributions to the PSD occur from a number of mechanisms, over a significant size range, along the length of the turbine. Accumulated errors make predictions of such things as machine efficiency or moisture erosion behavior very unreliable.

Beyond the simple monodispersed assumptions, there are several choices for representing the PSD in steam turbines. The representation of the second phase can be divided into Eulerian Lagrangian (EL) models [1–4], Eulerian–Eulerian (EE) methods based on class methods (CMs) [4], or those based on tracking moments of the PSD (MOM) [4,5]. The EL models are capable of directly evaluating the PSD and, if formulated fully on multiphase principles [3], can potentially include slip behavior. In EL methods, the time integration can be decoupled from the Eulerian phase as individual droplet packets are integrated in time through space. Time step control is beneficial since flow conditions change rapidly in steam turbines, for example in phase transition regions or through shocks, and the droplet heat/mass transfer models can then be more accurately evaluated. The EL methods become inefficient for large-scale unsteady simulations, which will be required to fully investigate multiphase issues in steam turbines. The EE methods are more easily applied to large unsteady 3D problems but suffer from some drawbacks. Foremost is that the PSD must be represented by a system of transport equations integrated in time and space at the same resolution as all of the other transport equations (for the continuous and dispersed phases) in the problem. This impacts the accuracy of the nonlinear heat/mass transfer models that govern the two-phase flow behavior. Increased mesh and time resolution during calculations can alleviate this somewhat; however, for EE methods to be truly effective, it is important that accurate approaches for discretizing and tracking the PSD also be developed. This is particularly true for steam turbine applications due to the complexity of the two-phase flow, a fact which will be described in the next section.

1.1 Two-Phase Droplet Dynamics in Low-Pressure Steam Turbines. In the last stages of the turbine, very high expansion rates are achieved, leading to supercooled flow conditions and nonequilibrium droplet formation by several mechanisms. The nonequilibrium phase transition is highly irreversible and has a significant impact on turbine efficiency. Figure 1 is provided to assist in further describing the two-phase flow behavior in a LP turbine, much of which can be derived from Refs. [1–7]. The solid lines, with letters at the beginning and ending, denote typical nonequilibrium phase transition lines or zones of secondary droplet behavior. Dashed lines indicate equilibrium phase transition. The first transition line (*a-a*) denotes the saturation line where, under equilibrium, assumptions phase transition would appear. Transition line *b-b* denotes heterogeneous nucleation transition, which occurs on contaminants in the flow, and is generally insufficient in number to bring the flow to equilibrium conditions. Typical sizes for droplets generated in this manner are 0.01–0.1 μm. Under rapid expansion, supercooling continues up to line *c-c* (also called the Wilson line), where primary homogeneous nucleation occurs, creating droplet sizes in the range of 0.001–0.01 μm and following with the reversion of the flow to near equilibrium conditions. Note that transition line *c-c* can be highly curved such that primary nucleation toward the shroud occurs in the following stage component (the third rotor) [6]. As flow expansion continues into the final stage, significant supercooling is again possible, leading to further secondary homogeneous nucleation along line *d-d*. Finally, smaller droplets generated along lines *b-b* and/or *c-c* can collect on blades and be re-entrained, as secondary droplets, into the flow at the trailing edges of rotating components [7], in particular. Centrifugal action generally confines these droplets toward the shroud as shown by boundary *e-e* [7]. Importantly, the droplets generated along lines *b-b* through *d-d* remain quite small, but with a broad (possibly bimodal) distribution and can be adequately approximated with a no-slip assumption relative to the continuous vapor phase [6]. Droplets in region *e-e* are entrained at sizes that are generally greater than 100 μm and have a considerable slip relative to the vapor. These droplets have a significant influence on blade erosion, and the fact that the small nucleated droplets provide the source for entrainment of large droplets into region *e-e* describe a highly coupled two-phase flow system.

The PSD at any point at the exit of the last stage of the turbine will depend on the various phase transition contributions, including subsequent droplet growth, leading up to that point. To high-

Contributed by the Fluids Engineering Division of ASME for publication in the JOURNAL OF FLUIDS ENGINEERING. Manuscript received September 15, 2006; final manuscript received May 31, 2007. Review conducted by Timothy J. O'Hern. Paper presented at the 2006 ASME Fluids Engineering Division Summer Meeting and Exhibition (FEDSM2006) Miami, FL, July 17–20, 2006.

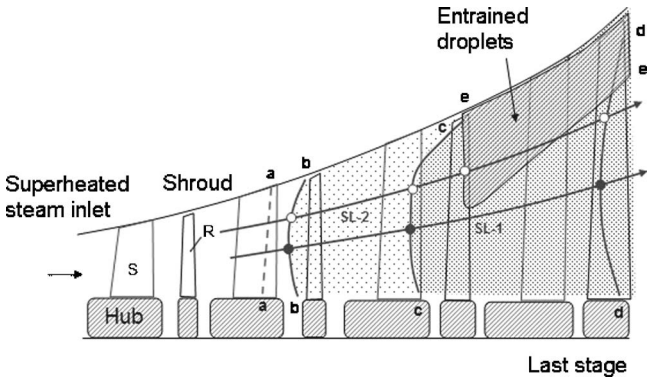

Fig. 1 Topology of phase transition in a LP steam turbine: *a-a*, saturation line; *b-b*, heterogeneous nucleation transition; *c-c*, primary homogeneous nucleation transition; *d-d*, secondary primary homogeneous nucleation transition; *e-e*, secondary droplet region originating from trailing edges of rotating blades. Stator and rotor components labeled with S and R, respectively.

light this two streamlines, SL-1 and SL-2 (superimposed on the transition lines/zones previously described) are depicted in Fig. 1, assuming steady conditions. The contributions to SL-1 (shown with solid circles where SL-1 intersects transition lines) would be

1. heterogeneous nucleation (0.01–0.1 μm) at intersection SL-1/*b-b*
2. primary homogeneous nucleation (0.001–0.01 μm) at intersection SL-1/*c-c*
3. possible secondary homogeneous nucleation (0.001–0.01 μm) at intersection SL-1/*d-d*

Along SL-2, we have the same PSD contributions, except that between intersection SL-2/*c-c* and SL-2/*d-d* there is the introduction of secondary droplets with slip. Secondary droplets can also experience a break-up of the larger sizes, but in all cases coalescence is generally not important. It should be noted that as we progress along a streamline significant droplet growth occurs in a highly supercooled vapor. For example, once intersection SL-1/*c-c* is reached along SL-1, the droplets generated at SL-1/*b-b* may have grown significantly by an order of magnitude or more. The same can be said between SL-1/*c-c* and SL-1/*d-d*. On a final note, in the passage through the turbine passages, and in particular in the last stage, fluid velocities are transonic and the PSD may pass through oblique shocks of varying strength. An evaluation of a method for representing the PSD in steam turbines should also consider such strong flow discontinuities.

From the above description, the two-phase flow behavior in steam turbines can be characterized as having a broad PSD with possible bimodal attributes. The range of the distribution can span several orders of magnitude and may include slip. Furthermore, it can pass through strong flow continuities such as shocks. On the basis of this complexity, representing the PSD with CM becomes intractable. This is because transport equations are applied for size bins that range between the minimum and maximum sizes in the distribution. Obvious problems occur with such a broad distribution. The MOM is much more attractive as it is based on solving a set of transport equations that conserve the moments of the distribution [8]. The number of transport equations is much reduced; generally six will suffice as will be discussed subsequently, leading to considerable savings in CPU time. Furthermore, the size range of the underlying distribution can evolve with the solution and need not be prescribed.

Of the various MOM approaches available, those based on the QMOM are particularly attractive. Recent studies have shown that the method can handle the growth laws used in the steam turbine models without approximation, and show good accuracy for representing the PSD with very broad size distributions [9]. In this study, the QMOM approach is applied to conditions similar to SL-1 using supersonic nozzle calculations with expansion rates found in LP steam turbines and including heterogeneous and homogeneous PSD contributions (of different relative strengths) with shocks. This emphasizes an important contribution of the present work: the development of a realizable approach, using a QMOM based method, for representing the complex PSD present in steam turbines. Conditions for SL-2 will be considered in subsequent studies that will incorporate the influence of slip and where a related algorithm to QMOM, the direct QMOM (DQMOM) [10], shows promise.

2 Governing Equations

In the present study, we consider 1D nozzle flows in order to isolate our study of the QMOM method for phase transition conditions similar to that described for SL-1 in Fig. 1. Furthermore, the study considers two modes of nucleation as active in the flow. The first is heterogeneous nucleation on foreign nuclei in the size range of 0.01–1 μm, and the second is homogeneous nucleation, introducing droplets initially in the range of 0.005 μm and after growth in the range of 0.01–0.1 μm. Since the droplets in this study remain nominally below 1 μm in size, the effect of slip can be neglected. The transport equations for mass and momentum can then be formulated in terms of mixture properties with additional transport equations to represent the droplet distribution. Significant thermal nonequilibrium conditions develop in the flow requiring a transport equation for mixture energy. Associated thermodynamic irreversibilities are incorporated through a heat transfer model in the droplet growth calculation. Details on the various formulations now follow.

2.1 Gas (Continuous) Phase. The governing equations of fluid motion for quasi-one-dimensional compressible flow of a two-phase mixture in full conservative form with no body force can be written as [11]

$$\frac{\partial(S\mathbf{Q})}{\partial t} + \frac{\partial \mathbf{F}}{\partial x} - H_s = 0 \tag{1}$$

where t is time, x is a space coordinate, and S is the cross sectional area of the duct. Furthermore, $\mathbf{Q}$, $\mathbf{F}$ and H_s are, respectively, the conservative vector, flux vector, and source term responsible for the area change, all shown here as

$$\mathbf{Q} = \begin{bmatrix} \rho \\ \rho u \\ \rho e_t \end{bmatrix} \quad \mathbf{F} = S\begin{bmatrix} \rho u \\ \rho u^2 + p \\ \rho u H \end{bmatrix} \quad H_s = \frac{\partial S}{\partial x}\begin{bmatrix} 0 \\ p \\ 0 \end{bmatrix} \tag{2}$$

where ρ is the two-phase mixture density, u is the velocity, e_t is the total mixture internal energy, p is the pressure, and H is the total mixture enthalpy. Due to the small size of the droplets considered, the temperature of the condensed phase can be determined as a function of its size and will be elaborated on subsequently.

2.2 Liquid (Dispersed) Phase. The liquid phase influences the governing transport equations for mass, momentum, and energy through the wetness (or mass fraction) level. Determination of the condensed phase wetness and diameter distribution in the flow is based on the moment transport equations solved in conjunction with the QMOM method. The appearance of the condensed phase in the flow depends on the nucleation models and the developed meta-stable conditions in the flow. The growth of released droplets in the flow field depends on droplet growth models, which embody the local heat transfer conditions that drive heat and mass transfer in supercooled vapor conditions. The discussion of the interaction of these models begins with a description of the method of moments for representing size distributions.

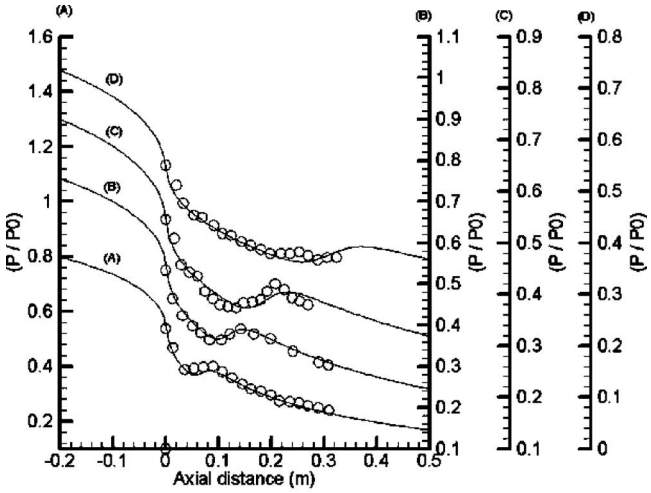

(*a*)

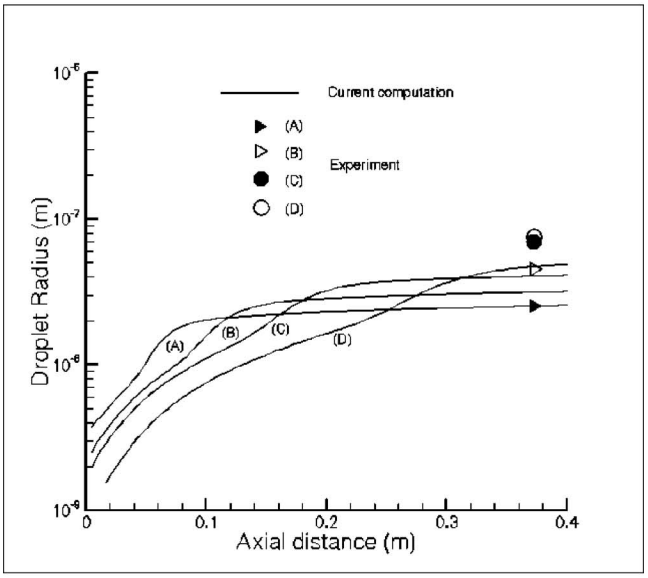

(*b*)

Fig. 2 (*a*) Comparison of calculated pressure distribution to experiment for nozzles A–D (p_{0in}=25 kPa, $(T_{0in})_{A,B,C,D}$=354.6 K, 357.6 K, 358.6 K, 361.8 K); (*b*) comparison of calculated mean droplet radius to measured values at a specified location

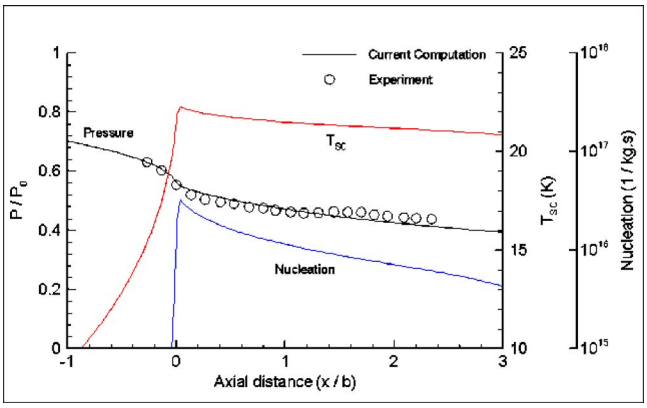

Fig. 3 Comparison of calculated pressure distribution (with p_{0in}=25 kPa, inlet d_{het}=1.25 μm and N_{het}=5×10^{12} kg^{-1}) to nozzle E experiments, which include droplets generated heterogeneously in the system

2.2.1 Moment Transport Equation. The MOM, as applied in our tests, is based on using lower-order moments to represent the droplet size distribution, with the advantage that no additional information of the distribution function is required [8]. The moments evolve in response to particle growth and nucleation, and are used to close any integrals of the droplet number function (f) that may appear in transport equations. The development of the MOM equations and their relation to the number equation have been described in a previous paper [9], and only the highlights are presented here. Considering only one internal coordinate (the droplet radius), the number transport equation, including the change in internal coordinate (G) (the growth law), change in external coordinate (u_i) (the local velocity), and nucleation (h), is shown below

$$\frac{\partial \rho f}{\partial t} + \sum_{i=1}^{3} \frac{\partial (u_i \rho f)}{\partial x_i} + \frac{\partial (G \rho f)}{\partial r} = \rho h \tag{3}$$

where h has the units of number of particles introduced into the system per unit of mixture mass per unit time. Both the growth law and nucleation function depend on droplet radius and are considered as known relations. This enables Eq. (3) to be solved together with the mass, momentum, and energy equations for the two-phase system. The main problem in dealing with Eq. (3) is the unknown distribution function f. To handle this problem, f is represented through its lower-order moments. With the internal dimensions reduced to the droplet radius r, the moments of f are the following:

$$\mu_k = \int r^k f dr \quad k = 0, 1, \ldots, 2n-1 \tag{4}$$

This allows Eq. (3) to be represented instead through transport equations of its moments now written as

$$\frac{\partial \rho \mu_k}{\partial t} + \sum_{i=1}^{3} \frac{\partial (u_i \rho \mu_k)}{\partial x_i} - k \int r^{k-1} \rho G f dr = \rho (J_{het} R^k + J_{hom} r_{crit}^k)$$
$$k = 0, 1, \ldots, 2n-1 \tag{5}$$

where J_{het} and J_{hom} are nucleation rates per unit mass of mixture per unit time. Nucleation occurs only at certain critical radii depending on the nucleation model, so that here h and J are related through Dirac delta functions as

$$h = J_{het} \delta(r - R) + J_{hom} \delta(r - r_{crit}) \tag{6}$$

The solution of Eq. (5) involves integrals of the number density function and is therefore limited to a specific form of growth law where

$$G(r) = a_1 + a_2 r \tag{7}$$

This is the form of equation used in the MOM with any other form having to be approximated using various means [5]. To avoid this limitation, McGraw [12] developed QMOM that involves replacing the integral in Eq. (5) by a summation of weights (w_i) and abscissas (r_i), which are obtained as a result of a Gaussian quadrature procedure. The integral would then be written in the form

$$k \int r^{k-1} G(r) f dr \cong k \sum_{i=1}^{n} r_i^{k-1} G(r_i) w_i \quad k \geqslant 1 \tag{8}$$

It should be noted that abscissas and weights are independent of particle growth law G and distribution function f. The moments are written in the new form of

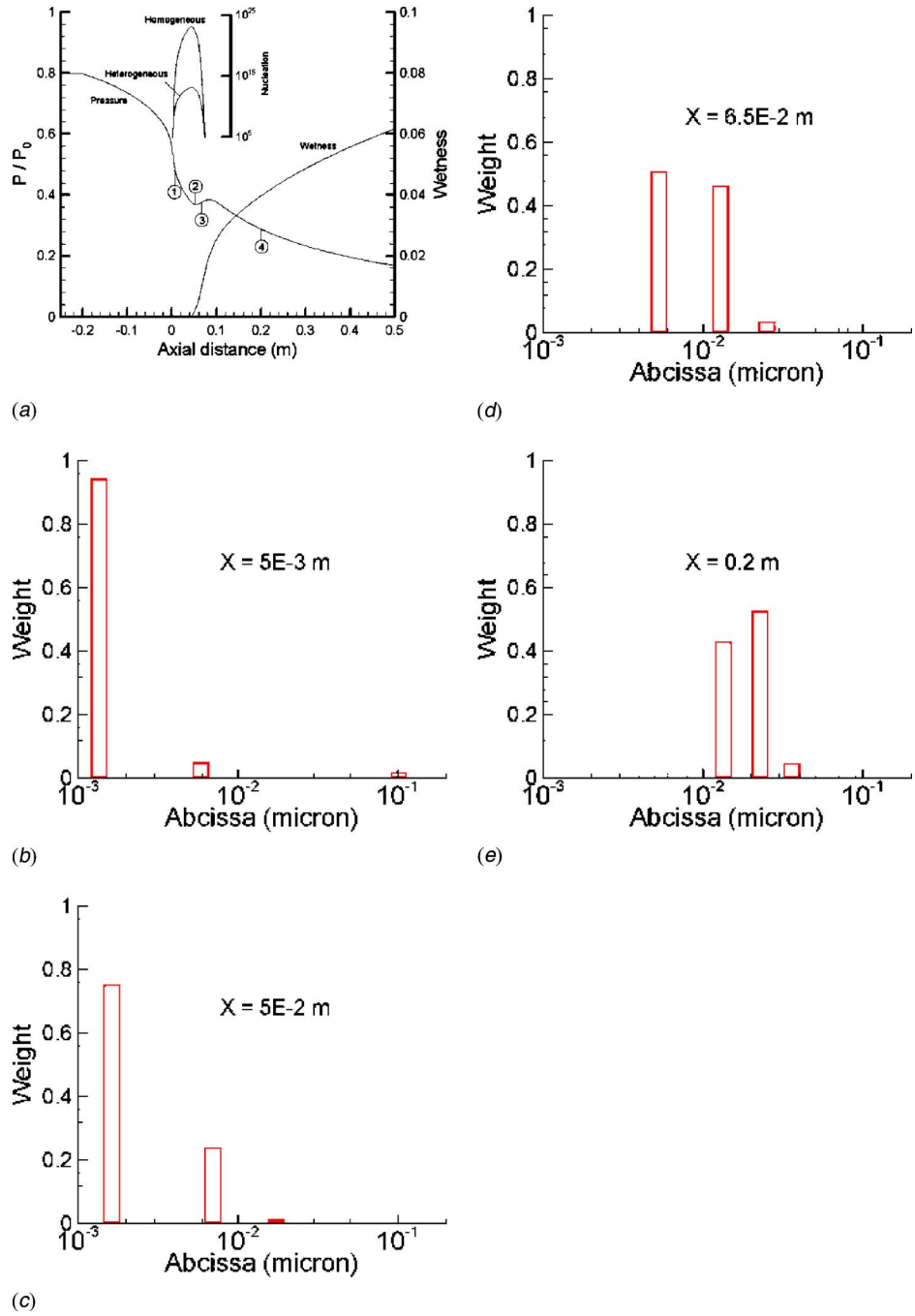

Fig. 4 (*a*) **QMOM results for normalized pressure, wetness, and nucleation, with $N_{het}=10^8$ kg^{-1} and $R_{het}=0.1$ μm. ((*b*),(*c*),(*d*), and (*e*)) Droplet size and weight distribution at locations (1), (2), (3), and (4) (nozzle A conditions).**

$$\mu_k = \int r^k f(r) dr = \sum_{i=1}^{n} r_i^k w_i \tag{9}$$

Finally, for 1D flow, the moment transport equations—originally presented in Eq. (5)—now becomes

$$\frac{\partial \rho \mu_k}{\partial t} + \frac{\partial (u \rho \mu_k)}{\partial x} - \rho k \sum_{i=1}^{n} r_i^{k-1} G(r_i) w_i = \rho (J_{het} R^k + J_{hom} r_{crit}^k)$$

$$k = 0, 1, \ldots, 2n-1 \tag{10}$$

The number of moments is $2n$, where the optimum value of n is based on accuracy and efficiency considerations and is recommended by Marchisio et al. [13] to be 3. This is the value of n chosen in this work. With the moments of the distribution available, the weights w_i and sizes r_i are obtained by applying a product difference algorithm as described in Ref. [12].

2.2.2 Droplet Nucleation and Growth. Appearance of the liquid phase occurs through the process of homogeneous and heterogeneous nucleation, which in either case occurs when free energy barriers to the formation of small spherical droplets are overcome. In the case of heterogeneous nucleation, foreign nuclei are present, which reduces the barriers and phase transition can occur at lower levels of critical supercooling. In the case of homogeneous nucleation, the phase transition occurs spontaneously out of

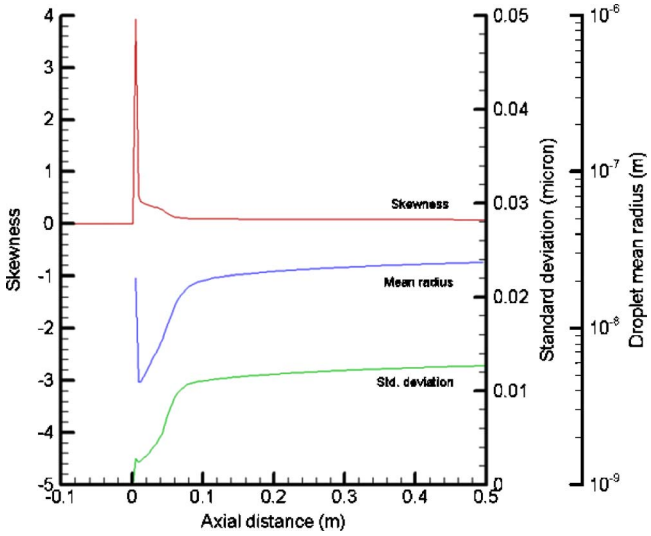

Fig. 5 Centerline value of mean droplet radius, skewness, and standard deviation, with $N_{het}=10^8$ kg^{-1} and $R_{het}=0.1$ μm (nozzle A)

the vapor phase and generally requires significantly more supercooling than the heterogeneous case. The nucleated droplets by either mechanism affect the gas temperature through heat and mass transfer and, with sufficient quantities of droplets, can bring the two-phase system back to near equilibrium conditions. Heterogeneous nucleation forms droplets close to the size of the initial contaminant, while for homogeneous nucleation, the droplets appear at a critical radius calculated based on gas phase conditions to be

$$r_{\text{crit}} = \frac{2\sigma T_s}{\rho_f h_{fg} \Delta T} \tag{11}$$

where T_s is the saturation temperature at local pressure, ρ_f is the density of the water, h_{fg} is the equilibrium latent heat, σ is the liquid surface tension, and ΔT is the supercooling temperature equal to $T_g - T_s(p)$.

The number of particles released into the flow as a result of homogeneous nucleation is calculated based on the classical nucleation theory [14] to be

$$J_{\text{hom}} = \frac{q_c}{1+\eta}\left(\frac{2\sigma}{\pi m^3}\right)^{1/2}\frac{\rho_g}{\rho_f}\exp\left(-\frac{4\pi r_{\text{crit}}^2\sigma}{3KT_g}\right) \tag{12}$$

where η is defined as follows:

$$\eta = \frac{\gamma-1}{\gamma+1}\frac{h_{fg}}{RT_g}\left(\frac{h_{fg}}{RT_g}-\frac{1}{2}\right) \tag{13}$$

q_c is the condensation coefficient, K is the Boltzmann's constant, m is the mass of one water molecule, γ is the specific heat ratio, and R is the gas constant. Equations (11)–(13) present the generally accepted form (with only minor variations) of the classical nucleation model for wet steam in turbines and are discussed thoroughly in Ref. [15].

Heterogeneous nucleation follows a similar formulation as homogeneous nucleation, with modifications for the presence of foreign nuclei and water interfacial contact conditions. In the heterogeneous nucleation model used for this study, only spherical nucleation sites are considered, and we do not consider water chemistry issues. For the purposes of the present study, a more sophisticated nucleation model was not deemed necessary. The general form of the heterogeneous nucleation equation is then [16]

$$J_{\text{het}} = 4\pi R^2 n_p J_0 \exp\left(-\frac{G^*}{KT_g}\right) \tag{14}$$

where J_0 is the nucleation prefactor and is reported as 10^{25} cm^{-2} s^{-1} in many studies [16,17]. In addition, n_p is the number of foreign particles per mixture mass present in the domain, R is the average radius of the particles, and G^* is the critical free energy of the cluster calculated with

$$G^* = \frac{4\pi r_{\text{crit}}^2\sigma}{3} f(m,z) \tag{15}$$

where $f(m,z)$ is a correction factor [16] to account for contact conditions between the water droplet and the foreign nuclei. The correction factor is calculated from

$$f(m,z) = \frac{1}{2}\left\{1+\left(\frac{1-mz}{\kappa}\right)^3 + z^3\left[2-3\left(\frac{z-m}{\kappa}\right)+\left(\frac{z-m}{\kappa}\right)^3\right] + 3mz^2\left(\frac{z-m}{\kappa}-1\right)\right\} \tag{16}$$

where here $m=\cos\theta$, θ is the contact angle, and z and κ are functions of the form

$$z = \frac{R}{r_{\text{crit}}} \qquad \kappa = (1+z^2-2mz)^{1/2} \tag{17}$$

The preceding equations describe the models for initiating phase transition and the appearance, including how many and the initial size, of a second phase into the flow.

Following phase transition, models are required to describe the growth of the droplets in an initially supercooled environment. Applying an energy balance around a spherical droplet undergoing phase change results in a growth law G for the droplet. Considering the small sizes of the droplets considered in this work, thermal inertia of the droplet can be neglected, leaving the balance of surface heat transfer and latent energy to give the equation

$$(h_g - h_p)\frac{dm_p}{dt} = \alpha_p A_p (T_p - T_g) \tag{18}$$

where m_p is the mass of one droplet of water, α_p is the convective heat transfer coefficient, and A_p is the surface area of a water droplet. The droplet temperature T_p is obtained as a function of droplet radius [1] as

$$T_P = T_s(p) - \Delta T\frac{r_{\text{crit}}}{r} \tag{19}$$

The convective heat transfer coefficient is obtained through the Nusselt number

$$\text{Nu} \equiv \frac{\alpha_p d_p}{k_g} = \frac{2}{1+3.78(1-\nu)\hat{l}/d_p \text{Pr}_g} \tag{20}$$

where d_p is the diameter of water droplet, k_g is the thermal conductivity of the gas, and Pr_g is the Prantdl number, the factor $(1-\nu)$ is a correction factor defined by Young [2] for improving the agreement of theoretical growth law with experimental condensation results at LP conditions. The mean free path of the gas molecules, $\hat{l}$, has the following definition:

$$\hat{l} = 1.5\mu_g\frac{\sqrt{RT_g}}{p} \tag{21}$$

Here, μ_g is the gas dynamic viscosity. Applying Eqs. (19) and (20) to Eq. (18) gives the final equation for the growth law,

$$G = \frac{k_g \Delta T(1-r_{\text{crit}}/r)}{\rho_f(h_g-h_p)(r+1.89(1-\nu)\hat{l}/\text{Pr}_g)} \tag{22}$$

The above equation is considerably more complex than the form allowed in the MOM formulations, as shown in Eq. (7). However,

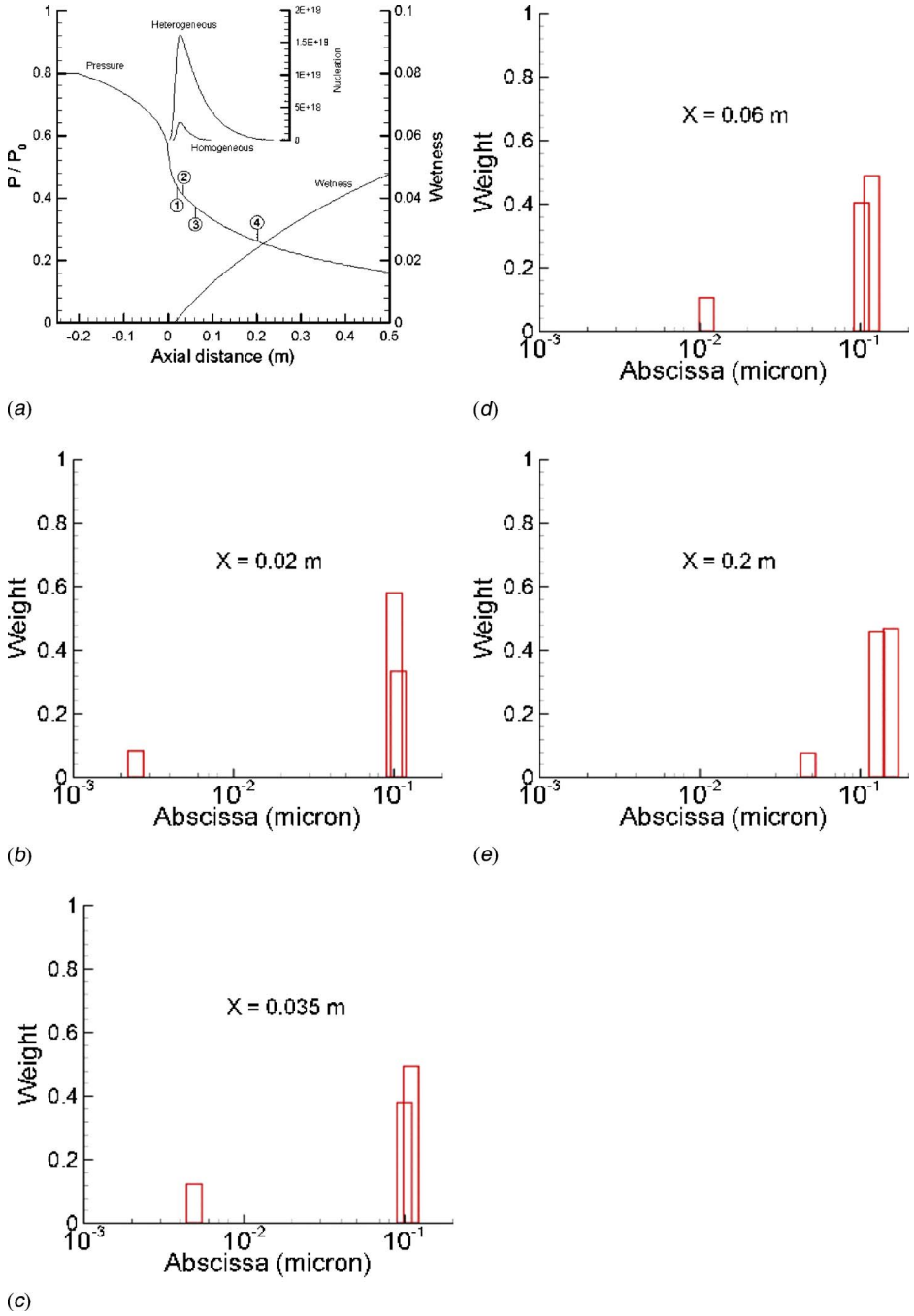

Fig. 6 (*a*) **QMOM results for normalized pressure, wetness, and nucleation, where $N_{het}=10^{16}$ kg^{-1} and $R_{het}=0.1$ μm. ((*b*), (*c*), (*d*), and (*e*)) Droplet size and weight distribution at locations (1), (2), (3), and (4) (nozzle A conditions).**

the QMOM methodology allows Eq. (22) to be directly applied with Eq. (10) and highlights the advantage of the QMOM method, which is not restricted to a particular form of growth law.

2.2.3 Mixture Thermodynamic Properties. The governing equations are formulated for mixture properties, with a mass fraction defining the extent of the liquid phase. The mass fraction can be obtained from the solution of the moments via the relation

$$y = \frac{m_f}{m_m} = \rho_f \frac{4\pi}{3}\mu_3 \tag{23}$$

Furthermore, the mean diameter required in transfer models, including standard deviation and skew of the distribution, can be calculated as follows:

$$d_{32} = \frac{2\mu_3}{\mu_2}$$

$$\sigma = 4\sum_{i=1}^{3}(r_i - \bar{r})^2 w_i$$

$$\gamma = \frac{1}{\mu_0}\sum_{i=1}^{3}\left(\frac{r_i - \bar{r}}{\sigma}\right)^3 w_i \tag{24}$$

where d_{32} is the Sauter mean diameter, σ is the standard deviation, and γ is the skewness. Phase transition as modeled in this study occurs under metastable conditions of which there is very little

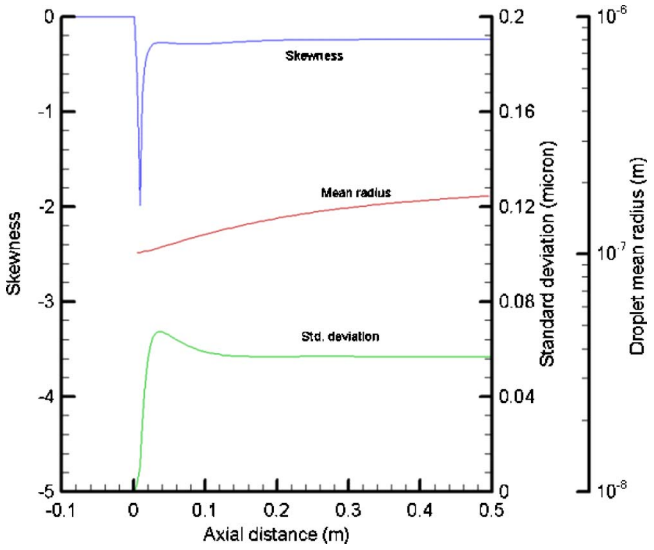

Fig. 7 Centerline value of mean droplet radius, skewness, and standard deviation, where $N_{het}=10^{16}$ kg^{-1} and $R_{het}=0.1$ μm (nozzle A)

experimental data. Standard practice is to extrapolate equations of state (developed for superheated conditions) into the metastable region. An important variable in the solution is the gas phase temperature, which is supercooled leading up to phase transition. Knowing the value of the mixture internal energy e obtained from the total internal energy in Eq. (1), the gas phase value (e_g) is calculated with

$$e_g = \frac{e-(ye_f)}{1-y} \tag{25}$$

from which the gas temperature is derived. Furthermore, the gas density can be obtained using

$$\rho_g = \frac{\rho(1-y)}{1-y\rho\rho_f^{-1}} \tag{26}$$

after which the local pressure of the mixture is calculated through the equation of state. Due to the LPs in the examples considered, an ideal equation of state is applied. Other properties are derived from steam tables.

3 Numerical Solution

3.1 Discretization of Transport Equations. For the discretization of the mixture governing equations (Eq. (1)), we use a high resolution upwind Roe scheme [18,19]. The second order Lax–Wendroff explicit scheme is selected for the time discretization. The predictor step determines flow conditions at an intermediate step $n+1/2$,

$$\frac{1}{\Delta t/2}[(SQ)^{n+1/2}-(SQ)^n]+\frac{1}{\Delta x}(F_E^n-F_W^n)-H_s^n=0 \tag{27}$$

where the F_W^n and F_E^n are the numerical fluxes evaluated at the west (W) and east (E) faces of the control volume. With the flow conditions obtained at time level $n+1/2$, the corrector step completes the time step to the level of $n+1$ as follows:

$$\frac{1}{\Delta t/2}[(SQ)^{n+1}-(SQ)^n]+\frac{1}{\Delta x}(F_E^{n+1/2}-F_W^{n+1/2})-H_s^{n+1/2}=0 \tag{28}$$

For the spatial discretization, a third-order upwind-biased algorithm with a MUSCL extrapolation method is used [18]. This extrapolation strategy provides the left (L) and right (R) values of the flow conditions at the cell face of each control volume. In this approach, the nodal values are assumed to be known and the extrapolation provides values on both L and R sides of each cell face, such that

$$q_E^L = q_j + \frac{1}{4}[(1-\kappa)(q_j-q_{j-1})+(1+\kappa)(q_{j+1}-q_j)]$$

$$q_E^R = q_{j+1} + \frac{1}{4}[(1-\kappa)(q_{j+2}-q_{j+1})+(1+\kappa)(q_{j+1}-q_j)] \tag{29}$$

where $\kappa=\frac{1}{3}$ corresponds to a choice of third-order upwind bias for spatial discretization and q denotes the flow conditions described above.

Based on the acquired L and R side fluxes and using Roe's scheme, the numerical flux at the face of a cell is obtained as

$$F_E = \frac{1}{2}(F_E^R+F_E^L)-\frac{1}{2}\sum_{k=1}^{3}|\hat{\lambda}_E^{(k)}|\,\delta\mathbf{w}_E^{(k)}\hat{\mathbf{T}}_E^{(k)} \tag{30}$$

where λ is the eigenvalue of the Jacobian flux matrix, $\mathbf{T}$ is the related eigenvector, and δw is the wave amplitude vector. The same formulation applies for the west face of the control volume.

3.2 Overall Solution Strategy. With all of the relevant equations now presented, we can present the overall solution methodology as follows. Beginning at time level n:

- Solve hydrodynamic properties (u, ρ, and e_t) at time $n+\frac{1}{2}$ based on the methodology outlined in Sec. 3.1.
- Compute growth law (Eq. (22)) and nucleation (Eqs. (11)–(17)) for each node using droplet sizes r_i and weights w_i of PSD at time n.
- Solve moment transport equations (Eq. (10)) with quadrature level of $n=3$ to obtain moments at time $n+\frac{1}{2}$.
- With new moments, use the QMOM approach [12] to obtain droplet sizes r_i and weights w_i of PSD at time $n+\frac{1}{2}$.
- Update PSD statistics and thermodynamic properties (Eqs. (23)–(26)).

Repeat the above procedure for time level $n+1$ to complete the time step.

4 Validation

Before exploring the application of the QMOM methodology to more complex two-phase flow situations, some initial testing was undertaken. Here, the experimental data of Moore et al. [20] for LP steam flow ($p<0.25$ bars) are used. The calculations are performed on nozzles A to E as presented in Ref. [20]. In these experiments, homogeneous nucleation is dominant for nozzles A to D with inlet conditions $p_{0in}=25$ kPa and $(T_{0in})_{A,B,C,D}=354.6$ K, 357.6 K, 358.6 K, and 361.8 K, respectively, while for nozzle E inlet droplets are present due to an early upstream nucleation and will be tested as a separate case. Figure 2(a) shows the predicted centerline pressure profiles along the first four nozzles compared to experimental data. The numerical results are in good agreement with experimental data across the four nozzles. In addition, Fig. 2(b) shows a comparison between calculated droplet mean radius (based on Eq. (24)) and the experiments. While the predicted droplet sizes show the same trends with decreasing expansion rate (nozzle A has the highest expansion rate), the absolute levels of the predictions are somewhat off. However, considering the experimental uncertainty in droplet size measurements, there is a good qualitative agreement.

As a final test, the heterogeneous and homogeneous nucleation models are both activated in calculating the pressure distribution for nozzle E (with $p_{0in}=25$ kPa), which is compared to the experiment in Fig. 3. In this case, foreign nuclei of diameter 1.2 μm are introduced at the inlet of the nozzle to initiate heterogeneous

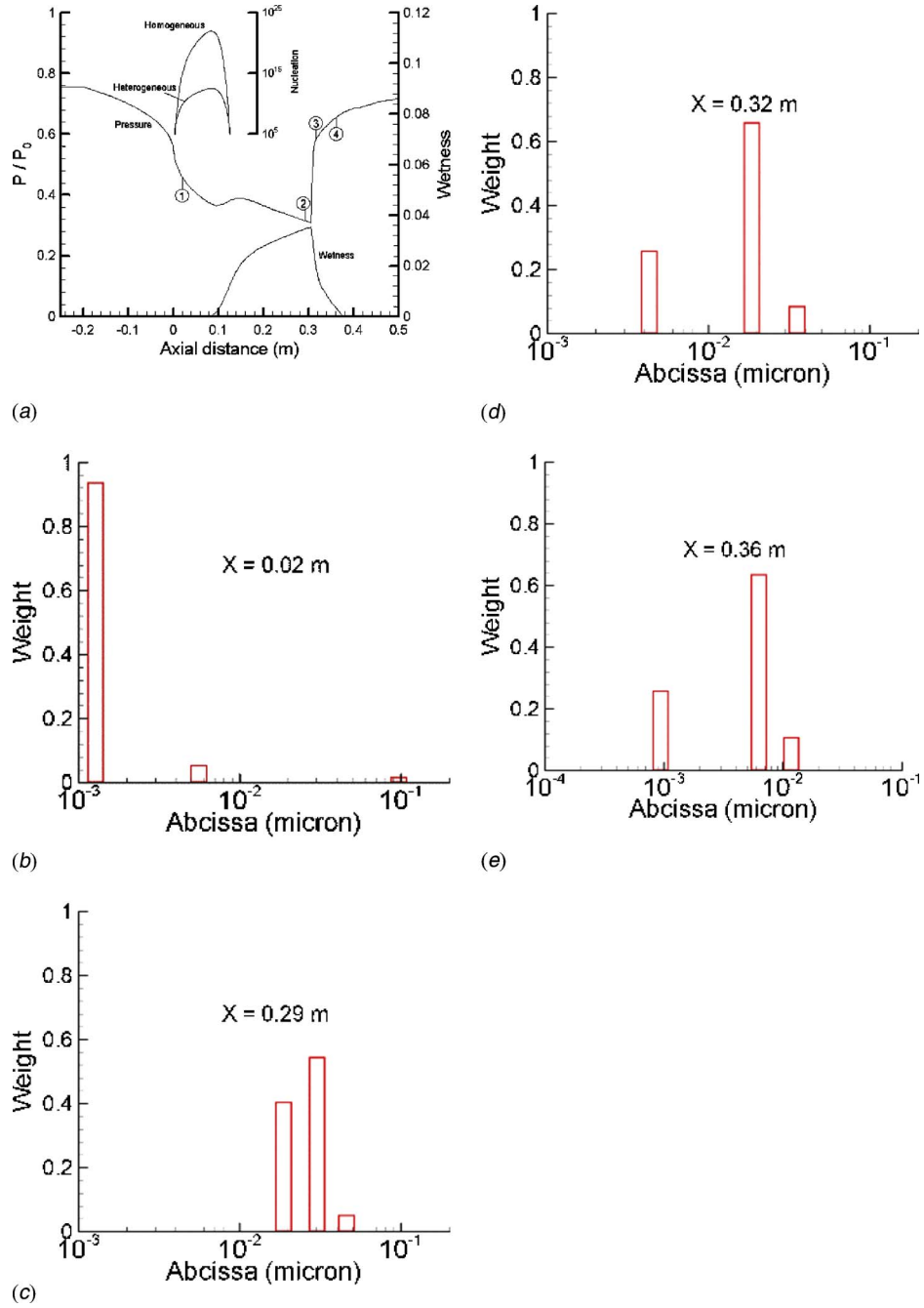

Fig. 8 (*a*) **QMOM results for normalized pressure, wetness and nucleation, where $N_{het}=10^8$ kg^{-1} and $R_{het}=0.1$ μm. ((*b*), (*c*), (*d*), and (*e*)) Droplet size and weight distribution at locations (1), (2), (3), and (4), back pressure $P_{out}=18$ kPa (nozzle B conditions).**

nucleation. The calculated pressure is in good agreement with experiment, including supercooling at the throat, which compares well to the 22°C reported in Ref. [20]. The predicted droplet diameter (d_{32}) at the nozzle location $x/b=2.64$ is 1.4 μm and also quite close to the reported value of 1.45 μm.

5 Results and Discussion

The performance of QMOM is now evaluated through tests that examine the evolution of the polydispersed droplet statistics under combinations of heterogeneous and homogeneous nucleation with normal shocks, all relevant to fluid path SL-1 of Fig. 1 (one exception is that oblique shock structures would be present in the turbine blade passages). Before proceeding, an important clarification should be made regarding the distributions predicted by QMOM. The Gaussian quadrature that underlies QMOM does not rely on a fixed range of droplet sizes, but allows the size range (and the associated weights) to evolve with the solution. This type of quadrature is known to have a high level of accuracy in representing the integral properties of the underlying distribution [9,13]. For nonequilibrium predictions, the essential quantities for accuracy are the integral surface area and volume of the distribution that impact heat and mass transfer, and subsequent transport of conserved properties. Therefore, while the distributions to be presented may appear very coarse, i.e., only three sizes and weights, they preserve with high accuracy the integral quantities that appear in Eq. (10) (via summations).

The test cases are conducted using nozzles A and B of Moore et al. [20]. The first case has a foreign nuclei concentration of $N_{het} = 10^8$ kg^{-1} with a mean radius of 0.1 μm, and the results are presented in Figs. 4 and 5. In Fig. 4(a), it can be seen that with this low foreign nuclei count, homogeneous nucleation dominates (as is seen in the nucleation rate inset), providing the primary contribution to the polydispersed droplet size spectrum. The evolving size distribution along the nozzle is now presented at four locations, as indicated in Fig. 4(a) with details given in Figs. 4(b)–4(e). By location 1 (see Fig. 4(b) at $x=0.005$ m), both nucleation processes have contributed to the abscissa readings, with clearly both opposing nucleation size scales present and the weight significantly skewed to the homogeneously generated droplets. At locations 2–4, we see the influence of the growth of small droplets in the supercooled environment as the distribution moves toward larger sizes. Note that the largest droplet sizes associated with heterogeneous nucleation are still present in the underlying PSD, but insignificant, with no representation in the new calculated distribution. This is in line with the QMOM procedure, which emphasizes an accurate representation of the integral properties not the exact shape of the PSD.

Figure 5 shows the evolution of the mean, standard deviation, and skew of the distribution along the nozzle length obtained with Eq. (24). The appearance of the homogeneous nucleated droplets is apparent in the sudden reduction in mean size. An increase in the standard deviation of the distribution occurs as the small homogeneously generated droplets grow in size and have more influence. The droplet skew that is initially large at the moment of homogeneous nucleation disappears as the small droplets move toward the larger sizes. The larger droplets interact with the vapor phase at a slower time scale (i.e., their growth is small), and their dynamics have little influence over the length of the nozzle.

The second test case considers a significant level of heterogeneous nucleation interacting with homogeneous nucleation. In this case, the foreign particle concentration is 10^{16} kg^{-1}, and the average particle size remains at the previous size of 0.1 μm. Similar to the results of the previous test case, predictions are shown in Figs. 6 and 7. Increasing the number of foreign particles leads to a much higher level of heterogeneous nucleation and consequently decreases the influence of homogeneous phase transition. This can be seen in the nucleation inset in Fig. 6(a). The heterogeneous nucleation has a lower threshold for initiation of water droplets. Therefore, larger droplets appear earlier in the nozzle. The reduction in strength of the homogeneous nucleation removes the typical pressure rise associated with purely homogeneous phase transition.

Figure 6(b) shows the droplet size distribution at location 1, which now appears quite different from that in the first case (Fig. 4(b)). The significant weights have moved toward the heterogeneous droplet sizes where a slight distribution has developed according to their earlier appearance in the nozzle. However, the small droplets are more reactive in the supercooled environment and grow quickly so that the distribution narrows toward the larger size regimes (as seen in Figs. 6(c)–6(e)). In the end, we have a distribution straddling the 0.1 μm, size range. The evolution of the statistics is shown in Fig. 7, with the mean diameter growing much more slowly, relative to the previous case, with the dominance of the larger droplet sizes. Furthermore, in comparison to test 1 (Fig. 5), the resulting standard deviation is much larger as the homogeneously nucleated droplets and heterogeneously generated ones are both influential.

Similar nucleation scenarios, as presented for nozzle A, are now conducted for nozzle B but also include a normal shock in the flow passage. Here, the properties of the PSD are examined before and after the shock. Figure 8 shows the case of low foreign nuclei loading so that strong homogeneous nucleation is present in conjunction with a weak heterogeneous contribution. The nozzle pressure profile and wetness is shown in Fig. 8(a) with locations along the nozzle indicated by numbers as in the previous examples. At

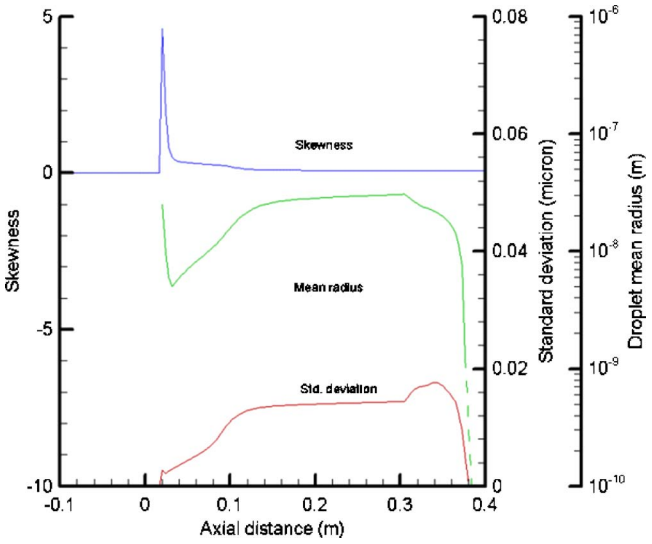

Fig. 9 Centerline value of mean droplet radius, skewness, and standard deviation, where $N_{het}=10^8$ kg^{-1} and $R_{het}=0.1$ μm (nozzle B)

location 1, the QMOM weights and abscissa are shown just before the significant phase transition (Fig. 8(b)) and are highly skewed toward the small homogeneously nucleated droplets as expected. This is followed by rapid growth, as indicated by the location 2 distribution now in the 0.1–0.1 μm range (Fig. 8(c)), and precedes the normal shock. Through the shock, there is a rapid decrease in supercooling, and evaporation immediately reduces the overall size (Fig. 8(d)). As pressure recovery following the shock continues, evaporation proceeds with all sizes losing mass, as shown in Fig. 8(e). The largest droplet sizes, populated primarily by the heterogeneous nucleation, respond more slowly to the increasing pressure. Figure 9 shows the corresponding changes in the statistics of the PSD along the length of the nozzle.

Another physical situation to test, including a normal shock, is the one where a large concentration of foreign nuclei is present in the flow such that homogeneous nucleation is weakened considerably (Fig. 10(a)). The distribution of weights and abscissa following nucleation then becomes that as shown at location 1 in Fig. 10(b), where now the heterogeneously generated droplets are strongly represented at around 0.1 μm. These larger droplets remain relatively inert, over the short residence time in the nozzle, while the small homogeneously nucleated droplets react quickly. This is apparent in examining the QMOM weights and abscissa at locations 2–4 (Figs. 10(c)–10(e)). The small droplets homogeneously generated grow quickly but are removed as rapidly through and following the shock. The large quantity of heterogeneously generated droplets respond much more slowly in terms of size change, but the rate of size reduction increases rapidly as the smaller size ranges are approached (this effect is also obvious in the previous shock example in Figs. 8 and 9). All of this behavior is consistent with known behavior and is readily understood by the fact that the derivative dr/dm for a spherical particle of a given mass m, is inversely proportional to the square of the radius r. Figure 11 shows the corresponding changes in the statistics of the PSD along the length of the nozzle.

6 Conclusions

The QMOM methodology for representing polydispersed droplet distributions has been successfully applied to transonic flow conditions with phase transition. The conditions, including phase transition mechanisms and shocks, are similar to that present in LP steam turbine flow.

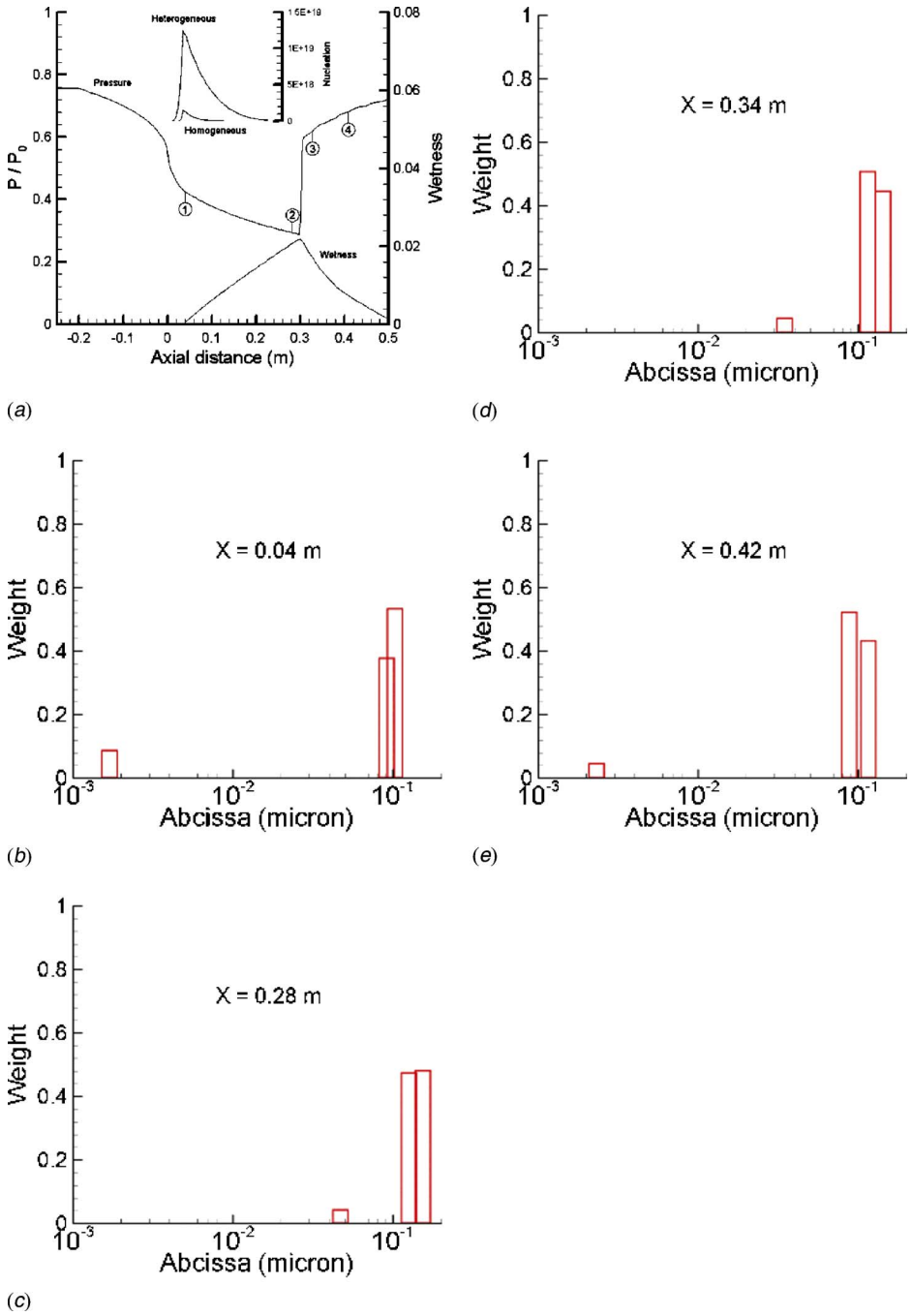

Fig. 10 (*a*) **QMOM results for normalized pressure, wetness, and nucleation, where $N_{het}=10^{16}$ kg^{-1} and $R_{het}=0.1$ μm. ((*b*), (*c*), (*d*), and (*e*)) Droplet size and weight distribution at locations (1), (2), (3) and (4), back pressure $P_{out}=18$ kPa (nozzle B conditions).**

Preliminary validation of QMOM by comparison of pressure distribution and the mean droplet size along the centerline of a supersonic nozzle indicates that the general physics of the phenomena are accurately captured. A verification of the heterogeneous nucleation model through its influence on nozzle centerline pressure distributions, with homogenous nucleation, also indicates physical realism when compared to experiment. It could be concluded that for the present study, the statistics of the polydispersed droplet could be accurately examined, and four droplet formation scenarios were subsequently chosen. The four cases considered the droplet distributions present with strong homogeneous/weak heterogeneous and moderate homogeneous/strong heterogeneous phase transitions, each of which was also considered with reduced back pressure to examine the influence of a normal shock on the predicted PSD. Results indicate that the QMOM predicts physically realistic statistics for the evolving distribution along the length of the nozzle.

The numerical tests conducted indicate that the QMOM methodology may provide a viable CFD modeling approach for handling polydispersed steam flow, as present in the LP stages of a steam turbine. However, the present study only examines distributions where droplets are transported at the gas phase velocity, which is an appropriate assumption for much of the phase transition activity in the turbine. However, in real turbine flows, larger secondary droplets, entrained from rotating surfaces, tend to move at their own velocity. Considering the influence of droplet slip on

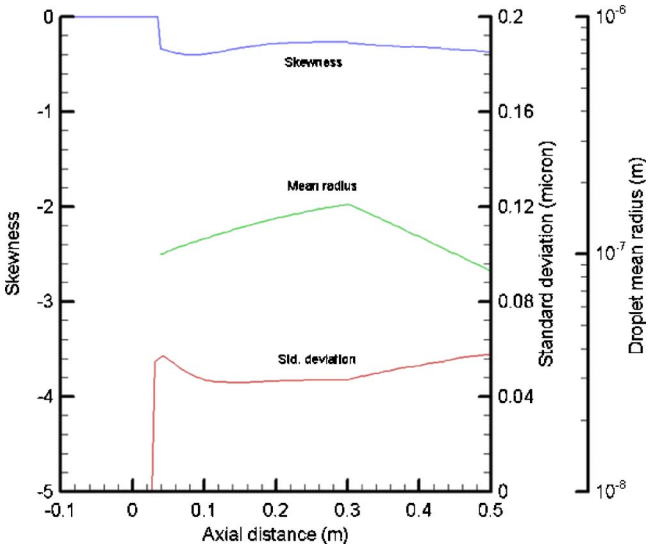

Fig. 11 Centerline value of mean droplet radius, skewness, and standard deviation, where $N_{het}=10^{16}$ kg^{-1} and $R_{het}=0.1$ μm

the PSD using a QMOM based approach would therefore be a requirement to include all of the significant droplet behaviors in the turbine. Such methods are under development [10] and should be explored in the future for steam turbine application.

Acknowledgment

The authors would like to acknowledge the support of the Natural Sciences and Engineering Research Council of Canada under an ongoing Discovery Grant.

References

[1] Bakhtar, F., Mahpeykar, M. R., and Abbas, K. K., 1995, "An Investigation of Nucleating Flows of Steam in a Cascade of Turbine Blading-Theoretical Treatment," ASME Trans. J. Fluids Eng., **117**, pp. 138–144.
[2] Young, J. B., 1992, "Two-Dimensional, Nonequilibrium, Wet Steam Calculations for Nozzles and Turbine Cascades," ASME J. Turbomach., **114**, pp. 569–579.
[3] Gerber, A. G., 2002, "Two-Phase Lagrangian/Eulerian Model for Nucleating Steam Flow," ASME J. Fluids Eng., **124**2, pp. 465–475.
[4] White, A. J, 2003, "A Comparison of Modeling Methods for Polydispersed Wet-Steam Flow," Int. J. Numerical Methods in Engineering, 57, pp. 819–834.
[5] White, A. J., and Hounslow, M. J., 2000, "Modelling Droplet Size Distribution in Polydispersed Wet-Steam Flows," Int. J. Heat Mass Transfer, **43**, pp. 1873–1884.
[6] Gerber, A. G., Sigg, R., Volker, L., and Casey, M. V., 2007, "Predictions of Nonequilibrium Phase Transition in a Model Low Pressure Steam Turbine," *Seventh European Turbomachinery Conference (ETC)*, Athens, March 5–9, Paper no. 176.
[7] Hesketh, J. A., and Walker, P. J., 2005, "Effects of Wetness in Steam Turbines," Proc. Inst. Mech. Eng., Part C: J. Mech. Eng. Sci., **219**, pp. 1301–1314.
[8] Hulburt, H. M., and Katz, S., 1964, "Some Problems in Particle Technology," Chem. Eng. Sci., **19**, pp. 555–574.
[9] Gerber, A., and Mousavi, A., 2006 "Application of Quadrature Method of Moments to the Polydispersed Droplet Spectrum in Transonic Steam Flows With Primary and Secondary Nucleation," Appl. Math. Model., **31**, 1518–1533
[10] Marchisio, D. L., and Fox, R. O., 2005, "Solution of Population Balance Equations Using the Direct Quadrature Method of Moments," J. Aerosol Sci., **36**, pp. 43–73.
[11] Hoffmann, K. A., and Chiang, S. T., 1993, "Computational Fluid Dynamics for Engineers," *Engineering Education System*, Wichita, Kansas, Vol. 2.
[12] McGraw, R., 1997, "Description of Aerosol Dynamics by the Quadrature Method of Moments," Aerosol Sci. Technol., **27**, pp. 255–265.
[13] Marchisio, D. L., Fox, O., and Vigil, R. D., 2003, "Quadrature Method of Moments for Population-Balance Equation," AIChE J., **49**, pp. 1266–1276.
[14] McDonald, J. E., 1962, "Homogeneous Nucleation of Water Vapor Condensation. I. Thermodynamic Aspects," Am. J. Phys., **30**, pp. 870–877.
[15] Bakhtar, F., Young, J. B., White, A. J., and Simpson, D. A., 2005 "Classical Nucleation Theory and Its Application to Condensing Steam Flow Calculations," Proc. Inst. Mech. Eng., Part C: J. Mech. Eng. Sci., **219**, pp. 1315–1333.
[16] Lee, T. D., 1998, "Surface Characterization by Heterogeneous Nucleation from the Vapor" Ph. D. thesis, Harvard University.
[17] Lee, Y. L., Chou, W. S., and Chen, L. H., 1998, "The Adsorption and Nucleation of Water Vapor on an Insoluble Spherical Solid Particle" Surf. Sci., **414**, pp. 363–373.
[18] Hirsch, C., 1990, *Numerical Computation of Internal and External Flows*, Wiley, New York, Vol. 2.
[19] Anderson, D. A., Tannehill, J. C., and Pletcher, R. H., 1997, *Computational Fluid Rechanics and Heat Transfer*, 2nd ed., Taylor & Francis, London.
[20] Moore, M. J., Walters, P. T., Crane, R. I, and Davidson, B. J., 1975, "Predicting the Fog Drop Size in Wet Steam Turbines," *Institute of Mechanical Engineers (UK), Wet Steam 4 Conference*, University of Warwick, Paper No. C37/73.

Kinematic and Dynamic Parameters of a Liquid-Solid Pipe Flow Using DPIV/Accelerometry

Joseph Borowsky
School of Engineering,
Mechanical and Aerospace Engineering Department,
Rutgers, The State University of New Jersey,
98 Brett Road,
Piscataway, NJ 08854
e-mail: borowsky@eden.rutgers.edu

Timothy Wei
Jonsson Engineering Center,
Department of Mechanical, Aerospace and Nuclear Engineering,
Rensselaer Polytechnic Institute,
110 8th Street,
Troy, NY 12180

An experimental investigation of a two-phase pipe flow was undertaken to study kinematic and dynamic parameters of the fluid and solid phases. To accomplish this, a two-color digital particle image velocimetry and accelerometry (DPIV/DPIA) methodology was used to measure velocity and acceleration fields of the fluid phase and solid phase simultaneously. The simultaneous, two-color DPIV/DPIA measurements provided information on the changing characteristics of two-phase flow kinematic and dynamic quantities. Analysis of kinematic terms indicated that turbulence was suppressed due to the presence of the solid phase. Dynamic considerations focused on the second and third central moments of temporal acceleration for both phases. For the condition studied, the distribution across the tube of the second central moment of acceleration indicated a higher value for the solid phase than the fluid phase; both phases had increased values near the wall. The third central moment statistic of acceleration showed a variation between the two phases with the fluid phase having an oscillatory-type profile across the tube and the solid phase having a fairly flat profile. The differences in second and third central moment profiles between the two phases are attributed to the inertia of each particle type and its response to turbulence structures. Analysis of acceleration statistics provides another approach to characterize flow fields and gives some insight into the flow structures, even for steady flows. [DOI: 10.1115/1.2786537]

Keywords: DPIV, two-phase flow, acceleration, accelerometry

1 Introduction

Multiphase flows have a large impact on society, ranging from environmental considerations to industrial processes. To better understand and take advantage of such flow phenomena, extensive studies have been made. For example, investigations have provided insight into the changes that occur in mean and fluctuating components of the flow due to the additional phases. Tsuji et al. [1] showed the large variations in air and polystyrene particle velocity distributions that occur depending on particle size and concentration. Kulick et al. [2] showed that solid particles in gas phase caused an attenuation of turbulence intensity for conditions of large Stokes number and mass loading. By simultaneously measuring fluid phase and solid phase velocities using phase Doppler anemometry (PDA), Righetti and Romano [3] were able to explain the effects that near wall turbulence structures have on the individual phases and their fluctuating velocity components. They found, for example, that the fluctuating velocity component is greater for a glass sphere solid phase than the liquid phase. This was attributed to the ability of near-wall vortical structures to transfer momentum between the phases. This is possible by the dynamics of these vortical structures, which both eject the fluid near the wall outwardly in a "burst" event and bring fluid far from the wall inward by a "sweep" event [4]. For two-phase flows, the transfer of momentum between the phases occurs because the solid phase particles can also be ejected outward or swept inward [3,5].

As described above, most of the investigations have focused on kinematic parameters, such as velocity and turbulence intensity, and the interaction between the phases. This is appropriate, as velocity and turbulence parameters are ideal for describing most bulk situations, in addition to being readily measurable. From such information, the basis of practical design considerations can be determined, such as system pressure drop and steady-state heat and mass transfer rates. However, dynamic quantities, such as force and acceleration, are also of great interest in many engineering problems. As an example, the analysis of fluid-structure interactions using the Hamiltonian system contains acceleration of the "solid-phase" structure [6]. With regard to multiphase flows, interfacial momentum terms have simultaneous time dependent velocity contributions from both the fluid phase and solid phase [7]. In addition, many industrial processes rely on the increase in particle drag and heat/mass transfer rates due to acceleration of the solid phase in the gas or liquid phase [8]. In fact, the drag coefficient of a particle in a time-varying flow has a term associated with the acceleration of the particle [9]. It is noted that these multiphase flow examples focus on the acceleration of the individual particle. In addition, characterization of the acceleration flow field can also be of interest. Such characterizations are important, for example, when knowledge of flow regions associated with certain acceleration values are required for time-varying flows, especially to determine drag and mass transfer. Likewise, central moment statistics of acceleration can be used to characterize a flow field and provide some insight into the flow structures, even for steady flows.

This paper will focus on measurements from a particular two-phase liquid-solid turbulent pipe flow. The experimental technique that allowed the measurement of velocity and acceleration of the fluid phase and solid phase simultaneously is described. Fluid phase and solid phase mean and fluctuating velocity data are presented first. Characterization of a turbulent pipe flow is then provided by presenting distributions of the second central moment and third central moment of the acceleration, which give some insight into the effect of turbulent flow structures.

2 Apparatus and Experimental Technique

A digital particle image velocimetry (DPIV)-based technique that allowed velocity and acceleration flow field measurements of

Contributed by the Fluids Engineering Division of ASME for publication in the JOURNAL OF FLUIDS ENGINEERING. Manuscript received October 23, 2006; final manuscript received June 13, 2007. Review conducted by Juergen Kompenhans.

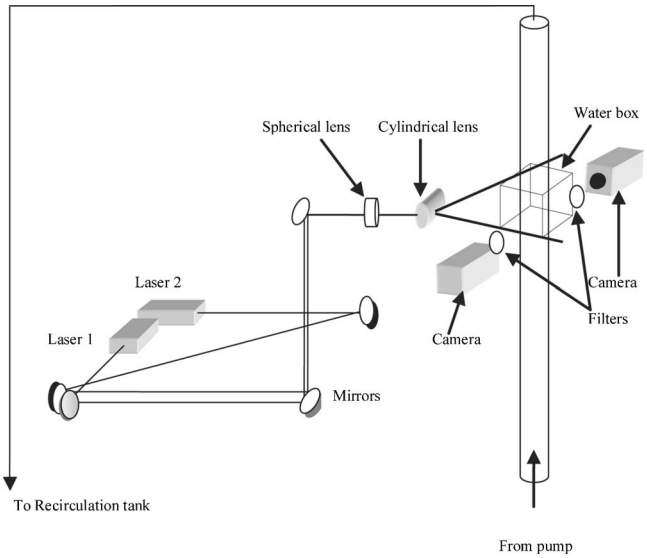

Fig. 1 Schematic of apparatus including optics and cameras

the fluid phase and solid phase simultaneously was developed using readily available equipment found in university and industrial laboratories [10]. A recirculation loop provided the means of directing fluid and solid particles from a reservoir feeding a centrifugal pump to the test section. This test section consisted of a 28 mm inside diameter (i.d.) acrylic tube that was 1.2 m in length ($L/D=43$) and oriented in the vertical direction (see Fig. 1). The vertical orientation removed the asymmetric effects that would result from gravitational forces on the particles. The measurement technique described below, however, could record the trajectories of the two phases in both vertical and horizontal orientations, which exist in many piping layouts found in industry. Details of the test section and instrumentation have been discussed previously [11].

The source of the light sheet that illuminated and bisected the test section was a dual pulse Nd:YAG laser (SoloPIV, New Wave Research), which provided coherent light at a wavelength of 532 nm. The time between adjacent laser pulses was 1.55 ms. High power laser mirrors, a spherical lens, and a cylindrical lens were used to direct the light to the test section. Two Redlake/Kodak Megaplus ES1.0 charge coupled device (CCD) cameras were positioned 180° apart such that both focused on the same briefly illuminated region of flow passing vertically through the acrylic tube test section. Images were recorded at 30 Hz in the camera's continuous mode. The basis of the two-color technique [11,12] was the placement of optical filters in front of each camera so that the cameras recorded the trajectories of either the solid particles or the neutrally buoyant fluorescent fluid tracer particles [11]. A 532 nm interference filter with a 10 nm bandwidth was placed in front of one camera to record the trajectories of the silver-coated glass spheres that reflected the Nd:YAG laser light. These particles had D_{10} and D_{90} particle sizes of 52 μm and 139 μm, respectively. A long pass filter with a cut-on wavelength of 600 nm was placed in front of the other camera lens that recorded the rhodamine fluorescence from the fluid tracer particles. These fluorescent acrylic particles had a size range between 60 μm and 80 μm and a particle response time less than the Kolmogorov time scale, thus acting as fluid tracer particles by following the flow.

Velocity and acceleration flow fields were calculated using DPIV-based algorithms, which analyzed images (1008 pixel $\times$1018 pixel) of the illuminated particles. An 8 bit analog-to-digital (A/D) converter transformed the relative brightness of the illuminated region to discrete intensity gray values between 0 (black) and 255 (white). With this methodology, the digital images were discretized into an ordered array of subwindows, also known as interrogation zones. The illuminated particles that were recorded within each interrogation zone, whether of the solid phase or fluid tracer, depended on the filter that was placed in front of the camera. Once the images were discretized, a two-dimensional fast Fourier transform (FFT) function was applied, thereby transforming each image to a frequency space. A cross-correlation algorithm was performed on the transformed interrogation zones separated by the time period between laser pulses, resulting in an area-averaged particle displacement at the interrogation zone position [13]. Initially, a 128 pixel$\times$128 pixel interrogation zone was analyzed to resolve the correlation peak. With this information, a more refined calculation of particle displacement resolution was performed using a 64 pixel$\times$64 pixel interrogation window. There was 75% overlapping of the interrogation zones. The particle displacement and the time between laser pulses allowed the calculation of velocity. Combining the velocities of the entire set of interrogation zones resulted in a two-dimensional vector profile of the test section from which data analysis was performed. A similar algorithm was used to determine the acceleration of the fluid tracer particles and solid glass spheres. First, two double exposure images were recorded sequentially by the rapid pulsing of the lasers. Each double exposure digital image was discretized into an ordered array of interrogation zones. From this two-dimensional signal, an autocorrelation of the FFT frequency space associated with the interrogation zone was performed from which velocity was determined. Acceleration was then determined by subtracting the pair of velocities and dividing by the millisecond time period between them, which was much less than the 0.1 s eddy characteristic time period in order to achieve improved temporal resolution. Further details of the methodology have been discussed previously [11]. The experimental technique described can be used for additional situations where simultaneous measurements of multiple phases are desired. Although the present investigation focused on a steady-state application, the methodology is also applicable to unsteady flows where knowledge of acceleration terms is essential for computing interfacial momentum terms.

Table 1 Process conditions associated with single-phase pipe flow

Reynolds number (based on diameter)	4610
Bulk velocity	0.15 m/s
Water temperature	25°C
Specific gravity of tracer particle	1.01
Mean tracer particle size	72 μm

3 Results and Discussion

3.1 Kinematic Results. A single-phase flow was initially investigated in order to gain an understanding of velocity profiles and to provide results that acted as a baseline for comparison with the subsequent two-phase flow. Process conditions for the single-phase flow are listed in Table 1. The single-phase and two-phase velocity data were based on analyzing over 1000 image pairs. From the resulting calculated flow fields, velocity values were averaged for each radial location. The velocity uncertainty associated with pixel scale and particle displacement resolution amounted to less than 0.2 cm/s. The mean axial velocity (U) distribution is plotted in Fig. 2 (top) as a function of radial location normalized with the tube diameter. The velocity distribution was also compared with the well-known Clauser profile [14] by plotting the data as a function of normalized viscous units from the tube wall ($y+=yu^*/v$, where v represents kinematic viscosity) to yield a friction velocity (u^*) of 0.01 m/s (Fig. 2 bottom). The profile reported by White [15] is also included for comparison.

The two-phase flow condition was studied by introducing glass

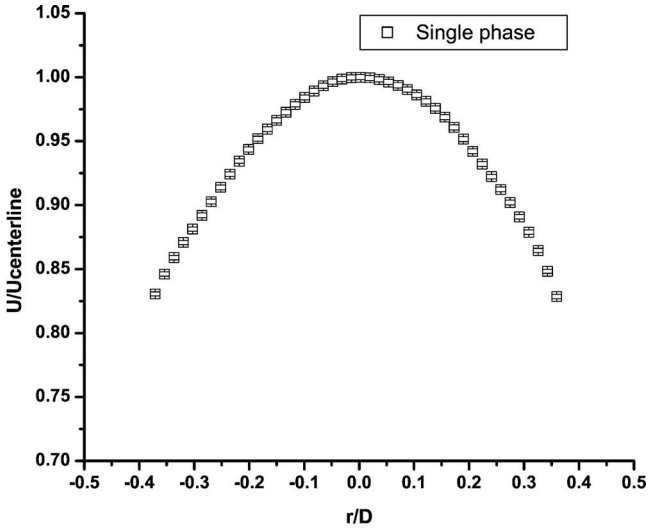

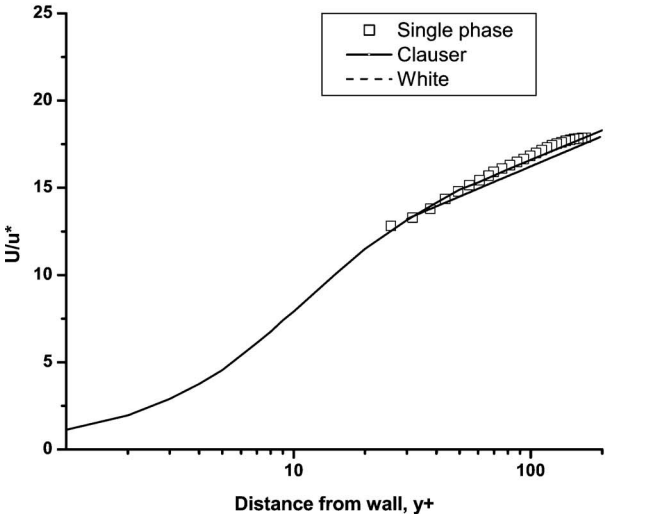

Fig. 2 (Top) Normalized mean axial velocity distribution across the tube diameter. Uncertainty bars due to particle displacement resolution are small relative to the size of the data symbol. (Bottom) Mean axial velocity distribution normalized with inner variables (U/u^* and $y+=yu^*/\nu$) and plotted with the Clauser profile and White profile.

spheres with a mean diameter of 89 μm into the flow loop, resulting in a solid volume concentration of approximately 0.001. This concentration was sufficient to ensure a coupling of the fluid phase and solid phase but was small enough to minimize particle-to-particle interactions [16]. Details of the solid particles and the process conditions studied for the two-phase flow are presented in Table 2.

The pipe Reynolds number for the two-phase flow was very close to that of the single-phase flow, differing by only 1.6%.

Table 2 Process conditions and particle details associated with two-phase pipe flow

Reynolds number (based on diameter)	4680
Bulk velocity	0.15 m/s
Water temperature	25.5°C
Specific gravity of glass sphere	2.6
Mean particle size	89 μm
D_{90} particle size	139 μm
D_{10} particle size	52 μm

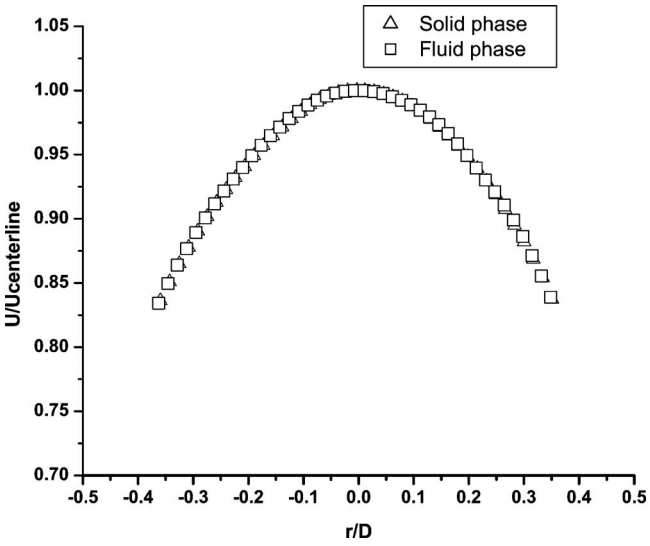

Fig. 3 Normalized mean axial velocity distribution of two-phase flow across the tube diameter

Therefore, the variations in mean and fluctuating velocity components between the single-phase and two-phase conditions were essentially due to the loading of the glass spheres. The normalized mean axial velocity profiles of the fluid phase and solid phase across the tube are presented in Fig. 3 and show a profile that is similar for both phases. The volumetric solid loading is relatively light and therefore, as shown in Fig. 4, the velocity distributions of the two-phase flow and single-phase flow conditions are similar.

The fluid phase axial turbulence intensity (u') and radial turbulence intensity (v') as a function of normalized viscous units from the tube wall and normalized with the friction velocity are shown in Fig. 5. The plot indicates that the two-phase turbulence intensities have similar distributions in form when compared with the single-phase turbulence intensities. However, there are variations in their respective values. For both the axial and radial turbulence intensities, two-phase flow values are less than corresponding single-phase flow values across the tube radius. As stated previously, the difference in pipe Reynolds number of the two-phase

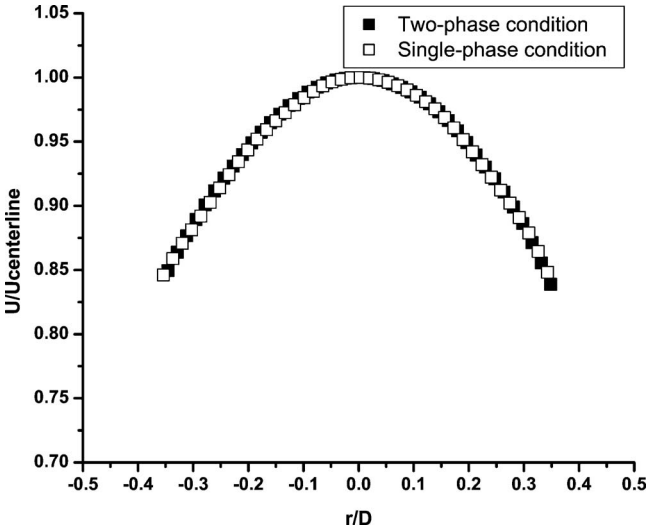

Fig. 4 Comparison of single-phase and two-phase mean axial velocity distributions of the fluid phase across the tube diameter

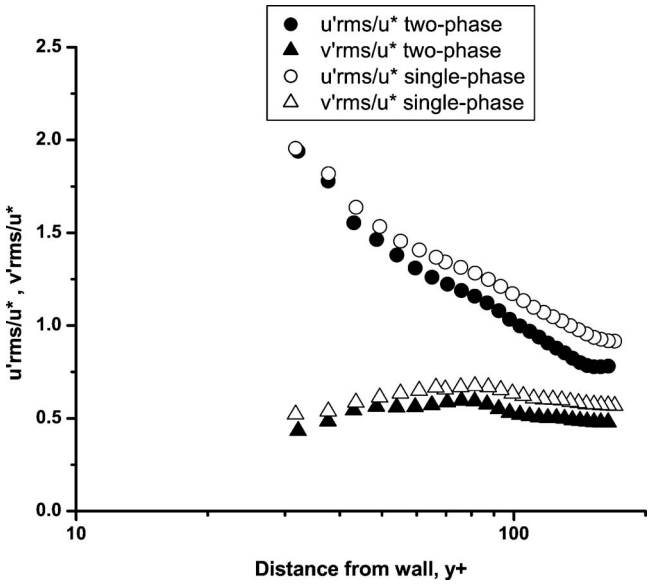

Fig. 5 Comparison of normalized axial (u'_{rms}) and radial (v'_{rms}) turbulence intensities of the fluid phase for single-phase flow and two-phase flow. Data points include from the wall to the tube centerline.

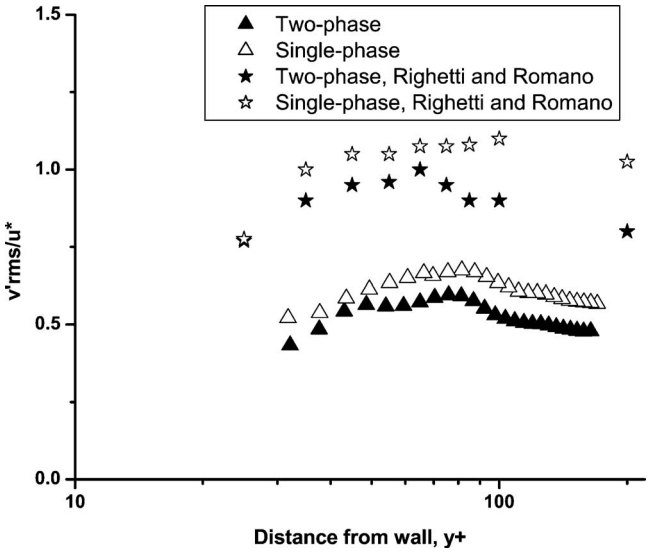

Fig. 7 Comparison of the normalized radial turbulence intensity distribution of the fluid phase with Righetti and Romano [3]. Data points include from the wall to the tube centerline.

flow condition and single-phase flow condition was only 1.6%. In general, the slightly greater Reynolds number of the two-phase flow would tend to result in greater turbulence intensity values [17]. The fact that the turbulence intensity is reduced for two-phase flow would then be explained by the presence of the solid phase, indicating that this particular solid phase regime at the specific volume concentration tends to suppress turbulence. This has been observed in a number of investigations at similar conditions, including those by Righetti and Romano [3]. Figure 6 is a plot of the axial turbulence intensity for the present work and Righetti and Romano's PDA results; both experiments used a similar solid phase material and concentration in a water carrier phase. The data points attributed to Righetti and Romano [3] were visually resolved from their reference. Although their higher system Reynolds number based on channel width of 60,000 is greater than that of the present work, as mentioned above the most significant difference in the results would tend to be a greater magnitude in turbulence intensity of the higher Reynolds number flow [17]. This is found to be the case when comparing the two experiments; magnitude values are greater but similar trends exist. For example, the single-phase turbulence intensity is greater than the two-phase condition in both cases with there being a similar overlap in the region of $25 < y^+ < 45$ for both experiments. Likewise, the radial turbulence intensity is reduced for the two-phase flow conditions of both experiments, as shown in Fig. 7.

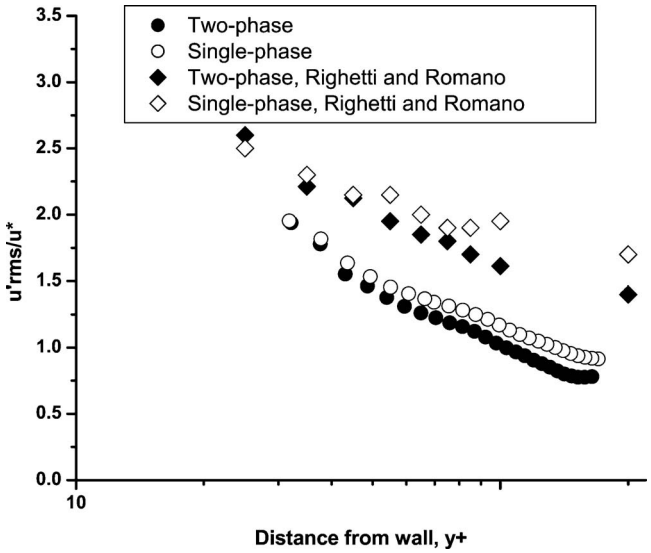

Fig. 6 Comparison of the normalized axial turbulence intensity distribution of the fluid phase with Righetti and Romano [3]. Data points include from the wall to the tube centerline.

3.2 Acceleration Statistics. In the previous section, the distributions of kinematic parameters associated with the fluid phase and solid phase, which serve to characterize the particular flow, were calculated and analyzed. It was natural to extend this form of analysis to dynamic parameters, such as the temporal acceleration associated with each phase. This was accomplished by calculating second and third moment statistics of the fluid and solid phase accelerations that were measured simultaneously by the two-color DPIV/digital particle image accelerometry (DPIA) technique. The acceleration data presented below were found by analyzing over 1000 images. From the resulting calculated flow fields, acceleration values were averaged for each radial location. Based on the pixel displacement resolution of the DPIA algorithm, the acceleration uncertainty was found to be 0.8 m/s^2.

Figures 8 and 9 show histograms of the fluid phase and solid phase axial acceleration values for two interrogation zones located across the tube radius. The histograms of both phases are also overlapped in the figures. As mentioned in the literature [18–20], the particle acceleration probability distribution is non-Gaussian with a significant number of counts closely centered near the mean and with only a small percentage found far from the mean. As an example, the number of counts greater than 15 m/s^2 at a radial location near the wall is approximately 8% of the total for the solid phase and 3% of the total for the fluid phase. It is also observed that the solid phase histograms tend to show an excess of acceleration counts near the tails. The excess is small, representing approximately an increase of 50 counts out of a total of 14,000, and has a minor effect on the statistics. In general, the shape of the histogram reflects the behavior of the different sized particles, which are individually influenced by flow field turbulence structures over the course of the data collection. Overall, it is observed from the histograms of the two phases that the acceleration is statistically zero. This is to be expected, as the particle

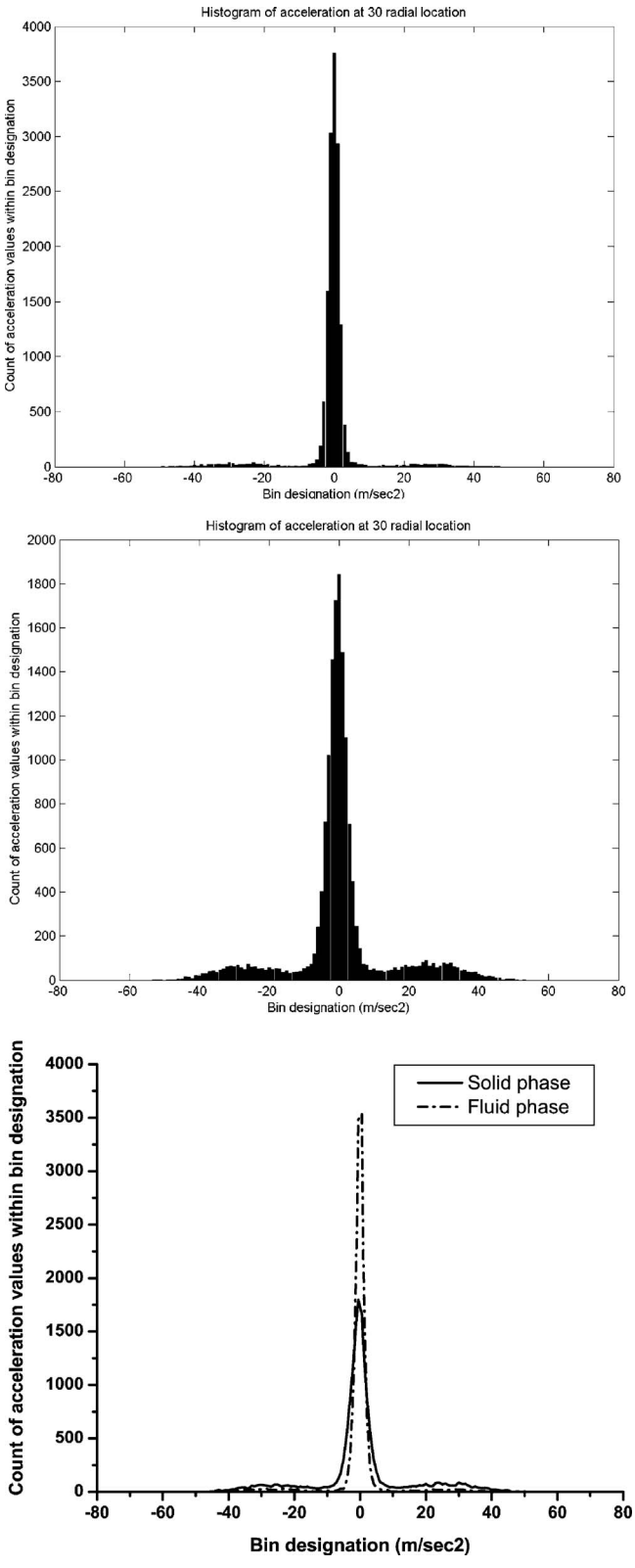

Fig. 8 Histogram of axial acceleration at $r/D=0.09$. Fluid phase (top) and solid phase (middle) and overlapping distributions of both phases (bottom).

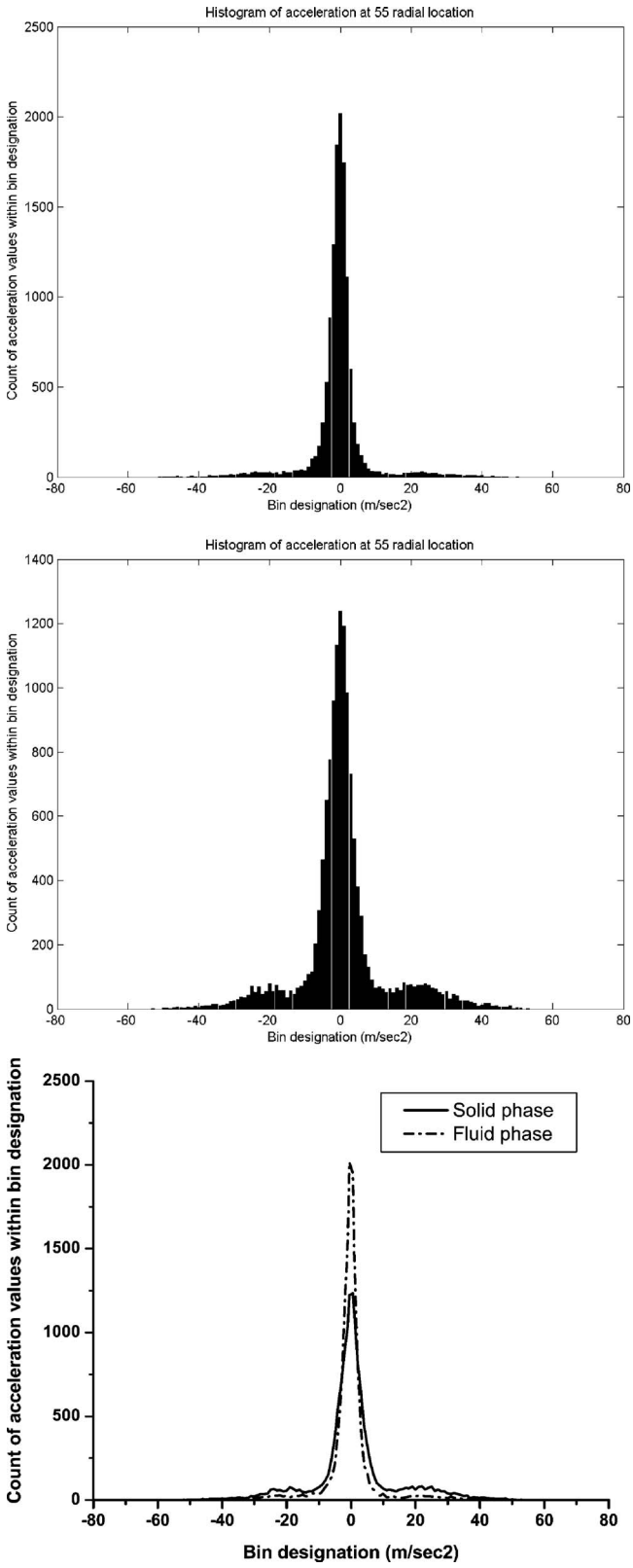

Fig. 9 Histogram of axial acceleration at $r/D=0.4$. Fluid phase (top) and solid phase (middle) and overlapping distributions of both phases (bottom).

relaxation time of 0.001 s is much shorter than the 7 s transit time between the tube entrance and test section location, the solid phase having reached equilibrium with the fluid within this time period [21].

In a statistical sense, the mean, or first moment of acceleration, confirmed expectations but did not offer more information. Higher order central moments were then calculated to provide additional insight into the solid phase and fluid phase acceleration fields.

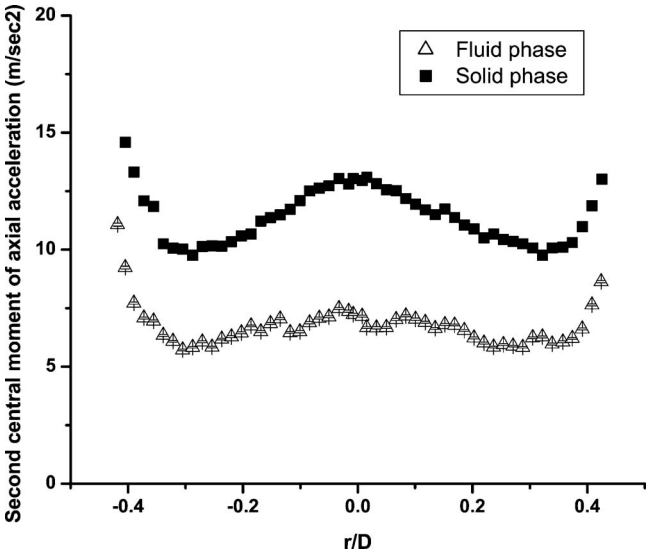

Fig. 10 Profiles of the second central moment of the fluid phase and solid phase axial acceleration probability distributions. Estimated uncertainty bars are small relative to the size of the data symbol.

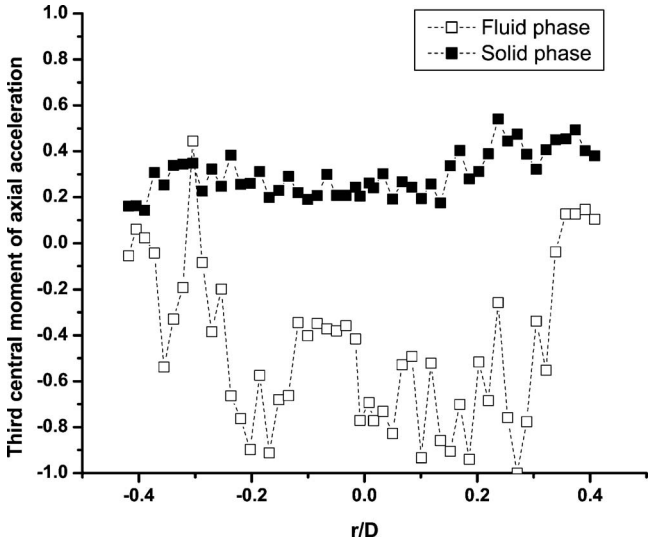

Fig. 11 Profiles of the third central moment of the fluid phase and solid phase axial acceleration probability distributions

One such calculation follows from the differences in the widths of the histograms (Figs. 8 and 9) between the two phases where it is readily observed that the solid phase has a wider histogram, indicating a wider range of acceleration values near the mean. The second central moment (i.e., rms), which quantifies this characteristic of the histogram, was calculated for both phases across the tube, as shown in Fig. 10. It is observed that the acceleration rms of the solid phase is consistently greater in magnitude than that of the fluid phase and indicates the effect of the particle's inertia. As discussed by Crowe et al. [22], the glass particle, with a higher inertia than the tracer particle, can move beyond the local influence of turbulent structures and fall under the influence of neighboring eddies; Righetti and Romano [3] described this effect as a "dynamic connection." In the Righetti and Romano channel study, it was found that the glass sphere solid phase had greater rms velocities than the corresponding fluid tracer particles due to the quasisteady burst and sweep events associated with near-wall turbulence structures that transfer momentum between the phases. Specifically, the intense ("high velocity") fluctuations associated with the burst event were maintained by the relatively high inertia solid particle as it moved to its new location, hence the dynamic connection of a particle's motion from one local region to another [3]. This effect is also manifested by the larger second central moment of acceleration. Another observation of Fig. 10 is the shape of the fluid phase and solid phase profiles, which show symmetric variations across the tube radius with a fairly abrupt increase near the walls. This increase in the second central moment near the wall at r/D of approximately 0.4 occurs where vortices are centered ($y+ \sim 30$) [4] and where the vortical structures have their strongest influences in transporting the particles through the burst and sweep events, thereby resulting in greater second central moment values.

The analysis was extended to the third central moment statistic, which describes the symmetry of a probability distribution. Specifically, a positive third central moment is an indication that the distribution is weighted to the positive side whereas a negative value is an indication that the distribution is weighted to the negative side. It is recognized that values of the third central moment, and all higher order moments, are sensitive to the data points near the tails of the distribution [23]. Therefore, the critical observation presented herein is the difference in the nature of the fluid and solid phase profiles. These differences are shown in Fig. 11, which plots the variations of the fluid phase and solid phase third central moments of acceleration across the tube diameter; each data point is the third central moment of an acceleration histogram at a particular radial location. Beyond the differences in values, it is observed that the fluid phase profile has an oscillatory-type shape with large, changing values relative to the solid phase profile, which has a small variation across the tube. The details of the experimental technique (cameras, DPIV methodology, etc.) are the same for measuring each phase; therefore, the differences can be explained by the effect that fluid structures have on each particle type. The fluid phase tracer particles have such low inertia that they follow the influence of the local structure [24]. The fluid phase results, therefore, more accurately reflect the conditions associated with the fluid structures such that the oscillating nature of the fluid phase plot would indicate the varying behavior of eddies across the tube. Likewise, the trend of the fluid phase profile to be symmetric tends to indicate the axisymmetric influence of the turbulence structures. The sharp change in magnitude near the wall of the fluid phase profile reveals the abruptness of the vortical fluid structures in that region. This effect is similar to that observed with the second central moment statistic; both statistics show increases in magnitude where vortical structures are located and where their influence is greatest [3,5].

4 Conclusion

An experimental investigation of a two-phase pipe flow was undertaken to study kinematic and dynamic parameters of the fluid and solid phases. This was performed by recording simultaneous, two-color, DPIV/DPIA data of a water carrier phase and dilute glass sphere solid phase in a vertically upward pipe flow. The simultaneous, two-color DPIV/DPIA measurements provided flow field information on the characteristics of two-phase kinematic and dynamic quantities. For the flow and loading condition studied, turbulence suppression due to the presence of the solid phase was observed. Statistical parameters of fluid phase and solid phase acceleration were then calculated to characterize the particular two-phase flow. The profiles of the second central moment of acceleration indicated a higher value for the solid phase than the fluid phase; both phases had increased values near the wall. The profiles of the third central moment of acceleration indicated an oscillatory-type distribution of fluid phase acceleration data across the tube compared to the relatively flat solid phase profile. The differences in second and third central moment profiles between the two phases were attributed to the inertia of each particle

type and its response to turbulence structures. Further studies at different flow and loading conditions would show the extent of differences that can occur in characterizing two-phase flows using acceleration statistics and provide some insight into dynamic related fluid-particle interactions.

References

[1] Tsuji, Y., Morikawa, Y., and Shiomi, H., 1984, "LDV Measurements of an Air-Solid Two-Phase Flow in a Vertical Pipe," J. Fluid Mech., **139**, pp. 417–434.

[2] Kulick, J. D., Fessler, J. R., and Eaton, J. K., 1994, "Particle Response and Turbulence Modification in Fully Developed Channel Flow," J. Fluid Mech., **277**, pp. 109–134.

[3] Righetti, M., and Romano, G. P., 2004, "Particle-Fluid Interactions in a Plane Near-Wall Turbulent Flow," J. Fluid Mech., **505**, pp. 93–121.

[4] Robinson, S. K., 1991, "The Kinematics of Turbulent Boundary Layer Structure," Report No. NASA TM-103859, NASA Langley Research Center, Hampton, VA.

[5] Marchioli, C., and Soldati, A., 2002, "Mechanisms for Particle Transfer and Segregation in a Turbulent Boundary Layer," J. Fluid Mech., **468**, pp. 283–315.

[6] Dong, P., 2002, "Phase Averaged Transport in the Vortex-Induced Oscillation of a Cylinder: Experiment and Modeling," Ph.D. thesis, Rutgers, The State University of New Jersey, Piscataway, NJ.

[7] Drew, D. A., 1983, "Mathematical Modeling of Two-Phase Flow," Annu. Rev. Fluid Mech., **15**, pp. 261–291.

[8] Clift, R., Grace, J. R., and Weber, M. E., 1978, *Bubbles, Drops, and Particles*, Academic, New York.

[9] Torobin, L. B., and Gauvin, W. H., 1959, "Fundamental Aspects of Solids-Gas Flow Part III: Accelerated Motion of a Particle in a Fluid," Can. J. Chem. Eng., **37**, pp. 224–236.

[10] Borowsky, J., 2005, "An Experimental Investigation of Liquid-Solid Two-Phase Pipe Flow by Simultaneous Two Color Digital Particle Image Velocimetry/Accelerometry," Ph.D. thesis, Rutgers, The State University of New Jersey, Piscataway, NJ.

[11] Borowsky, J., and Wei, T., 2006, "Simultaneous Velocimetry/Accelerometry Measurements in a Turbulent Two-Phase Pipe Flow," Exp. Fluids, **41**, pp. 13–20.

[12] Tokuhiro, A., Maekawa, M., Iizuka, K., Hishida, K., and Maeda, M., 1998, "Turbulent Flow Past a Bubble and an Ellipsoid Using Shadow-Image and PIV Techniques," Int. J. Multiphase Flow, **24**, pp. 1383–1406.

[13] Hsu, T. Y., Grega, L. M., Leighton, R. I., and Wei, T., 2000, "Turbulent Kinetic Energy Transport in a Corner Formed by a Solid Wall and a Free Surface," J. Fluid Mech., **410**, pp. 343–366.

[14] Clauser, F. H., 1956, "The Turbulent Boundary Layer," Adv. Appl. Mech., **4**, pp. 1–51.

[15] White, F., 1974, *Viscous Fluid Flow*, McGraw-Hill, New York.

[16] Elghobashi, S., 1994, "On Predicting Particle-Laden Turbulent Flows," Appl. Sci. Res., **52**, pp. 309–329.

[17] Wei, T., and Willmarth, W. W., 1989, "Reynolds-Number Effects on the Structure of a Turbulent Channel Flow," J. Fluid Mech., **204**, pp. 57–95.

[18] La Porta, A., Voth, G. A., Crawford, A. M., Alexander, J., and Bodenschatz, E., 2001, "Fluid Particle Accelerations in Fully Developed Turbulence," Nature (London), **409**, pp. 1017–1019.

[19] Sawford, B. L., Yeung, P. K., Borgas, M. S., Vedula, P., La Porta, A., Crawford, A. M., and Bodenschatz, E., 2003, "Conditional and Unconditional Acceleration Statistics in Turbulence," Phys. Fluids, **15**, pp. 3478–3489.

[20] Mordant, M., Crawford, A. M., and Bodenschatz, E., 2004, "Experimental Lagrangian Acceleration Probability Density Function Measurement," Physica D, **193**, pp. 245–251.

[21] Suzuki, Y., Ikenoya, M., and Kasagi, N., 2000, "Simultaneous Measurement of Fluid and Dispersed Phases in a Particle-Laden Turbulent Channel Flow With the Aid of 3-D PTV," Exp. Fluids, **29**, pp. S185–S193.

[22] Crowe, C., Chung, J. N., and Troutt, T. R., 1993, "Particle Dispersion by Organized Turbulent Structures," in *Particulate Two-Phase Flow*, Rocco, M. C., ed., Butterworth-Heinemann, Boston, pp. 626–669.

[23] Heinz, O., Ilyushin, B., and Markovich, D., 2004, "Application of a PDF Method for the Statistical Processing of Experimental Data," Int. J. Heat Fluid Flow, **25**, pp. 864–874.

[24] Hestroni, G., 1989, "Particles-Turbulence Interaction," Int. J. Multiphase Flow, **15**, pp. 735–746.

Takayuki Suzuki[1]
e-mail: taka8170@me.es.osaka-u.ac.jp

Romain Prunières

Hironori Horiguchi

Department of Mechanical Science and Bioengineering,
Graduate School of Engineering Science,
Osaka University,
1-3 Machikaneyama, Toyonaka,
Osaka 560-8531, Japan

Tomonori Tsukiya

Yoshiyuki Taenaka

Department of Artificial Organs,
National Cardiovascular Center of Japan,
5-7-1 Fujishiro-dai, Suita,
Osaka 565-8565, Japan

Yoshinobu Tsujimoto
Department of Mechanical Science and Bioengineering,
Graduate School of Engineering Science,
Osaka University,
1-3 Machikaneyama, Toyonaka,
Osaka 560-8531, Japan

Measurements of Rotordynamic Forces on an Artificial Heart Pump Impeller

In centrifugal pumps for artificial hearts, a magnetic drive with lightly loaded journal bearing system is often used. In such a system, the rigidity of the bearing is small and the impeller usually rotates over the critical speed. In such cases, the rotordynamic fluid forces play an important role for shaft vibration. In the present study, the characteristics of the rotordynamic fluid forces on the impeller were examined. The rotordynamic fluid forces were measured in the cases with/without the whirling motion. It was found that the rotordynamic forces become destabilizing in a wide range of positive whirl. The effect of leakage flow was also examined. [DOI: 10.1115/1.2786477]

Introduction

In centrifugal pumps for artificial hearts, a journal bearing with a large clearance or a magnetic bearing is often used to avoid a hemolysis due to the shear stress around the bearing. The rigidity of bearings is usually small and in many cases, the pumps are operated over the critical speed. In such cases, rotordynamic fluid forces on the impeller that arise in response to shaft vibration may cause self-excited shaft vibration. Therefore, we need to evaluate the forces to provide sufficient damping to the bearing system.

In a centrifugal blood pump NCVC-2 developed by National Cardiovascular Center in Japan, a magnetic drive with lightly loaded journal bearing system is used. However, the impeller exhibits a whirling motion and bearing rub occurs under certain operating condition [1]. In centrifugal blood pumps driven by a magnetic drive with lightly loaded magnetic or journal bearings, impeller behavior is common concern. Reference [2] examined the response of the rotor to the excitation on the housing and to the pulsating flow rate. Reference [3] discussed about the methods for the measurements of the rotor displacement. To avoid excessive shaft vibration, it is necessary to clarify the characteristics of the rotordynamic forces on the impeller under whirling motion.

For industrial pumps, the forces on whirling centrifugal impellers are basically stabilizing [4] except at low flow rate. However, the forces can become destabilizing due to the interaction with a volute casing or vaned diffuser [5,6]. For closed-type impellers, the clearance flow through a narrow gap between the front shroud and the casing can cause instability [7–9]. For open-type impellers, pressure forces on the hub cause instability while the tip leakage flow provides damping [10,11].

The design of blood pumps is significantly different from industrial pumps in the following aspects. First, blood pumps have a large tip clearance to avoid the damage on blood cells. Second, larger blade angle is used to obtain needed head rise at lower speed. This may cause flow separation at the inlet. Tight casings are used to match higher head at lower flow rate. From these large differences in design, it is difficult to evaluate the rotordynamic forces from available data on industrial pumps.

In the present study, the rotordynamic forces on NCVC-2 impeller under the whirling motion are investigated. To secure the accuracy, the measurements are made on a scaled up model of NCVC-2 with a factor of 7.5, which is chosen to match an existing facility for rotordynamic force measurement.

Experimental Facilities

Figure 1 shows the schematic of the experimental facility. The impeller is driven by a main motor (No. 1 in Fig. 1) and the whirling motion is generated by rotating the eccentric sleeve (No. 9) by a servo motor (No. 5). The working fluid is water and it flows through the inlet pipe (No. 13), the impeller (No. 10), the casing (No. 11), the outlet pipe (No. 12), and returns to the tank (No. 14). The blood is a non-Newtonian fluid but the viscosity of blood is almost constant when the shearing velocity is larger than about 100 s^{-1}. The shear velocity of NCVC-2calculated from the tip speed (4.19 m/s) and tip clearance (2 mm) is about 2000 s^{-1} and it is expected that we can use water as the working fluid [12].

Figure 2 shows the cross section of the sleeve to generate the whirling motion. The eccentricity of ε is given to the inner bear-

[1]Corresponding author.

Contributed by the Fluids Engineering Division of ASME for publication in the JOURNAL OF FLUIDS ENGINEERING. Manuscript received November 15, 2006; final manuscript received June 13, 2007. Review conducted by Chunill Hah.

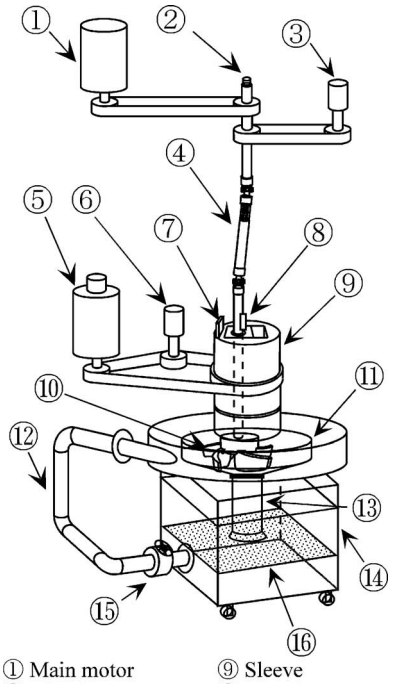

Fig. 1 Experimental facility

ing (No. 5 in Fig. 2) supporting the main shaft (No. 1), relative to the outer bearing (No. 4) supported by a stationary frame. The whirling motion is given by rotating the sleeve system by a servo motor (No. 5 in Fig. 1). In the present study, the angular velocity of impeller Ω was fixed to 41.9 rad/s (400 rpm) and the eccentricity ε was set to 1.08 mm. The ratio of the whirling angular velocity ω to the angular velocity of impeller Ω, which is called as the whirl speed ratio ω/Ω, was varied over the range from −1.2 to +1.2. The geometries of the impeller and casing are shown in Fig. 3. The specification of the impeller is shown in Table 1. The clearance c between the blade and the casing is 15 mm (c/D =0.05) all around the blade to avoid the hemolysis in real pump. On the sidewalls, the clearance is more than one order larger than industrial pumps and causes huge amount of leakage flow. On the other hand, the clearance between the outer radius of the impeller and the casing is extremely smaller than industrial pumps. This may cause instability due to the interaction with casing. The impeller and the casing are made of aluminum and stainless steel, respectively, and no deformation is expected during the experiment.

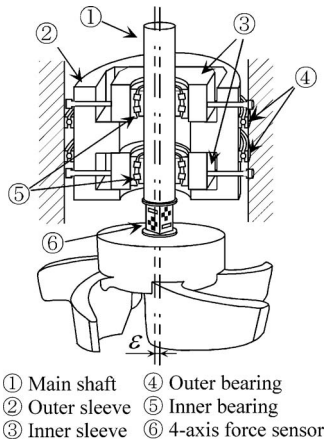

Fig. 2 Cross section of the sleeve

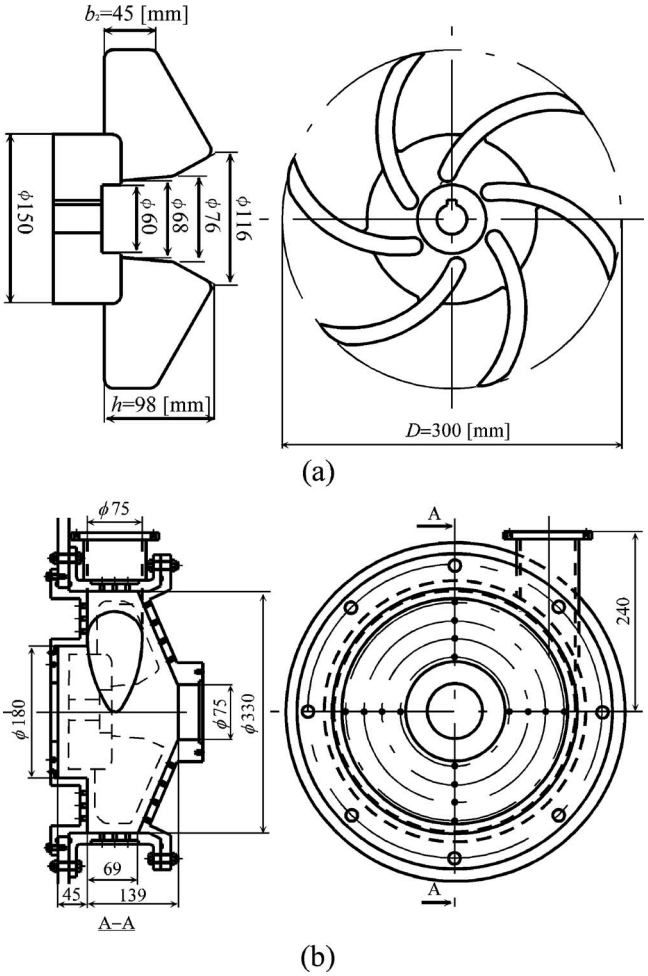

Fig. 3 Impeller and casing geometry: (*a*) impeller and (*b*) casing

The effect of the leakage flow through the seal was also examined by generating the leakage flow from the back side of the impeller. Figure 4 shows the schematic of the flow path of the leakage flow. The leakage flow was taken out through two holes on the shaft cover and the leakage flow rate Q_L was measured by a flow meter.

The forces on the impeller were measured by a four-axis force sensor (No. 6 in Fig. 2). The force sensor is composed of the two couples of parallel plates with four strain gauges on each plate. The output signals **G** of the strain gauges are converted to the

Table 1 Specification of the impeller

Diameter D (mm)	300
Outlet blade width b_2 (mm)	45
Maximum blade height h (mm)	98
Blade configuration	2D
Blade number	6
Inlet blade angle (deg)	60
Outlet blade angle (deg)	37
Tip clearance (mm)	15
Reynolds number	1.88×10^6

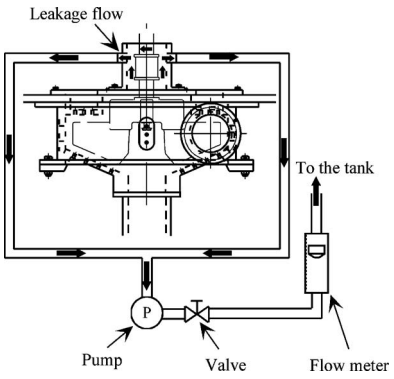

Fig. 4 Leakage flow system

force vector $\mathbf{F}_{x,y}=\{F_x,F_y\}$ in a frame (x,y) fixed to the impeller by using a 2×2 transfer matrix $[\mathbf{A}]$ (i.e., $\mathbf{F}_{x,y}=[\mathbf{A}]\mathbf{G}$), which is obtained by dynamic calibration tests. Output signals $\mathbf{G}$ are ensemble averaged over 32 whirls based on a triggering signal and then the whirl frequency component is evaluated by Fourier series expansion.

Figure 5 shows the coordinate system in a plane perpendicular to the shaft located at the center of gravity of fluids surrounded by the outer surface of the impeller. The coordinate (x,y) is fixed to the rotating and whirling impeller. The coordinate (n,t) is fixed to the whirling motion; the axis n is normal to the circular whirling orbit and in the direction of eccentricity ε. The axis t is tangential to the whirling orbit and is positive in the direction of whirl with $\omega>0$.

The force vector $\mathbf{F}_{x,y}$ in the rotating frame is represented with the components in n and t directions; $\mathbf{F}_{n,t}=\{F_n,F_t\}$. $\mathbf{F}_{n,t}$ is not steady due to the asymmetry of the casing and averaged values over the whirling motion are obtained as mentioned before. If the tangential force F_t is in the direction of the whirl $(F_t\cdot\omega>0)$, it promotes the whirling motion (destabilizing) and vice versa. This is the reason why we use the coordinate (n,t).

The forces thus measured include fluid forces and inertia forces on the impeller. The inertia forces are evaluated from a test with the impeller in air. Fluid forces are evaluated by subtracting the inertia forces and normalized as $(f_n,f_t)=(F_n,F_t)/(\rho\pi {r_2}^2b^2\varepsilon\omega^2)$.

Results and Discussions

Pressure Performance. Figure 6 shows the performance curve. The static pressure coefficient ψ is determined from the inlet static pressure p_1 measured at five inlet pipe diameters upstream from the inlet flange and the outlet pressure p_2 at 6.5 diameters from the outlet flange. The performance of original NCVC-2 is also shown

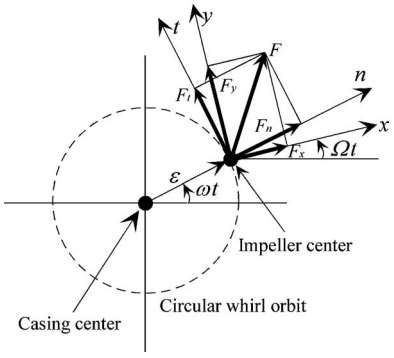

Fig. 5 Coordinate system. F_n and F_t are the normal and tangential components to the whirl orbit. (ε, eccentricity, Ω, shaft rotational speed, ω, whirling speed, (x,y), rotating frame of the shaft, and (n,t), normal and tangential to the whirl orbit.)

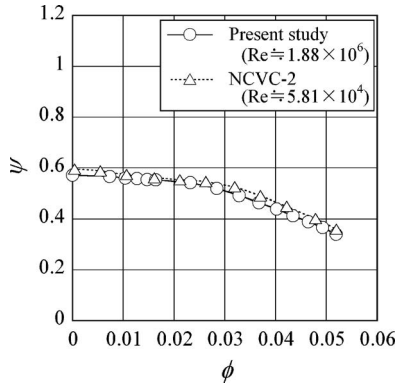

Fig. 6 Pressure performance of the test impeller ($\varepsilon=0$, $\omega/\Omega=0$) and pressure coefficient ψ versus flow coefficient ϕ

in Fig. 6. The Reynolds number in the present study $\mathrm{Re}\fallingdotseq1.88\times10^6$ is significantly larger than that of the original NCVC-2 test, $\mathrm{Re}\fallingdotseq5.81\times10^4$ using a mixture of glycerin and normal saline with the same viscosity (0.00317 Pa s) as blood. The size and speed in the present study are determined to maximize the accuracy of the force measurement. The Reynolds number effect on the rotordynamic forces should be clarified in future study. However, the similar performance curve obtained is encouraging since it may suggest the usefulness of the rotordynamic forces measured in the present experiment.

Fluid Forces. Figure 7 shows the dimensionless (f_n,f_t) and dimensional (F_n,F_t) normal and tangential fluid forces at various flow coefficients. For all flow rates, f_t is positive in the region $0<\omega/\Omega<0.7-0.8$ and promotes positive whirl. The magnitude of f_t decreases as the value of ω/Ω increases. In other regions of ω/Ω, the tangential force is opposite to the whirling motion and has an effect to stabilize the whirl. Although the magnitude of the forces changes, the functional forms of $f_n(\omega/\Omega)$ and $f_t(\omega/\Omega)$ are similar for all flow rates. It is also interesting that the forces are largely independent of the flow coefficient in larger whirl speed ratios, $|\omega/\Omega|>0.5$, where the whirl angular velocity ω is closer to the impeller angular velocity Ω. Around $\omega/\Omega=-0.1$, f_t exhibits a maximum while f_n changes largely. This can be observed for all flow rates although the changes are larger at smaller flow rates.

We now discuss about the results by comparing them with those on an open-type centrifugal impeller with the type number 1.3 [10] of conventional compressor design. It was tested in a vaneless diffuser with the radius ratio 1.6. Even with the large difference of design, the magnitude and general tendencies are similar. A destabilizing region $f_t>0$ can be found in both cases although the region is slightly larger for the present case. For the conventional design [10], it was found by theoretical analysis [11] that the destabilizing region is caused by the forces on the hub. In the present case, the impeller does not have a hub but the clearance between the impeller outer radius and the casing is very small. So, the destabilizing region is caused by the strong interaction with the casing as shown in Refs. [7,8] for industrial design impellers. With the conventional open impeller [10], a larger change in the forces similar to those observed in Fig. 7 around $\omega/\Omega=-0.1$ was found at $\omega/\Omega=0.8$ only around a flow rate where a dip in the performance curve was found. It was associated with a pressure pattern rotating with $\omega/\Omega=0.79$ at the inlet with an inlet backflow. In the present study, the pressure fluctuation was examined at all pressure taps shown in Fig. 10. But, no significant component other than whirl and blade passing components was found. In addition, the large change is found at all flow rates and no dip of the performance curve is found in the present case. So, the large change around $\omega/\Omega=-0.1$ is not associated with the inlet flow recirculation for the present case and the reason is not known yet. As discussed above, the flow mechanism causing the rotordy-

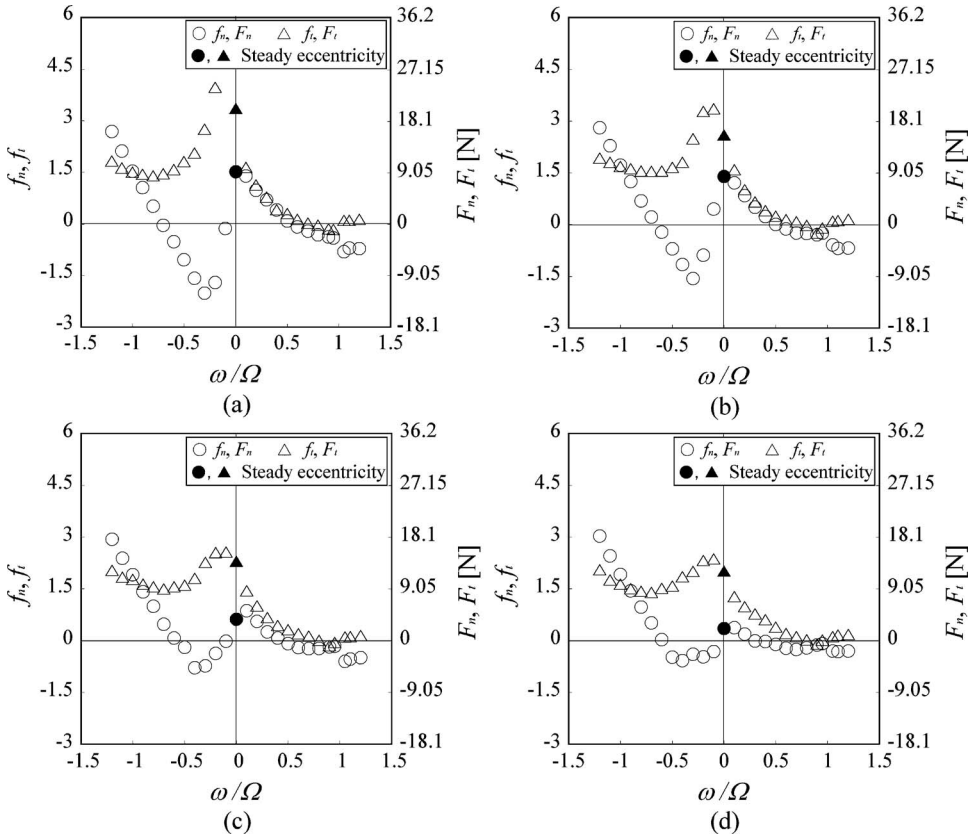

Fig. 7 Dimensionless normal and tangential fluid forces f_n, f_t, the dimensional fluid forces F_n, F_t, and steady eccentricity value on the impeller versus whirl speed ratio ω/Ω at various flow coefficients ϕ (ε=1.08 mm): (*a*) ϕ=0.01, (*b*) ϕ=0.02, (*c*) ϕ=0.03, and (*d*) ϕ=0.04

namic forces is quite different from that of conventional design impellers, although the magnitude and the character are similar.

Radial Forces. The casing geometry is asymmetric with one discharge pipe. Therefore, a steady radial force on the impeller occurs due to the nonaxisymmetric flow caused by the discharge flow. In the rotordynamic force measurement system, the quasisteady forces at $\omega/\Omega=0$ could not be obtained since the data acquisition system was triggered by the whirling motion. In order to determine the steady radial forces and quasisteady rotordynamic forces, force measurements were carried out with the center of the impeller fixed at eight eccentric locations with the circumferential interval of 45 deg. The steady radial forces for the case with $\varepsilon=0$ were estimated by averaging the values at eight eccentric locations.

Figure 8 shows the magnitudes and directions of the radial forces $F_{x'}$, $F_{y'}$ at various flow coefficients, where (x',y') is a stationary frame. The radial forces are in the direction toward the outlet and the magnitude increases as the flow rate increases. In the NCVC-2, it has been observed that the center of the impeller moves toward the outlet as the flow rate increases. This agrees with the result shown in Ref. [13] and is known to be caused by the pressure distribution in the casing.

The quasisteady rotordynamic forces F_n and F_t at $\omega/\Omega=0$ were evaluated from the differences of $F_{x'}$ and $F_{y'}$ measured at eight eccentric locations. The results are shown in Fig. 7 by the symbols ●, ▲. The fluid forces at $\omega/\Omega=0$ are consistent with the unsteady fluid forces with $\omega/\Omega \fallingdotseq 0$. This confirms the validity of the rotordynamic force measurement system.

Estimation of Fluid Forces Due to Unsteady Pressure Distribution. The rotordynamic forces on the impeller can be decomposed into (i) pressure force on a control surface, (ii) momentum transfer across the surface, and (iii) rate of change of the momentum of the fluid within the control surface. The contribution of pressure force is evaluated from the pressure fluctuation on the casing. Figure 9 shows the location of pressure taps.

The circumferential locations are shown by the symbols A, B, C, and D and radial axial locations are shown by 1–7. For the calculation of the fluid forces, the blade contour is approximated by seven line segments (segments 1-2, 2-3,…, 5-6, 7-8) and the surfaces (surfaces I, II,…,VII), which are obtained by rotating these line segments around the axis of the impeller, as shown in Fig. 10. It is assumed that the pressures on these surfaces are the same as the pressure at the corresponding positions on the casing. The circumferential pressure distribution was obtained by linear

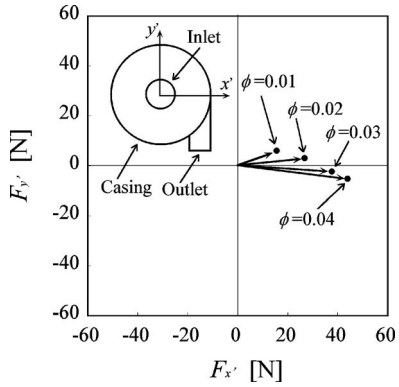

Fig. 8 Radial forces $F_{x'}$ and $F_{y'}$ on the impeller at various flow coefficients ϕ (ε=1.08 mm, ω/Ω=0)

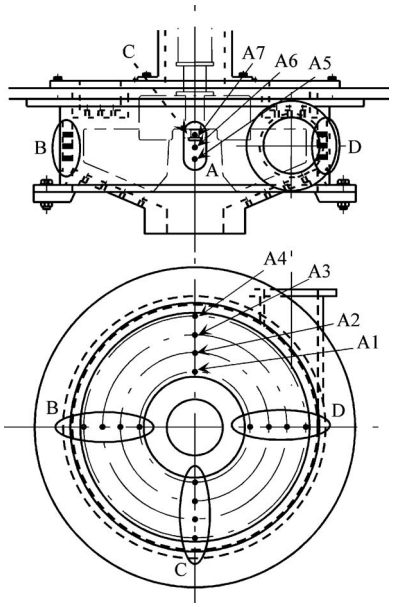

Fig. 9 Location of pressure measuring points on the casing

interpolation of the pressures measured at four circumferential locations. The fluid forces were calculated from the pressure obtained under the above assumptions and represented by f_n', f_t'.

Another force evaluation was made by assuming that the circumferential pressure distribution can be evaluated from the pressure fluctuation at B1, B2,…, B7 by simply considering the phase difference at other circumferential locations. The results are shown by f_n'' and f_t''.

Figure 11 shows the components of fluid forces f_n', f_t' and f_n'', f_t'' at the flow coefficient $\phi=0.02$ with f_n and f_t, which were measured by four-axis force sensor. Figures 11(a) and 11(b) show the normal and tangential components, respectively. The behaviors of f_n', f_n'' and f_t', f_t'' are similar to that of f_n and f_t although the magnitudes of f_n and f_t are much larger. This shows that the pressure force on the impeller can represent the character of the forces but other components are also important.

Effect of Leakage Flow. As shown in Fig. 12, NCVC-2 has a washout hole in the shaft to promote a leakage flow through the bearing clearance to avoid the generation of thrombus by stagnation of flow. The leakage flow enters the gap between the "impeller magnet" and "casing magnet" from behind the impeller and returns to the impeller inlet through the washout hole. This flow may affect the rotordynamic forces. To determine the effect of the leakage flow on the impeller forces, the leakage flow was intentionally produced, as shown in Fig. 4.

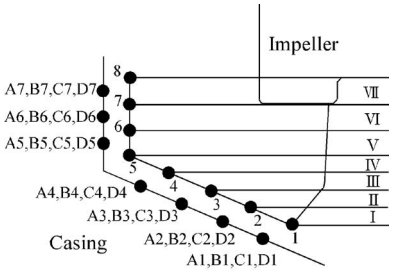

Fig. 10 Blade shape and corresponding pressure points on the blade

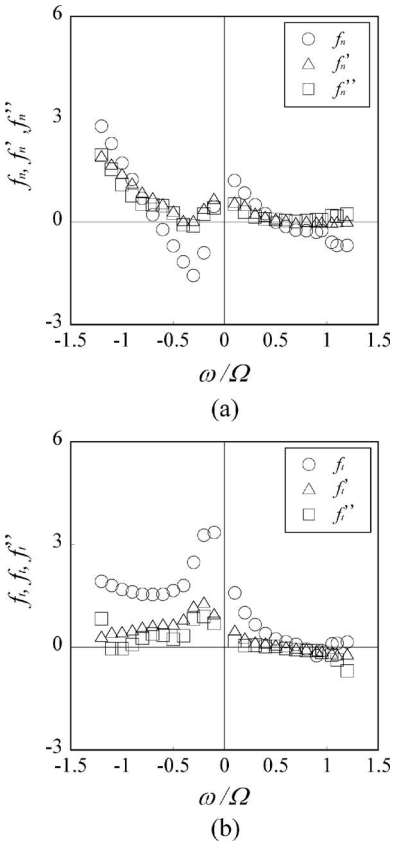

Fig. 11 Comparison of the dimensionless normal direct f_n, pressure f_n', f_n'' and tangential direct f_t, pressure f_t', f_t'' fluid forces with estimated forces from unsteady pressure at flow coefficient $\phi=0.02$ ($\varepsilon=1.08$ mm): (a) dimensionless normal fluid forces f_n, f_n', f_n'' and (b) dimensionless tangential fluid forces f_t, f_t', f_t''

Figures 13(a) and 13(b) show the dimensionless normal and tangential components f_n, f_t at the flow coefficient $\phi=0.02$ with the leakage flow. It is found that the values of f_n, f_t change only slightly even with a large quantity of leakage flow ratio $Q_L/Q=24.4\%$. The large change of the forces near $\omega/\Omega=-0.1$ occurs irrespective of the flow rate. This may suggest that the large change is not caused by the force on the cylindrical part supporting blades, as shown in Fig. 3.

Conclusions

The results of the present study can be summarized as follows.

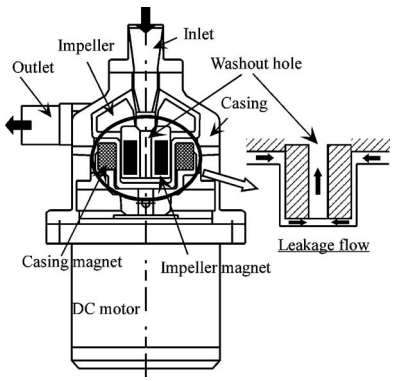

Fig. 12 Leakage flow in the NCVC-2

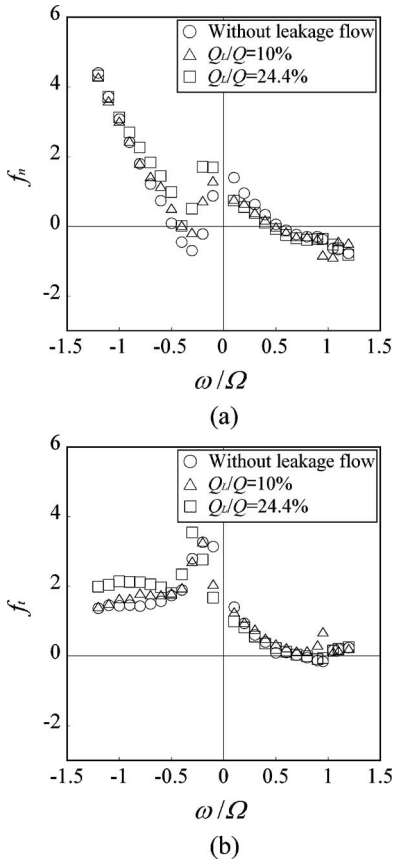

Fig. 13 Effect of the leakage flow at flow coefficient ϕ=0.02 (ε=1.08 mm): (*a*) dimensionless normal fluid forces f_n and (*b*) dimensionless tangential fluid forces f_t

(1) The rotordynamic forces encourage the forward motion in the region $0<\omega/\Omega<0.7-0.8$.
(2) The magnitude of rotordynamic forces becomes larger with the decrease of flow rate. The dependence on the whirl speed ratio is nearly the same for all flow rates.
(3) In the plot of the rotordynamic forces against the whirl speed ratio ω/Ω, the normal force f_n changes largely and the tangential force f_t becomes maximum around $\omega/\Omega=-0.1$. This behavior is found for all flow rates.
(4) The rotordynamic forces evaluated from the casing pressure fluctuations show similar dependence on the whirl speed ratio to the results of direct force measurement.
(5) The leakage flow from the back of the impeller has minor effect on the rotordynamic forces.

Acknowledgment

The authors would like to express their sincere gratitude to Dr. Yoshiki Yoshida of JAXA for setting up the facility.

Nomenclature

$[\mathbf{A}]$ = transfer matrix
b_2 = outlet blade width
c = clearance between blade and casing
D = diameter of impeller
g = acceleration of gravity
F = fluid force on impeller
$\mathbf{F}_{n,t}$ = force vector, F_n, F_t
$\mathbf{F}_{x,y}$ = force vector, F_x, F_y
f = dimensionless fluid force,$=F/(\rho\pi r_2{}^2 b^2 \varepsilon\omega^2)$
f', f'' = dimensionless fluid forces which were calculated from pressure distribution on casing
$\mathbf{G}$ = two-component vector which consists of signals from strain gauges
H = head
h = maximum blade height
M = fluid force moment
Q = volumetric flow
Q_L = volumetric flow of leakage flow
$p_{1,2}$ = inlet and outlet static pressure
Re = Reynolds number,$=u_2 D/\nu$
r_2 = radius of impeller
t = time
n, t = normal and tangential coordinate axes which rotate with whirling motion
u_2 = circumferential velocity of impeller at outlet, $=r_2\Omega$
x, y = coordinate axes which rotate with main shaft
x', y' = coordinate axes which are fixed on casing
ε = radius of the circular orbit (eccentricity)
ρ = fluid density
ν = dynamic viscosity
ϕ = flow coefficient, $=Q/(2\pi r_2 b_2 u_2)$
ψ = pressure coefficient, $=(p_2-p_1)/\rho u_2{}^2$
Ω = angular velocity of impeller
ω = angular velocity of whirling motion
ω/Ω = whirl speed ratio

Subscript

n, t = directions of the axes n, t
x, y = directions of the axes x, y
x', y' = directions of the axes x', y'

References

[1] Tsukiya, T., Taenaka, Y., Tsujimoto, Y., and Horiguchi, H., 2005, "Whirling Motion of the Impeller of a Centrifugal Pump as a Ventricular Assist Device," *Proceedings of the Third International Symposium on Stability Control of Rotating Machinery (ISCORMA-3)*, Cleveland, OH, pp. 1–8.
[2] Asama, J., Shinshi, T., Hoshi, S., Takatani, S., and Shimokohbe, A., 2007, "Dynamic Characteristics of a Magnetically Levitated Impeller in a Centrifugal Blood Pump," Artif. Organs, **31**(4), pp. 301–311.
[3] Chung, M. K. H., Zhang, N., Tansley, G. D., and Woodand, J. C., 2004, "Impeller Behavior and Displacement of the VentrAssist Implantable Rotary Blood Pump," Artif. Organs, **28**(3), pp. 287–297.
[4] Ohashi, H., and Shoji, H., 1987, "Lateral Fluid Forces on Whirling Centrifugal Impeller (2nd Report: Experiment in Vaneless Diffuser)," ASME J. Fluids Eng., **109**(2), pp. 100–106.
[5] Tsujimoto, Y., Acosta, A. J., and Brennen, C. E., 1988, "Theoretical Study of Fluid Forces on a Centrifugal Impeller Rotating and Whirling in a Volute," ASME J. Vib., Acoust., Stress, Reliab. Des., **110**, pp. 263–269.
[6] Tsujimoto, Y., Acosta, A. J., and Yoshida, Y., 1988, "A Theoretical Study of Fluid Forces on a Centrifugal Impeller Rotating and Whirling in a Vaned Diffuser," NASA Report No. CP 3026.
[7] Jery, B., Acosta, A. J., Brennen, C. E., and Caughey, T. K., 1985, "Forces on Centrifugal Pump Impellers," *Proceedings of the Second International Pump Symposium*, Houston, TX, pp. 21–32.
[8] Ohashi, H., Sakurai, A., and Nishihama, J., 1988, "Influence of Impeller and Diffuser Geometries on the Lateral Fluid Forces of Whirling Centrifugal Impeller," NASA Report No. CP 3026.
[9] Childs, D. W., 1989, "Fluid Structure Interaction Forces at Pump-Impeller-Shroud Surfaces for Rotordynamic Calculations," ASME J. Vib., Acoust., Stress, Reliab. Des., **111**, pp. 216–225.
[10] Ishii, N., Yoshida, Y., Tsujimoto, Y., Ohashi, H., and Kano, F., 1999, "The Rotordynamic Forces on Open-Type Centrifugal Compressor Impeller in Whirling Motion," ASME J. Fluids Eng., **121**(2), pp. 259–265.
[11] Hiwata, A., and Tsujimoto, Y., 2002, "Theoretical Analysis of Fluid Forces on an Open-Type Centrifugal Impeller in Whirling Motion," ASME J. Fluids Eng., **124**, pp. 342–347.
[12] Shu, C., 1970, "Shear Dependence of Effective Cell Volume as a Determinant of Blood Viscosity," Science, **168**(3934), pp. 977–979.
[13] Stepanoff, A. J., 1957, *Centrifugal and Axial Flow Pumps*, Wiley, New York.

Frequencies in the Vibration Induced by the Rotor Stator Interaction in a Centrifugal Pump Turbine

C. G. Rodriguez[1]
Department of Mechanical Engineering,
University of Concepcion,
Casilla 160-C,
Concepcion, Chile
e-mail: cristian.rodriguez@udec.cl

E. Egusquiza
Center of Industrial Diagnostics and Fluid Dynamics,
Technical University of Catalonia,
Avenida Diagonal 647,
08028 Barcelona, Spain
e-mail: egusquiza@mf.upc.edu

I. F. Santos
Department of Mechanical Engineering,
Technical University of Denmark,
DK-2800 Kongis Lyngby, Denmark
e-mail: ifs@mek.dtu.dk

The highest vibration levels in large pump turbines are, in general, originated in the rotor stator interaction (RSI). This vibration has specific characteristics that can be clearly observed in the frequency domain: harmonics of the moving blade passing frequency and a particular relationship among their amplitudes. It is valuable for the design and condition monitoring to count on these characteristics. A CFD model is an appropriate tool to determine the force and its characteristics. However, it is time consuming and needs highly qualified human resources while usually these results are needed immediately and in situ. Then, it is useful to determine these characteristics in a simple, quick, and accurate method. At present, the most suitable method indicates a large amount of possible harmonics to appear, without indicating the relative importance of them. This paper carries out a theoretical analysis to predict and explain in a qualitative way these frequencies and amplitudes. The theoretical analysis incorporates the number of blades, the number of guide vanes, the RSI nonuniform fluid force, and the sequence of interaction. This analysis is compared with the method currently in use, and both methods are applied to a practical case. The theoretical analysis gives a resulting force over the pump turbine, which corresponds well to the measured behavior of a pump turbine in terms of its frequencies and the relationship between their amplitudes. A corrective action is proposed as a result of the analysis and after it is carried out in one of the units, the vibration levels are reduced. The vibration induced by the RSI is predicted considering the sequence of interaction and different amplitudes in the interactions between the same moving blade and different stationary blades, giving a different and original interpretation about the source of the vibration characteristics. A successful corrective action is proposed as a consequence of this new interpretation. [DOI: 10.1115/1.2786489]

Keywords: rotor stator interaction (RSI), frequency content, pump turbine, vibration analysis

1 Introduction

The current trend of increasing the power concentration in large hydraulic pump turbines (over 75 MW) either for new power plants or during the upgrade of existing ones together with the trend of increasing the operating range to allow higher regulation capacities have lead to a rise in the pressure and fluid velocities, a reduction in the thickness of the impeller-runner, and extreme off-design operating conditions. As a consequence, the vibration levels have increased and the fatigue problems have become more common. Generally, in large pump turbines, the highest vibration levels are originated in the rotor stator interaction (RSI) (Ohura et al. [1], Tanaka [2], Egusquiza et al. [3,4], Egusquiza [5] Fisher et al. [6], and Mateos [7]). This vibration has specific characteristics that can be clearly observed in the frequency domain: harmonics of the moving blade passing frequency at a particular relationship among their amplitudes. This relationship depends on the design and the operation of the pump turbine. The amplitudes of these harmonics are significantly increased when the machine is operated under specific conditions. This rise in the amplitudes is not equal for all the harmonics and some are more affected than others (Mateos [7]). This rise is a consequence of the new requirements and trends. At present, this behavior limits the power output of new designs and conditions the operation of installed machines; for these reasons, it is important to identify which harmonics have significant amplitude and are prone to be increased and how to avoid them.

An important difficulty for designers is to avoid the harmonics with significant amplitudes to coincide with a natural frequency; this condition can produce an accelerated fatigue, an excessive wear, or even a catastrophic failure (Egusquiza [5]). For condition monitoring, it is important to know the source of the vibration; this information allows the correction of possible bad practices or to detect faults in the machine. For both designers and condition analysts, it is useful to count on a tool that identifies the significant harmonics and the source of that vibration. This information is usually needed immediately and/or in situ.

Mateos [7], Tsukamoto et al. [8], Shi and Tsukamoto [9], Wang and Tsukamoto [10], and Zhang and Tsukamoto [11] predict the RSI pressure pulsation with a reasonable accuracy using CFD. Recently, Zhang and Tsukamoto [11] also determined the resulting hydrodynamic force on the impeller. The simulations referred above consider one [7,9–11] or two [8] combinations of a number of stationary and moving blades, which is known to be an important aspect to determine the significant harmonics as can be noticed by comparing the two cases studied by Tsukamoto et al. [8]. These simulations are time consuming and needs highly qualified human resources. They are also a complex challenge due to the geometry, the mesh, and especially the boundary conditions. From

[1]Formerly at the Center of Industrial Diagnostics and Fluid Dynamics, Technical University of Catalonia.

Contributed by the Fluids Engineering Division of ASME for publication in the JOURNAL OF FLUIDS ENGINEERING. Manuscript received February 9, 2006; final manuscript received May 26, 2007. Review conducted by Akira Goto.

Table 1 Expected frequencies and diameter modes

	h					
N	1	2	3	4	5	…
1	—	—	—	(−) q=9	—	
2	(−) q=2	—	—	—	—	
3	—	(+) q=5	—	—	(−) q=11	
4	—	(−) q=4	—	—	(+) q=12	
5	(+) q=3	—	—	—	—	
6	—	—	(−) q=6	(+) q=10	—	
7	—	—	—	—	—	
8	—	(−) q=4	—	(−) q=8	—	
9	(−) q=1	—	—	—	—	
…						…

the experimental point of view, the efforts have been focused on quantifying the influence of some construction and operating practices as the angles of the blades (Ohashi et al. [12] and Iino and Kasai [13]), the flow, the rotational speed and the distance between the stationary and moving blades (Ohashi et al. [12] and Arndt et al. [14,15]), and the combination of number of stationary and moving blades (Guo and Okamoto [16] and Guo and Maruta [17] consider three different combinations). These studies have shown that the harmonics with higher amplitude depend mainly on the number of stationary and moving blades, on the distance between the stationary and moving blades, and on the operating conditions. From the previous studies, Zhang and Tsukamoto [11] and Ohashi et al. [12] work with the resultant hydrodynamic force over the impeller-runner, which is the result of all the RSI pressure pulsations acting around the perimeter of the impeller-runner. These studies give an understanding of the fluid dynamic principles of the RSI and its resulting force over the impeller-runner. With respect to the frequencies, they indicate that the pressure pulsation and the hydrodynamic force have harmonics of the moving blade passing frequency, but they do not give guidelines to determine a priori the most significant ones and/or the relationship among their amplitudes.

At present, the method used to determine these vibration characteristics is the one developed by Kubota et al. [18]. It proposes the equation $hZ_V \pm N = qZ_B$, where h and q are positive integers, Z_B and Z_V are the number of moving and stationary blades, and N is the excited diameter mode. The excited diameter mode is a fixed pattern of vibration rotating in the same or opposite direction of the impeller-runner. The direction is given by the sign used to satisfy the equation, a positive value means forward direction, and a negative one, backward direction. When the equation is satisfied, the value of q indicates which harmonic of the moving blade passing frequency f_B is excited. As an example, let us consider Z_B=7 and Z_V=16. The equation is satisfied for several values, some of them are listed in Table 1. For example, for N=1 and h=1, the equation takes $1\times16\pm1=q\times7$, which cannot be satisfied. For N=2 and h=1, the equation take $1\times16\pm2=q\times7$, which is satisfied if the sign is negative and q is 2, then the expected harmonic is the second one, with a backward excited diameter Mode 2. Kubota et al. indicate with Table 1 a possible vibration at f_B (q=1), $2f_B$ (q=2), …, and others (all the values of q). This procedure gives a large amount of possible diameter modes and harmonics of f_B to appear. It is indicated that the most probable harmonics to appear are corresponding to the lower diameter modes. Considering the values in Table 1 for this particular case, it is expected that the highest component in the spectrum will be the 9th harmonic, then the 2nd, followed by the 5th, the 11th, the 4th, and so on.

In summary, the study of Kubota et al. limits the frequencies to harmonics of the moving blade passing frequency, and assumes diameter modes that are prone to be excited. The excited diameter mode will depend on which is the highest harmonic of the vibration. These results have been widely used by several authors as Tanaka [2], Guo and Okamoto [16], Guo and Maruta [17], and Franke et al. [19].

In this paper, the approach of Kubota et al. is complemented with geometrical and timing considerations that allow us to go further with the equation. The clue is the sequence of interaction. Some other important characteristics of the pump turbine are incorporated, such as the distance between the stationary and moving blades. Then, the proposed procedure is applied to a pump turbine, showing that the source of the vibration can be detected.

2 Theoretical Analysis

In order to characterize the resulting force over the impeller-runner related to the RSI, let us consider an impeller-runner with Z_B blades (moving blades) and a spiral case that has Z_V guide vanes (stationary blades). Any time a blade passes in front of a guide vane, there is an interaction that produces a fluid force over the blade and the guide vane. Let us assume, for the moment, that when the nth blade passes in front of the mth guide vane, it receives the same fluid force as passing in front of the next (m+1)th guide vane and so on. After an entire revolution, the nth blade receives Z_V times the same force. If the rotating speed Ω is constant, then the blade takes $2\pi/\Omega$ s to complete an entire revolution, receiving a repetitive force with period $T_V=2\pi/\Omega Z_V$. This periodic force can be described by a Fourier series as follows:

$$f_n = \sum_i F_{i,n} \sin(iZ_V\Omega t - \phi_{i,n}) \tag{1}$$

Here F is the amplitude of the force, ϕ the phase, and the subscripts i and n indicate that the force or phase corresponds to the ith harmonic of $Z_V\Omega$ at the nth blade. Equation (1) incorporates the action of the nonuniform flow between two different pairs of guide vanes and considers that this nonuniform flow is the same between the different pairs of guide vanes. The force in Eq. (1) is moving together with the nth blade and is referred to the rotating system of reference, as is shown in Fig. 1.

It can be observed in Fig. 1 that f_n in the x axis of the inertial system of reference ($f_{n,x}$) is given by

$$f_{n,x} = f_n \cos(\Omega t + \Omega_{0,n}) \tag{2}$$

where $\Omega_{0,n}$ is the initial angular position of the nth blade:

$$\Omega_{0,n} = n\frac{2\pi}{Z_B} + \Omega_0 \tag{3}$$

Here Ω_0 is the initial angular position of the runner. Then, taking Eqs. (1)–(3) into account,

$$f_{n,x} = \frac{1}{2}\sum_i F_{i,n}\{\sin[(iZ_V+1)\Omega t - \phi_{i,n} + \Omega_{0,n}] + \sin[(iZ_V-1)\Omega t - \phi_{i,n} - \Omega_{0,n}]\} \tag{4}$$

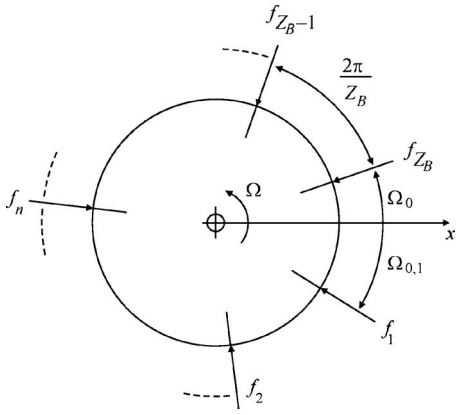

Fig. 1 Scheme of the forces over the runner at the reference initial time $t=0$

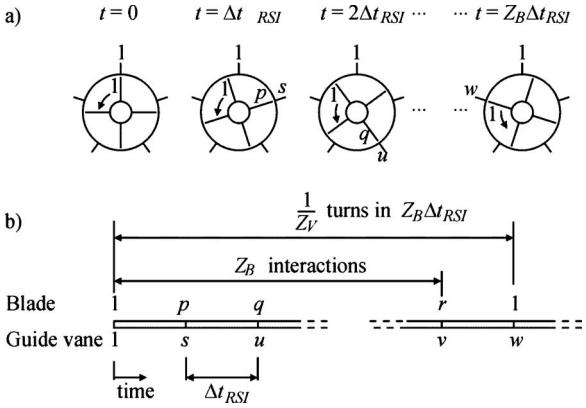

Fig. 2 Time between interactions

The resultant force over the runner in the inertial system of reference is obtained adding the forces over the Z_B blades as follows:

$$f_x = \sum_{n=1}^{Z_B} f_{n,x} = \frac{1}{2}\sum_{n=1}^{Z_B}\sum_i F_{i,n}\{\sin[(iZ_V+1)\Omega t - \phi_{i,n} + \Omega_{0,n}] + \sin[(iZ_V-1)\Omega t - \phi_{i,n} - \Omega_{0,n}]\} \quad (5)$$

Using trigonometric identities in Eq. (5) and arranging the terms,

$$f_x = \frac{1}{2}\sum_i\sum_{n=1}^{Z_B} F_{i,n}\left\{\sin[(iZ_V+1)\Omega t + \Omega_0]\cos\left(\phi_{i,n} - n\frac{2\pi}{Z_B}\right) + \cdots \quad \cdots - \cos[(iZ_V+1)\Omega t + \Omega_0]\sin\left(\phi_{i,n} - n\frac{2\pi}{Z_B}\right)\right\} + \cdots \quad \cdots + \frac{1}{2}\sum_i\sum_{n=1}^{Z_B} F_{i,n}\left\{\sin[(iZ_V-1)\Omega t - \Omega_0] \times\cos\left(\phi_{i,n} + n\frac{2\pi}{Z_B}\right) + \cdots \quad \cdots - \cos[(iZ_V-1)\Omega t - \Omega_0]\sin\left(\phi_{i,n} + n\frac{2\pi}{Z_B}\right)\right\} \quad (6)$$

Kubota et al. [18] obtain a similar result at this point, but they do not go further with the equation. To go further in Eq. (6), it is necessary to consider the sequence of interaction. During an entire revolution, each of the Z_B blades interacts with all the Z_V guide vanes, so that there are a total of Z_BZ_V interactions separated in time by

$$\Delta t_{\mathrm{RSI}} = \frac{2\pi}{Z_BZ_V\Omega} \quad (7)$$

Figure 2 schematically shows the time sequence for blade-guide vane interactions. Figure 2(*a*) shows the impeller-runner rotating and its corresponding interactions that are shown in a time line in Fig. 2(*b*). At the beginning, $t=0$, Blade 1 interacts with Guide Vane 1. After Δt_{RSI}, Blade p interacts with Guide Vane s, etc. After Z_B interactions in $1/Z_V$ turns, Blade 1 interacts again with a guide vane. The interactions begin at different times for different blades and this lag produces a phase difference depending on the corresponding frequency $iZ_V\Omega$ in Eq. (6).

Figure 3 shows the time lag at $Z_V\Omega$ and $2Z_V\Omega$, respectively. The phase difference corresponding to the time lag between two consecutive interactions (Blade 1 and then Blade p) is constant for the same harmonic (value of i) and is given by

$$\phi_{i,p} - \phi_{i,1} = i\Delta t_{\mathrm{RSI}}Z_V\Omega = i\frac{2\pi}{Z_B} \quad (8)$$

Equation (8) gives the phase difference between two consecutive interactions but does not consider the order of interaction. The order of interaction depends on the combination of Z_B and Z_V and as an example, Tables 2–4 summarize the order for combinations of $Z_B=2,3,4$, and $Z_V=5$, respectively. These tables are listed for an entire revolution. At the end of each row, there is the interaction of Blade 1 and Guide Vane 1, where all the sequence starts again. This order is graphically shown in Figs. 4 and 5 for the inertial and rotating system of reference, respectively.

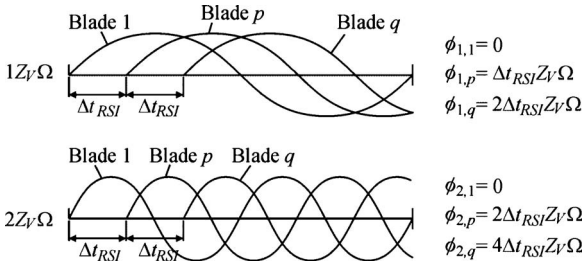

Fig. 3 Phase for a signal of frequency $Z_V\Omega$

Table 2 Interaction order for $Z_V=5$ and $Z_B=2$

Blade	1	2	1	2	1	2	1	2	1	2	1
Guide vane	1	4	2	5	3	1	4	2	5	3	1

Table 3 Interaction order for $Z_V=5$ and $Z_B=3$

Blade	1	2	3	1	2	3	1	2	3	1	2	3	1	2	3	1
Guide vane	1	3	5	2	4	1	3	5	2	4	1	3	5	2	4	1

Table 4 Interaction order for $Z_V=5$ and $Z_B=4$

Blade	1	4	3	2	1	4	3	2	1	4	3	2	1	4	3	2	1	4	3	2	1
Guide vane	1	5	4	3	2	1	5	4	3	2	1	5	4	3	2	1	5	4	3	2	1

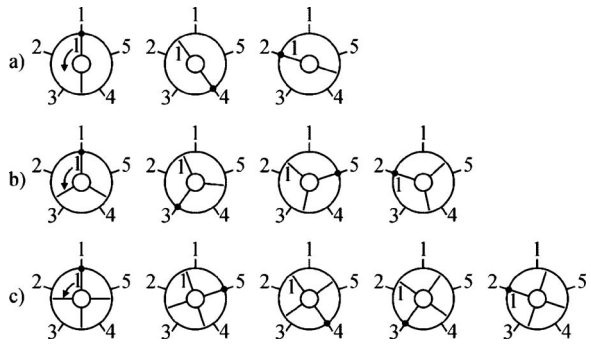

Fig. 4 Blade and guide vane interaction in the inertial system of reference for a combination of five guide vanes and (*a*) 2, (*b*) 3, and (*c*) 4 blades

It can be observed that the position of interaction moves with respect to the inertial system of reference in different directions around the stator: clockwise in Figs. 4(*a*) and 4(*c*) and counterclockwise in Fig. 4(*b*). This is also observed with respect to the rotating system of reference where the directions of motion are alternative (not rotating) in Fig. 5(*a*), counterclockwise in Fig. 5(*b*), and clockwise in Fig. 5(*c*).

In both systems of reference, the interaction position moves a fixed integer number of blades or guide vanes. For example, in Fig. 5(*c*), the position moves three blades from Blade 1 to Blade 4, after that it moves other three blades to reach Blade 3. As a consequence, the values of $\phi_{i,1}$, $\phi_{i,2,\ldots}$, ϕ_{i,Z_B} are separated by the same angle that is an entire multiple s ($s=3$ in Fig. 5(*c*)) of the phase lag between two consecutive interactions in Eq. (8):

$$\phi_{i,2} - \phi_{i,1} = is\frac{2\pi}{Z_B} \tag{9}$$

After all the Z_B blades have interacted, the angle in Eq. (9) completes entire circular angular displacements.

Now, it is necessary to calculate the value of s. Figure 6 shows a schematic of the first four interactions for $Z_B=4$ and $Z_V=5$ (the case shown in Figs. 4(*c*) and 5(*c*)). The entire perimeter where the interactions occur is drawn in a bar divided by all the Z_BZ_V interactions experienced during one revolution.

The first interaction corresponds to Blade 1 and Guide Vane 1. After Δt_{RSI} Blade 4 interacts with Guide Vane 5. After $3\Delta t_{\mathrm{RSI}}$ Blade 2 interacts with Guide Vane 3, in this case, $s=3$. The quantity of time intervals (Δt_{RSI}) for the interaction of the nth blade and the mth guide vane can be determined from Fig. 6:

$$s_{n,m} = (m-1)Z_B - (n-1)Z_V \tag{10}$$

It can be noticed that $s_{1,1}=0$ and that the following interaction of Blade 2 with Guide Vane m is given by

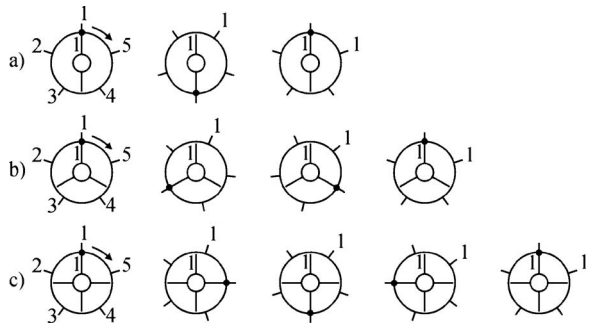

Fig. 5 Blade and guide vane interaction in the rotating system of reference for a combination of five guide vanes and (*a*) 2, (*b*) 3, and (*c*) 4 blades

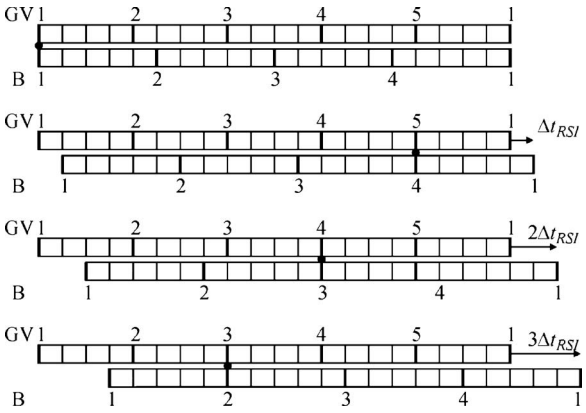

Fig. 6 Time between the interactions of two consecutive blades

$$s_{2,m} = (m-1)Z_B - Z_V \tag{11}$$

The first guide vane that interacts with Blade 2 can be determined as follows:

$$m_{1\mathrm{st}} = \left\lceil \frac{Z_V}{Z_B} \right\rceil + 1 \tag{12}$$

where the operator $\lceil\ \rceil$ rounds the corresponding value to the upper integer number. It follows that s in Eq. (9) is

$$s_{2,m1\mathrm{st}} = \left\lceil \frac{Z_V}{Z_B} \right\rceil Z_B - Z_V \tag{13}$$

From Eq. (6), it can be observed that given a fixed harmonic, the value of the terms depends on the behavior of the phase $\phi_{i,n} \mp n2\pi/Z_B$. This behavior can be deduced from Eq. (9): The addition of cosines and sines of $\phi_{i,n} \mp n2\pi/Z_B$ is zero unless $[\phi_{i,n+1} \mp (n+1)2\pi/Z_B] - (\phi_{i,n} \mp n2\pi/Z_B) = z2\pi$, with $n=1,2\ldots$, (Z_B-1) being z an integer. This condition has to be satisfied to obtain a nonzero term at the corresponding frequency $(iZ_V \pm 1)\Omega$ of Eq. (6). This condition can be graphically shown in Fig. 7 for the case of $Z_B=5$. The difference between two consecutive angles in the summation in Eq. (6) is $\phi_{i,n+1} - \phi_{i,n} \mp 2\pi/Z_B$. Observing Eq. (8), it can be noticed that this value is a multiple of $2\pi/Z_B$. For the case presented in Fig. 7, the angles advance $s=2$, 3, 4, and 5 entire multiples of $2\pi/Z_B$ and the only condition where the cosine or sine summation is not equal to zero is when the phase difference is $5\times 2\pi/5$, an integer multiple of 2π.

Taking the explanation given above into account, Eq. (5) can be simplified using the following derived condition:

$$\sum_i \sum_{n=1}^{Z_B} \sin[(iZ_V+1)\Omega t - \phi_{i,n} + \Omega_{0,n}] = 0 \quad \text{if} \quad is-1 \neq jZ_B$$

$$\sum_i \sum_{n=1}^{Z_B} \sin[(iZ_V-1)\Omega t - \phi_{i,n} - \Omega_{0,n}] = 0 \quad \text{if} \quad is+1 \neq jZ_B \tag{14}$$

Finally, the excitation obtained is

$$f_x = \frac{1}{2}\sum_{n=1}^{Z_B} \sum_i F_{i,n} \sin[(iZ_V \pm 1)\Omega t - \phi_{i,n} \pm \Omega_{0,n}] \quad \text{with } is \mp 1 = jZ_B \tag{15}$$

Equation (15) gives the frequencies in the resultant force over the runner when the interactions between the blades and different pairs of guide vanes are equal. In practice, this condition cannot be satisfied and there are differences between the amplitude of the interactions of one blade and two different guide vanes (Mateos

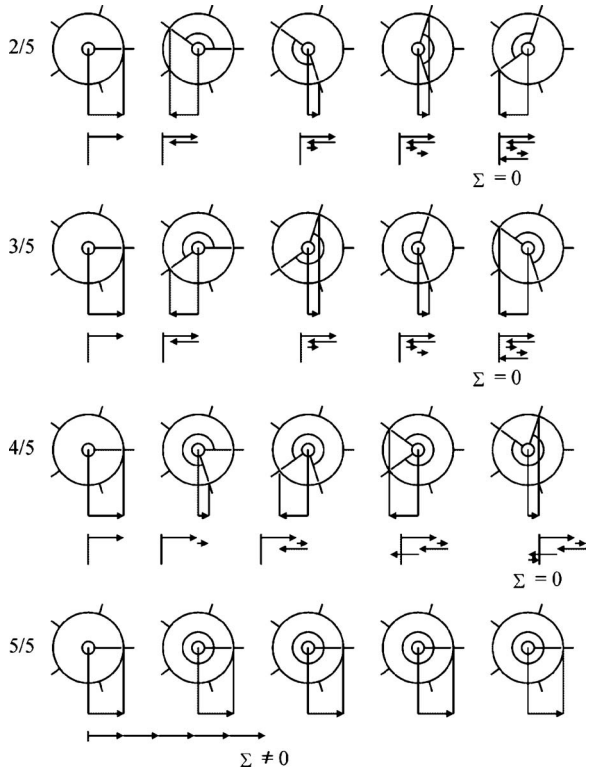

Fig. 7 Graphical explanation of the zero amplitude components

[7]). These differences can be interpreted as the consequence of two main effects, shown in Fig. 8, which are related to the construction and mounting of the impeller-runner: because of the cut water and because of the static eccentricity of the runner. In the first case, the cut water has different design and working conditions, presenting a pressure difference that is higher than in any other pair of guide vanes. In the second case, the distance between the blades and the guide vanes varies; this distance is an important factor that affects the amplitude of the pressure pulsation: the higher the distance, the more uniform the flow and the excitation amplitude is reduced (Arndt et al. [14,15]).

In both cases, the amplitude of the forces depends on which guide vane is interacting with the blade; this is equivalent to modulate in amplitude the excitation over the nth blade in Eq. (1) with a signal a of period $T=2\pi/\Omega$:

$$a = 1 + \sum_{k} A_{k,n} \sin(k\Omega t - \phi_{k,n}) \tag{16}$$

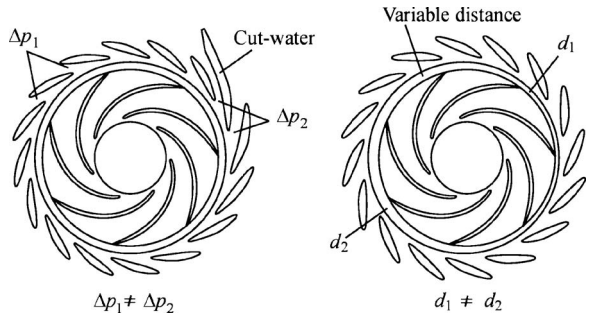

Fig. 8 Nonuniform distribution of the RSI. Cut water and static eccentricity.

The modulated force obtained multiplying Eqs. (1) and (16) incorporates the nonuniform flow effect of Eq. (1) together with the change in the amplitude depending on the circumferential position. This modulated force includes the behavior documented in the references cited by this article.

Using the same procedure as the one used for the no modulated force, the excitation obtained is

$$f_x = \frac{1}{2}\sum_{n=1}^{Z_B}\sum_{i} F_i \sin[(iZ_V \pm 1)\Omega t - \phi_{i,n} \pm \Omega_0] + \cdots \quad \text{with } is \mp 1 = jZ_B$$

$$\cdots + \frac{1}{2}\sum_{n=1}^{Z_B}\sum_{i}\sum_{k} A_{k,n}F_{i,n} \sin[(iZ_V \pm k \pm 1)\Omega t - \phi_{i,n} \pm \Omega_{0,n}] \quad \text{with } is \mp k \mp 1 = jZ_B \tag{17}$$

It should be observed that if there is no modulation and the excitations have the same amplitude in all the perimeter of the runner, then $A_{k,n}=0$ and the frequencies are at $(iZ_V \pm 1)\Omega t$. The frequencies given by $(iZ_V \pm k \pm 1)\Omega t$ appear only when the values of $A_{k,n} \neq 0$ and are a consequence of the different amplitudes of the interactions around the perimeter of the runner.

The frequencies in Eq. (17) are resumed in Eq. (18), which includes the frequencies $jZ_B\Omega$ that are measured in hydraulic turbomachinery.

$$iZ_V \pm k \pm 1 = jZ_B \quad \text{with } is \mp k \mp 1 = j'Z_B \tag{18}$$

It should be noticed that Eq. (18) is similar to the equation given by Kubota et al. [18]. The difference lies on the value of k that in this analysis represents the pattern of the forces between different pairs of guide vanes around the perimeter of the runner, while Kubota et al. used the value of $\pm k \pm 1$ to define a diameter mode. Other important difference in Eq. (18) is that the value of s has also to be satisfied; this restriction incorporates the sequence of interaction and reduces the amount of possible harmonics to appear.

To illustrate the difference between both methods, let us consider the same case of $Z_B=7$ and $Z_V=16$ used in the Introduction (Table 1). The first step is to determine the values of i in the equations above. This value indicates the harmonics presented in the radial force over a blade. Ohura et al. [1], Tanaka [2], and Ohashi et al. [12] show that the stress of a rotating point in the impeller-runner is found to be mainly a sinusoidal wave at the guide vane passing frequency: $Z_V\Omega$. If we assume this, then i in the above equations take the single value of 1. After this assumption, the force in Eq. (1) can be modulated by the signal in Eq. (16).

For a 7-16 combination, the value of s is equal to 5. If there is no modulation, and all the amplitudes are equal, then the condition in Eq. (18) takes the following values: $1\times5\mp0\mp1=j\times7$. This cannot be satisfied, then this condition should not show any harmonic.

For the eccentricity and the cut water, the forces are modulated as shown in Fig. 9. Considering a static eccentricity, the amplitude modulation is a single sinusoidal at the rotating speed (Rodriguez [20]). In that case, $k=1$, and the condition in Eq. (18) takes $1\times5\mp1\mp1=j'\times7$; this is satisfied for $5+1+1=7$ where $j'=1$, then the corresponding frequency is $1\times16-1-1=2\times7$ and the excited harmonic is the $2Z_B\Omega$. For the cut water, the modulating signal includes harmonics of the rotating speed, which is equivalent to modulate the signal by a step function.

The forces in Fig. 9 are applied to the blades considering the corresponding time lag between different blades. Equation (6) in combination with Eq. (16) is numerically solved and the obtained frequencies in the resulting force are shown in Fig. 10 for both cases.

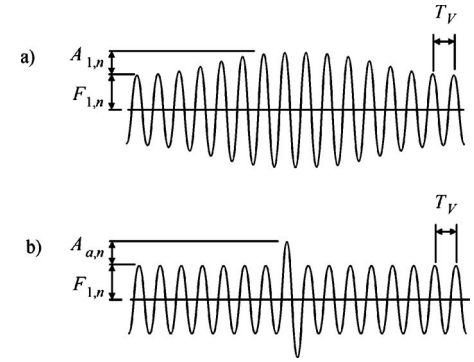

Fig. 9 Excitation force over a blade considering (*a*) an eccentricity and (*b*) the cut water

The results shown in Fig. 10 correspond to the amplitude in the harmonic of the resulting force divided by the amplitude of the no modulated force over a blade; this result is shown as a function of the level of modulation $A_{0,n}/F_{1,n}$. In the eccentricity, the resulting force (Fig. 10(*a*)) is a single sinusoidal at $2Z_B\Omega$ as predicted with the theoretical analysis. For the cut water, the relation between the amplitude of the harmonics of $Z_B\Omega$ is fixed and corresponds to a 24% for the first harmonic, 32% for the second, 22% for the third, 7% for the fourth, 3% for the fifth, 3% for the sixth, and 9% for the rest of the harmonics. The harmonic with higher amplitude is in both cases $2Z_B\Omega$. Notice that for the same level of modulation, the rise in the amplitude of the resulting force is higher for the eccentricity. For instance, for a level of modulation 0.5, the amplitude in the second harmonic of the resulting force is 0.60 times the amplitude of the force over a blade in the eccentricity, while this level of modulation in the cut-water effect produces a force 0.17 times the amplitude of the force over a blade.

The previous analysis leads to the following: If there is only one component at $2Z_B\Omega$, then the source is the eccentricity. If there are several harmonics where the relationship between their amplitudes is the one shown in Fig. 10(*b*), then the source is an excessive pressure pulsation at the cut water. The prediction of this method is summarized in Table 5.

Table 5 Expected frequencies

	Amplitude in the interactions		
Harmonic	Uniform	Eccentricity	Cut water
1	—	—	24%
2	—	100%	32%
3	—	—	22%
4	—	—	7%
5	—	—	3%
6	—	—	3%
Others	—	—	9%

3 Comparison With a Pump-Turbine Application

A pump turbine with a combination of $Z_B=7$ and $Z_V=16$ is studied in order to corroborate the accuracy in the predictions of both methods. The machine nominal power is 96 MW operating as a pump and 105 MW operating as a turbine. The rotating speed is 600 rpm. In pump nominal operating conditions, the flow rate is 25 m^3/s and the net head is 379 m. In turbine nominal operating conditions, the flow rate is 32 m^3/s and the net head is 376 m.

The prediction for the frequencies in the force originated in the RSI for a combination of $Z_B=7$ and $Z_V=16$ is exposed in Table 1 for the approach of Kubota et al. and in Table 5 for the analysis of this article. Both methods predict the force acting over the impeller-runner. Especially in a prototype, this force is difficult to measure; for that reason, it is preferred to measure vibration. The force acting over the impeller-runner produces a vibration in the machine. This vibration is not equal to the force and is modified by the response of the machine. The vibration is a consequence of the force in combination with the response of the machine. To discriminate if the resulting vibration characteristics are due to the RSI force or to the response of the system, it is necessary to determine the response between the position where the force is applied and the measuring position. The response analysis of Rodriguez [20] including start-up and run-down analysis, experimental modal analysis, and the consideration of the added mass effect of water (Rodriguez et al. [21] and Liang et al. [22]) indicates that there is no resonance or antiresonance near the first five harmonics of the blade passing frequency. This allows us to compare the amplitudes of the vibration with those of the force. Taking these considerations into account, the vibration should at least include

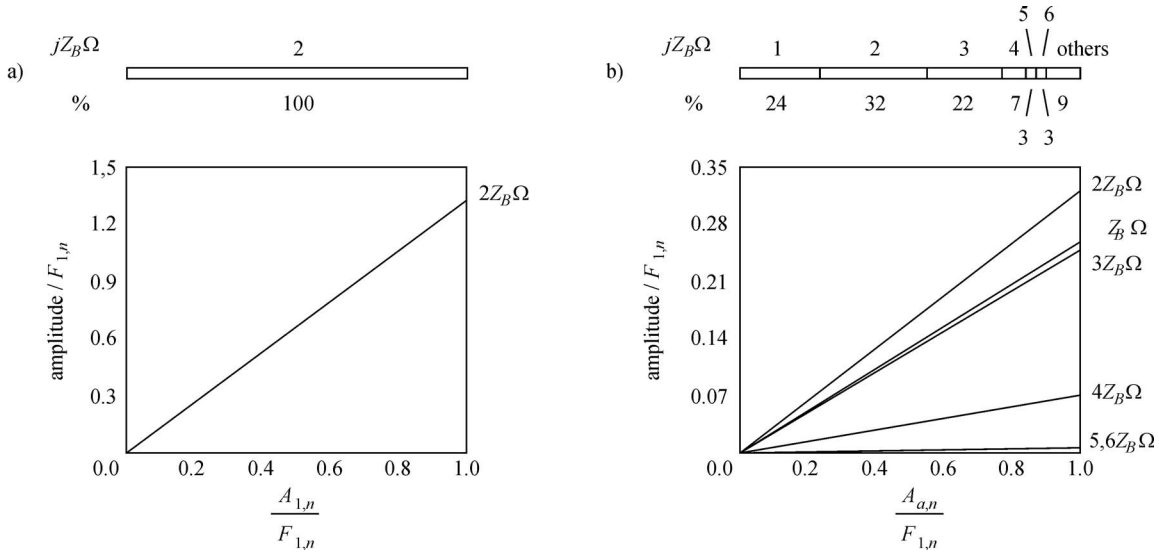

Fig. 10 Frequency content of the resultant excitation considering (*a*) an eccentricity and (*b*) the cut water

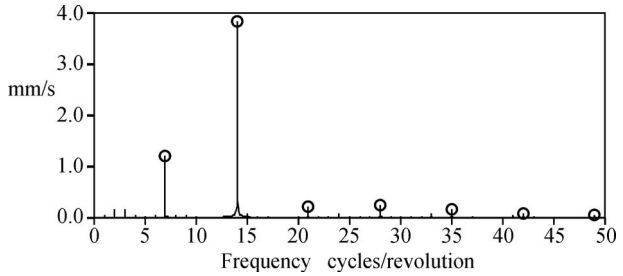

Fig. 11 Spectrum of vibration measured in the rotating shaft. Spots indicate harmonics of blade passing frequency.

the harmonics of the RSI force and the relationship among their amplitudes. This should be corresponded with the predicted force in Table 1 and/or Table 5.

The response analyzed above relates the impeller-runner to the nearest accessible position to the impeller-runner on the shaft surface. Because of constructive characteristics of large hydraulic turbomachinery, displacement probes to measure shaft vibration cannot be mounted on the foundation and are usually mounted on the bearing housing which vibrates significantly. To avoid the effect of the bearing housing, the shaft vibration is measured using telemetric on-board accelerometers that rotate with the shaft. This measuring position avoids the uncertainties introduced by the response of the bearing fluid film and the bearing housing. The vibration measured on the shaft surface is referred to the rotating system of reference and can be converted to the inertial system of reference combining both perpendicular directions (Rodriguez et al. [23]). The instrumentation used includes two accelerometers, a multichannel telemetry system, and an acquisition system.

The spectrum of the vibration with respect to the inertial system of reference is shown in Fig. 11. The frequencies above 50 times the rotating speed are not shown because their energy represents less than a 0.1% of the rms global value below 5000 Hz. For the frequency range below 50 cycles per revolution, the harmonics of the blade passing frequency represents the 99.3% of the rms global value. Table 6 lists the amplitude of the harmonics in this frequency range and the relative importance between them.

The highest amplitude found in the measured vibration corresponds to the second harmonic $2f_B$, which is predicted by both

Table 7 Harmonics of f_B expected in the cut-water effect

Harmonic	Amplitude	
	mm/s	%
1	1.21	24
2	1.61	32
3	1.11	22
4	0.35	7
5	0.15	3
6	0.15	3

Table 6 Harmonics of f_B found in the measured vibration

Harmonic	Amplitude	
	mm/s	%
1	1.21	8.9
2	3.85	90.2
3	0.22	0.3
4	0.25	0.4
5	0.16	0.2
6	0.09	0.0
7	0.06	0.0
Total	5.82	100.0

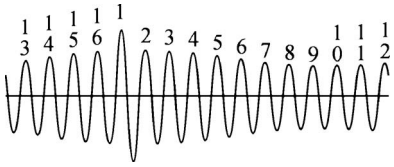

Fig. 12 Resulting force over a blade

methods. Kubota et al. indicate that this vibration corresponds to a diameter Mode 2. The analysis carried out in this article indicates that it could correspond to two possible cases: an eccentricity or the cut water.

The next harmonic presenting the highest amplitude is f_B. To predict this harmonic, Kubota et al. need the excitation of the diameter Mode 9. A diameter Mode 9 is a difficult vibration pattern to obtain, especially because the impeller-runner has seven blades. Moreover, it is expected that some other diameter modes should be excited before the ninth because it is indicated that lower diameter modes are more prone to be excited. For this particular case, Kubota et al. propose excited diameter Modes 2 and 9.

The analysis carried out in this article indicates that the f_B could correspond to the effect of the cut water, then it proposes a combination of an eccentricity and a cut-water effect. If it is considered that the amplitude of f_B comes from the cut water, then the amplitudes for the rest of the harmonics should be consistent with Table 6. In Table 7 are listed the expected amplitudes for a cut-water effect that produces a component at f_B with amplitude 1.21 mm/s rms.

If Table 7 is compared with Table 6, it can be noticed that the amplitudes are similar except for the second and the third harmonic. If we assume that the difference with the second harmonic comes from the fact that there is a combination of the eccentricity and the cut water, then the rest of $2f_B$ can be obtained from the eccentricity and the only disagreement with Table 6 is the third harmonic. Using the computer, the excitation for each blade can be determined. This excitation is shown in Fig. 12 where the numbers over the peaks indicate which guide vane is interacting with the blade. Guide Vane 1 corresponds to the cut water. The combination of both effects can be observed in Fig. 12, where the single rise in the amplitude occurs when the blade passes in front of the cut water.

Large hydraulic turbomachinery is especially difficult to align and to balance; for that reason, the eccentricity effect cannot be avoided. Nevertheless, the single rise in the magnitude of the interaction in the cut water can be reduced. From this analysis, it can be proposed to perform a drill in the cut water to decrease the pressure difference encountered by the blade when it passes from the back to the front of the cut water. This corrective proposition was performed by the power plant and the global vibration levels were reduced.

4 Conclusions

This article presents a theoretical analysis that allows us to describe the characteristics in the frequency domain of the vibration originated in the RSI. The analysis is based on the sequence of interaction. This approach allows us to interpret the vibration as a consequence of a modulation in the amplitudes of the interactions and not as a consequence of an excited diameter mode as has been usually considered. This interpretation suggests directions for the solution of design and condition monitoring problems. It helps to determine the origin of the harmonics that gives guidelines to get lower amplitude at specific harmonics or to avoid them. For instance, a clearly single rise in the amplitude of the interactions will show that there is a specific problem in a guide vane, and a drill in this guide vane will reduce the vibration levels.

This approach looks attractive, but is contrasted with a single practical case and it is necessary to analyze more cases to corroborate the approach.

Nomenclature

A = amplitude of the modulating signal
F = amplitude of the excitation (N)
N = referred to the N-diameter mode
T = period of one revolution (s)
T_V = stationary blade passing period (s)
Z_B = number of moving blades
Z_V = number of stationary blades
a = modulating signal
f = excitation as a function of time (N)
h = positive integer
q = excited harmonic of the moving blade passing frequency
s = positive integer
z = positive integer
Δt_{RSI} = time interval between two consecutive interactions (s)
Ω = rotating speed (rad/s)
Ω_0 = initial angular position (rad)
ϕ = phase (rad)

Subscripts

i = referred to the ith harmonic in the excitation of each moving blade
j = referred to the jth harmonic of the moving blade passing frequency
k = referred to the kth harmonic in the amplitude modulating signal
m = referred to the mth stationary blade
n = referred to the nth moving blade
x = referred to the x axis of the inertial system of reference

References

[1] Ohura, Y., Fujii, M., Sugimoto, O., Tanaka, H., and Yamagata, I., 1990, "Vibration of the Powerhouse Structure of a Pumped Storage Power Plant," *U2, IAHR Symposium*, Belgrade, Yugoslavia.

[2] Tanaka, H., 1990, "Vibration Behavior and Dynamic Stress of Runners of Very High Head Reversible Pump-Turbines," *A1, IAHR Symposium*, Belgrade, Yugoslavia, Sec. U2.

[3] Egusquiza, E., Nascimento, L. P., Valero, C., and Jou, E., 1994, "El Diagnóstico De Daños En Grupos Hidroeléctricos Mediante El Análisis de Vibraciones," Ingeniería del Agua, **1**(3), pp. 69–80; also available at: http://www.ingenieriadelagua.com/2004/bib_detalle.asp?Id=26

[4] Egusquiza, E., Mateos, B., and Escaler, X., 2002, "Analysis of Rotor-Stator Interaction in Operating Pump-Turbines," *Proceedings of the XXI IAHR Symposium on Hydraulic Machinery and Systems*, Lausanne, Switzerland.

[5] Egusquiza, E., 2003, *Comportament Dinàmic de Màquines Hidràuliques*, Edicions UPC, Catalan.

[6] Fisher, R. K., Seidel, U., Grosse, G., Gfeller, W., and Klinger, R., 2002, "A Case Study in Resonant Hydroelastic Vibration: The Cause of Runner Cracks and the Solutions Implemented for the Xiaolangdi Hydroelectric Project," *Proceedings of the XXI IAHR Symposium on Hydraulic Machinery and Systems*, Lausanne, Switzerland.

[7] Mateos, J. B., 2005, "Contribution to Rotor-Stator Interaction in Pump Turbine Prototypes," Ph.D. thesis, Technical University of Catalonia (UPC), Barcelona, Spain.

[8] Tsukamoto, H., Uno, M., Hamafuku, N., and Okamura, T., 1995, "Pressure Fluctuation Downstream of a Diffuser Pump Impeller," *The Second Joint ASME/JSME Fluids Engineering Conference, Forum of Unsteady Flow, FED*, Vol. 216, pp. 133–138.

[9] Shi, F., and Tsukamoto, H., 2001, "Numerical Study of Pressure Fluctuations Caused by Impeller-Diffuser Interaction in a Diffuser Pump Stage," ASME J. Fluids Eng., **123**, pp. 466–474.

[10] Wang, H., and Tsukamoto, H., 2001, "Fundamental Analysis on Rotor-Stator Interaction in a Diffuser Pump by Vortex Method," ASME J. Fluids Eng., **123**, pp. 737–747.

[11] Zhang, M., and Tsukamoto, H., 2005, "Unsteady Hydrodynamic Forces Due to Rotor-Stator Interaction on a Diffuser Pump With Identical Number of Vanes on the Impeller and Diffuser," ASME J. Fluids Eng., **127**, pp. 743–751.

[12] Ohashi, H., Sakurai, A., and Nishihama, J., 1988, "Influence of Impeller and Diffuser Geometries on the Lateral Fluid Forces of Whirling Centrifugal Impeller," *NASA Conference Publication 3026: Rotordynamic Instability Problems in High-Performance Turbomachinery*, pp. 285–306.

[13] Iino, T., and Kasai, K., 1985, "An Analysis of Unsteady Flow Induced by Interaction Between a Centrifugal Impeller and a Vaned Diffuser," Trans. Jpn. Soc. Mech. Eng., Ser. B, **51**(471), pp. 154–159.

[14] Arndt, N., Acosta, A. J., Brennen, C. E., and Caughey, T. K., 1989, "Rotor-Stator Interaction in a Diffuser Pump," ASME J. Turbomach., **111**, pp. 213–221.

[15] Arndt, N., Acosta, A. J., Brennen, C. E., and Caughey, T. K., 1990, "Rotor-Stator Interaction in a Centrifugal Pump With Several Vaned Diffusers," ASME J. Turbomach., **112**, pp. 98–108.

[16] Guo, S., and Okamoto, H., 2002, "An Experimental Study on the Fluid Forces Induced by Rotor-Stator Interaction in a Centrifugal Pump," *The Ninth International Symposium on Transport Phenomena and Dynamics of Rotating Machinery*, Honolulu, HI, Feb. 10–14.

[17] Guo, S., and Maruta, Y., 2005, "Experimental Investigations on Pressure Fluctuations and Vibration of the Impeller in a Centrifugal Pump With Vaned Diffusers," JSME Int. J., Ser. B, **48**(1), pp. 136–143.

[18] Kubota, Y., Susuki, T., Tomita, H., Nagafuji, T., and Okamura, T., 1983, "Vibration of Rotating Bladed Disc Excited by Stationary Distributed Forces," Bull. JSME, **26**, pp. 1952–1957.

[19] Franke, G., Fisher, R., Powell, C., Seidel, U., and Koutnik, J., 2005, "On Pressure Mode Shapes Arising From Rotor Stator Interactions," Sound Vib., **39**(3), pp. 14–18.

[20] Rodriguez, C. G., 2006, "Feasibility of On Board Measurements for Predictive Maintenance in Large Hydraulic Turbomachinery," Ph.D. thesis, Technical University of Catalonia (UPC), Barcelona, Spain.

[21] Rodriguez, C. G., Egusquiza, E., Escaler, X., Liang, Q. W., and Avellan, F., 2006, "Experimental Investigation of Added Mass Effects on a Francis Turbine Runner in Still Water," J. Fluids Struct., **22**, pp. 699–712.

[22] Liang, Q. W., Rodríguez, C. G., Egusquiza, E., Escaler, X., Farhat, M., and Avellan, F., 2007, "Numerical Simulation of Fluid Added Mass Effect on a Francis Turbine Runner," Comput. Fluids, **36**, pp. 1106–1118.

[23] Rodriguez, C. G., Egusquiza, E., Escaler, X., and Liang, Q. W., 2006, "Feasibility of On-Board Measurements in a Hydraulic Turbines," *23rd IAHR Symposium on Hydraulic Machinery and Systems, Yokohama, Japan*, Paper Code 265.

Transient Behavior of Turbomachineries: Applications to Radial Flow Pump Startups

Antoine Dazin
e-mail: antoine.dazin@lille.ensam.fr

Guy Caignaert

Gérard Bois

Laboratoire de Mécanique
de Lille-UMR CNRS 8107,
Ecole Nationale Supérieure des Arts et Métiers 8,
Boulevard Louis XIV,
59046 Lille Cedex, France

A theoretical analysis of the fast transients of turbomachineries, based on the study of unsteady and incompressible fluids mechanics equations applied to an impeller, is proposed. It leads to internal torque, internal power, and impeller head of an impeller during transient periods. The equations show that the behavior of a pump impeller is not only depending on the acceleration rate and flow rate, as it is usually admitted, but also on velocity profiles and their evolution during the transient. Some hypotheses on the flow in a radial flow pump are proposed. They are validated by comparison with the experimental results of a single stage, single volute radial flow pump during some fast acceleration periods. The model is also used to analyze the behavior of the pump during a fast startup. [DOI: 10.1115/1.2776963]

Keywords: fast transient, turbomachinery, radial flow pump

1 Introduction

The need for transient simulations of hydraulic or energy systems is becoming greater. Whereas the models for pipe flows, even in cavitating operations, are becoming more and more realistic (Bergant et al. [1]), it is still usual to model the turbomachineries with a quasisteady hypothesis (Venturini [2]). Nevertheless, it has been observed that the performance of machines and, in particular, of centrifugal pumps in transient operations can be rather different from the quasisteady one. In the past 20 years, many studies have concerned this subject through several aspects: starting period (Tsukamoto and Ohashi [3], Saito [4], Ghelici [5], Bolpaire [6], Lefebvre and Barker [7]), stopping period (Tsukamoto et al. [8]), vane opening or closure (Picavet [9]), and fluctuating rotational speed (Tsukamoto et al. [10]). More recently, Tanaka and Tsukamoto [11–13] have explored the transient behavior of a cavitating centrifugal pump.

For noncavitating starting periods, all the authors noticed that at the very beginning of the startup, the total pressure coefficient is much larger than the quasisteady value whereas, in the following period of the startup, this coefficient becomes smaller than the quasisteady value. Bolpaire [6] observed the modification of the recirculating flow due to transient effects. During stopping periods, Tsukamoto et al. [8] observed also important modifications of the performances of a pump.

Some analyses of these phenomena have been proposed in the literature: Tsukamoto et al. [3,8,10] proposed a model based on nonviscous linear cascade calculations whereas Saito [4] and Ghelici [5] proposed one-dimensional models based on the integration of the momentum equation above a streamline. The models give predictions, which are qualitatively good but quantitatively far from experimental results. Our purpose is to improve the analysis of the fast transient behavior of turbomachinery by using the angular momentum and energy equations for a rotating impeller and an incompressible flow (Sec. 2). The aim is to obtain the equations governing the internal torque, power, and head of an impeller during transient operations. These equations are used to give predictions of the evolution of the total head of a centrifugal pump in order to compare them to the experimental results obtained by Bolpaire [6] (Sec. 3). The experimental test rig is presented in Sec. 3.1. The hypothesis of the model is presented in Sec. 3.2. Its results are compared with experimental results in Sec. 3.3. An analysis of the results is proposed in Sec. 3.4.

Contributed by the Fluids Engineering Division of ASME for publication in the JOURNAL OF FLUIDS ENGINEERING. Manuscript received April 14, 2006; final manuscript received April 13, 2007. Review conducted by Akira Goto.

2 Analysis: Fundamental Equations of Fluid Dynamics Applied to an Impeller

The incompressible angular momentum and energy equations are applied to an impeller during transient operations.

2.1 Angular Momentum Equation. The moment of momentum equation is applied to a control volume V including the fluid inside the impeller. The volume V is bounded by a surface S (Fig. 2).

$$\frac{d}{dt}\iiint_V \mathbf{OM} \wedge \rho \mathbf{c} dV = \iiint_V \mathbf{OM} \wedge \rho \mathbf{F} dV + \iint_S \mathbf{OM} \wedge \boldsymbol{\tau} dS \quad (1)$$

In this equation, **M** is a point belonging to the volume V and **O** the origin of the coordinate system. **O** is located on the axis of the pump. The term on the left hand side of Eq. (1) represents the moment of momentum variation of volume V. The first and second terms of the right hand side of Eq. (1) represent the moment of the body forces acting on the volume and of the stresses acting on the control surface S.

That is,

$$\frac{\partial}{\partial t}\iiint_V \mathbf{OM} \wedge \rho \mathbf{c} dV + \iint_S \rho \mathbf{c} c_m dS = \iiint_V \mathbf{OM} \wedge \rho \mathbf{F} dV + \iint_S \mathbf{OM} \wedge \boldsymbol{\tau} dS \quad (2)$$

In steady conditions, the average flow is steady and the first term of the left hand side of this equation is zero on average.

Projecting then the equation on the axis of the impeller, and neglecting, as it is usually done, the shear stresses on S_e (where S_e is the part of S located at the inlet and outlet of the impeller (Fig. 2)) give the classical angular momentum equation for turbomachinery (Comolet [14]):

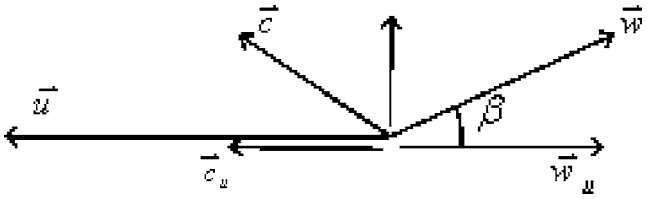

Fig. 1 Velocity triangle

$$\iint_{S_e} \rho r c_u c_m dS = T_i \tag{3}$$

where T_i is the internal torque and r the radial coordinate of **OM** (Fig. 2).

If we consider transient operations, we need to evaluate the term

$$\left(\frac{\partial}{\partial t} \iiint_V \mathbf{OM} \wedge \rho \mathbf{c} dV \right) \cdot \mathbf{z} = \frac{\partial}{\partial t} \iiint_V \rho r c_u dV \tag{4}$$

Using the velocity triangle (Fig. 1), we can get the internal torque in transient operation (neglecting the shear stresses acting on S_e like it is done for Eq. (3)), that is,

$$T_i = \rho \iint_{S_e} c_u c_m dS + I_z \frac{\partial}{\partial t}[\omega(t)] - \rho \frac{\partial}{\partial t} \left(\iiint_V r w_u dV \right) \tag{5}$$

where I_z is the moment of inertia about $O\mathbf{z}$ of the fluid which is inside the impeller.

So, the internal torque in transient operation is the sum of three terms:

(1) The first one is the steady one (calculated as in steady conditions but with the instantaneous values of the velocity components).
(2) The second one is the product of a moment of inertia with the impeller angular acceleration. It corresponds to the torque necessary to give a solid body rotation motion to the fluid.
(3) The third one represents the derivative of the relative angular momentum and corresponds to an additional torque due to the evolution of the flow during the transient phase.

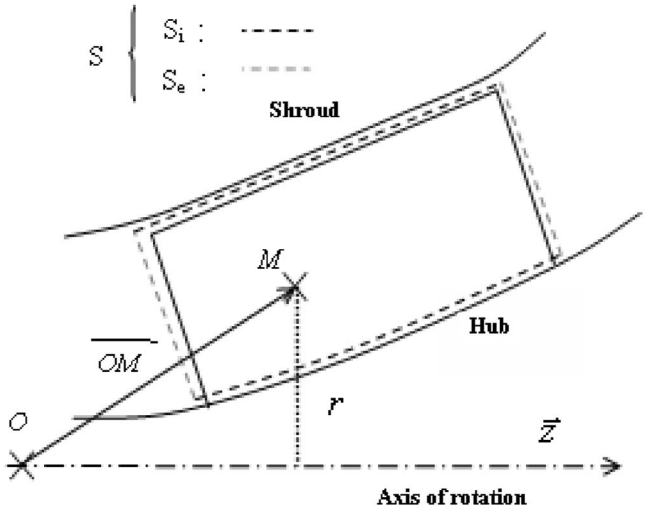

Fig. 2 Definition of the control volume

2.2 Energy Equation. The energy equation applied to the control volume V is

$$\frac{d}{dt} \iiint_V \rho \left(e + \frac{c^2}{2} \right) dV = \iiint_V \rho \mathbf{F} \cdot \mathbf{c} dV + \iint_S \tau \cdot \mathbf{c} dS + \iint_S \frac{d\Theta}{dt} dS \tag{6}$$

This equation is the expression of the first law of thermodynamics, which says that the change of internal energy and of kinetic energy (left hand term of Eq. (6)) is equal to sum of the following.

(1) the external forces (the body forces acting on the volume and the stresses acting on the control surface), work (first and second term of the right hand side of Eq. (6))
(2) the heat added to the system (last term of Eq. (6))

The last term of Eq. (6), which represents the heat transferred to the fluid by conduction, is neglected here.

It results

$$\frac{\partial}{\partial t} \iiint_V \rho \left(e + \frac{c^2}{2} \right) dV + \iint_S \rho \left(e + \frac{c^2}{2} \right) \cdot c_m dS = \iiint_V \rho \mathbf{F} \cdot \mathbf{c} dV + \iint_S \boldsymbol{\tau} \cdot \mathbf{c} dS \tag{7}$$

In steady conditions, the average flow is steady and the first term on the left hand side of the previous equation is zero on average.

Equation (8) then gives the power transferred from the impeller to the fluid (internal power Π_i), which is equal to the total enthalpy flux through S (Comolet [14]):

$$\iint_{Se} \rho \left(e + \frac{p}{\rho} + \frac{c^2}{2} \right) c_m dS = \prod_i \tag{8}$$

The unsteady term has to be evaluated during transient operations:

$$\frac{\partial}{\partial t} \iiint_V \rho \left(e + \frac{c^2}{2} \right) dV = \underbrace{\frac{\partial}{\partial t} \iiint_V \rho e dV}_{B} + \underbrace{\frac{\partial}{\partial t} \iiint_V \rho \frac{c^2}{2} dV}_{C} \tag{9}$$

The first term of the right hand side of Eq. (9) corresponds to the variation with time of the internal energy and can be written in the case of an incompressible fluid:

$$B = T \frac{\partial S}{\partial t}$$

where S is the entropy of the fluid.

The second term of the right hand side of Eq. (9) corresponds to the variation with time of the kinetic energy of the fluid, which is inside the impeller. Using the velocity triangle (Fig. 1), it comes

$$C = \frac{\rho}{2} \frac{\partial}{\partial t} \iiint_V \left(\frac{c_m^2}{\sin^2 \beta} \right) dV + I_z \omega \frac{\partial \omega}{\partial t} - \rho \frac{\partial}{\partial t} \left(\omega \iiint_V \frac{r c_m dV}{\tan \beta} \right) \tag{10}$$

And finally the internal power of an impeller in transient operations is

$$\Pi_i = \iint_{Se} \rho\left(e + \frac{p}{\rho} + \frac{c^2}{2}\right) c_m dS + T\frac{\partial S}{\partial t} + \frac{\rho}{2}\frac{\partial}{\partial t}\iiint_V (w^2) dV + I_z \omega \frac{\partial \omega}{\partial t}$$

$$- \rho \frac{\partial}{\partial t}\left(\omega \iiint_V r w_u dV\right) \tag{11}$$

The internal power of a pump in transient operations appears as the sum of five terms.

(1) The first term is a steady term.
(2) The second term represents the entropy variation of the fluid.
(3) The third, fourth, and fifth terms represent the variation of kinetic energy of the fluid inside the impeller.

- The third one represents the variation of relative kinetic energy of the fluid inside the impeller.
- The fourth one represents the power necessary to give a solid body rotation motion to the fluid.
- The last one represents the derivative of the product of angular speed with the relative angular momentum. It depends on the variation of rotation speed of the impeller, flow rate, and direction as well as velocity profiles.

2.3 Determination of the Impeller Head. As $\Pi_i = \omega T_i$ and

$$H_{\text{imp}} = \frac{1}{Q_v} \iint_{S_e} \left(\frac{p}{\rho g} + \frac{c^2}{2g}\right) c_m dS$$

it is thus possible to combine Eqs. (5) and (11) in order to obtain the expression of the instantaneous impeller head.

$$H_{\text{imp}} = \frac{1}{g Q_v}\left[\iint_{S_e} (u c_u - e) c_m dS_e - \frac{T}{\rho}\frac{\partial S}{\partial t} + \left(\iiint_V r w_u dV\right)\frac{\partial \omega}{\partial t} - \frac{1}{2}\frac{\partial}{\partial t}\iiint_V w^2 dV\right] \tag{12}$$

The impeller head is thus the sum of four terms:

(1) a steady term
(2) a term which represents the variation of the entropy of the fluid with time
(3) the product of the angular acceleration with the relative angular momentum divided by the flow rate
(4) the derivative of the relative kinetic energy divided by the flow rate

As can be seen, the impeller head is not only affected by the angular acceleration and flow acceleration (as it is usually admitted Saito [4], Ghelici [5]) but also by the velocity profile variations in the impeller.

Some hypotheses on the flow of a radial flow pump are proposed in Sec. 3.3 in order to predict the total head during transient operations. The model is compared to experimental results.

3 Comparison to Experimental Results

Experimental results obtained by Bolpaire [6] are used to validate a model based on Eq. (12). The experimental setup is briefly reminded in Sec. 3.1. The model derived from the analysis of the previous paragraph is presented in Sec. 3.2. The results are compared to the experimental ones in Sec. 3.3 and analyzed in Sec. 3.4.

3.1 Experimental Setup

3.1.1 Experimental Test Rig. The experiments have been performed on a test rig called DERAP (Fig. 3). A single stage vaneless diffuser single volute type radial flow pump is used for the experiment. The main specifications of the impeller are summarized in Table 1 and Fig 4.

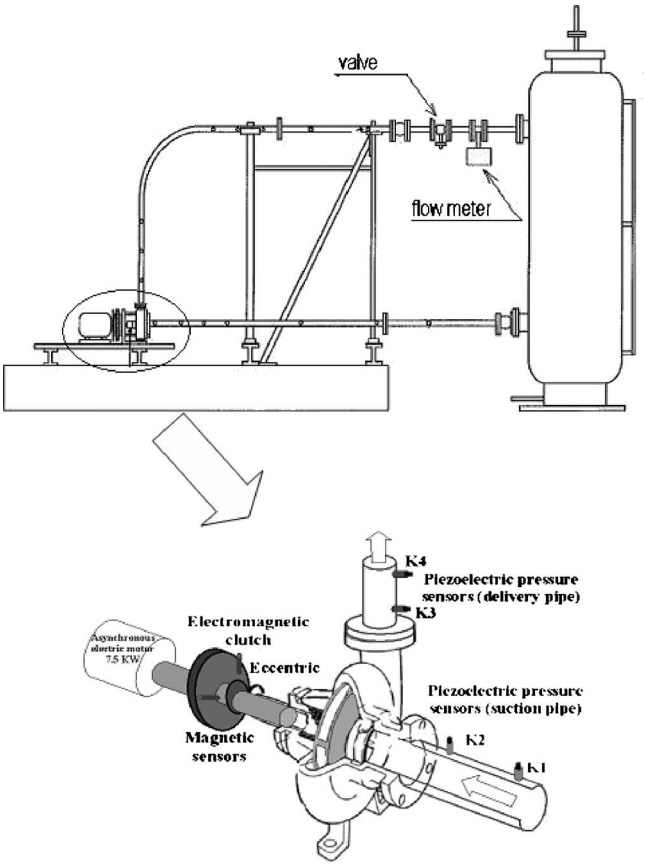

Fig. 3 Experimental setup

The pump is driven by an asynchronous electric motor through an electromagnetic clutch, in order to perform fast startups. The

Table 1 Impeller specifications

Geometric specifications		*Hydraulic specifications*	
Inlet vane angle $\beta_{1\alpha}$	32.2 deg	Nominal speed	2900 tr/min
Outlet vane angle $\beta_{2\alpha}$	23 deg	Nominal flow rate	23 m^3/h
Number of vanes	5	Nominal total head	50 m
Inlet diameter D_1	38.5 mm		
Outer diameter D_2	202.5 mm		
Outer width b_2	7 mm		

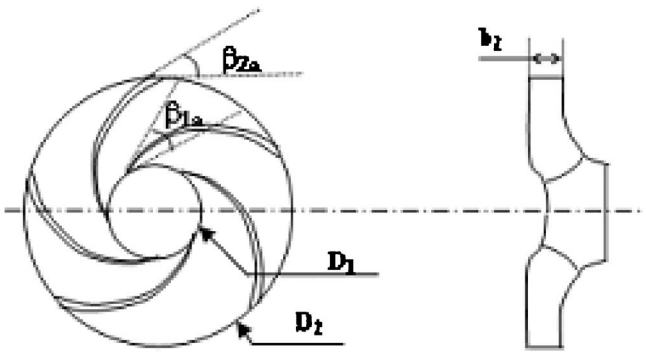

Fig. 4 Schematic view of the impeller

fast startups are obtained by engaging the clutch, once the motor is running at its final rotation speed. Slower startups are also possible by starting the motor, once the clutch is engaged. The motor shaft rotation speed is measured by a photoelectric cell. An eccentric is mounted on the shaft of the impeller and two magnetic sensors are pointed at it. The recording of their signals allows for calculating the instantaneous rotation speed of the machine. The pump is connected to a hydraulic circuit, with pipes connected to a vessel. The suction and delivery pipes have the same inner diameter (40 mm) and are both instrumented with two piezoelectric pressure transducers.

3.1.2 Data Processing. The data from the four pressure transducers, the two magnetic sensors, and the electromagnetic flow meter are acquired by a LMS Difa-Scadas system. Time acquisitions were realized. The sampling frequency was 8192 Hz. The acquisition duration was 3 s, so the total data number for each acquisition channel was about 25,000.

3.1.2.1 Rotation Speed. The use of a photoelectric cell to measure the impeller shaft rotation speed is not well adapted to the study of fast transient phenomena. An original method has been developed [5] using two magnetic sensors measuring the distances (x and y) between them and an eccentric mounted on the shaft. (Fig. 5(a)). x and y are related to the angular position of the shaft:

$$(R+x)^2 = (L-\varepsilon\cos\theta)^2 + \varepsilon^2\sin^2\theta \quad \text{and}$$
$$(R+y)^2 = (L-\varepsilon\sin\theta)^2 + \varepsilon^2\cos^2\theta \tag{13a}$$

Consequently, at the first order in (ε/L), we have x' and y', the variable part of x and y, which are

$$x' = -\varepsilon\cos\theta = -\varepsilon\cos(\omega\,.\,t) \quad \text{and} \quad y' = -\varepsilon\sin\theta = -\varepsilon\sin(\omega\,.\,t) \tag{13b}$$

A typical sensor response as a function of time is plotted Fig. 5(b). The curve is a sine function whose frequency (which is the angular speed of the shaft) increases with time.

At each time, the least squares method is used to fit the sensor signal data with a cosine function ($x' = -\varepsilon\cos(\omega\,.\,t)$) in order to obtain the best value for the parameter ω. In order to evaluate the validity and the uncertainty of this method, the final rotation speed obtained with this method is compared to the one obtained with a tachymeter using a photoelectric cell device. The gap between the two rotation speed measurements is less than 1%.

3.1.2.2 Total Head and Flow Rate. The transient total head and flow rate are calculated from the piezoelectric transducers. Figure 6(a) represents the static pressures p_{inlet} measured at the inlet, p_{outlet} measured at the outlet of the pump, and $p_{\text{outlet}} - p_{\text{inlet}} = \rho g H_t$, where H_t is the total head provided by the pump. The measurement uncertainty of the transient total head is one of the piezoelectric pressure sensors that is about 0.5% of the final total head.

The flow rate (Fig. 6(b)) is obtained from the pressure measurements registration of two sensors located in the same pipe (Wylie and Streeter [15]).

The one dimensional unsteady pipe flow equations (Wylie and Streeter [15]) are

$$\frac{\partial(\rho S_p)}{\partial t} + \frac{\partial(\rho S_p c)}{\partial x} = 0$$

$$\frac{\partial(\rho c)}{\partial t} + \frac{\partial(\rho c^2)}{\partial x} = -\frac{\partial p}{\partial x} - \frac{\rho f}{D_p}\frac{1}{2}\rho c|c| \tag{14}$$

where S_p is the section of the pipe and where the gravity forces are neglected here.

Using the method of characteristics (Brennen [16]), these two equations lead to a relation between flow rates at different time step and pressure measurements:

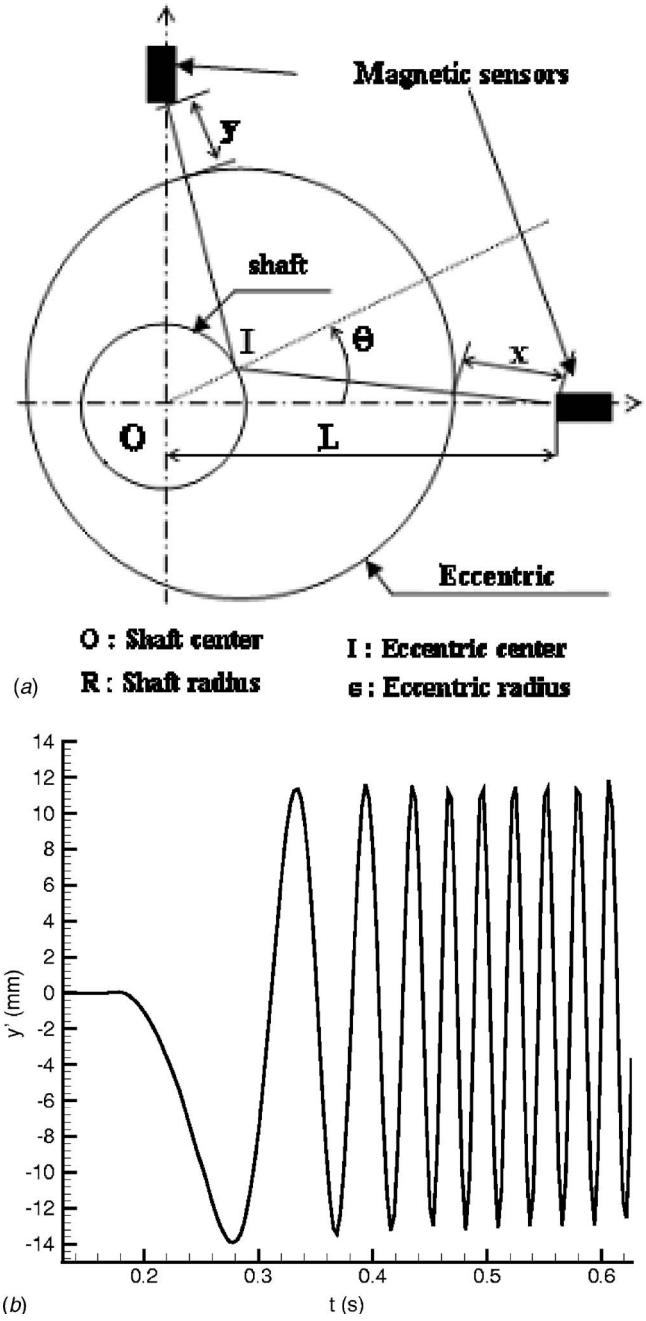

Fig. 5 Magnetic sensor implementation (*a*) and response (*b*)

$$\frac{Q_{ti+1} - Q_{ti-1}}{2dt} = \frac{S_p(p_{a\_ti} - p_{b\_ti})}{\rho dL} - \frac{f}{2D_p S_p}Q_{ti}|Q_{ti}| \tag{15}$$

where $Q_{ti-1}, Q_{ti}, Q_{ti+1}$ are the volume flow rates at three consecutive time steps, p_{a_ti}, p_{b_ti} are the pressure measurements of the two sensors at the time step ti, dt is the time interval between two acquisitions, and dL the distance between the two sensors.

The flow rate at the time step ti is deducted from Eq. (15) and the flow rate at the two previous time steps, as well as the pressure measurements of the two pressure sensors. The friction coefficient f is calculated at each time step, using the Colebrook formulas (Comolet [14]).

In order to evaluate the validity and the uncertainty of this method, the final flow rate obtained with this method is compared to the one obtained with an electromagnetic flow meter. The gap between the two flow rate measurements is less than 1%.

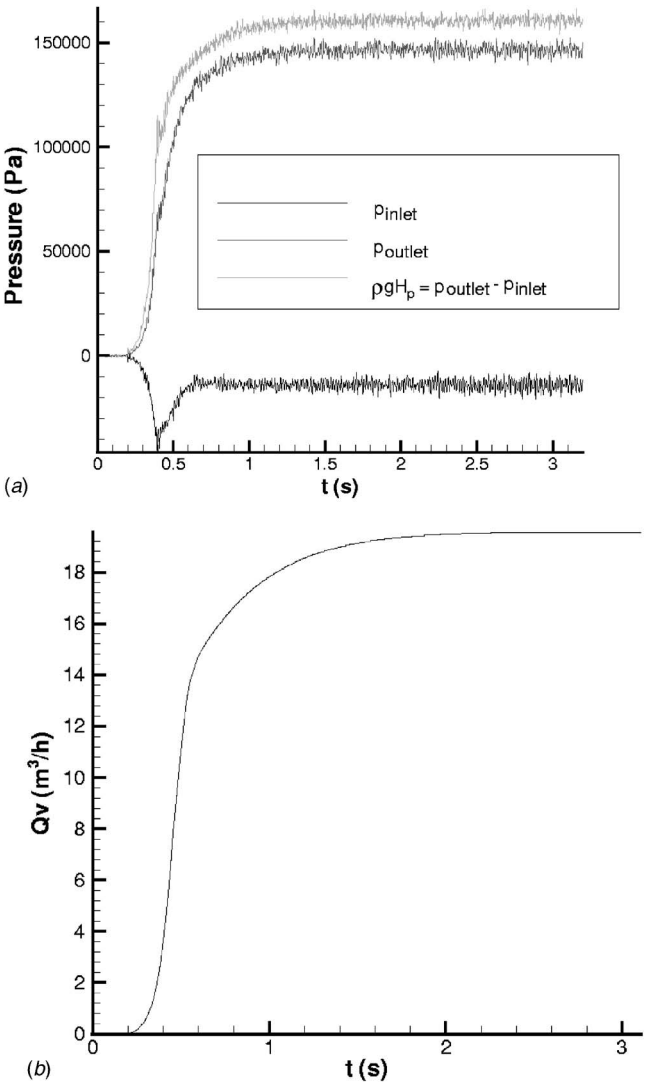

Fig. 6 Evolution of pressure at the inlet and the outlet of the pump (*a*); evolution of the flow rate (*b*)

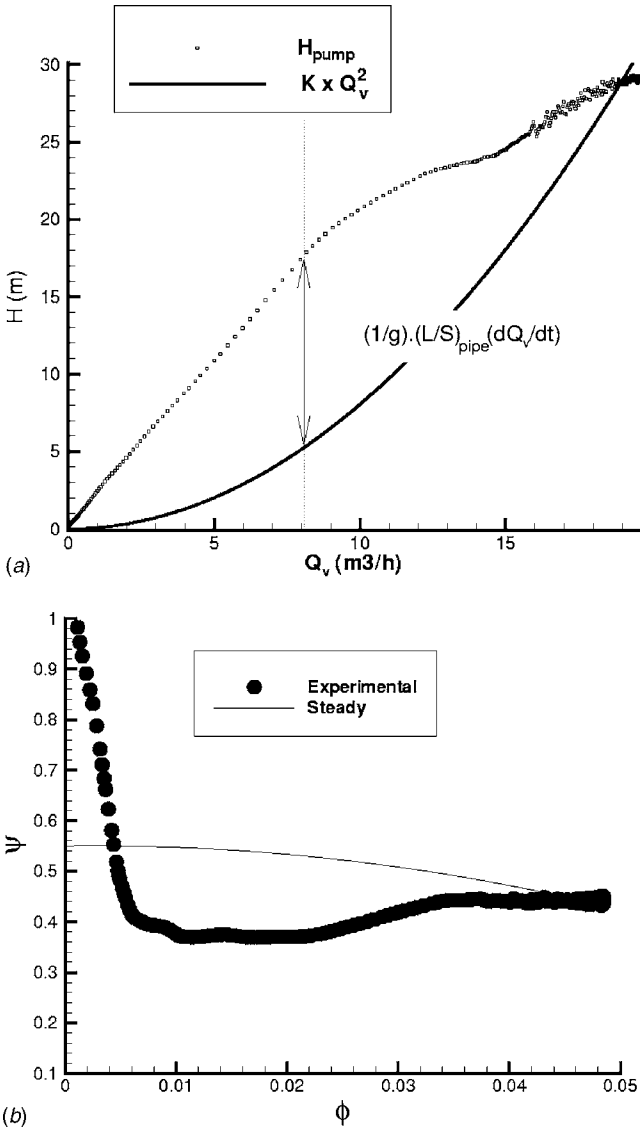

Fig. 7 (*a*) Evolution (H, Q_v) during a fast startup; (*b*) nondimensional evolution (ϕ, ψ) during a fast startup; experimental conditions 1.

3.1.3 Experimental Conditions. Various experimental conditions (final rotation speed, final flow rate, and acceleration rate) have been tested. They are summarized in Table 2.

The experimental conditions 1 (fast startup and nominal flow rate) are the reference conditions. The experimental conditions 2, 3, and 4 present variations of the rotation speed, the flow rate, and the acceleration rate with respect to conditions 1.

Typical dimensional (Q_v, H_{pump}) and nondimensional (ϕ, ψ) evolution of pressure and flow rate during a fast startup are presented Fig. 7:

Figure 7(*a*) presents the evolution of the total head as a function of the flow rate during a fast startup. The total head is higher than the classical parabola representing the resistance of the system (the resistance of the pipes is supposed to be equal to $H_{\text{losses}} = KQ_v^2$, where K is a constant). It is evaluated for the final operating point, and consequently, the evolution of total head during a quasisteady startup. At each time, the total head of the pump can be written as

$$H_{\text{pump}} = KQ_v^2 + \frac{L_{\text{pipe}}}{S_{\text{pipe}}}\frac{\partial Q}{\partial t}$$

If the flow acceleration is known and assuming that $H_{qs} = KQ_v^2$, the gap between the two curves is due to the inertial effects in the pipes of the system.

Figure 7(*b*) shows the evolution of the pressure coefficient. At the very beginning of the startup, the total pressure coefficient is much larger than the steady value whereas, in the following period of the startup, it becomes smaller than the steady value (as already mentioned by Tsukamoto and Ohashi [3]).

Table 2 Experimental conditions

Test reference	Final rotation speed (rpm)	Final flow rate (m^3/h)	Mean acceleration rate (rad/s^2)
1	2391	19.5 (Q_n)	967
2	1793	14.7 (Q_n)	928
3	2391	28.62 (1.5 Q_n)	878
4	2408	19.27 (Q_n)	29

3.2 Description of the Model. A model based on Eq. (12) is used to predict the instantaneous value of the total head during the

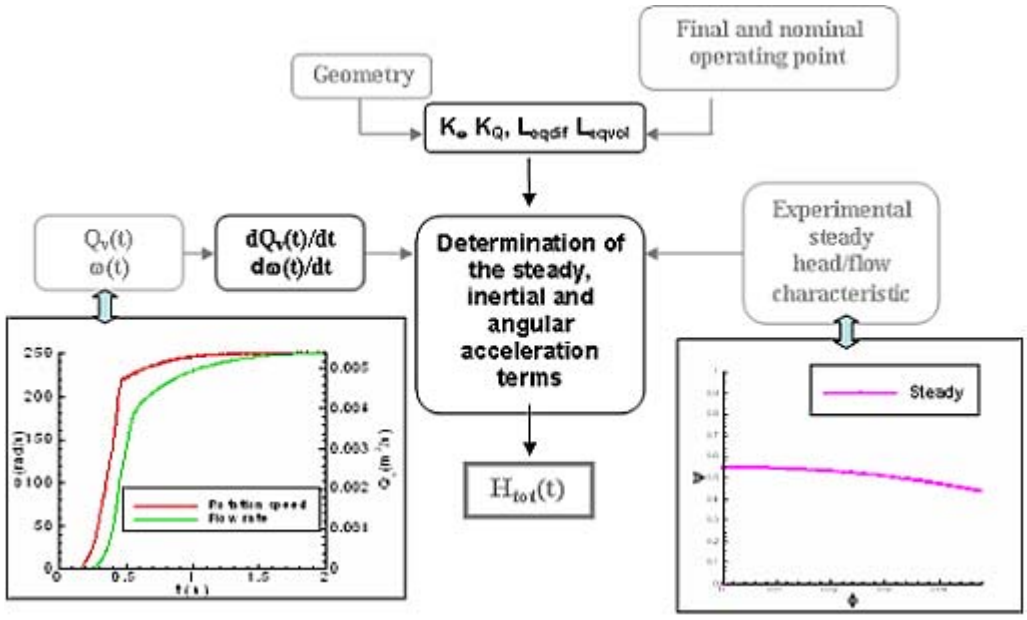

Fig. 8 Model

startup periods of the pump described in the previous paragraph.

Additional hypothesis are presented, in order to evaluate the terms of Eq. (12).

(1) As this is a radial flow pump, the meridional velocity is supposed to be radial in the impeller, that is $c_m = c_r$ in Fig. 1.
(2) The radial component c_r of the velocity is supposed to be depending only on the radial position and the time.
(3) The relative flow angle β is supposed to depend only on the radial position. It is supposed as follows:

- To be equal to the vane angle at the inlet.
- to be equal to the outlet vane angle corrected by the Wiesner slip factor (at nominal conditions) at the outlet.

Wiesner [17] gives the value of the slip factor:

$$\sigma = \frac{C_{u2}}{C_{u2\infty}} = 1 - \frac{\sqrt{\sin \beta_{2b}}}{Z^{0.7}} \tag{16}$$

In the case of radial flow pumps for which the outer radius to inner radius ratio is

$$\frac{R_2}{R_1} > \exp\left(\frac{8.16 \sin \beta_{2b}}{Z}\right) \tag{17}$$

- To be equal to $\beta(r) = \beta_b(r) + \beta_2 - \beta_{2b}/(R_2 - R_1)(r - R_1)$ between the inlet and the outlet of the impeller. (The difference between $\beta(r)$ and the vane angle is then supposed to be a linear function of r between the inlet and the outlet.)

(4) The inertial effects in the diffuser and the volute are modeled by two equivalent pipe lengths and sections. These lengths are supposed to be constant and equal to the ones at the final operating point.

- The equivalent pipe length of the diffuser is taken as the length of a logarithmic spiral whose angle is taken equal to the absolute flow angle estimated at the inlet of the diffuser in steady and nominal conditions.
- The equivalent pipe length of the volute is estimated from the geometrical data.
- The equivalent sections of the diffuser and the volute are the mean sections of these two components.

(5) The hydraulic losses during transient operations, as well as the velocity profiles at the inlet and outlet of the impeller at a given operating point (ω, Q), are supposed to be equal to the ones in steady operations at the same operating point. Consequently, the value of the term

$$\frac{1}{gQ_v}\left[\iint_{S_e}(uc_u - e)c_r dS_e\right]$$

in transient operations is considered to be equal to the total head of the pump operating under steady conditions. It is defined as the steady state head (H_s) in this paper. H_s is given by the expression

$$\frac{gH_s}{R_2^2\omega^2} = a_1\left(\frac{Q_v}{R_2^3\omega}\right)^2 + a_2\frac{Q_v}{R_2^3\omega} + a_3$$

Constants a_1, a_2, a_3 are estimated through experimental results of the pump in steady operations.

(6) The variation of entropy with time is neglected.

The total head thus becomes

$$H_{\text{pump}} = H_s + \frac{1}{g}\left(K_\omega\frac{\partial\omega}{\partial t} - K_Q\frac{\partial Q_v}{\partial t} - \frac{L_d}{A_d}\frac{\partial Q_v}{\partial t} - \frac{L_{\text{vol}}}{A_{\text{vol}}}\frac{\partial Q_v}{\partial t}\right) \tag{18}$$

with

$$K_\omega = \left[\int_{R1}^{R2}\frac{rdr}{\tan\beta(r)}\right] \text{ and } K_Q = \left[\frac{1}{4\pi}\int_{R1}^{R2}\left(\frac{dr}{rb(r)\sin^2\beta(r)}\right)\right]$$

which are two constant parameters.

The total head is thus the sum of three terms:

(1) a steady term
(2) an angular acceleration term which will increase the total head for positive angular accelerations
(3) an inertial term including the inertial effects in the impeller, the diffuser, and the volute. This term decreases the total head for positive flow accelerations.

This equation is the basis of the model schematically presented Fig. 8.

The geometry of the impeller and the nominal and final condi-

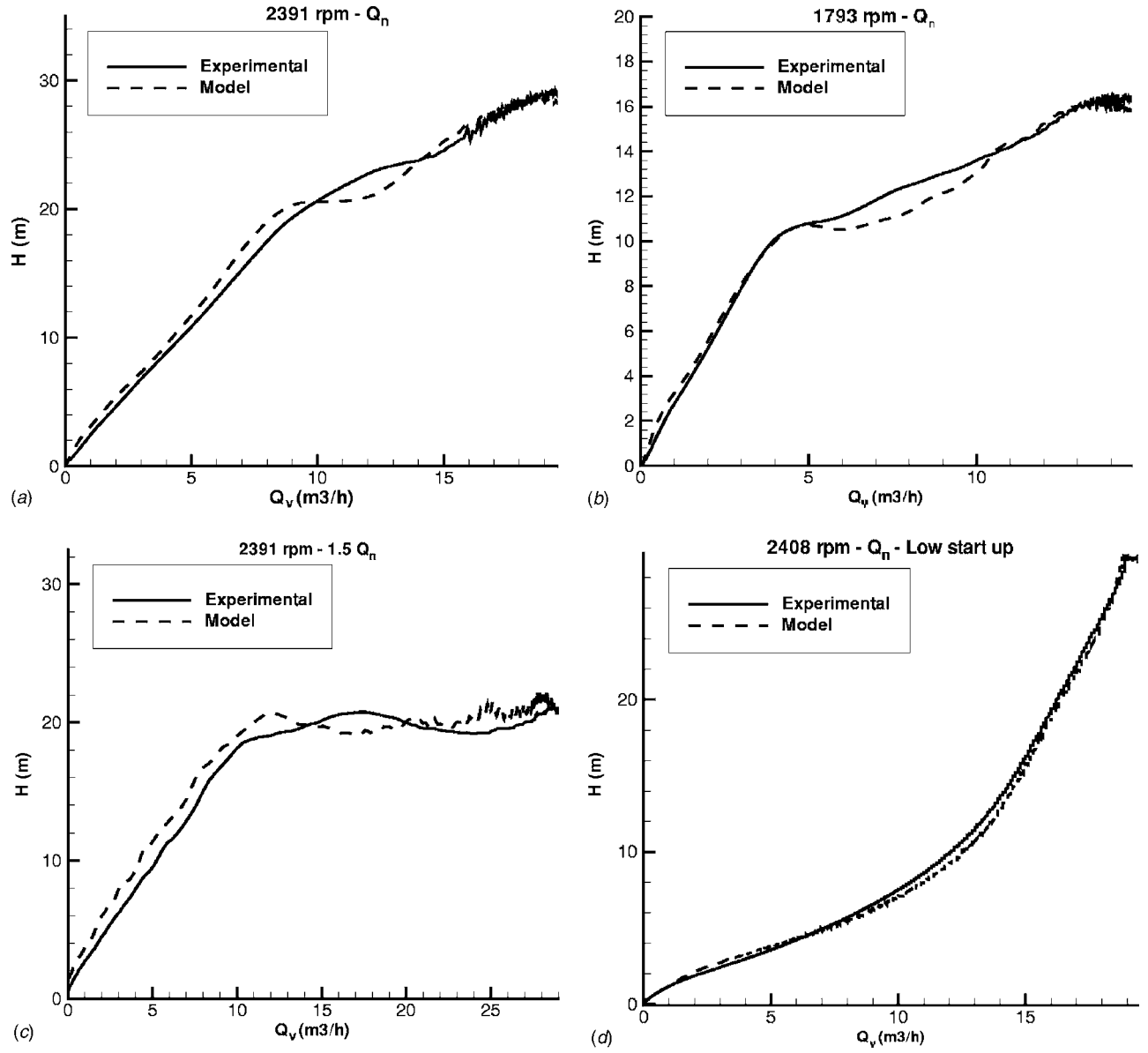

Fig. 9 Comparison between experimental and model results

tions are needed in order to evaluate the inertial and angular acceleration terms. At each time step, the flow rate and rotation speed are taken from experimental results. They are used to evaluate the steady total head, the flow and angular accelerations, and finally the transient total head.

3.3 Comparison Between the Model and the Experimental Results. The results of this model are compared to experimental results for the various experimental conditions (Fig. 9). The model predictions are good in all cases. The difference between the experimental and theoretical results never exceeds 5%. However, it overestimates the total head in the first stage of the startup (0–8 m^3/h, 0–4 m^3/h, and 0–12 m^3/h, respectively, for experimental conditions 1, 2, and 3) and underestimates it in a second stage. These differences can mainly be attributed to the hypothesis on the flow inside the impeller presented at the beginning of Sec. 3.2 and on the modeling of the inertial effects in the vaneless diffuser. These models can certainly be improved but additional experiment results on the velocity profiles and pressure evolutions in the impeller, the diffuser, and the volute would be useful to provide more realistic hypothesis to the model.

3.4 Analysis. The results are detailed and analyzed for experimental conditions 1. The contribution of the steady, angular acceleration, and inertial terms are plotted as a function of the instantaneous flow rate (Fig. 10(*a*)). It appears that the unsteady effects are not negligible during all the startup, and that the inertial effects are, for this pump, more important than the angular acceleration ones. The inertial effects are more important in the stator than in the rotor. Their relative contributions are 15% for the impeller, 40% for the diffuser, and 45% for the volute. For a low acceleration rate (Fig. 9(*b*)), the unsteady effects are negligible (Fig. 10(*b*)).

The model is then used to describe the various mechanisms leading to the evolution of the total head of the pump during a fast startup. The evolution of the pressure coefficient with time is plotted Fig. 11(*a*). It is compared with the rotation speed, flow rate, and steady head coefficient evolutions. A (Φ,Ψ) diagram is also presented Fig. 11(*b*). At the very beginning of the startup (0 s $< t <$ 0.11 s), the pressure coefficient is largely higher than the steady one for low value of ϕ (Figure 11(*b*)). This very short period corresponds to a phase where there is a strong rotation

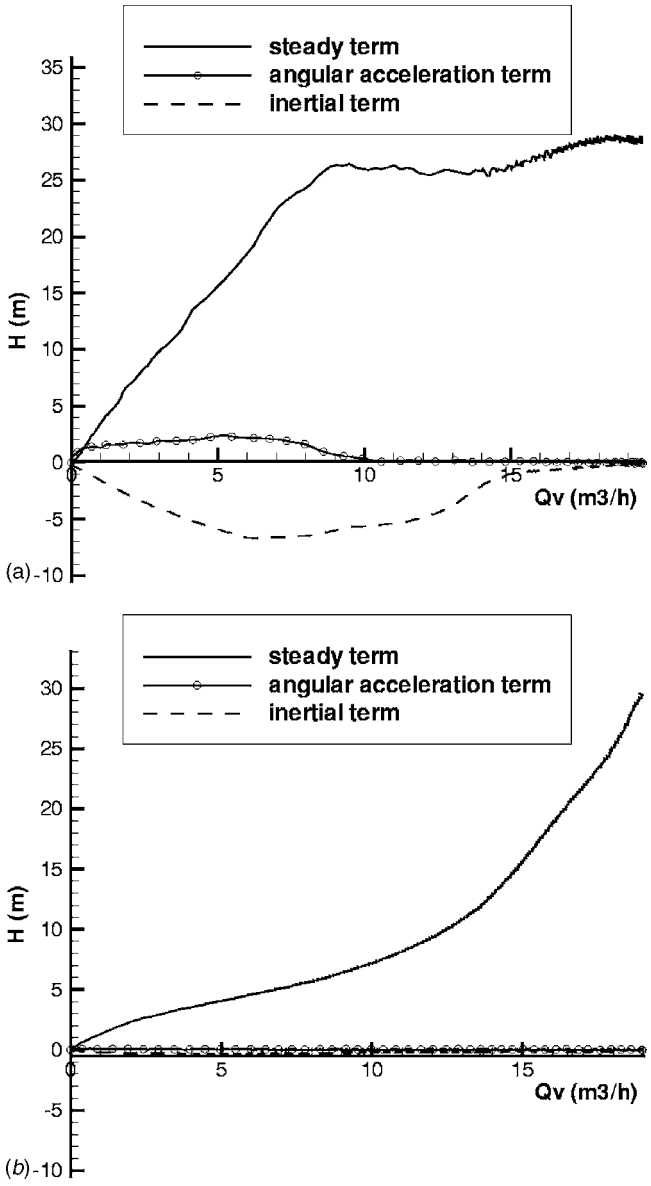

Fig. 10 Evolution of the steady, angular acceleration terms as a function of the flow rate; (*a*) experimental conditions 1; (*b*) experimental conditions 4.

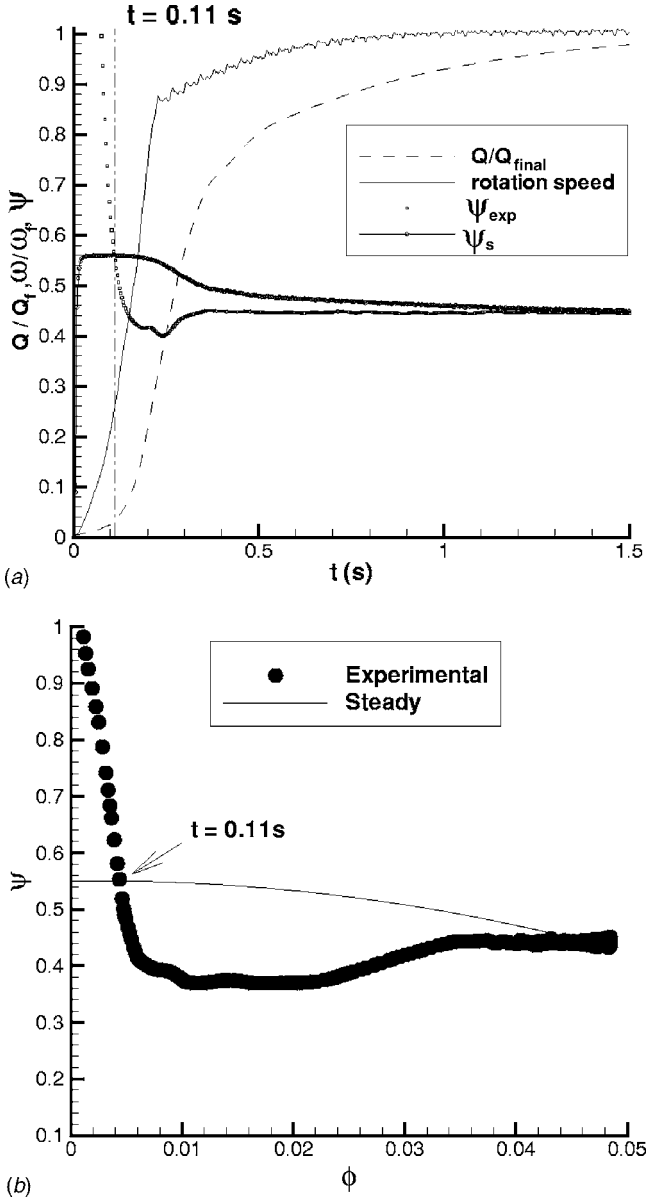

Fig. 11 (*a*) Evolution of the total and steady pressure coefficient, rotation speed, and flow rate with time; (*b*) evolution of the pressure coefficient with the flow coefficient; experimental conditions 1

speed gradient associated with very small flow rate variations. Therefore, the angular acceleration effects are dominant and according to Eq. (15), the total head and the pressure coefficient are much higher than steady ones. In the next stage of the startup ($0.11\ \text{s} < t < 1\ \text{s}$), the flow rate and the rotation speed both grow, and so do the unsteady effects. However, since the inertial effects are more important than the angular acceleration ones (Fig. 10), the pressure coefficient during this period is lower than the steady one. It then tends to its final and steady value and then stays more or less steady. At the same time, the flow rate and flow coefficient grow to reach their final value.

After $t = 1$ s, the inertial and acceleration terms become negligible compared with the steady term. And the flow and pressure coefficient are very close to the steady characteristic curve.

4 Conclusion

A model based on the angular momentum and energy equation is proposed to give a prediction of the internal torque (Eq. (5)), power (Eq. (11)), and impeller head (Eq. (12)) for an incompressible flow turbomachinery operating in transient conditions. The last equation is used to predict the total head evolution of a single stage, volute type radial flow pump during fast startup periods. The model results are compared to experimental ones. It shows that this new model fits well with experimental results. The model is then used to analyze the head coefficient evolution during a fast startup. This one begins with a short period during which the transient head coefficient is very much higher than the steady one. This is due to a strong angular acceleration associated with very little flow variation. It results a dominant influence of the angular acceleration effects, which increases the total head. On the other hand, the next stage of the startup is characterized by a great flow acceleration. The inertial effects become then dominant and the head coefficient becomes rapidly smaller than the steady one.

The model may certainly be improved by a better evaluation of losses, flow profiles, and of equivalent pipe lengths. However, it would be interesting to undergo new experiments including torque measurements, more unsteady pressure measurements, and par-

ticle image velocimetry (PIV) in order to support hypothesis, which are made on the flow and to validate more accurately the predictions.

Nomenclature

Roman Letters

- A = cross-sectional area (m^2)
- b = vane width (m)
- $\mathbf{c}$ = fluid velocity in the nonrotating frame (Fig. 1) ($m\ s^{-1}$)
- e = specific internal energy (J/kg)
- f = friction coefficient
- $\mathbf{F}$ = volume force ($m\ s^{-2}$)
- g = acceleration due to gravity ($m\ s^{-2}$)
- H = Total head (m)
- I_z = the moment of inertia about $O\vec{z}$ of the fluid which is inside the impeller
- L = distance from the magnetic sensor to the eccentric (m)
- L = equivalent length (m)
- $\mathbf{M}$ = point belonging to a volume V
- $\mathbf{O}$ = origin of the coordinate system
- p = pressure (Pa)
- Q = Volume flow rate (m^3/s)
- r = radial coordinate (m)
- R = radius (m)
- S = surface (m^2)
- S = entropy ($J\ K^{-1}$)
- t = time (s)
- T = temperature (K)
- T = torque (N m)
- u = peripheral velocity ($u=\omega R$) (Fig. 1) ($m\ s^{-1}$)
- V = control volume (m^3)
- w = fluid velocity in the rotating frame (Fig. 1) ($m\ s^{-1}$)
- $\mathbf{z}$ = axial coordinate (m)
- Z = number of blades

Greek Letters

- β = relative flow angle (measured from tangential direction) (rad)
- ε = shaft radius (m)
- ϕ = flow coefficient: $\phi=c_{r2}/u_2$
- ψ = head coefficient. $\psi=H/gu_2^2$
- Π = power (W)
- σ = slip factor
- ρ = fluid density ($kg\ m^{-3}$)
- $\boldsymbol{\tau}$ = stress ($N\ m^{-2}$)
- θ = azimuthal coordinate
- Θ = heat per unit of surface ($J\ m^{-2}$)
- ν = kinematic viscosity ($m^2\ s^{-1}$)
- ω = angular rotation speed ($rad\ s^{-1}$)

Subscripts

- 1 = value at impeller inlet
- 2 = value at impeller outlet
- b = blade
- dif = diffuser
- i = internal
- imp = impeller
- m = meridional component
- n = nominal
- p = pipe
- pump = pump
- r = component in the radial direction
- tot = total
- u = component in the azimuthal direction
- vol = volute

References

[1] Bergant, A., Simpson, A. R., and Tijsselin, A. S., 2006, "*Water Hammer With Column Separation: A Historical Review*," J. Fluids Struct., **22**(2), pp. 135–171.

[2] Venturini, M., 2005, "Development and Experimental Validation of a Compressor Dynamic Model," ASME J. Turbomach., **127**(3), pp. 599–608.

[3] Tsukamoto, H., and Ohashi, H., 1982, "Transient Characteristics of a Centrifugal Pump During Starting Period," ASME J. Fluids Eng., **104**, pp. 6–14.

[4] Saito, S., 1982, "The Transient Characteristics of a Pump During Start Up," Bull. JSME, **25**(201), pp. 372—379; paper No. 201–10.

[5] Ghelici, N., 1993, "Etude du régime transitoire de démarrage rapide d'une pompe centrifuge," Ph.D. Thesis, Ecole Nationale Supérieure d'Arts et Métiers.

[6] Bolpaire, S., 2000, "Etude des écoulements instationnaires dans une pompe en régime de démarrage ou en régime établi," Ph.D. thesis, Ecole Nationale Supérieure des Arts et Métiers..

[7] Lefebvre, P. J., and Barker, W. P., 1995, "Centrifugal Pump Performance During Transient Operation," ASME J. Fluids Eng., **117**, pp 123–128.

[8] Tsukamoto, H., Matsunaga, S., and Yoneda, H., 1986, "Transient Characteristics of a Centrifugal Pump During Stopping Period," ASME J. Fluids Eng., **108**(4), pp. 392–399.

[9] Picavet, A., 1996, "Etude des phénomènes hydrauliques transitoires lors du démarrage rapide d'une pompe centrifuge," Ph.D. thesis, Ecole Nationale Supérieure d'Arts et Métiers.

[10] Tsukamoto, H., Yoneda, H., and Sagara, K., 1995, "The Response of a Centrifugal Pump to Fluctuating Rotational Speed," ASME J. Fluids Eng., **117**, pp 479–484.

[11] Tanaka, T., and Tsukamoto H., 1999, "Transient Behaviour of a Cavitating Centrifugal Pump at Rapid Change in Operating Conditions—Part 1: Transient Phenomena at Opening/Closure of Discharge Valve," ASME J. Fluids Eng., **121**, pp. 841–849.

[12] Tanaka, T., and Tsukamoto H., 1999, "Transient Behaviour of a Cavitating Centrifugal Pump at Rapid Change in Operating Conditions—Part 2: Transient Phenomena at Pump Start-up/Sutdown," ASME J. Fluids Eng., **121**, pp. 850–856.

[13] Tanaka, T., and Tsukamoto H., 1999, "Transient Behaviour of a Cavitating Centrifugal Pump at Rapid Change in Operating Conditions—Part 3: Classifications of Transient Phenomena." ASME J. Fluids Eng., **121**, pp. 857–865.

[14] Comolet, R., 1963, "Mécanique expérimentale des fluides, Tome II: Dynamique des fluides réels, Turbomachines," Masson et Cie.

[15] Wylie, E. B., and Steeter, V. L., 1978, *Fluid Transients*, Mc-Graw-Hill, New York.

[16] Brennen, C. E., 1994, *Hydrodynamics of Pumps*, Oxford University Press and Concepts, ETI Inc., Oxford.

[17] Wiesner, F. J., 1967, "A Review of Slip Factors for Centrifugal Impellers," ASME J. Eng. Power, **89**, pp. 558–572.

A. Olivieri

F. Pistani

INSEAN,
National Ship Research Institute,
Via di Vallerano 139,
00128 Rome, Italy

R. Wilson
IIHR, Hydroscience & Engineering,
The University of Iowa,
Iowa City, Iowa 52242-1585;
UT SimCenter,
The University of Tennessee at Chattanooga,
Chattanooga, TN 37403

E. F. Campana
INSEAN,
National Ship Research Institute,
Via di Vallerano 139,
00128 Rome, Italy

F. Stern
IIHR, Hydroscience & Engineering,
The University of Iowa,
Iowa City, IA 52242-1585

Scars and Vortices Induced by Ship Bow and Shoulder Wave Breaking

Experimental data are provided for physical understanding and computational fluid dynamics (CFD) validation for the surface combatant David–Taylor model basin Model 5415 bow and shoulder wave breaking. A photographic study was conducted using 5.72 m *replica and* 3.05 m *geosim models of Model 5415 over a range of Froude numbers (Fr) to identify Fr and scale effects on wave breaking and choose the best Fr for the local flow measurements, which include near- and far-field means and rms wave elevation and mean velocity under the breaking waves. The larger model and* Fr=0.35 *were selected due to the large extents of quasisteady plunging bow and spilling shoulder wave breaking. A direct correlation is shown between regions of wave slope larger than* 17 deg *and regions of large rms in wave height variation. Scars characterized by sudden changes in the mean wave height and vortices induced by wave breaking were identified. Complementary CFD solutions fill the gaps in the relatively sparse measurements enabling a more complete description of the bow and shoulder wave breaking and induced vortices and scars. The combined results have important implications regarding the modeling of the bubbly flow around surface ships, especially for bubble sources and entrainment.* [DOI: 10.1115/1.2786490]

1 Introduction

The importance of wave breaking on ship bow, shoulder, and stern waves has long been recognized. Baba [1] identified the large contribution of bow wave breaking to resistance. Miyata and Inui [2] and Doi et al. [3] studied the structure of bow and stern wave breaking, respectively, making the analogy to oblique shock waves. More recently, Dong et al. [4] and Roth et al. [5] performed particle-image-velocimetry (PIV) measurements and free surface visualizations on bow wave breaking with focus on the initial formation of the bow wave sheet prior to the plunging breaking. Longo and Stern [6] performed mean velocity measurements using a five-hole Pitot and wave elevation measurements using capacitance wires and point gauges for the static drift condition showing the presence of a bow wave breaking induced vortex on the windward side of the model. Tulin and Landrini [7] described some aspects of the ship bow wave breaking by using the 2D+t parabolic approach combined with a meshless Euler solver. By using a single-phase level set approach implemented into a Reynolds-averaged Navier–Stokes (RANS) solver, Di Mascio et al. [8] showed for the first time the impact of the bow wave breaking on the free surface with splash-up as the jet impinges on the free surface. In general, ship wave breaking includes both spilling (steady) and plunging (unsteady) breakers (see Ref. [9] and literature cited therein). Whereas theory and modeling of the former is fairly well developed (see Refs. [10,11] and Ref. [12] for two-dimensional (2D) and three-dimensional (3D) models, respectively), detailed physical description and accurate modeling are lacking for the latter. The requirements of reduced signatures for current ship designs provides additional motivation for improved physical understanding, modeling, and CFD prediction capability of ship wave breaking and air bubble sources and entrainment [13].

The objectives of the present research are to provide physical understanding and CFD validation experimental data for bow and shoulder wave breaking as part of a long term international collaboration between IIHR-Hydroscience & Engineering (IIHR) and the Italian Ship Model Basin (INSEAN) concerning complementary computational fluid dynamics (CFD), experimental fluid dynamics (EFD), and uncertainty analysis for ship hydrodynamics [14]. The geometry of interest is the surface combatant David–Taylor model basin (DTMB) Model 5415, shown in Fig. 1. A photographic study was conducted using 5.72 m replica and 3.05 m geosim models of Model 5415 over a range of Froude numbers (Fr) to identify Fr and scale effects on wave breaking and choose the best Fr for the local flow measurements, which include near- and far-field means and rms wave elevation and mean velocity under the breaking waves. The larger model and Fr=0.35 were selected for the local flow measurements due to the large extents of quasisteady plunging bow and spilling shoulder wave breaking. Scars and vortices induced by wave breaking were identified. Complementary CFD solutions fill the gaps in the relatively sparse measurements enabling a more complete description of the bow and shoulder wave breaking and induced vortices and scars. The present paper describes the experimental methods and procedures, uncertainty analysis and descriptions of Fr and scale effects, and detailed local flow measurements for Fr=0.35, including explication of the scars and vortices using the complementary CFD. Details of the complementary CFD are provided by Ref. [15], including additional results for lower Fr=0.28 and higher Fr=0.41.

Contributed by the Fluids Engineering Division of ASME for publication in the JOURNAL OF FLUIDS ENGINEERING. Manuscript received April 17, 2006; final manuscript received June 7, 2007. Review conducted by Yu-Tai Lee.

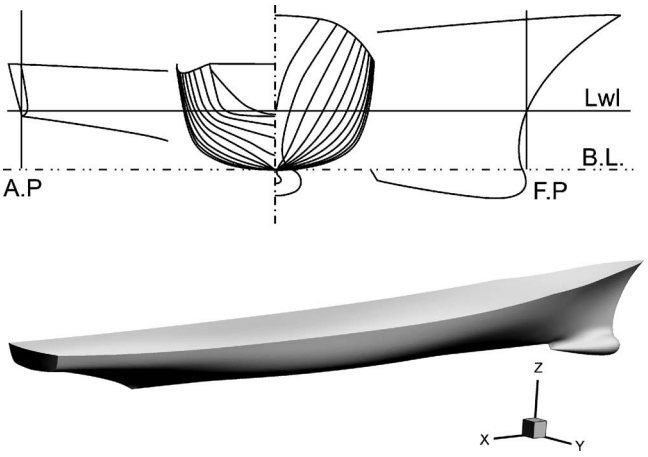

Fig. 1 Cross sections and profile views of IIHR Model 5512 and INSEAN Model 2340 with reference frame

2 Test Design

The tests were conducted at INSEAN using INSEAN Model 2340 (5.720 m long, $\lambda=24.824$), which is a replica of the DTMB Model 5415. A photo study of the wave breaking pattern was conducted for Fr varying from Fr=0.28 (design speed) to Fr =0.45, including Fr=0.41 (flank speed). A similar photo study was conducted in parallel at IIHR using a smaller IIHR Model 5512 with the same geometry (3.048 m long, $\lambda=46.6$) for comparison and evaluation of scale effects. DTMB Model 5415 is an internationally recognized ship hydrodynamics benchmark for CFD validation, which has a bulbous bow and transom stern. Additionally, relevant photographs of full-scale wave breaking for similar geometry and conditions are used to compare model and full-scale flows. The Fr=0.35 condition for the local flow measurements on Model 2340 was selected based on the photo studies. The near-field mean and rms wave elevation were measured from the bow to about amidships by single point measurements using a finger probe. The far-field mean wave elevation was reconstructed by longitudinal wave cuts that were obtained by means of an array of capacitance wire wave gauges mounted on a sliding guide. The measurements of the three components of the mean velocity field were carried out by a five-hole Pitot probe on four cross planes along the port side of the model in correspondence of the location of both the bow and the shoulder wave breaking. The uncertainty assessment was evaluated for the wave elevation and flow velocity measurements. The reference coordinates are fixed to the hull with the origin at the intersection of the forward perpendicular with the undisturbed water plane. The x, y, and z axes are, respectively, in the downstream direction, the starboard side of the hull, and upward, as shown in Fig. 1. All lengths and velocities are normalized by using the model length between perpendiculars L_{PP} and the model speed U_c, respectively.

2.1 Facilities. The INSEAN 200 m long, 9 m wide, and 3.6 m deep basin is equipped with a single drive carriage capable of speeds up to 10 m/s. Sidewall and end-wall beaches enable 20 min intervals between carriage runs. The IIHR towing tank is 100 m long, 3.048 m wide, and 3.048 m deep and equipped with an electric-motor operated drive carriage, pulled by a cable driven by a 15 hp motor and capable of maximum speeds of 3 m/s. Sidewall and end-wall beaches enables 12 min intervals between carriage runs. Both the INSEAN and IIHR towing tanks use fresh water whose salinity is less than 0.5 ppt (parts per trillion), while for sea water it is about 30 ppt. This difference mainly influences the amount of air entrainment in the breaking waves. Table 1 summarizes the IIHR and INSEAN facilities, water quality, and physical quantities.

Table 1 Towing tank dimensions, water quality and physical quantities

Towing Tanks			
		IIHR	INSEAN
Length (m)		100	220
Width (m)		3.048	9
Depth (m)		3.048	3.6
Water Quality and Physical Quantities			
		IIHR	INSEAN	Full scale
Water type	—	Tap water	Spring water	Sea water
Water density	ρ (kg/m^3)	999	998.5	1030[a]
Kinematic viscosity	ν (m^2/s)	1.12×10^{-6}	1.09×10^{-6}	1.17×10^{-6}
Surface tension	σ (N/m)	0.0734	0.0734	0.0734
Salinity	ppt	<0.5	<0.5	≈30
Gravity acceleration	g (m/s^2)	9.8031	9.8033	9.806[a]
Test temperature	T (°C)	15.6	16.6	—

[a]Data taken from literature.

2.2 Model Geometries. The geometric data of Models 5512 and 2340 are given in Table 2. All tests were performed in the bare hull condition. INSEAN Model 2340 was constructed in 1998 at the INSEAN model workshop from laminated wood with a CNC machine. The turbulence stimulation is composed of cylindrical studs having 3.0 mm diameter, 3.0 mm height, spaced 30.0 mm, and positioned at $x=0.05$. IIHR Model 5512 was constructed in 1996 at the DTMB model workshop from molded fiber-reinforced Plexiglas. Turbulence stimulation, at $x=0.05$, is obtained with cylindrical studs having 3.2 mm diameter, 1.6 mm height, and 10.0 mm spacing. The measurement system for estimating the error in the geometry offsets consists of computer-aided design, hand-cut templates, level table, right angle, plumb, rulers, and feeler gauges. The data are reduced by computing the crossplane and global averaged values of the offset error for each coordinate and for the surface area.

2.3 Conditions for Local Flow Measurements for Model 2340. Special consideration was given to surface tension effects, which, depending on the size and speed of the model, can inhibit wave breaking and air entrainment. Photographic studies showed that fairly steady well-developed breaking conditions occur for Model 2340 in the Fr range of 0.3–0.4. The flow pattern was nearly steady at Fr=0.3, but the extent of the breaking was not very large and its intensity was not very high. At a higher velocity Fr=0.41, the wave breaking extent and intensity were both larger, whereas the flow pattern was observed to be less steady. Eventually, Fr=0.35 was selected for the local flow measurements as a trade-off among the opposite needs of having an extended region of wave breaking but also a relatively steady wave pattern. During the tests, the model was held fixed with sinkage and trim set to the

Table 2 Geometry data for Model 5512, Model 2340, and full-scale ship

Parameters		5512	2340	Full scale
Scale factor	λ	46.6	24.824	1
Length between perpendiculars	L_{PP} (m)	3.048	5.720	142.0
Beam	B (m)	0.406	0.760	18.9
Draft	T (m)	0.132	0.248	6.16
Displacement	Δ (tons)	0.083	0.550	8636.0
Displaced Volume	∇ (m^3)	0.083	0.550	8425.4
Wetted surface area	S_W (m^2)	1.358	4.786	2949.5
Hull Coefficients				
L_{PP}/B	7.530	$C_B=\nabla/(L_{PP}BT)$		0.506
B/T	3.091	$C_P=\nabla/(L_{PP}A_X)$		0.613
Entrance angle α (deg)	11.0	$C_X=A_X/BT$		0.825

Table 3 Test conditions for wave elevation and mean velocity measurements for model 2340

Test Conditions	
Towing tank	INSEAN
Speed (m/s)	2.621
Trim (deg) (fixed)	0.069
Sinkage (Lpp) (fixed)	0.0032
Other measured quantities	
Total resistance (N)	80.64
C_{TM}	$4.91E-03$
C_F (ITTC 57)	$2.84E-03$
C_R ($k=0$)	$2.07E-03$

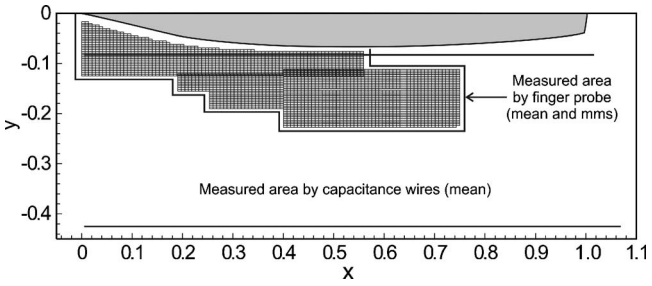

Fig. 2 Finger probe and capacitance wires measured area

values previously determined in unrestrained conditions [16]. Table 3 summarizes the test conditions for the local flow measurements for Model 2340.

3 Measurement Systems, Procedures, Locations, and Data Reduction Equations

3.1 Photographic Study. Photographs of the free surface around the bow were taken for a wide range of Fr=0.28, 0.3, 0.325, 0.35, 0.375, 0.41, and 0.45. The wave breaking is clearly observable on both model scales at all these conditions. Relevant full-scale photos at Fr=0.28 and Fr=0.35 are also shown for comparison.

3.2 Wave Elevation. The near-field wave elevations were obtained by pointwise measurements of the free surface elevation on a grid extending from the bow to about amidships using a servomechanic Kenek SH probe connected to a system of guides fixed to the carriage. Part of the port side of the model was cut off in order to measure the wave elevation as close as possible to the hull. The slope of the speed ramp of the carriage was lowered as much as possible in order to reduce the wave fluctuations due to the transient wave components that are generated at the start. The time history and running mean and rms values corresponding to a point inside the breaking region at $x=0.15$, $y=-0.09$ show that the mean and rms converge to asymptotic values quite rapidly. Based on these results, the acquisition time interval of $t_a^{NF}=2.2$ s with a sampling rate $f_s^{NF}=1000$ Hz was used. The near-field free-surface measurements were carried out at the vertices of a regular grid with spacing $\Delta x^{NF}=4$ cm $\cong 0.007L_{PP}$, $\Delta y^{NF}=2$ cm $\cong 0.0035L_{PP}$. The longitudinal displacements (4 cm) were set by hand, while the transverse displacements (2 cm) were automatically actuated during the run of the carriage by a guide equipped with a controlled step motor. The system has a resolution of 200 steps per revolution through a maneuvering screw with a pitch of 10 mm, the final accuracy of the transverse displacements resulting in 0.05 mm.

The far-field wave elevations were obtained by capacitance wires fixed on the side of the tank, as described in Ref. [16]. The rms value of the wave elevation was not evaluated due to the limitations of the measuring technique. The distance between the longitudinal cuts in the far field was $\Delta y^{FF}=0.0017L_{PP}$. The axial resolution is determined from the sample rate ($f_s^{FF}=300$ Hz) and the carriage speed ($U_0=2.621$ m/s) as $\Delta x^{FF}=U_0/f_s^{FF} \cong 0.0015L_{PP}$. Figure 2 shows the areas measured by both the finger probe and the capacitance wires.

3.3 Mean Velocity. The mean velocity field was measured on the port side of the model at the x-station locations $0.15L_{PP}$, $0.2L_{PP}$, $0.4L_{PP}$, and $0.5L_{PP}$. A five-hole Pitot wake probe was used. This probe is less intrusive than the boundary layer probe used for the flow map at Fr=0.28 reported in Ref. [16]. A classical one component Pitot tube was used to measure the static pressure in the undisturbed flow region located sufficiently upstream from the model. Five Valydine DP15 differential pressure transducers were connected to the five Pitot holes and to the static pressure hole of the Pitot tube. The acquisition system ran automatically, during the carriage run, controlled by the same software used for the near-field wave elevation measurements. Two orthogonal guides, actuated by two step motors, drove the Pitot to the underwater measuring point. The two step motors have a resolution of 200 steps per revolution and the maneuvering screw has a pitch of 10 mm, so that the spatial resolution of the device is 0.05 mm in the vertical and transverse directions. The carriage speed signal was checked by the software before starting and during the acquisition. The acquisition started when the carriage speed was within a predefined range (±2.5 cm/s). A regular grid of square cells, whose side dimensions were $\Delta x_g^V=\Delta z_g^V=0.0025L_{PP}$, was used for measuring just below the free surface. The sampling rate was $f_s^V=100$ Hz. The acquisition time interval was set to $t_a^V=4-6$ s. The acquisition time interval was chosen in consideration of the time needed to have a steady average of the signal at various distances from the free surface. Three-velocity components and one pressure coefficient were calculated at each point through the calibration maps. The velocity components are u (axial), v (transverse), and w (vertical). They are normalized by the carriage velocity $U_c=2.621$ m/s. The measuring grid used for the midship section $x=0.5$ is shown in Fig. 3. The corresponding transverse wave cut and the boundary of the hull are also shown. The locations of the sections at which the velocity field was measured were chosen in order to investigate the flow produced by both the bow and shoulder wave breaking. The $x=0.15$ and $x=0.2$ sections were chosen to investigate the flow produced by the bow wave breaking. The $x=0.4$ section is the only one in which the flow resulting from both the bow and the shoulder wave breaking are included. The midship section $x=0.5$ was selected to examine the flow corresponding to the shoulder wave breaking. A perspective view of the locations of the investigated cross sections with respect to the wave field is shown in Fig. 4.

3.4 Data Reduction Equations. The wave elevation h data reduction equation (DRE) is

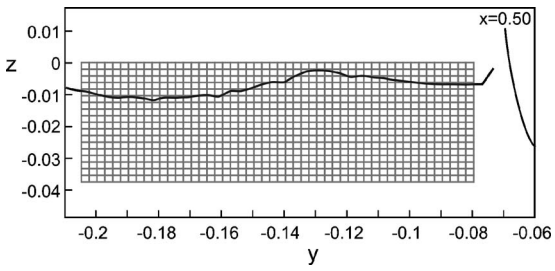

Fig. 3 Measurement grid at $x=0.5$

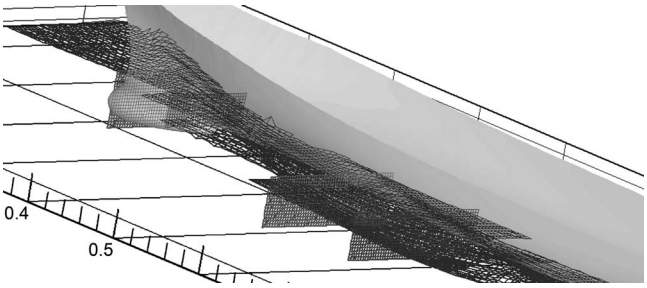

Fig. 4 Selected cross planes for the velocity measurements

$$h = \frac{K_K(e - e_0)}{L_{\mathrm{PP}}} \tag{1}$$

where e is the acquired voltage and K_K is the calibration coefficient. e_0 is the voltage related to the undisturbed free surface that was acquired before the start of every carriage run. The measurement system consisted of the Kenek SH servo-mechanic probe, a signal conditioner, a 2D traversing system, a 12 bit AD card, and a carriage personal computer (PC) for data acquisition. The measurement system was statically calibrated on the traverse guides to determine the voltage-wave elevation relationship.

The mean velocity and pressure field quantities (u, v, w, and C_p) were measured by the five-hole Pitot probe and differential pressure transducer system and acquired by a PC. Their respective DREs are

$$u(x,y,z) = (VX \cos \alpha_p \cos \phi_p + VY \sin \phi_p + VZ \sin \alpha_p \cos \phi_p)/U_c \tag{2}$$

$$v(x,y,z) = (-VX \cos \alpha_p \sin \phi_p + VY \cos \phi_p - VZ \sin \alpha_p \sin \phi_p)/U_c \tag{3}$$

$$w(x,y,z) = (VZ \cos \alpha_p - VX \sin \alpha_p)/U_c \tag{4}$$

$$C_p(x,y,z) = \frac{2(p - p_o)}{\rho U_c^2} = \frac{2H_c' - \rho PV'^2}{\rho U_c^2} \tag{5}$$

where VX, VY, and VZ are functions of the measured pitch and yaw angles (α, ϕ) of the velocity vector in the five-hole Pitot probe coordinates through the calibration coefficients. The Pitot was calibrated in a wind tunnel and more details on the coefficients, formulas, and procedures can be found in Ref. [16].

4 Uncertainty Assessment

The uncertainty assessment of the results for both the wave elevation and the mean velocity measurements included evaluation of the bias limit by taking into account the more important sources of error and the precision limit from repeated tests following the AIAA Standard S-071 1995 [17].

4.1 Wave Elevation. The wave elevation DRE is given in Eq. (1). The bias limit was evaluated based on the propagation of the elemental biases into the wave elevation bias, while the precision limit was evaluated using ten repeated tests directly on the wave elevation data. The wave elevation depends on a series of variables including the measuring point and the carriage velocity U_c:

$$h = f(K_K, e, e_0, L_{\mathrm{PP}}, x, y, U_c) \tag{6}$$

The sensitivity coefficients for the first four variables are as follows:

$$\theta_{K_K} = \frac{\partial h}{\partial K_K} = \frac{e - e_0}{L_{\mathrm{PP}}} \tag{7}$$

$$\theta_e = \frac{\partial h}{\partial e} = \frac{K_K}{L_{\mathrm{PP}}} \tag{8}$$

$$\theta_{e_0} = \frac{\partial h}{\partial e_0} = -\frac{K_K}{L_{\mathrm{PP}}} \tag{9}$$

$$\theta_{L_{\mathrm{PP}}} = \frac{\partial h}{\partial L_{\mathrm{PP}}} = -\frac{1}{L_{\mathrm{PP}}} h = -\frac{K_K(e - e_0)}{L_{\mathrm{PP}}^2} \tag{10}$$

The sensitivity coefficients related to the measuring point coordinates are obtained using the acquired data and finite differences:

$$\theta_x = \frac{\partial h}{\partial x} \tag{11}$$

$$\theta_y = \frac{\partial h}{\partial y} \tag{12}$$

The last term

$$\theta_{U_c} = \frac{\partial h}{\partial U_c} \tag{13}$$

should be determined for the measured field by performing the test at different speeds. Nonetheless, the velocity bias was neglected since the estimation of its bias limit is very small $\cong 3$ mm/s. The bias on e and e_0 was obtained by the ratio between the voltage range of the acquisition board (± 10 V) and its resolution (2^{12}). This value was normalized with the range used by the sensor $\Delta e = \pm 3$ V. This bias was present both on e and on e_0, thus the total bias due to the A/D conversion is obtained by $B_{\mathrm{A/D}} = \sqrt{2} B_e$. The bias on K_K is given by the manufacturer of the sensor as 0.2% and it was checked before and after the tests (B_{K_K} in Table 4). The bias on the model length is $B_{L_{\mathrm{PP}}} = 1$ mm and it was considered negligible with respect to the other elemental biases, as given in Ref. [16]. The biases on x and y, for each measuring point, were determined considering the sequence of the measurements needed to set the position of the sensor in the model reference frame ($B_x = 0.707$ mm, $B_y = 0.866$ mm). The evaluation of the sensor position with respect to the model involves many complicated measurements, including the use of squares and plumb line. For this reason, both the model and the sensor were dismounted every carriage run for the evaluation of the precision limit. In this way, the errors on the measuring point could be treated as random-type errors and they were automatically included in the h precision limit. The precision limit was determined at three different points: in the nonbreaking region ahead of the wave crest, close to the breaking wave crest where the water surface was somewhat unstable, and in the breaking region. The locations of the three points are reported in Table 4 together with the values of the considered biases $B_{\mathrm{A/D}}$ and B_{K_K}, the precision limits and the total uncertainties for the mean and for the rms value of the wave elevation.

4.2 Mean Velocities. The bias limit on the velocity was determined following the procedure elaborated in [16]. The elemental errors associated with the five pressure values acquired by the Pitot, the Pitot position with respect to the model, the preset angles, the flow angles, the carriage velocity, the coefficients, and the velocity gradient were considered for estimating the bias limit. Its value is comparable with the ones obtained in a previous study on the boundary layer flow of the same model at Fr=0.28 [16]. The precision limit was determined directly on the three-velocity components for a measuring point just under the breaking ($y = -0.1015$, $z = -0.005$) at section $x = 0.20$ and its value is comparable with the ones of the Fr=0.28 boundary layer data. Here the percentage values are lower because of the larger range of variation

Table 4 Uncertainty assessment results for the wave elevation: wave height (mean and rms) nondimensionalized using L_{PP}; uncertanties are in percentage of the related dynamic ranges ($\langle h \rangle$=−60.6 to 103 mm; $h_{rms\ max}$=11.3 mm)

x	y	$\langle h \rangle$	$\langle h_{rms} \rangle$	$U_{\langle h \rangle}$	$U_{h_{rms}}$
0.100	−0.09	3.91×10^{-3}	5.81×10^{-5}	$B_{A/D}$=0.21% B_{K_K}=0.20% P=0.26% U=0.40%	$B_{A/D}$=3.1% B_{K_K}=0.20% P=0.5% U=3.1%
0.125	−0.09	5.20×10^{-3}	7.96×10^{-5}	$B_{A/D}$=0.21% B_{K_K}=0.20% P=0.29% U=0.41%	$B_{A/D}$=3.1% B_{K_K}=0.20% P=0.70% U=3.1%
0.150	−0.09	9.07×10^{-3}	8.53×10^{-4}	$B_{A/D}$=0.21% B_{K_K}=0.20% P=0.56% U=0.63%	$B_{A/D}$=3.1% B_{K_K}=0.20% P=1.0% U=3.2%

of the transverse and vertical velocity components. Bias limit, precision limit, and total uncertainty are given in Table 5 for the points x=0.20, y=−0.1015, and z=−0.005.

5 Froude Number and Scale Effects

As already mentioned, the tests were performed in the range of medium and not too high Fr because for too low Fr the effect of the surface tension inhibits the formation of wave breaking and for too high Fr spray and unsteadiness in the free surface reduce the accuracy of the local flow measurements. A similar perspective and camera's field of view was used at both INSEAN and IIHR. The following provides an overview of the most important results. The complete results are provided by Ref. [18].

5.1 Photographic Study. Fr=0.28. Model 5512 (Figs. 5(*a*) and 5(*b*)) shows small regions of bow wave curling and a weak spilling-type breaking with capillary waves along the toe of the bow and shoulder waves. Model 2340 (Figs. 5(*c*) and 5(*d*)) shows more curling and a more developed spilling-type bow wave breaking. The role of the surface tension is shown by the enlarged view in Fig. 5(*e*). Moving downstream with the flow, the breaking grows in amplitude and ripples become visible just upstream of the "toe" of the wave similarly, as described in Ref. [19]. The shoulder wave breaking [not visible in Figs. 5(*c*) and 5(*d*)] is similar to a 2D spilling wave breaking for both of the models but the breaking for Model 2340 is more intense. Full-scale images taken from a helicopter are shown in Figs. 5(*f*) and 5(*g*) for comparison. Figure 5(*g*) shows that, even at this relatively low Fr, the full-scale bow wave is a well-developed spilling breaking wave with generation of spray, splash, and droplets, which leads to a significant production of white water. The shoulder wave is also a spilling breaker type with generation of white water along its crest.

Fr=0.3 and 0.325 (figures not shown). The free surface characteristics are similar to those of Fr=0.28, showing, however, a more extended bow breaking region and an increased curling of the bow wave close to the hull, especially for Model 2340. Furthermore, small longitudinal scar lines appear at the back of the bow wave. At Fr=0.3, Model 5512 shows a slightly more intense bow wave breaking, still affected by the action of the surface tension. The shoulder wave breaking is quite similar to the one observed at Fr=0.28, with the crest more swept back than in the previous case. Small scars form just behind the bow wave breaking. Model 2340 shows a more intense bow wave breaking with respect to Fr=0.28 and two pronounced streamlined scars appear on the free surface, although they disappear rapidly downstream. They will become more visible at higher Fr. At Fr=0.325, the breaking scenario is quite similar to the one observed at Fr=0.3 for both models, although a number of details begin to emerge: The bow wave breaking is more intense and the wake of the breaker extends further normal to the wave front, i.e., toward the hull. Small scale surface disturbances appear behind the breaking wave front.

Fr=0.35. At this Fr (Fig. 6), more details are identifiable. Model 5512 exhibits (Fig. 6(*b*)) a bow wave breaking. Moving along the crest of the bow wave, the wave front begins to rise at the extreme bow and a thick bulge grows onto the top of the bow wave, right upstream of the turbulence stimulators (the row of white dots in Fig. 6(*b*)). The air entrainment is still strongly limited by the action of the surface tension and no white water is visible. Figures 6(*c*) and 6(*d*) show downstream and upstream perspectives of the bow wave breaking for Model 2340. Large regions of the bow wave breaking show almost steady plunging breaking close to the hull and spilling breaking further from the hull. In Fig. 6(*c*), two

Table 5 Uncertainty assessment results for the three-velocity components at the measuring point (x=0.20, y=−0.1015, z=−0.005); U^*=2.621 m/s for the axial velocity component, while for transverse and vertical components U^* corresponds to their range of variation in the measured field

	$\langle u \rangle$	$\langle v \rangle$	$\langle w \rangle$
Velocity	2.45 m/s $0.94U_0$	−0.33 m/s $-0.12U_0$	0.06 m/s $0.02U_0$
Uncertainty	$B=1.99 \times 10^{-2}$ m/s $P=8.04 \times 10^{-3}$ m/s Unc.$=2.15 \times 10^{-2}$ m/s Unc./U^*=0.82%	$B=9.62 \times 10^{-3}$ m/s $P=2.59 \times 10^{-3}$ m/s Unc.$=9.96 \times 10^{-3}$ m/s Unc./U^*=1.63%	$B=9.52 \times 10^{-3}$ m/s $P=9.38 \times 10^{-4}$ m/s Unc.$=9.56 \times 10^{-3}$ m/s Unc./U^*=1.56%

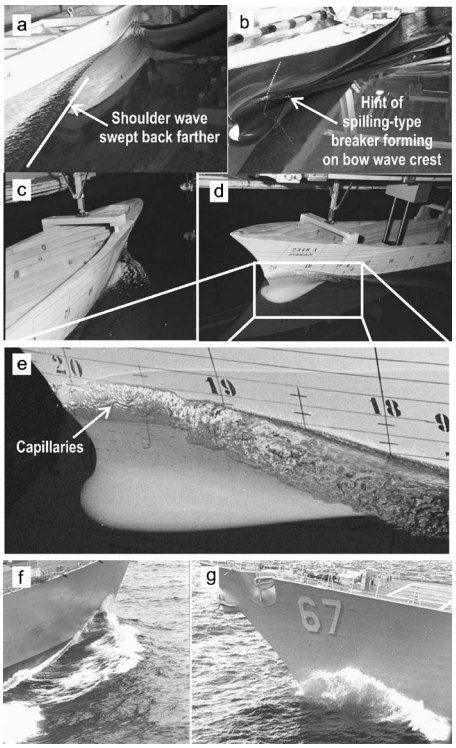

Fig. 5 Fr=0.28: Model 5512 side and front views ((*a*) and (*b*)); Model 2340 side and front views ((*c*) and (*d*)); evidence of capillaries for 2340 (*e*); full-scale side and front views ((*f*) and (*g*)).

large scars downstream of the bow wave are visible, strong enough to persist in the complete camera field of view. The free surface in the region between the hull and the scars seems to be stretched with striations evident perpendicular to the wave front. Striations are also evident between the two scars. The former are more straight and uniform than the latter. Scars and striations were previously observed in the study of the interaction of a vortex couple with a free surface [20]. A spilling breaking wave appears in the region past the outermost scar. Full-scale pictures are shown in Figs. 6(*e*) and 6(*f*) the latter of which shows the extreme bow region. The bow wave seems initially of the plunging type and then becomes of the spilling type, with white water along its crest. In Fig. 6(*e*), this wave seems to merge with the shoulder wave,

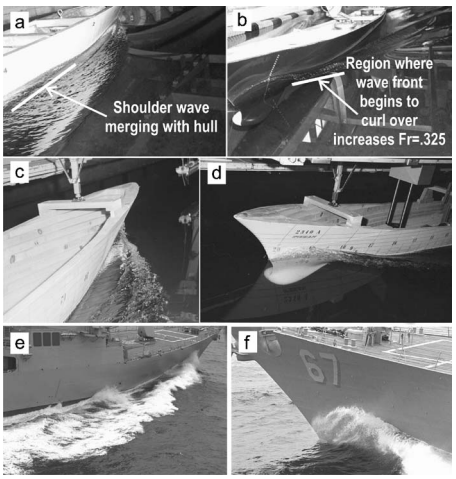

Fig. 6 Fr=0.35: Model 5512 side and front views ((*a*) and (*b*)); Model 2340 side and front views ((*c*) and (*d*)); full-scale side and front views ((*e*) and (*f*)).

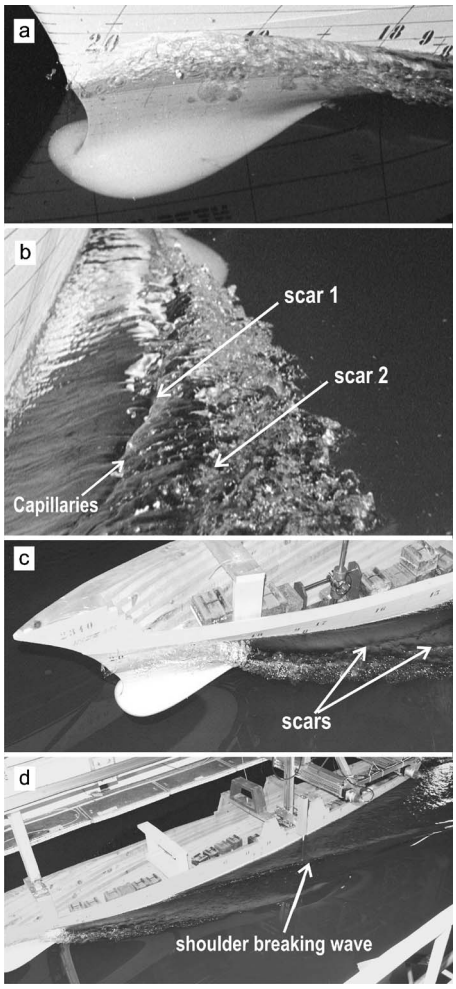

Fig. 7 Fr=0.35 rolls and scars generation and development ((*a*)–(*c*)); shoulder breaking wave (*d*)

producing a splash. Figure 7(*a*) shows the rise of the free surface at the extreme bow and the beginning of the overturning of the wave crest for Model 2340. Figure 7(*b*) is a zoom of Fig. 6(*c*): The two scars on the back of the bow wave breaking and the striations are observable in the region between the two scars and between the scars and the hull. The downstream extension of these scars is limited by the shoulder wave breaking (Figs. 7(*c*) and 7(*d*)), which exhibits a lower energetic content with respect to the bow wave and develops a "2D spilling-like" wave breaking, as shown in Fig. 7(*d*). In summary, the wave breaking characteristics observed for Model 2340 qualitatively resembles the full-scale scenario except for the amount of white water generated (Figs. 6(*e*) and 6(*f*)).

Fr=0.375 and 0.41 (Figures not shown). Both Model 5512 and Model 2340 show similar trends, including increasing unsteadiness (e.g., ejections, etc.). At Fr=0.375, Model 5512 shows a developed spilling bow breaker. The shoulder wave is merging with the hull. The near-field waves generated by Model 2340 are similar to the previous case (Fr=0.35), except for the presence of stronger water ejections. For Fr=0.41, the bow wave breaking of Model 5512 appears in the form of a plunging breaker. Air entrainment is considerably increased in this case, but the action of the surface tension on the bow wave breaking for Model 5512 is still important. Model 2340 manifests bow wave breaking of the plunging type with evidence of the overturning of the wave crest.

Fr=0.45. The bow wave breaking of Model 5512 is characterized by the presence of both plunging-type (upstream) and spilling-type breakers (downstream), as shown in Figs. 8(*a*) and

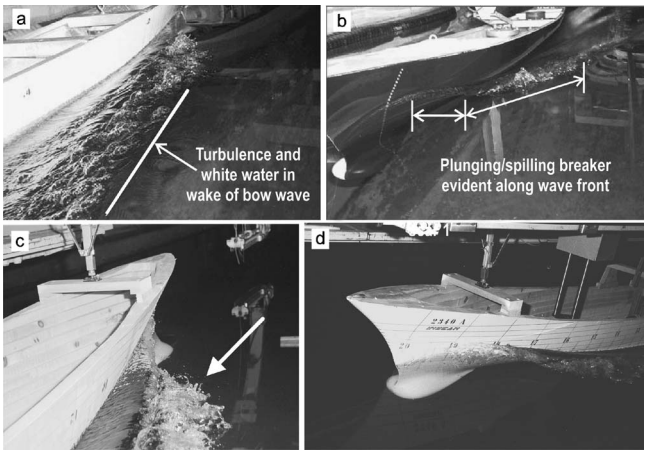

Fig. 8 Fr=0.45: Model 5512 side and front views ((*a*) and (*b*)); Model 2340 side and front views ((*c*) and (*d*));

8(*b*). The bow wave breaking of Model 2340 is entirely plunging type (Fig. 8(*d*)) and generates a system of streamlined rolls that evolve along the hull (Fig. 8(*c*)) with a considerable amount of air entrainment.

As a summary of the photo study, it can be stated that, in the range of investigated speeds, scale effects in wave breaking are important when comparing the flow for Model 5512 versus the flow for Model 2340. Scale effects are still observable between Model 2340 and the full scale, although some particular features of the full-scale flow seem to be well reproduced by Model 2340. Fr=0.35 is the lowest speed with quasisteady well-developed breaking. Unsteadiness appears for Fr higher than Fr=0.375 and the bow wave breaking generates strong water ejections that would make the measurements difficult. Consequently, Fr=0.35 was selected for the near- and far-field wave and mean velocity measurements for Model 2340.

5.2 Surface Tension and Viscous Effects. Based on the photo study and literature concerning waves and wave breaking, the physical quantities that might influence the wave breaking development in a model scale experiment are analyzed. As known from the literature, small scale wave breaking is strongly influenced by surface tension [19,21]. Furthermore, the wave breaking is also intimately connected with turbulence generation, which is a viscous phenomenon. Hence, the parameters to be considered other than the Fr are the We and Re. Their definitions are as follows:

$$\mathrm{Fr} = \frac{U_c}{\sqrt{gL}} \tag{14}$$

$$\mathrm{We} = U_c \sqrt{\frac{\rho L}{\sigma}} \tag{15}$$

$$\mathrm{Re} = \frac{U_c L}{\nu} \tag{16}$$

where U and L are the model speed and length, g the gravity acceleration, ρ and ν the fluid density and kinematic viscosity, and σ the water-air interface surface tension. In Table 6, the Fr, We, and Re for Model 2340 and Model 5512 and full-scale ship are given for the experimental conditions whereas the corresponding physical quantities are listed in Table 1. In order to satisfy the Fr similarity, the scaled model experiments were conducted at a lower velocity with respect to the full scale, which results in the violation of the We and Re similarity.

The role played by surface tension may be quite different for breaking and nonbreaking waves because the surface tension pressure jump depends on the magnitude of the radius of curvature of the free surface and in the latter case the wavelength is also relevant. In previous work [14], scale effects were analyzed for resistance, sinkage and trim, wave pattern, and mean velocity in the nominal wake plane measurements using the same model geometry (DTMB 5415) between three institutes: DTMB and INSEAN used 5.720 m long Models 5415 and 2340, respectively, whereas IIHR used 3.048 m long Model 5512. Scale effects for Model 5512 were evident only for resistance and trim tests and for Fr >0.26 and Fr>0.33, respectively, which was attributed to wave breaking. In the lower Fr range, corresponding to a nonbreaking wave pattern, scale effects were found to be negligible. Present observations confirm this trend. The photo study revealed that Model 5512 did not generate a well-developed wave breaking for Fr lower than Fr=0.41 (We=456), while Model 2340 exhibited a well-developed wave breaking starting from Fr=0.3 (We=627). The limiting condition corresponds for both cases to a velocity of 2.24 m/s. Note that even though the minimum wavelength needed in order to have pure gravity waves is about 1 m [19], it is commonly accepted that for wavelength larger than 40 cm the effects of surface tension are not dominant. Duncan's experiment on 2D waves [22], produced by a submerged hydrofoil, gave a wavelength of about 41 cm, and is often used as a benchmark in the development and validation of CFD codes that do not take into account surface tension effects. In the present experiments, both the photo study and the detailed free surface measurements revealed that the wavelength of the diverging waves of Model 2340 at Fr=0.35 is about 60 cm, i.e., sufficiently long for the surface tension effects not to be dominant.

The influence of the viscosity is considered using a *local* Re $=Ux/\nu$ in order to relate the wave breaking to the laminar/turbulent transition. The full-scale Re was about two orders of magnitude larger than the corresponding model Re. Considering the critical Re for the laminar/turbulent transition for a flat plate ($\mathrm{Re}_c \cong 3.5\times10^5$), the flow past Model 5512 is in the transitional regime up to $x=0.08$ at Fr=0.28 and up to $x=0.05$ at the maximum speed (Fr=0.45). For Model 2340, these values were $x=0.03$ and $x=0.02$, respectively, whereas the full-scale flow is turbulent for $x>0.005$. On the other hand, both models were provided with turbulence stimulators placed at $x=0.05$. Nonetheless,

Table 6 Velocity and nondimensional parameter ranges for Model 5512 and Model 2340 test conditions and full-scale ship

Fr	U_{5512} (m/s)	U_{2340} (m/s)	$U_{\text{full scale}}$ (m/s)	$U_{\text{full scale}}$ knots	We_{5512}	We_{2340}	$\mathrm{We}_{\text{full scale}}$	Re_{5512}	Re_{2340}	$\mathrm{Re}_{\text{full scale}}$
0.28	1.531	2.097	10.450	20	312	585	14800	4.17×10^6	1.10×10^7	1.27×10^9
0.3	1.640	2.246	11.197	22	334	627	15800	4.46×10^6	1.18×10^7	1.36×10^9
0.325	1.777	2.434	12.130	24	362	679	17100	4.83×10^6	1.27×10^7	1.47×10^9
0.35	1.913	2.621	13.063	25	390	731	18400	5.21×10^6	1.37×10^7	1.59×10^9
0.375	2.050	2.808	13.996	27	418	783	19800	5.58×10^6	1.47×10^7	1.70×10^9
0.41	2.241	3.070	15.303	30	456	856	21600	6.10×10^6	1.61×10^7	1.86×10^9
0.45	2.460	3.370	16.795	33	501	940	23700	6.69×10^6	1.76×10^7	2.04×10^9

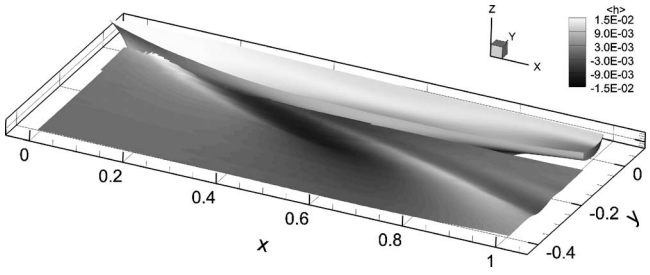

Fig. 9 Perspective view of the mean value of the wave pattern

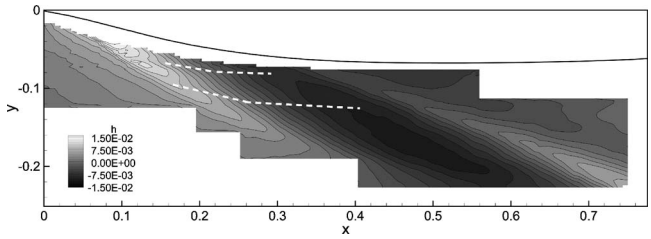

Fig. 10 Mean wave elevation measured by servo-mechanic probe; dash-dot lines indicated the scars locations

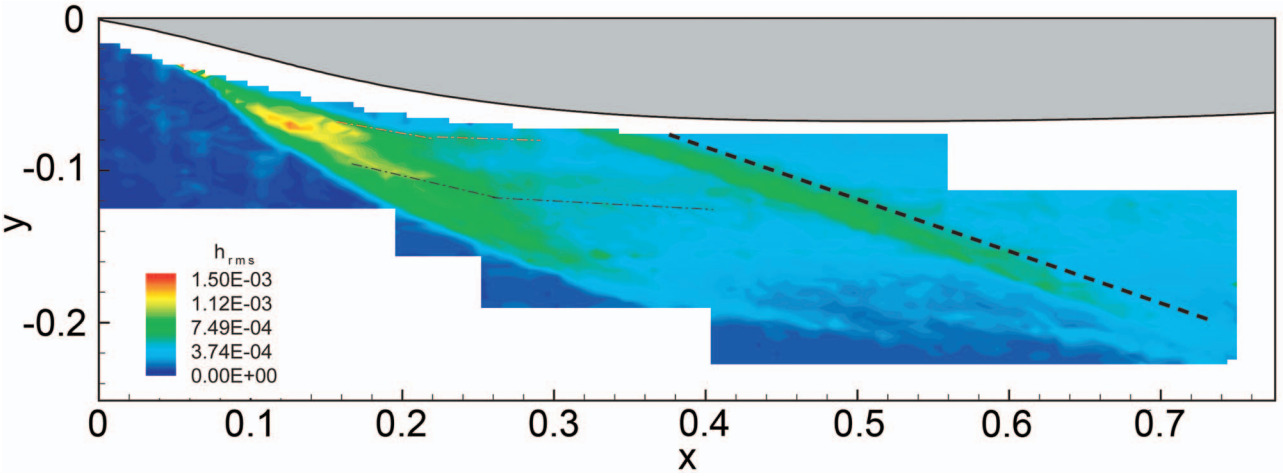

Fig. 11 rms value of the wave elevation measured by servo-mechanic probe; thin dash-dot lines indicate the scars locations and straight thick dash-dot line indicates the shoulder wave breaking

Figs. 5(*a*) and 5(*b*) show that wave breaking at Fr=0.28 for Model 5512 starts to develop more downstream with respect to Model 2340 and this could be related to the low Re nature of the flow around Model 5512 upstream of $x=0.08$. Furthermore, Figs. 5–8 show that the bow wave breaking of Model 2340 generates free surface turbulence for all the analyzed cases, while Model 5512 generates free surface turbulence only for Fr$\geqslant$0.41. The scars generated by Model 2340 at Fr=0.35 were clearly turbulent, whereas the scars generated by Model 5512 appeared to be laminar.

Differences in salinity between the seawater and the water used for the experiments should be considered. Salinity changes the density and consequently Re and We, although for the present values of these two parameters, the differences caused by density changes of these two parameters are very small. In addition, the surface tension increases with salinity, although the role of the surface tension in the full-scale breaking can be neglected, due to the large value of the wave's radius of curvature. The more important effect of salinity is related to air entrainment and production of white water. In fact, the percentage of the dissolved gases decreases as salinity increases[1], so that bubble generation and air entrainment could be rather different in laboratory wave breaking with respect to seawater wave breaking. Nevertheless, the influence of the salinity on free surface topology and flow evolution can be considered a minor source of discrepancies between the model and the full-scale breaking with respect to scale effects [23].

[1]http://www.chesapeakebay.net/info/ecoint3cfm

6 Froude Number 0.35 Wave Elevations and Mean Velocities

Figure 9 provides a reconstruction of the mean wave elevation that combines the near- and far-field data. Figures 10 and 11 show the near-field mean and rms wave elevation. The highest value of the mean wave elevation in the measured area is $h_{max}=1.8\times10^{-2}L_{PP}$ (=103.0 mm) and the minimum is $h_{min}=-1.06\times10^{-2}L_{PP}$ (=60.6 mm). The bow wave is visible in the mean wave elevations; the maximum of the rms value of the wave fluctuations, which is about 1/10 of the maximum mean wave height ($h_{rms}^{(max)}=1.97\times10^{-3}L_{PP}=11.3$ mm), occurs at the bow wave breaking crest. The shoulder wave breaking is spilling type and it is gentler than the bow wave breaking. Its highest peak lies outside the near field and can be observed in the far-field reconstruction (Fig. 9). The shoulder wave front appears to be a straight line (the dash-dot line in Fig. 11) with an angle of about 19 deg with the longitudinal x axis when looking at the contours of the rms of the free surface elevation. The bow wave front (Figs. 10 and 12, left) displays a bumpy shape and two scars are visible, as in the photo study (Figs. 6 and 7), which are characterized by sudden changes in the mean wave height: closer to the hull Scar 1 (Fig. 12) is more visible, whereas the other Scar 2, appears weaker, as shown in Fig. 7(*b*). The close-up view of the rms elevation (Fig. 12, right) displays large rms values along the bow and shoulder wave breaking crests with peak values at the bow wave crest between the two scars.

Figure 13 shows the mean velocity measurements under the bow and shoulder waves in four transverse planes: cross flow

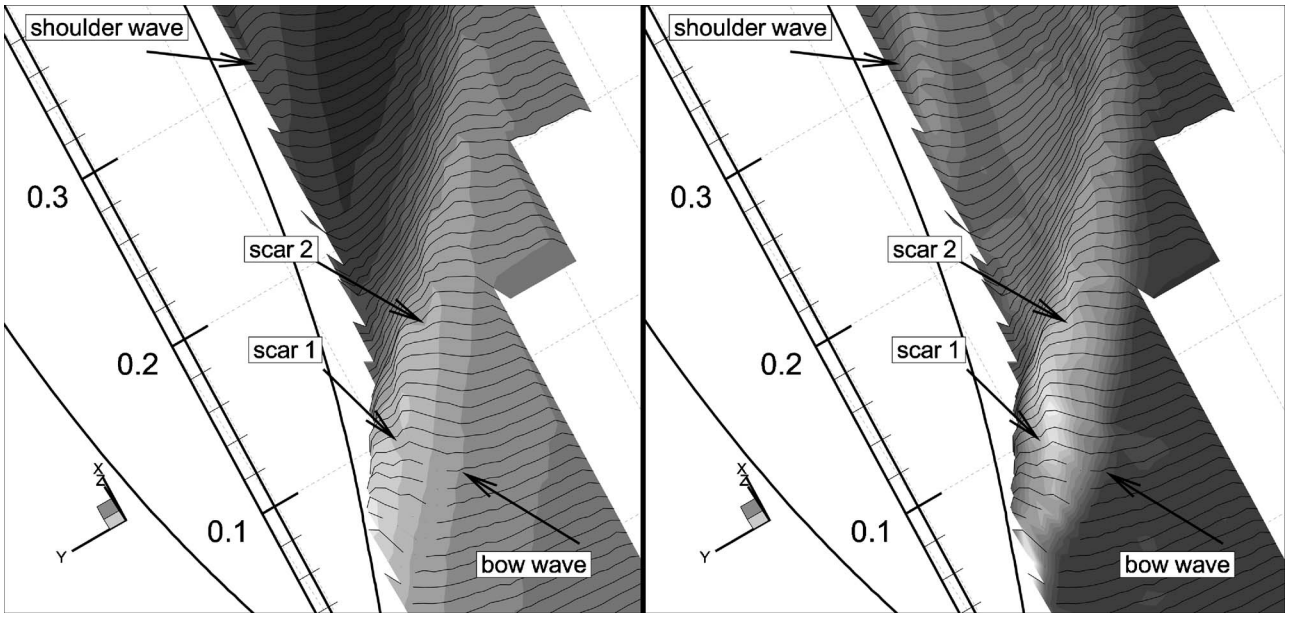

Fig. 12 Traces of the scars generated at the bow. Mean wave elevation (left) and rms value (right) of the wave elevation

vectors highlighted with axial velocity (Fig. 13, left) and vorticity (Fig. 13, right) contours. Due to the dimensions of the head of the five-hole Pitot tube and the unsteadiness of the free surface, it was not possible to measure very close to the free surface in order to carry out a complete reconstruction of the velocity and vorticity fields. In the following, the experimental data are discussed after mirroring them about the hull symmetry plane from the port to the starboard side of the hull. This was done to be consistent with the CFD solution which was for the starboard side. The x axis is positive outward of the plane of the figures and negative and positive vorticities corresponding to clockwise (CW) and counterclockwise (CCW) rotations, respectively. The labeling of the regions of negative and positive vorticities in Fig. 13 corresponds to those identified using the CFD solution, as will be discussed later. The closest vectors to free surface were not used for the vorticity calculations since it is presumed that the vorticity very close to the free surface could be affected by higher uncertainty than in the rest of the measured field and some boundary effects could compromise the results on the points close to the free surface.

$x=0.15$. There is an axial velocity defect and outward/upward cross flow under the bow wave crest. A large region of CW (V3) vorticity is evident.

$x=0.20$. Similar to the previous section, the flow exhibits an axial velocity defect and outward/upward cross flow under the bow wave crest. A large region of CW (V3) vorticity is evident.

$x=0.40$. The data indicate outward/upward cross flow under the shoulder wave crest and inward/downward cross flow under the shoulder wave trough and part of the velocity field related to the bow wave crest ($y>0.16$). As for the bow wave crest, the axial velocity under the shoulder wave has a local minimum; moving outboard, the axial velocity exhibits a local maximum, under the bow wave trough. The flow under the bow wave crest ($y>0.16$) is still characterized by low axial velocity, as for the upstream sections $x=0.15$ and $x=0.2$. Two regions of CW vorticity are evident under the shoulder wave crest (V1 at $y=0.085$, $z=-0.01$ and V3 at $y=0.11$, $z=-0.01$).

$x=0.5$. Similar to section $x=0.4$, the axial velocity under the shoulder wave crest has a local minimum with high cross flow nearby the breaker. The flow under the bow wave trough shows a maximum of the axial velocity. The axial vorticity pattern shows two CW vortices (V1 at $y=0.085$, $z=-0.01$ and V3 at $y=0.11$, $z=-0.01$) similarly as for the section $x=0.4$.

The shoulder wave flow exhibits some similarities with a 2D spilling breaker, although a fundamental difference occurs in the present 3D scenario. In 2D breaking, the flow direction is normal to the wave front (aligned with the wave vector), whereas in the present case the flow direction and the wave front form an angle of about 19 deg (Fig. 11), assuming that the flow is almost aligned with the x axis. Likely, this difference does not affect the mechanism responsible for the vorticity production at the toe of the wave breaking, but it might play a fundamental role in the vorticity convection and evolution. In a 2D breaker, the vorticity produced at the toe is advected downstream, normal to the wave front and generates a 2D shear layer. In the 3D case, the gradient of the velocity along the wave front can stretch or shorten the eddy generated at the breaking [9]. This mechanism affects the vorticity intensity and consequently the breaker intensity.

7 Complementary Computational Fluid Dynamics Observations

Concurrently to the described experimental campaign, a CFD simulation of the same flow was carried out at IIHR using CFDSHIP-IOWA RANS code (v.4), which is described in detail in Ref. [15]. CFDSHIP-IOWA is a general-purpose, multiblock, MPI-based high-performance, unsteady RANS CFD code developed for computational ship hydrodynamics, which solves the 3D unsteady incompressible RANS equations. In the version adopted for the present paper, a single-phase level set approach is used to capture the air-water interface. Reynolds-stress closure is accomplished through the k-ω turbulence model. The solution scheme is based upon the PISO algorithm and is fully implicit. The convective and viscous terms are discretized with second-order upwind and second-order central differences, respectively. The pressure equation is obtained by taking the divergence of the momentum equations. In the present paper, CFD data are used to complete the EFD data in order to better understand the flow under the bow and shoulder wave breaking.

7.1 Free-Surface Wave Field: Computational Fluid Dynamics Versus Experimental Fluid Dynamics. A comparison of the computed wave elevation contours with measurements at Fr $=0.35$ (Fig. 14) shows overall good agreement of the wave field and the locations of the scars, which are visible in the bow wave contours. The scars in the CFD results are even sharper than the

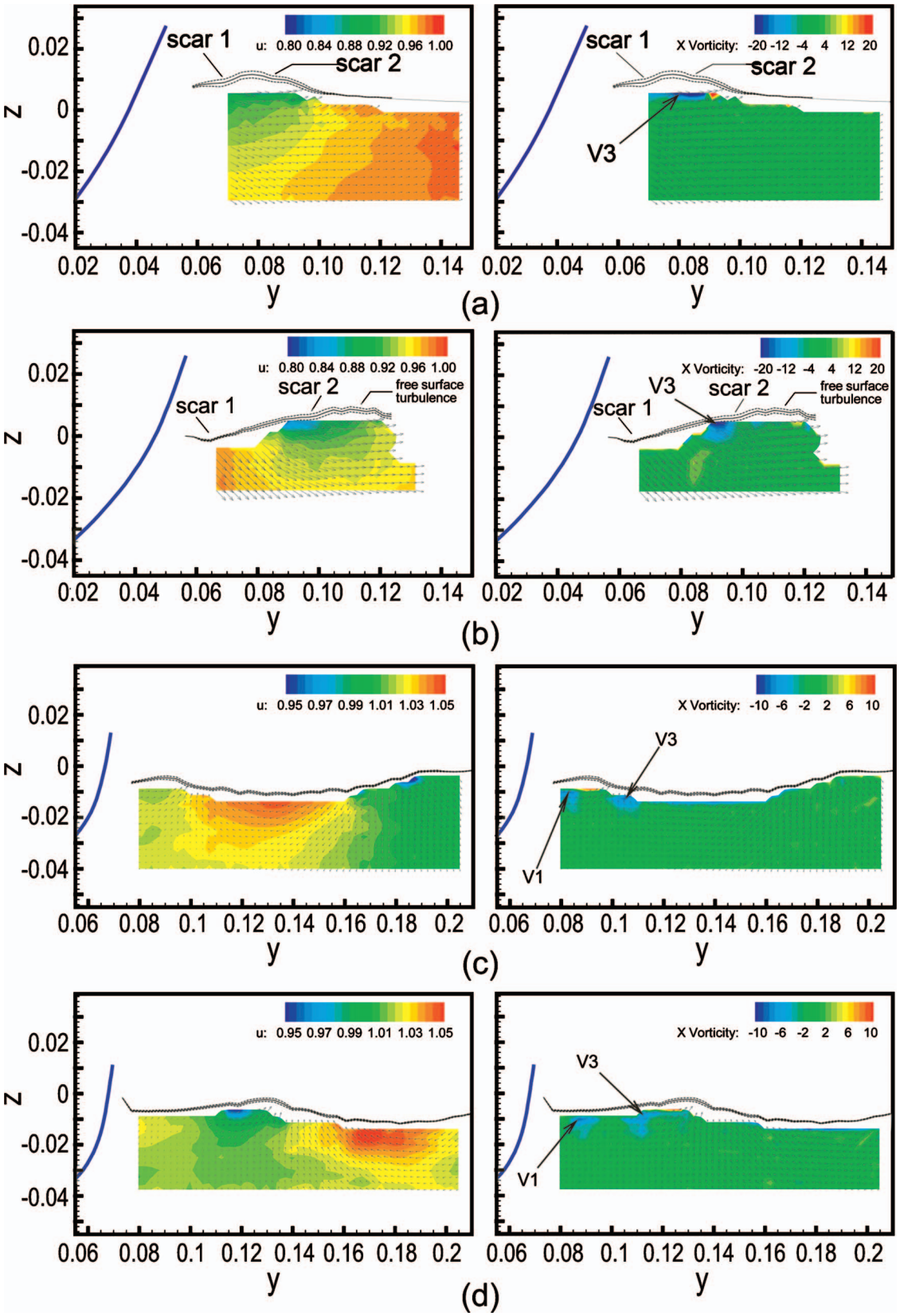

Fig. 13 The cross flow vectors and axial velocity contours (left) and axial vorticity contours (right) at the four measurement sections (*a*) x=0.15, (*b*) x=0.20, (*c*) x=0.40, and (*d*) x=0.50. Measured mean wave elevation transverse cuts (solid lines) +/− rms (dashed lines)

measurements, a result that might be related to the absence of a surface tension model in the CFD solution. In the experiments, the formation of the scars is accompanied by the presence of striations and by the high values of the rms of the wave height. The CFD

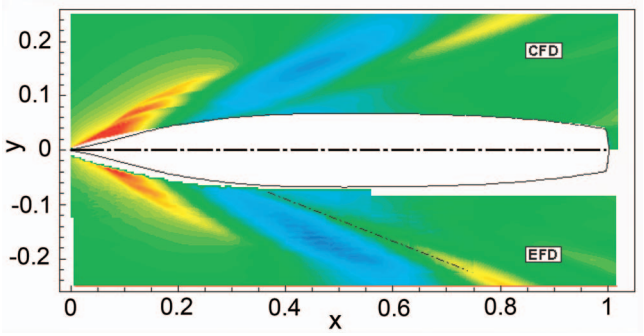

Fig. 14 CFD and experimental free-surface contours. The presence of the scars is clearly visible in the bow region.

solution bow wave details shown in Fig. 15 clearly display the overturning of the bow wave and the formation of the scars.

7.2 Velocity Field: Computational Fluid Dynamics Versus Experimental Fluid Dynamics. The computed wave height and contours of the three-velocity components are compared with the experimental data measured at the two cross sections $x=0.15$ (Figs. 16–18) and $x=0.40$ (Figs. 19–22). The two cross sections correspond to the bow and shoulder waves and flow patterns, respectively. The box on the CFD figures represents the area investigated experimentally. The agreement between CFD and EFD is satisfactory in both sections for the three-velocity components and for the free surface, with differences of the same order of the related uncertainties. In Fig. 22, the axial vorticity contours are compared with the data. Traces of the two vortices induced by the bow wave breaking and indicated as V1 and V3 are observed in both CFD and EFD results, although in the EFD data only part of the two vortices is captured due to the free surface proximity. The good agreement between CFD results and measurements allows us to use the CFD solution (much more complete with respect to EFD) for a more detailed description of the flow, especially of the one generated by the bow wave breaking.

7.3 Bow Wave Breaking Flow. Figure 23 shows axial vorticity contour slices and vortex nomenclature from the CFD solution with under free surface (left) and above free surface (right) views. The location of the vortex cores was found by tracing concentrations of axial vorticity near the free surface from $0.05 < x/L < 0.6$. V1–V6 are associated with the overturning bow wave, while V7 and V8 are weaker and associated with the shoulder wave and first trough, respectively. Figure 23 also clearly indicates that the bow wave breaking induces as many pairs of counter-rotating vortices as the number of breaking events. They evolve downstream, forming two distinct and one indistinct scars on the free surface, corresponding to the first two plunging breakers and to the last, less energetic, spilling-type breaker. The shoulder wave breaking generates a single CCW vortex.

Figure 24 shows the downstream evolution of the bow wave breaking. The axial vorticity contours and crossplane vectors are

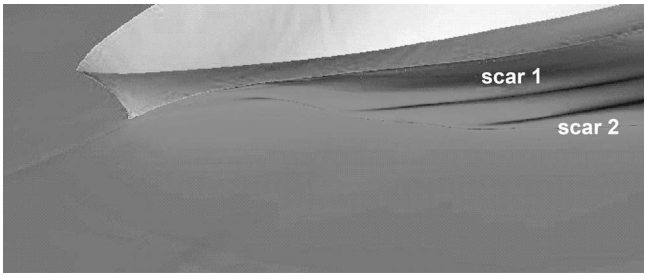

Fig. 15 Bow wave details for CFD solution

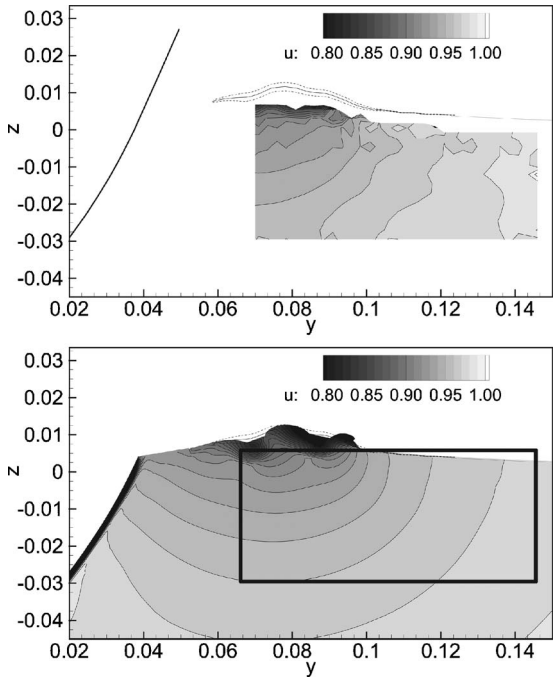

Fig. 16 Axial velocity ($x=0.15$): INSEAN experiments (top); IIHR CFD (bottom)

shown at various transverse planes from $x=0.05$ to 0.175. The bow wave breaking process is initiated by the pressure field generated by the model's bow. Section $x=0.05$ shows that the velocity field is mostly directed outward/upward, with the exception of the flow at the tip of the jet, which under the action of gravity is already falling toward the free surface below. A region of negative axial vorticity appears close to the throat of the plunger ($y \cong 0.26$, $z \cong 0.015$), induced by the small radius of curvature of the free surface. The flow at $x=0.065$ shows almost the same sce-

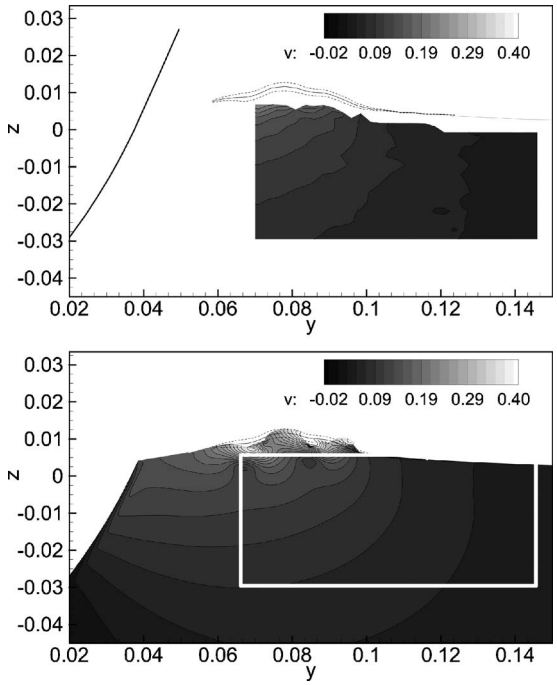

Fig. 17 Transverse velocity ($x=0.15$): INSEAN experiments (top); IIHR CFD (bottom)

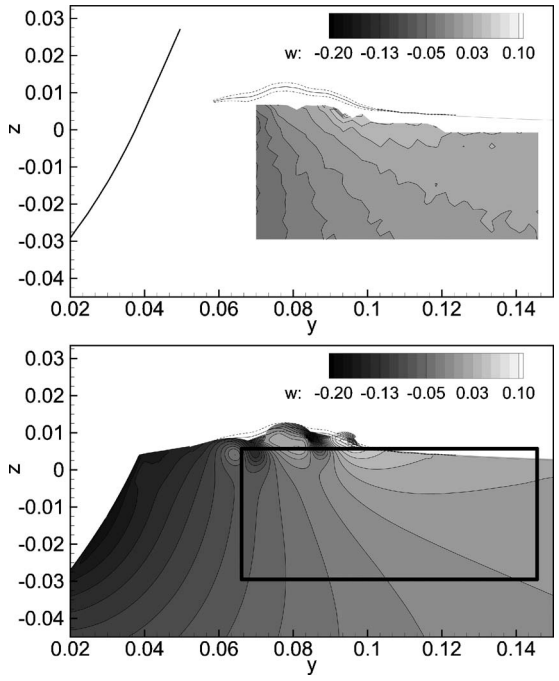

Fig. 18 Vertical velocity (x=0.15): INSEAN experiments (top); IIHR CFD (bottom)

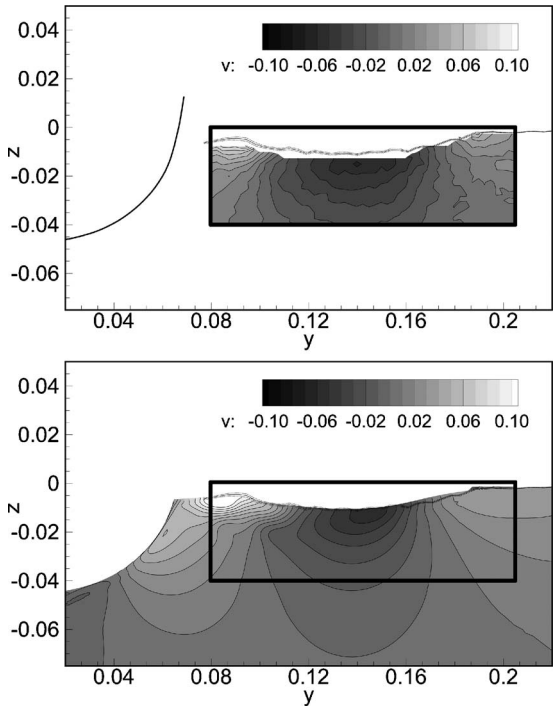

Fig. 20 Transverse velocity (x=0.40): INSEAN experiments (top); IIHR CFD (bottom)

nario, except that the flow field closer to the hull is more horizontal and that the fluid particles in the jet display higher velocities. At x=0.07 and 0.075, the jet impacts the undisturbed free surface, and a large CW vortex V1 is generated due to the reconnection of the plunger with the free surface. The circulation associated with V1 is also augmented by the large velocity gradients between the plunger tip and the free surface. The free surface is deflected outward/upward forming a new jet, which depends on the impact angle and on the momentum. At the deflection point ($y \cong 0.041$, $z \cong 0.011$), a CCW vortex V2 develops, smaller than V1 but of the same vorticity magnitude. The formation of the second jet is influenced by both V1 and V2. The downstream evolution of the vortex pair V1-V2 leads to the generation of the first scar. This process repeats itself between x=0.085 and 0.13 (V3 and V4 separated by Scar 2) and, with much less energy, between x=0.15 and

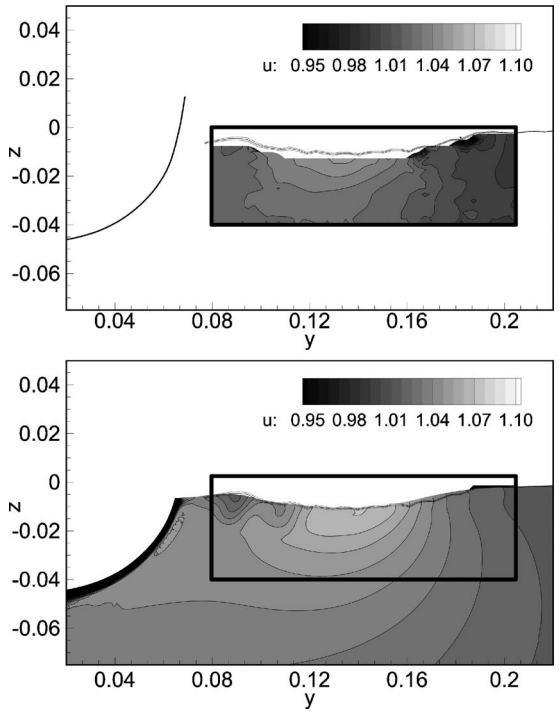

Fig. 19 Axial velocity (x=0.40) INSEAN experiments (top); IIHR CFD (bottom)

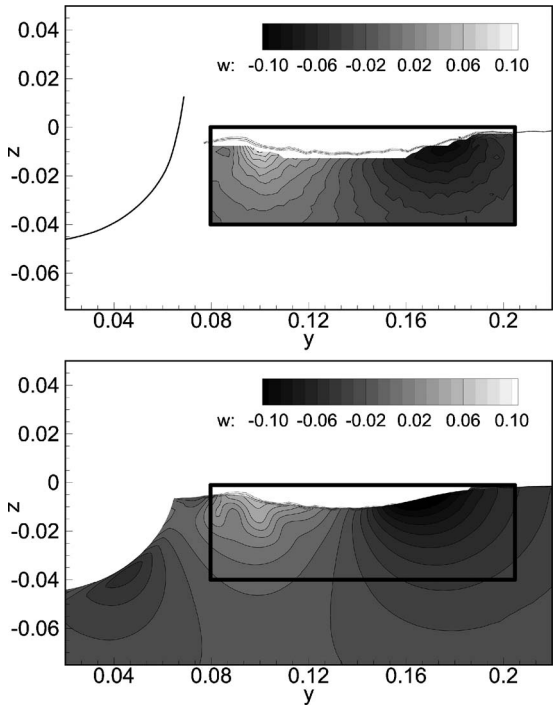

Fig. 21 Vertical velocity (x=0.40): INSEAN experiments (top); IIHR CFD (bottom)

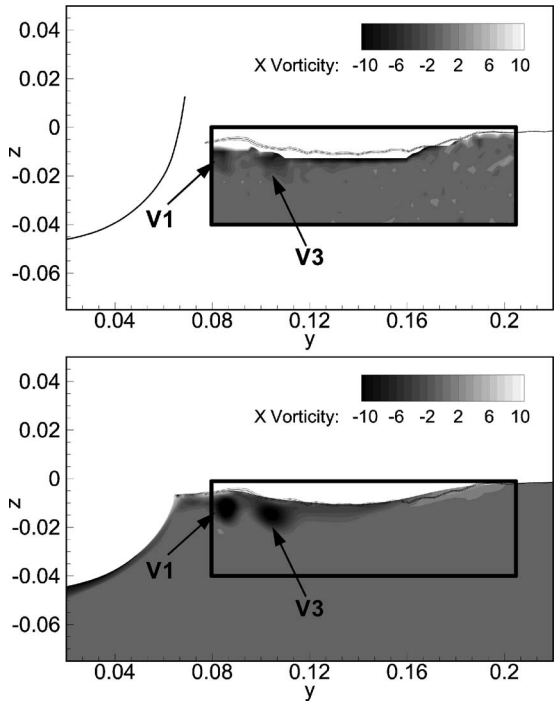

Fig. 22 Experimental (top) and numerical (bottom) axial vorticity contours at $x=0.40$

0.175 (only V5 is formed and no scar on the free surface is left). Note that the downward flow between the counter-rotating vortices persists downstream of the jet impact albeit with reduced magnitude (Fig. 24). The downward velocity beneath the scars is clearly visible in the CFD solution at $x=0.15$, as shown in Fig. 18, bottom.

Figure 25 shows an enlarged view, from above the free surface, of the CFD solution in the bow region. The free surface streamlines and the axial vorticity contours are shown. The scars correspond to lines of streamline convergence between the counter-rotating vortices along which fluid particles and possibly air bubbles are transported from the free surface into the bulk of the fluid.

8 Three Dimensional Breaking Detection Criterion

The shoulder wave breaking is similar to 2D spilling breaking, as discussed previously. The inception of the 2D spilling breaking generated by regular waves can be predicted on the basis of the wave steepness ($2a/\lambda \cong 0.1$). This criterion can also be expressed based on the related local wave slope $\theta=17.1$ deg ± 1.2 deg [22]. The steepness of the wave pattern at $Fr=0.35$ is determined by taking the derivative of the mean wave elevation normal to the wave front (Fig. 26, top). In order to identify the breaking regions predicted by the criterion, only two values of the wave slope are shown in the figure, whereas the rms values of the wave elevation are reported (Fig. 26, bottom) in order to highlight the measured breaking region. The comparison of the two plots in Fig. 26 shows that the "$\theta=17$ deg criterion" correctly predicts the inception of the breaking supporting the possibility of extending the "local form" of the 2D criterion to 3D wave fields, at least for quasi-steady plunging bow and spilling shoulder wave breaking. These results show that a direct correlation exists between regions of wave slope larger than 17 deg and regions of large rms. As shown in Fig. 14, the CFD accurately predicts the wave elevations and therefore as shown in Ref. [15] also accurately predicts the wave slope. Thus, the CFD at its current resolution can be used to identify the regions of large rms.

9 Conclusions and Future Work

The present paper reports a detailed study of the flow past a surface combatant model ship, with focus on the scars and the vortices induced by bow and shoulder wave breaking. The flow has been studied via the combined use of EFD and CFD, which provide a powerful tool in analyzing complex flows.

A preliminary photo study has been used to select the best conditions for the test, such as the speed and the location and the extent of the measured free surface area and of the cross sections. The bow and shoulder wave breaking have been analyzed acquiring both mean and rms wave elevation and mean velocity. The data showed sudden changes in the mean wave height between the scars and large rms values along the bow and shoulder wave breaking crests, with peak values at the bow wave crest between the two scars. A direct correlation is shown between regions of wave slope larger than 17 deg and regions of large rms. The mean velocity measurements revealed the complicated vortex structures beneath the free surface generated by the breakers.

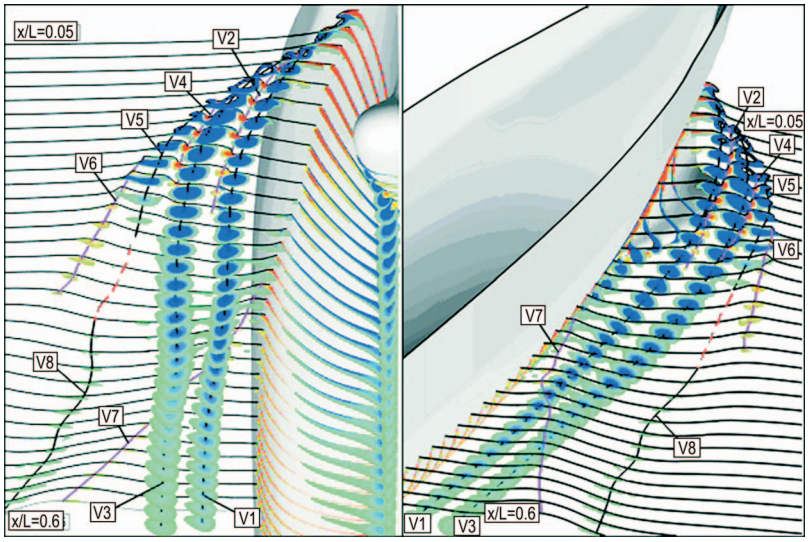

Fig. 23 CFD solution with under free surface (left) and above free surface (right): transverse sections of the wave contours are shown in black and axial vorticity contours are shown in blue (CW) and red (CCW)

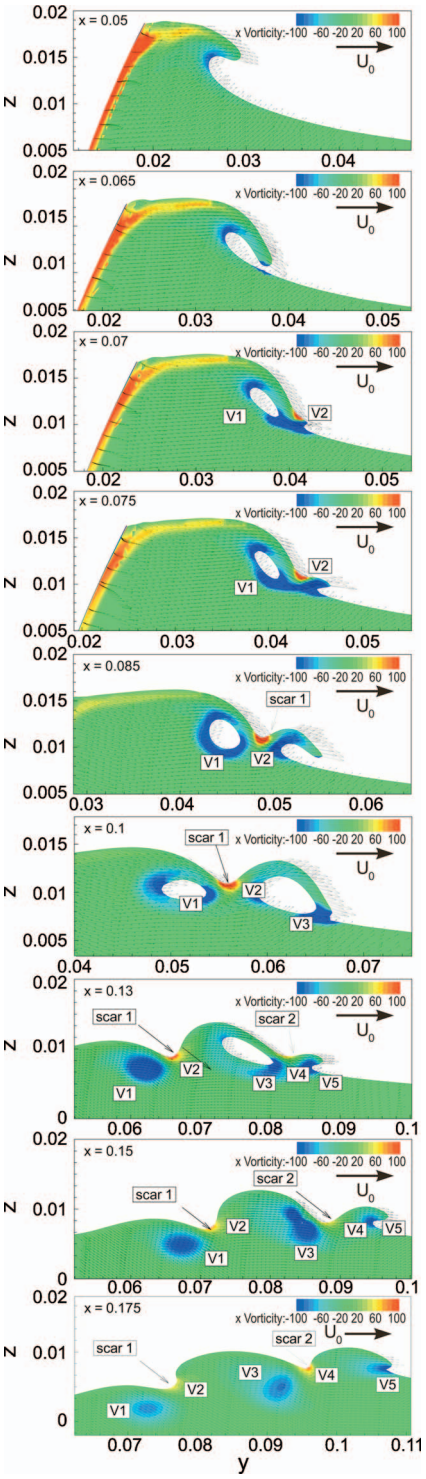

Fig. 24 CFD solution bow wave breaking and induced vortices and scars

A CFD simulation of the flow was carried out and the results were validated using the measured data, giving a satisfactory agreement. The CFD results were fundamental in filling the gaps between the measured cross sections and in providing also quantitative information close to the free surface where no data were collected, allowing a complete physical understanding of the bow wave breaking with the generated vortices and scars. CFD solutions for the present geometry at lower and higher Fr (0.28 and 0.41) [15] and for the Athena high-speed transom ship for Fr =0.25, 0.43, and 0.63 [24] show that the number of induced vortices and scars depend on Fr and hull form.

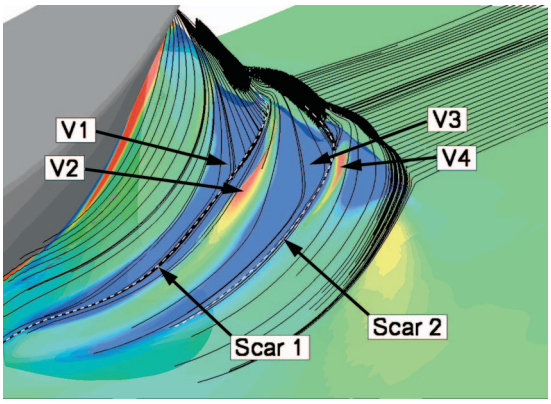

Fig. 25 Free-surface streamlines and vorticity contours near the bow

The present results show that the bow wave breaking induces large free surface rms values together with counter-rotating vortex pairs and scars and downward flow between them. EFD and observation show that regions of high free-surface rms values are correlated with bubble production. Bubbles produced in these regions with high free-surface energy are likely to be entrained in the scars, the degree of entainment will be related to the downward liquid velocity and bubble size. These finding are relevant to the modeling of bubble sources and the entrainment of these bubbles into the volume flow. Current bubble source modeling [13] can make no prediction regarding where bubbles are created, only where they can be entrained into the volume and that model (based on a threshold downward liquid velocity) correlates well with the present observations. The present work makes possible the prediction of bubble source location and opens the possibility of addressing the magnitude of the bubble source. In this regard, the primary limitation of the present results is the fact that bubbles created in experiments performed at model scale in fresh water are significantly different than those created at full scale in salt water.

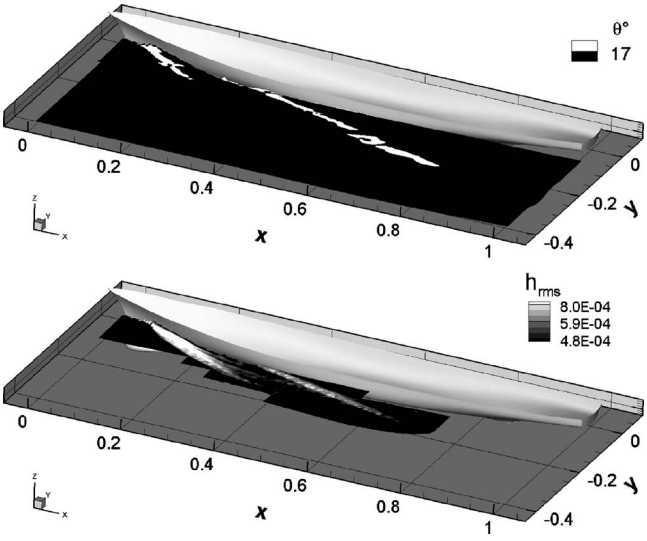

Fig. 26 Wave steepness (top) and rms value (bottom) of the wave elevation

Acknowledgment

The research at INSEAN and IIHR was sponsored by the Office of Naval Research under Grant Nos. NICOP: N00014-00-1-0344 and N00014-01-1-0073, respectively, under the administration of Dr. Patrick Purtell. The research at INSEAN was also partially sponsored by the Italian Ministry of Transportation and Navigation in the frame of Research Plan 2005-2007. Dr. M. Hyman is acknowledged for helpful discussions on bubbly ship flow.

References

[1] Baba, E., 1969, "A New Component of Viscous Resistance of Ships," J. Soc. Nav. Archit. Jpn., **125**, pp. 9–34.
[2] Miyata, H., and Inui, T., 1984, "Nonlinear Ship Waves," Adv. Appl. Mech., **24**, pp. 215–288.
[3] Doi, Y., Takeuchi, S., Hong, S., Kajatani, H., and Miyata, H., 1982, "Characteristics of Stern Waves Generated by Ships of Simple Hull Form (Second Report)," J. Soc. Nav. Archit. Jpn., **151**, pp. 9–34.
[4] Dong, R. R., Katz, J., and Huang, T. T., 1997, "On the Structure of Bow Waves on a Ship Model," J. Fluid Mech., **346**, pp. 77–115.
[5] Roth, G. I., Mascenik, D. T., and Katz, J., 1999, "Measurements of the Flow Structure and Turbulence Within a Ship Bow Wave," Phys. Fluids, **11**(11), pp. 3512–3523.
[6] Longo, J., and Stern, F., 2002, "Effects of Drift Angle on Model Ship Flow," Exp. Fluids, **32**, pp. 558–569.
[7] Tulin, M. P., and Landrini, M., 2000, "Breaking Waves in the Ocean and Around Ships," *Proceedings 23rd ONR Symposium on Naval Hydrodynamics*, National Academic, Val de Reuil, France.
[8] Di Mascio, A., Muscari, R., and Broglia, R., 2003, "Computation of Free Surface Flows Around Ship Hulls by a Level Set Approach," *Proceedings of the Eighth International Conference on Numerical Ship Hydrodynamics, Busan, Korea*.
[9] Duncan, J. H., 2001, "Spilling Breakers," Annu. Rev. Fluid Mech., **33**, pp. 519–547.
[10] Rhee, S. H., and Stern, F., 2002, "RANS Modeling of Spilling Breaking Waves," ASME J. Fluids Eng., **124**(2), pp. 424–432.
[11] Muscari, R., and Di Mascio, A., 2003, "A Model for the Simulation of Steady Spilling Breaking Waves," J. Ship Res., **47**(1), pp. 13–23.
[12] Muscari, R., and Di Mascio, A., 2004, "Numerical Modeling of Breaking Waves Generated by a Ship's Hull," J. Mar. Sci. Technol., **9**, pp. 158–170.
[13] Hyman, M., Moraga, F., Drew, D., and Lahey, R., 2006, "Computation of the Unsteady Two-Phase Flow Around a Maneuvering Surface Ship," *26th ONR Symposium on Naval Hydrodynamics*, National Academic, Rome, Italy.
[14] Stern, F., Longo, J., Penna, R., Olivieri, A., Ratcliffe, T., and Coleman, H., 2000, "International Collaboration on Benchmark CFD Validation Data for Surface Combatant DTMB Model 5415," *23rd ONR Symposium on Naval Hydrodynamics*, National Academic, Val de Reuil, France.
[15] Wilson, R., Carrica, P., and Stern, F., "Simulation of Ship Breaking Bow Waves and Induced Vortices and Scars," Int. J. Numer. Methods Fluids, **54**(4), 419–451 (2007).
[16] Olivieri, A., Pistani, F., Avanzini, G., Stern, F., and Penna, R., 2001, "Towing Tank Experiments of Resistance, Sinkage and Trim, Boundary Layer, Wake and Free Surface Flow Around a Naval Combatant INSEAN 2340 Model," IIHR Report No. 421.
[17] Coleman, H. W., and Steele, W. G., 1995, "Engineering Application of Experimental Uncertainty Analysis," AIAA J., **33**(10), pp. 1888–1895.
[18] Olivieri, A., Pistani, F., Wilson, R., Benedetti, L., La Gala, F., Campana, E. F., and Stern, F., 2004, "Froude Number and Scale Effects and Froude Number 0.35 Wave Elevations and Mean-Velocity Measurements for Bow and Shoulder Wave Breaking of Surface Combatant DTMB 5415," IIHR Report No 441.
[19] Longuet-Higgins, M. S., 1996, "Progress Towards Understanding how Waves Break," *21st Symposium on Naval Hydrodynamics*, National Academic, Trondheim, Norway.
[20] Sarpkaya, T., and Sutton, P. B. R., 1991, "Interaction of a Vortex Couple With a Free Surface," Exp. Fluids, **11**, pp. 205–217.
[21] Tulin, M. P., 1996, "Breaking of Ocean Waves and Downshifting," *Waves and Nonlinear Processes in Hydrodynamics*, J. Grue, B. Gjevik, and J. E. Weber, eds., Kluwer Academic, Dordrecht, pp. 177–190.
[22] Duncan, J. H., 1983, "The Breaking and Non-Breaking Wave Resistance of a Two-Dimensional Hydrofoil," J. Fluid Mech., **126**, pp. 507–520.
[23] Fu, T. C., Karion, A., Rice, R. J., and Walker, D. C., 2004, "Experimental Study of the Bow Wave of the R/V Athena I," *25th ONR Symposium on Naval Hydrodynamics*, National Academic, St. Johns, Canada.
[24] Wilson, R., Carrica, P., and Stern, F., 2006, "URANS Simulations for High-Speed Transom-Stern Ship With Breaking Waves," Int. J. Comput. Fluid Dyn., **20**(2), pp. 105–125.

The Effects of Air Preheat and Number of Orifices on Flow and Emissions in an RQL Mixing Section

James D. Holdeman[1]
e-mail: jjdholdeman@aol.com

Clarence T. Chang

National Aeronautics and Space Administration,
Glenn Research Center,
Cleveland, OH 44135

This study was motivated by a goal to understand the mixing and emissions in the rich-burn/quick-mix/lean-burn combustor scheme that has been proposed to minimize the formation of oxides of nitrogen (NO_x) *in gas turbine combustors. The study reported in this paper was a reacting jet-in-crossflow experiment at atmospheric pressure in a cylindrical duct. The jets were injected from the perimeter of the duct through round-hole orifices into a fuel-rich mainstream flow. The number of orifices investigated in this study gave over- to optimum to underpenetrating jets at a jet-to-mainstream momentum-flux ratio of 57. The size of individual orifices was decreased as their number increased to maintain a constant total area. The jet-to-mainstream mass-flow ratio was held constant at 2.5. The experiments focused on the effects of the number of orifices and inlet air preheat and were conducted in a facility that provided the capability for independent variation of jet and main inlet air preheat temperature. The number of orifices was found to have a significant effect on mixing and the distributions of species, but very little effect on overall* NO_x *emissions, suggesting that an aerodynamically optimum mixer may not minimize* NO_x *emissions. Air preheat was found to have very little effect on mixing and the distributions of major species, but preheat did increase* NO_x *emissions significantly. Although the air jets injected in the quick-mix section of a RQL combustor may comprise over 70% of the total air flow, the overall* NO_x *emission levels were found to be more sensitive to mainstream air preheat than to jet stream air preheat.*
[DOI: 10.1115/1.2786531]

Introduction

Many gas turbine combustor control strategies intended to modify mixing and emissions rely on jets in a crossflow of gas to mix fluids. One application of this technique is the mixer section in the rich-burn/quick-mix/lean-burn (RQL) combustor that has been proposed to minimize the formation of oxides of nitrogen (NO_x) in gas turbine combustors. In a RQL, jets of air are typically introduced from the wall of the quick-mix section into a richer than stoichiometric mainstream flow resulting in a combination of mixing and reaction. The goal is to bring the mixture to an overall fuel-lean condition as quickly as possible to try to minimize NO_x formation in the mixing section by minimizing the time during which regions exist that consist of near stoichiometric species concentrations at high temperatures. The success of this combustor strategy depends on the efficiency of the mixing section bridging the fuel-rich and fuel-lean stages of the combustor.

Numerous jet-in-crossflow (JIC) studies, summarized in Refs. [1–5], have yielded insight on flow field characteristics resulting from jet mixing. Most JIC research studies prior to 1970 contributed measures of centerplane parameters and jet shape for unconfined single jets [1,2]. Many of the studies summarized by Margason [1] were motivated by V/STOL aerodynamics. The summary by Demuren [2] focused on computational methods. The studies summarized by Holdeman [3] were motivated by the dilution process in conventional gas turbine combustors and those summarized in Holdeman et al. [4] (for cylindrical ducts) and Holdeman et al. [5] (for opposed rows of jets in rectangular ducts) were motivated by the RQL.

Nothing was identified for a steady confined JIC in the studies summarized in Refs. [3–5] that penetrated significantly farther or mixed faster than a single, round, unbounded jet. Thus, the penetration of the single unbounded jet should be considered as the maximum for confined JICs. Although the single jet is a key component in combustors and provides considerable insight, flows of interest to the combustor application are confined and the interaction between jets is a major factor in determining mixing performance.

Many of the studies summarized in Refs. [4,5] sought to define conditions to optimize the mixing. Nonreacting experiments have been used to investigate the mixing of air jets into a cross stream. The primary emphasis of these studies (e.g., Hatch et al. [6]) was directed at investigating the effects of varying the jet-to-crossflow momentum-flux ratio and the shape, orientation, and number of orifices. An optimization scheme, using a statistical approach, was subsequently applied (Kroll et al. [7]) to determine the orifice configurations that lead to optimal mixing in a cylindrical duct.

A journal article on NO_x emissions in a model RQL combustor with a single row of orifices was published by Meisl et al. [8]. Both inlet air streams were preheated to the same temperature and the operating pressure was varied. The crossflow was swirling, all tests were made using a 20 round-hole orifice configuration, and emission measurements were made with a ganged multiport probe at the exit of the model combustor, which was at an axial distance equal to more than ten duct radii downstream of the jet injection.

Meisl et al. [8] identified two potential sources for the emission of NO_x in a RQL combustor. One source was the formation of prompt NO in the rich-burn zone; the second source was the formation that may occur in the quick-mix section as a result of the

[1]Corresponding author.

Contributed by the Fluids Engineering Division of ASME for publication in the JOURNAL OF FLUIDS ENGINEERING. Manuscript received September 7, 2006; final manuscript received May 2, 2007. Review conducted by Joseph Katz.

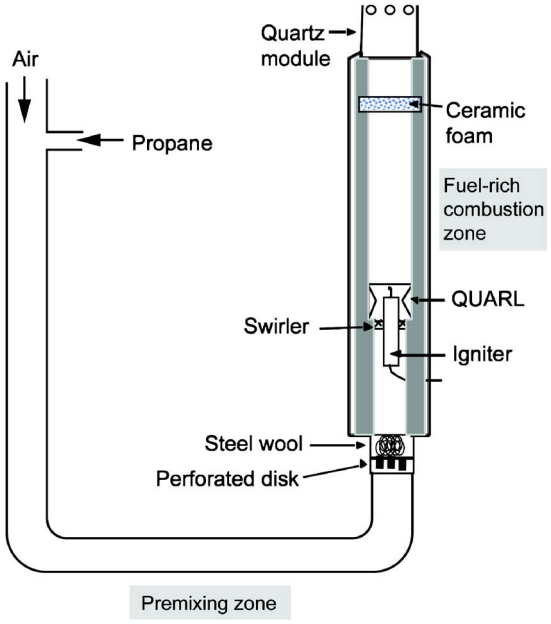

Fig. 1 Schematic of experimental rich product generator with quartz RQL module

formation of thermal NO_x. Meisl et al. [8] also suggested that mixing downstream of the rich zone was critical in a RQL and that the jet-to-mainstream momentum-flux and mass-flow ratios were important factors. They also concluded that optimal mixing would minimize NO_x.

Studies by Leong et al. [9,10] reported results for reacting flow JIC experiments in a cylindrical duct at atmospheric pressure without inlet air preheat. A carbon balance technique similar to that of Jones et al. [11] was used by Leong et al. [9,10] to obtain the equivalence ratio. Alternate methods for obtaining the local equivalence ratio in a reacting flow were investigated by Demayo et al. [12].

A study by Vardakas et al. [13] extended the work by Leong et al. [9,10] to address the effects on both mixing and emissions of varying inlet air preheat and varying the number of orifices with preheated inlet air. The experiments were conducted at atmospheric pressure in a facility that provided for independent variation of jet and main (crossflow) inlet air preheat temperature. In Vardakas et al. [13], measurements were made at 16 radial and circumferential locations at a downstream distance equal to the radius of the mixer section. This study investigated configurations with 8, 12, 14, and 22 round holes at $J=57$ to give over-to optimum to underpenetrating jets.

Representative results from the Vardakas et al. report [13] are presented in this paper. The focus is on the effect of independently preheating the jet and main air for an "optimum" mixer and the effect of varying the number of orifices with both the jet and main air preheated to the same temperature. As the air for both streams would emanate from the same plenum in a practical combustor, the jet inlet air temperature would be different than the main inlet air temperature only if the air in either stream was used for another function prior to entering the combustion chamber. Nonetheless the influence of independently preheating each stream was assessed to provide additional insight into the NO_x formation in RQL systems.

Experiment

Facility. The experimental facility used in this study consisted of a premixing zone, a fuel-rich combustion zone, and a jet-mixing section, as shown in Fig. 1. In the premixing zone, propane gas was mixed with air upstream of the ignition point. Fuel-rich combustion was stabilized downstream of the quarl by a swirl-induced recirculation zone. To dissipate the swirl in the flow and to introduce a uniform nonswirling flow into the mixing section, the fuel-rich product was passed through an oxide-bonded silicon carbide (OBSiC) ceramic foam matrix (Hi-Tech Ceramics) with a rated porosity of 10 pores/in.

The mixing section included a modular quartz section through which the mainstream effluent passed, and to which jet air was supplied from a surrounding plenum. The plenum for the jet air was fed by four equally spaced air ports located toward the base of the plenum. A high-temperature steel flow-straightening device installed in the plenum conditioned and equally distributed the jet air entering the mixing module.

The mixing modules were 280 mm (11 in.) in length with inner and outer wall diameters of 80 mm (3.15 in.) and 85 mm (3.35 in.). The row of orifices was positioned with its centerline 115 mm (4.5 in.) downstream from the module entrance. An alumina-silica blend of ceramic fiber paper provided sealing between the module and the stainless-steel mating surfaces to form the plenum for the air jets.

Recirculating heaters of 20 kW and 25 kW were utilized to supply the necessary preheat to the main and jet air lines, respectively. The preheat temperatures were independently established and controlled.

Table 1 Operating conditions

Parameter	Value
Momentum-flux ratio, J	57
Mass-flow ratio, MR	2.5
Discharge coefficient, C_d	0.72
(Total jet area)/(cross-sectional area of duct), A_J/A_M	25%
Nonpreheated inlet air temperature	22°C (72°F)
Jet inlet preheat temperature	260°C (500°F)
Main air preheat temperature	260°C (500°F)

Experimental Conditions. The flow and geometric conditions are presented in Tables 1 and 2. The experiments were performed for a jet-to-mainstream momentum-flux ratio (J) of 57 and a mass-flow ratio (MR) of 2.5, both typical of RQL mixer conditions. The fuel-rich equivalence ratio and overall equivalence ratios (ϕ) were 1.66 and 0.45, respectively. The operating pressure for the system was 1 atm. Operating conditions for the experimental parametric variations are noted in Table 1.

The optimum number of round holes in a cylindrical duct is $n=\pi(\sqrt{2J})/2.5$ [3]. For a momentum-flux ratio (J) of 57, the optimal mixer would thus have 13.4 holes. Thus, two of the four mixing modules adopted for the current study were 12-hole and 14-hole configurations. In order to provide unambiguous over- and underpenetrating cases, 8-hole and 22-hole modules were included as well (Table 2). The orifice diameters were varied between modules in order to maintain a constant total jet area of 1244 mm^2 (1.93 $in.^2$). In this study $A_J/A_M=25\%$, and as reported previously, the effective area was 18% (900 mm^2) so $C_d=0.72$.

Measurements. For each module, species concentration measurements were obtained in a two-jet sector for a plane at x/R

Table 2 Orifice configurations

n	d (mm)	R/d
8	14.07	2.84
12	11.49	3.48
14	10.64	3.76
22	8.49	4.71

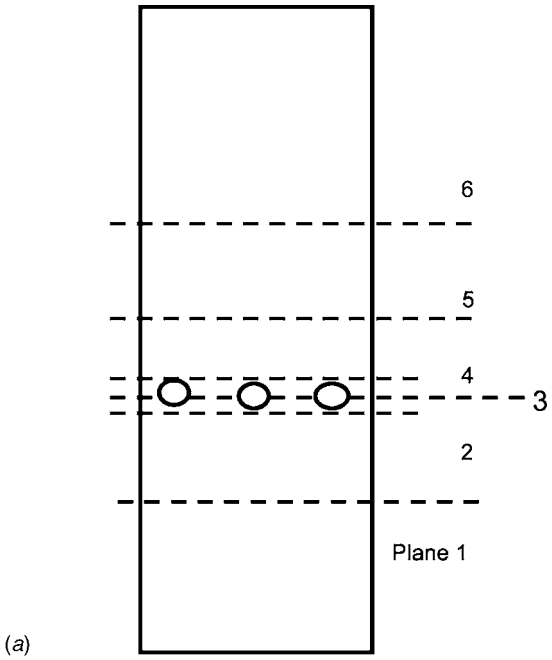

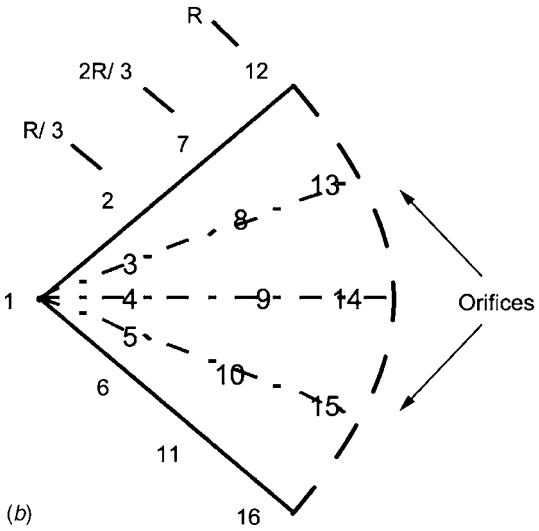

Fig. 2 Measurement locations: (*a*) data plane locations; (*b*) data point locations

=1 (plane 5 in Fig. 2(*a*)), where x/R is measured from the leading edge of the mixing module orifices. Thus $x/d=R/d$ for the data reported herein.

Each planar grid consisted of 16 points spread over a sector that included two orifices (Fig. 2(*b*)). The points included one point located at the center, and five points along each of the arcs at $r/R=1/3$, $2/3$, and 1. The points along each arc were distributed such that two points were aligned with the center of the orifices and three were aligned with the midpoint between orifice centers for all cases.

Area weighting was calculated by dividing the sector at circular arcs that passed through radii midway between measurement locations, and this arc was then divided circumferentially at points midway between measurement locations. The area ratios from this calculation were applied as weighting factors to the individual measurements.

Species concentration measurements were obtained by sampling through a water-cooled stainless-steel probe by routing the sample through a heated line connected to the emission analyzers.

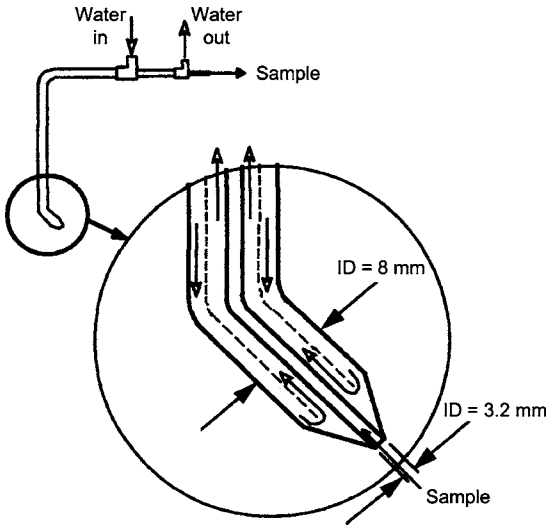

Fig. 3 Probe design

Water was condensed from the gas before the sample was analyzed by nondispersed infrared (NDIR) analysis for CO and CO_2, paramagnetic analysis for O_2, flame ionization detection (FID) for total hydrocarbons, and chemiluminesence (CLD) for NO_x. Data are reported as measured and were not "corrected" for either the ambient humidity or the expected water content of the flow.

Probe Design. A double-jacked water-cooled stainless-steel probe 762 mm (30 in.) in length was used to extract gas samples from the quick mixing section (Fig. 3). The probe measured 8 mm in outer diameter and tapered to 3.2 mm at the tip. A 45 deg bend was made 25.4 mm (1 in.) from the tip. The probe design was influenced by the research of Kroll et al. [7], who found that a thermocouple probe with a 45 deg angled tip was best for acquiring temperature data as it biased the mainstream and jet flows equally in the orifice region. The probe location was fixed and the rig was traversed to obtain the measurements. The plane of the angled probe tip was positioned such that the tip was pointed toward the center of the sector wall.

Measurement Uncertainty. The extractive emission measurement protocol was conventional. The analyzers are standardized equipment, which is checked frequently with span gases. Readings on the NO_x analyzer would be expected to be around 200 ppm for an aeroengine at cruise conditions and that number would be expected to vary about 5–10 ppm from the mean. CO_2 is typically around 7% with a data fluctuation of around 0.1%. The mean of O_2 is around 12% or less. That reading is usually very steady so the fluctuation is much below 0.1%. As for the relation between what exists in the flow and what is measured, this is a classical question, and they are assumed to be the same when standard procedures are followed.

A measure of the uncertainty of the data is given by analyzing the species measurements to determine the midplane and centerplane means and variances. In a perfect world, the three midplane measurements would be equal at a given radius and the two centerplane measurements would be equal, but they often are not. Their variability is a measure of both spatial and species uncertainties in the measurements. The averaged values (not area weighted) of NO_x, CO, CO_2, and O_2 for all 192 measurement locations are $NO_x=16.78\pm4.39$ ppm, $CO=2.99\pm1.77\%$, $CO_2=6.37\pm1.96\%$, and $O_2=8.01\pm3.30\%$, where the $\pm$ values are two standard deviations from the mean.

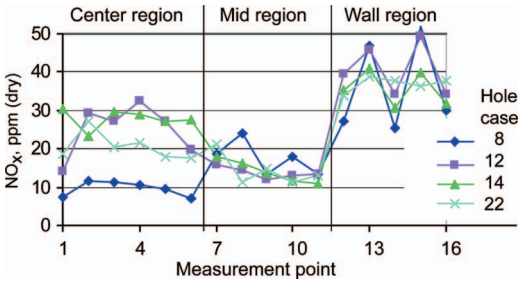

Fig. 4 Comparison of local NO_x data at $x/R=1$ and $J=57$ for modules with different numbers of round holes with both the main and jet air preheated

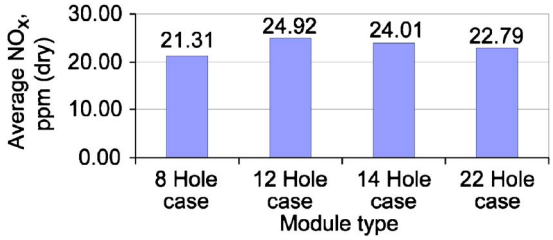

Fig. 6 Area-weighted planar average NO_x emissions at $x/R=1$ and $J=57$ for modules with different number of round holes with both the main and jet air preheated

Results and Discussion

This paper focuses on (1) the effect of the number of orifices with both streams preheated and (2) the effect of air preheat for the 12-hole module to illustrate the trends observed. Note that the trends are much more important than absolute values and that it was shown in Refs. [3–5] that trends were the same whether they came from CFD calculations, empirical model calculations, nonintrusive concentration measurements, or probe measurements. The flow and emission data collected for all the different preheat conditions and modules tested are presented in Vardakas et al. [13].

Effect of Number of Orifices With Preheated Inlet Air. Measurements are reported in this section with both the main and jet air preheated for modules with 8, 12, 14, and 22 round holes. This gives over-, optimum, and underpenetrating jets at $J=57$ to show the influence of the number of orifices on mixing and emissions. Previous studies by Leong et al. [9,10] identified optimal mixing configurations in a reacting flow for round-hole modules in the absence of inlet air preheat. The data presented in Figs. 4–7 are also for experimental conditions with $J=57$ and MR=2.5 but with both the main and jet air preheated to the same temperature as would probably be the case in a practical RQL combustor. Results are shown in Vardakas et al. [13] for other preheat conditions, but the trends in them are similar to those shown here.

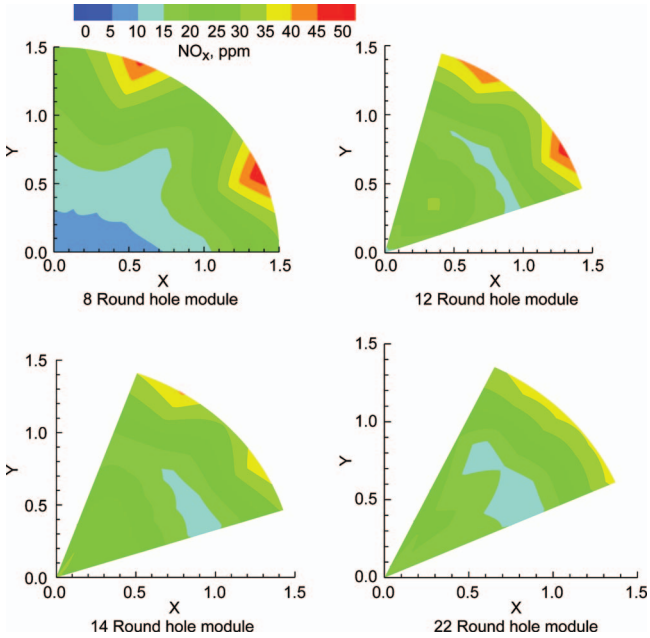

Fig. 5 NO_x distribution plots at $x/R=1$ and $J=57$ for modules with different number of round holes with both the main and jet air preheated. Average=24.15±2.83 ppm.

Figure 4 reveals the similarity of the NO_x concentrations in the mid- and wall regions for the several modules. The contour distributions in Fig. 5 also show that high NO_x concentrations were measured in the jet wakes for all modules. This suggests that a significant production of NO_x can occur downstream of the orifices in the region of the jet wakes. Note that there are substantial differences in the distribution of NO_x among the modules. The average value (not area weighted) ±2 standard deviations for the conditions shown are included in the title of Fig. 5.

The area-weighted average NO_x emission levels, shown in Fig. 6, are influenced most by the concentrations in the wall region. The area-weighted averages show that the various modules have remarkably similar overall NO_x emissions. The lowest area-weighted average NO_x (21.3 ppm) is only 14% lower than the highest (24.9 ppm). The minimal sensitivity of overall NO_x to the number of orifices is a significant result, particularly if it is also observed at elevated pressure as is typical of combustors in gas turbine engines.

For the nearly optimum mixers with 12 and 14 orifices, NO_x is high in both the wall region and near the center and lowest in the midspan region. Parenthetically, the prior studies by Leong et al. [9,10] identified the 12-hole module as the best mixer for $J=57$ and presumed that it would be most likely to produce the least NO_x. The results from the current study show that the 12-hole module produces the most overall NO_x at atmospheric pressure (see Fig. 6) and suggest that an aerodynamically optimum mixer may not minimize NO_x.

It can be seen in Figs. 4 and 5 that the NO_x concentrations in the center region for the 8-hole module are significantly lower than for the other three modules. Since the 8-hole module is an overpenetrating case, NO_x concentrations near the centerline of the combustor were expected to be lower for this case, but this has only a small impact on the area-weighted average NO_x concentration (Fig. 6), which, while lower for this case, is only slightly lower than the maximum. NO_x concentrations for the 8-hole module are very high in the jet wake region (Fig. 5), probably as the large jets that are necessary in this case to maintain a constant total area produce a very significant wake.

Although the jets underpenetrate in the 22-hole case as expected, they do not underpenetrate enough to avoid a region of near-stoichiometric concentration at high temperature adjacent to the wall. The sector plots of Fig. 5 suggest that the NO_x levels are again highest in the wake of the jets. The area-weighted NO_x emissions shown in Fig. 6 for all cases are dominated by the wall region and are there is only a small difference between the maximum and minimum values.

Figures 7 present the distributions of CO (*a*), CO_2 (*b*), and O_2 (*c*) for the four modules with jet and main air both preheated. The data for concentrations of the major species confirm that the number of orifices has a significant effect on the mixing distributions as expected. Jet penetration and mixing are shown best by the O_2 distributions. The penetration of the jets for the 12- and 14-hole module cases is observed to be nearly optimum while the 8- and

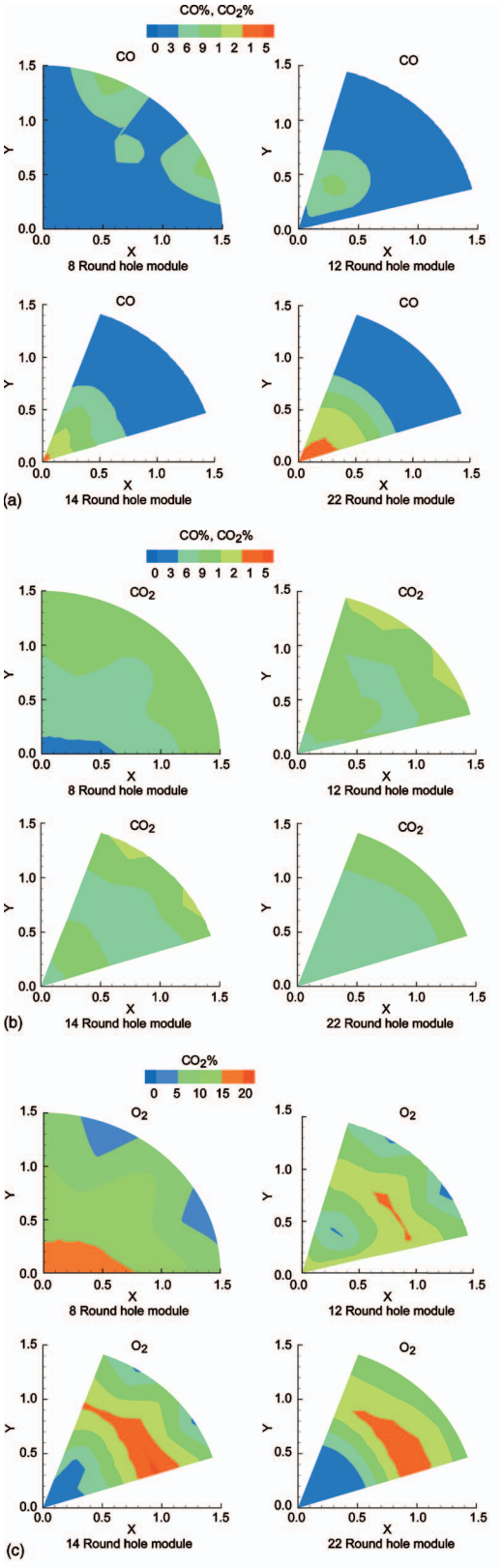

Fig. 7 (*a*) **CO distribution plots at $x/R=1$ and $J=57$ for modules with different number of round holes with both the main and jet air preheated. Average=2.91±1.98%** (*b*) **CO_2 distribution plots at $x/R=1$ and $J=57$ for modules with different number of round holes with both the main and jet air preheated. Average=6.39±1.15%.** (*c*) **O_2 distribution plots at $x/R=1$ and $J=57$ for modules with different number of round holes with both the main and jet air preheated. Average=7.96±3.13%.**

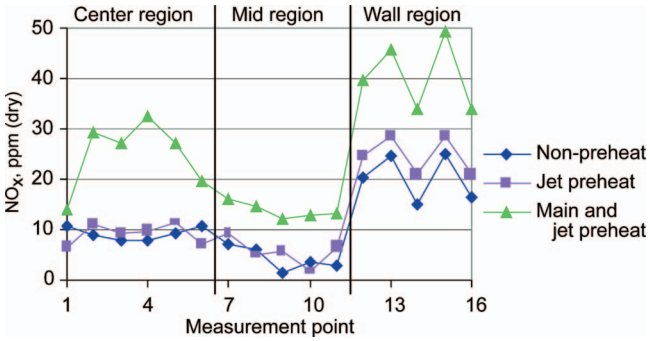

Fig. 8 Comparison of local NO_x data at $x/R=1$ and $J=57$ for the 12 round-hole module with different air streams preheated

22-hole modules result in over- and underpenetrating cases, respectively, as confirmed by the data in Fig. 7. Note that the highest concentrations of CO_2 are in the wall region for all the modules, and concentrations of CO are high in the center of the cylindrical duct for both the 14- and 22-hole modules, but the region of high CO is largest for the 22-hole module.

The average NO_x value is given in the title of Fig. 5, and the average value (not area weighted) ±2 standard deviations of CO, CO_2, and O_2 for these experiments are included in the title of Fig. 7.

Effect of Preheat for an Optimum Mixer. The effect on the measured NO_x values of heating the inlet air for the 12-hole module is illustrated in Fig. 8. Three preheat conditions are presented. The first set of conditions is for no air preheat and provides a comparison for the results for the elevated inlet air preheat temperature conditions. The second set of conditions is for jet air preheat only (no main air preheat) and the third set of conditions is for both the jet air and main air preheated to the same temperature as would probably be the case in a practical combustor. Figure 8 shows that preheating only the jet air results in relatively small increases in NO_x emissions compared to the case where both the main and jet air are preheated.

Figure 9 presents the corresponding NO_x sector plots. The condition in which both the main and jet air were preheated showed the largest NO_x increase for all the modules and shows the higher NO_x levels, also shown in Fig. 8. This result confirms the expectation that the absolute value of NO_x emissions would increase with the inlet air preheated. As in Fig. 5, the average NO_x value (not area weighted) ±2 standard deviations for these experiments are included in the title of Fig. 9. Unlike the variation of the averages for the 8-, 12-, 14-, and 22-hole modules, which are less than 2 standard deviations from the average, the variations of the averages for the preheat cases vary significantly from a low value of 10.56 ppm for the case without preheat to a high value of 26.47 ppm with both streams preheated.

Area-weighted average NO_x concentrations at $x/R=1$ are presented in Fig. 10 to show the effect of preheated air on overall NO_x emissions. This figure shows that preheating only the jet air increases the overall NO_x by only 20% from that obtained without preheat, whereas preheating both the main and jet air doubles the overall NO_x from that obtained with only the jet preheated.

The NO_x production in the fuel-rich zone was expected to be small compared to that produced in the mixing zone via the thermal (Zeldovich) mechanism, but Figs. 8–10 all show the dominating influence of the main air preheat on NO_x and the relatively small impact of preheating only the jet air. As the jet air is over 70% of the total air flow, the small effect of preheating the jets seems to be counterintuitive to the expectation that jet air preheat should be important because high temperatures and near-stoichiometric conditions may persist in the proximity of the jets and these are conditions that are important for NO_x production via

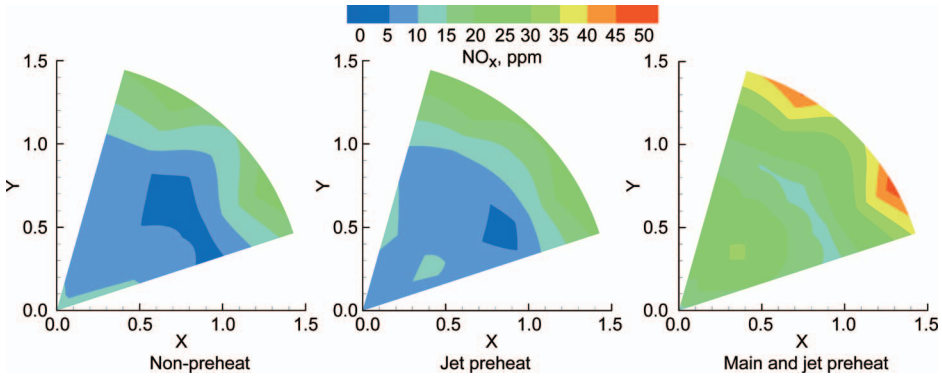

Fig. 9 NO_x distribution plots at $x/R=1$ and $J=57$ for the 12 round-hole module with different air streams preheated. Average=16.91±2.13 ppm.

the thermal mechanism.

Figure 11 presents the concentrations of CO (*a*), CO_2 (*b*), and O_2 (*c*), for the 12 round-hole configuration for no preheat (left), jet air preheated (center), and both jet and main air preheated (right). Note that the emission distributions are similar for species other than NO_x at all preheat conditions. The average values are given in the titles for Fig. 11. Unlike the average NO_x values, which vary significantly with preheat, the average values for CO, CO_2, and O_2 are all less than a standard deviation from their average. Similar results were observed for the other modules for these preheat conditions.

Conclusions

An experiment was performed to examine the effects of air preheat on NO_x production in RQL combustor configurations. Care was taken to design the experiment in a manner that allowed the jet air preheat to be controlled independent of the main air preheat. Mixing modules (80 mm inside diameter (i.d.)) with a varying number of round holes but the same total area (1244 mm^2) were evaluated while maintaining a constant jet-to-mainstream momentum-flux ratio ($J=57$) and mass-flow ratio (MR=2.5).

The results lead to the following conclusions:

a. The number of orifices was found to have a significant effect on mixing and the distributions of major species, but very little effect on overall NO_x emissions.
b. The spatial NO_x distribution varies among configurations, but the area-weighted NO_x data obtained for a fixed momentum-flux ratio and a constant total orifice area were relatively insensitive to the number of jets on the perimeter of the quick-mix section. A corollary of this result is that an aerodynamically "optimum" mixer may not lead to the minimization of overall NO_x emissions.
c. NO_x concentrations in RQL configurations are high in the wake of the air jets near the wall where jet induced wake recirculation offers both high temperatures and lengthened residence times.
d. Air preheat was found to have very little effect on mixing and the distributions of major species, but preheat did increase NO_x emissions significantly.
e. Although the jet air comprises over 70% of the total airflow and it was expected that higher jet air temperature would contribute significantly to NO_x production, the impact of preheating jet air alone on NO_x emissions was small compared to preheating both main and jet air.
f. Results from the current study (1) do not support the assumption that an optimal mixer would lead to the minimization of NO_x emissions and (2) show that preheat is most important in the mainstream.

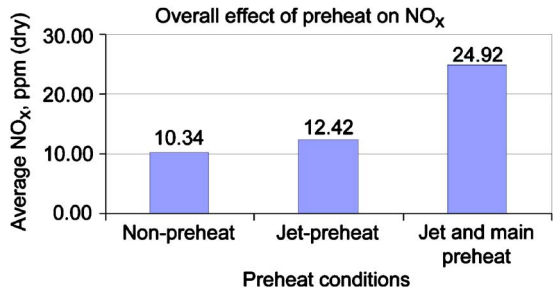

Fig. 10 Effect of air preheat on area-weighted NO_x data at $x/R=1$ and 57 for the 12 round-hole module with different air streams preheated

Acknowledgment

This work was supported by Cooperative Agreement No. NCC 3-412 from the NASA Glenn Research Center. Professor G. Scott Samuelsen, Director of the Advanced Power and Energy Program at the University of California, Irvine (UCI), was the Principal Investigator of this work and directed the experiments, which were performed at the UCI Combustion Laboratory (UCICL). The authors would like to thank Mark A. Vardakas (now at Solar Turbines) for his excellent experimental work done with the guidance and assistance of Dr. Jacob Brouwer. The authors also wish to thank Dr. May L. Corn (nee Leong—now at the United Technologies Research Center) for her contributions to this study and for making both her reacting flow JIC facility and details of her previous work available.

Nomenclature

A_J/A_M = jet-to-mainstream area ratio=$[(d/2)/(R)]^2$
C = $\pi^*\sqrt{2J}/n$, derived in Ref. [3]
C_d = orifice discharge coefficient
d = round-hole diameter
d_j = effective round-hole diameter=$(d)(\sqrt{C_d})$
DR = jet-to-mainstream density ratio, ρ_{jet}/ρ_{main}
J = jet-to-mainstream momentum-flux ratio=$(\rho V^2)_{jet}/(\rho U^2)_{main}$, $(MR)^2/DR/(C_d)^2/(A_J/A_M)^2$
MR = jet-to-mainstream mass-flow ratio=$(\rho V A_{total})_{jet}/(\rho U A_{can\ cross\text{-}section})_{main}$, $(DR)\times(V_J/U_M)(C_d)(A_J/A_M)$
n = number of round holes in quick-mix module
R = radius of the quick-mix module
r = radial distance from the module center
U = axial velocity

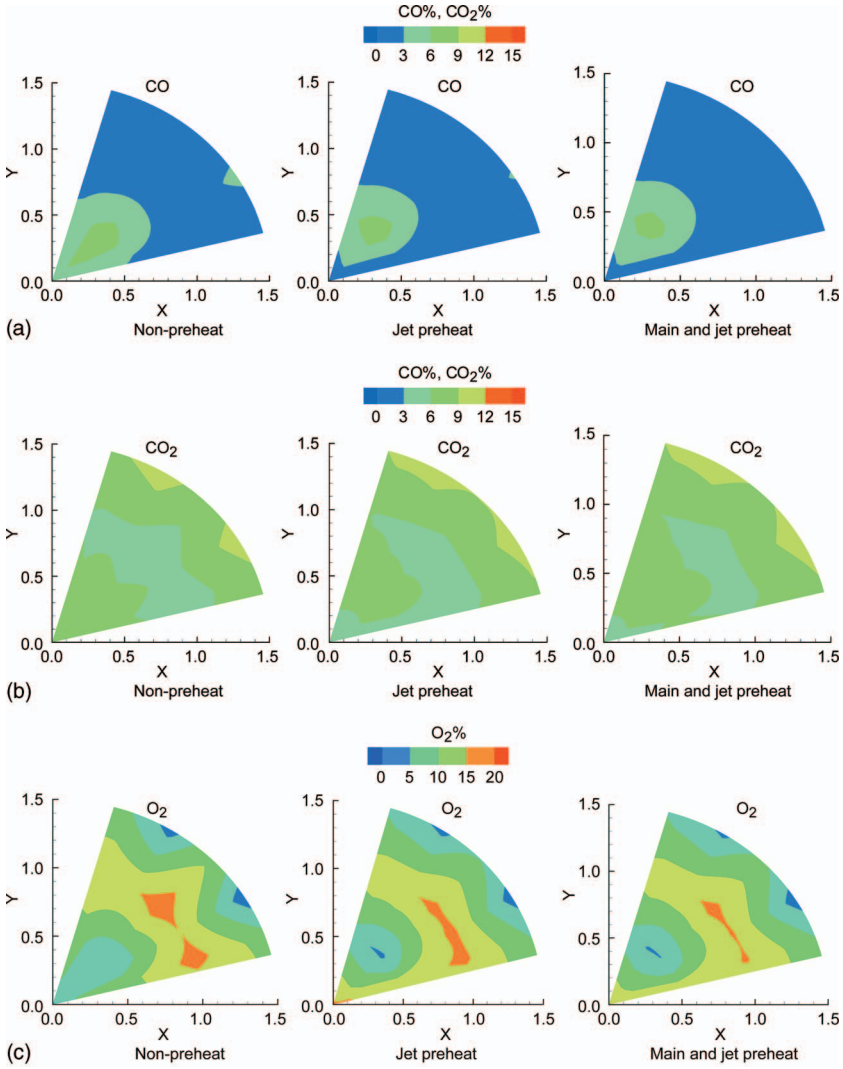

Fig. 11 (*a*) **CO distribution plots at $x/R=1$ and $J=57$ for the 12 round-hole module with different air streams preheated. Average=2.63±2.37%.** (*b*) **CO_2 distribution plots at $x/R=1$ and $J=57$ for the 12 round-hole module with different air streams preheated. Average=7.24±2.73%.** (*c*) **O_2 distribution plots at $x/R=1$ and $J=57$ for the 12 round-hole module with different air streams preheated. Average =7.46±3.33%.**

U_M = unmixed mainstream velocity
V_J = jet exit velocity
x = downstream distance, $x=0$ at leading edge of orifice
ϕ = equivalence ratio $=(\text{fuel/air})_{\text{actual}}/(\text{fuel/air})_{\text{stoichiometric}}$

References

[1] Margason, R. J., 1993, "Fifty Years of Jet in Cross Flow Research," *Presented at Computational and Experimental Assessment of Jets in Cross Flow*, April, AGARD Conference Proceedings 534.

[2] Demuren, A. O., 1994, "Modeling Jets in Cross Flow," NASA Contractor Report No. 194965; ICASE Report No. TR-94-71.

[3] Holdeman, J. D., 1993, "Mixing of Multiple Jets with a Confined Subsonic Crossflow," Prog. Energy Combust. Sci., **19**, pp. 31–70; see also AIAA Paper No. 91-2458 and NASA Report No. TM 104412.

[4] Holdeman, J. D., Liscinsky, D. S., Oechsle, V. L., Samuelsen, G. S., and Smith, C. E., 1997, "Mixing of Multiple Jets with a Confined Subsonic Crossflow: Part I—Cylindrical Ducts," ASME J. Eng. Gas Turbines Power, **119**(4), pp. 852–862; also ASME Paper No. 96-GT-482 and NASA Report No. TM 107185.

[5] Holdeman, J. D., Liscinsky, D. S., and Bain, D. B., 1999, "Mixing of Multiple Jets with a Confined Subsonic Crossflow: Part II—Opposed Rows of Orifices in a Rectangular Duct," ASME J. Eng. Gas Turbines Power, **121**(3), pp. 551–562; also ASME Paper No. 97-GT-439 and NASA Report No. TM 107461.

[6] Hatch, M. S., Sowa, W. A., Samuelsen, G. S., and Holdeman, J. D., 1995, "Jet Mixing Into a Heated Cross Flow in a Cylindrical Duct: Influence of Geometry and Flow Variations," J. Propul. Power, **11**(3), pp. 393–400; also Paper No. AIAA-92-0773 and NASA Report No. TM 105390.

[7] Kroll, J. T., Sowa, W. A., Samuelsen, G. S., and Holdeman, J. D., 2000, "Optimization of Orifice Geometry for Cross Flow Mixing in a Cylindrical Duct," J. Propul. Power, **16**(6), pp. 929–936; see also Paper No. AIAA-94-0219 and NASA Report No. TM 106436.

[8] Meisl, J., Koch, R., Kneer, R., and Wittig, S., 1994, "Study of Nox Emission Characteristics in Pressurized Staged Combustor Concepts," *25th Symposium (International) on Combustion*, 25, pp. 1043–1049.

[9] Leong, M. Y., Samuelsen, G. S., and Holdeman, J. D., 1999, "Mixing of Jet Air with a Fuel-Rich, Reacting Crossflow," J. Propul. Power, **15**(5), pp. 617–622; see also WSS/CI Paper No. 97S-034 and NASA Report No. TM 107430.

[10] Leong, M. Y., Samuelsen G. S., and Holdeman, J. D., 2000, "Optimization of Jet Mixing Into a Rich, Reacting Crossflow," J. Propul. Power, **16**(5), pp. 729–735; also Paper No. AIAA-98-0156 and NASA Report No. TM—97-206294.

[11] Jones, W. P., McDonell, V., McGuirk, J. J., Milosavljevic, V. D., Taylor, A. M. K. P., and Whitelaw, J. H., 1993, "The Calculation of Mean Mixture Fractions in Turbulent Non-Premixed Methane Flames From Aspiration-Probe Measurements," Department of Mechanical Engineering, Imperial College of Science, Technology, and Medicine, Report No. TFS/93/13.
[12] Demayo, T. N., Leong, M. Y., Samuelsen, G. S., and Holdeman, J. D., 2003, "Assessing Jet-Induced Spatial Mixing in a Rich, Reacting Crossflow," J. Propul. Power, **19**(1), pp. 14–21; see also NASA/CR Report No. 2004-212886.
[13] Vardakas, M. A., Leong, M. Y., Brouwer, J., Samuelsen, G. S., and Holdeman, J. D., 1999, "The Effect of Air Preheat at Atmospheric Pressure on the Formation of NO_x in the Quick-Mix Sections of an Axially Staged Combustor," NASA Report No. TM-1999-209431.

On the Applicability of a Spoked-Wheel Wake Generator for Clocking Investigations

Sven König
e-mail: koenig@tfa.tu-darmstadt.de

Bernd Stoffel

Turbomachinery Laboratory (TFA),
Darmstadt University of Technology,
64287 Darmstadt, Germany

A comprehensive investigation was carried out using two different experimental setups: A 1.5-stage axial turbine and a simplified model, a "spoked-wheel" setup with a rotating wake generator consisting of cylindrical bars. The second stator of the turbine was designed at MTU Aero Engines as a high-lift profile with a Reynolds number typical for low-pressure turbines in jet engines. At design conditions, the flow on the stator 2 suction side features a pronounced separation bubble. To study the behavior of the stator 2 boundary layer and the interaction mechanisms between stator and rotor wakes, different measurement techniques were used: X-wire probes, five-hole probes, static pressure tappings, and surface mounted hot-film gauges. It was found that a rotating wake generator of the spoked-wheel type is not capable of resolving the relevant clocking mechanisms that occur in a real engine. However, such a simplified setup is useful to separate some of the physical mechanisms, and in case that the interaction of the stator 1 wakes with the stator 2 boundary layer is negligible, a spoked-wheel setup is well suited to simulate the influence of periodically incoming wakes on the transition behavior of stator 2.
[DOI: 10.1115/1.2799523]

Introduction

Due to the relative motion of rotating rotors and stationary stators, the flow field in multistage turbomachines exhibits a strong periodic unsteadiness. Since the main flow in such turbomachines is highly turbulent, a superposition of the periodic fluctuations and high-frequency turbulent fluctuations takes place. The wakes from stator and rotor blades are characterized by a velocity deficit and enhanced turbulence intensities, and it is well known that the interaction of the wakes with downstream blade rows influences the boundary layer transition behavior and the heat transfer characteristics of the blade. The first investigations on wake flows were conducted using stationary cylindrical wake generators within straight channels. Fundamental work on this topic was carried out by Schlichting [1], Townsend [2], Ermshaus [3], Eifler [4] and Pfeil and Eifler [5,6]. Savill [7] and Nakayama [8] extended these ideas on wake flows within curved channels. Later, Schobeiri et al. [9,10] carried out systematic experimental investigations to develop a theoretical framework for the two-dimensional curvilinear wake flow behind a cylinder. In the early 1970s, it was found that the wakes of airfoils can be simulated by means of cylindrical bars (Kiok [11], Eifler [4], and Trost [12]). This assumption is valid in the far wake region for $x/d>100$, where x denotes the axial distance downstream of the wake generator and d the diameter of the cylinder. On the basis of this idea, many investigations on the wake characteristics of stationary and moving cylindrical bars for turbomachinery flow conditions were carried out (e.g., Pfeil and Schröder [13], Schröder [14], and O'Brien and Capp [15]). An overview on wake effects with special focus on the comparison between the wake flow of real blades and cylindrical bars is given by Stoffel [16]. In recent years, the need to reduce engine weight led to a reduction of the blade count of the LP turbine, which enormously advanced the importance of unsteady effects. Many investigations by different research groups addressed the boundary layer behavior of such high-lift LP turbine blades under the influence of periodic unsteady wakes using wake generators consisting of cylindrical bars (e.g., Schulte and Hodson [17], Stadtmüller et al. [18], Howell et al. [19], Coton et al. [20], and Schobeiri et al. [21–23]). The variety of publications dealing with wakes of cylindrical bars in a turbomachinery environment is due to the possibility to study the influence of periodic unsteady effects by means of a simplified setup with substantially reduced manufacturing costs. Furthermore, a simple variation of the wake frequency with only a small change of the incidence angle becomes possible, which allows systematic studies of the influence of the wake passing frequency.

To further increase the efficiency of multistage turbomachines, the inherently unsteady effects occurring in such engines are being exploited, especially in the LP turbine. Clocking (indexing) is one way of influencing the flow field in multistage turbomachinery by changing the relative circumferential position of rotors or stators with the same blade count of adjacent rows. Most clocking studies show a possible gain in efficiency in the order of 0.5 percentage points. A detailed literature review on clocking investigations can be found in König et al. [24]. Although it is well known that cylindrical bars can be used to simulate the influence of rotor wakes on the boundary layer behavior of a downstream stator row, no information is available in how far a simplified setup with a wake generator consisting of cylindrical bars can be used to simulate the relevant physical mechanisms affecting clocking. To obtain a reliable answer on this question, an extended investigation was carried out at TU Darmstadt. Three experimental setups with different levels of complexity were studied in great detail: A steady stator-stator setup, a spoked wheel setup with a wake generator consisting of cylindrical bars, and a real 1.5-stage axial turbine. The results of the first setup are presented in Heinke [25] and Heinke et al. [26], and the results of the 1.5-stage turbine in König et al. [27], König [28], and König et al. [24,29]. The present paper summarizes the results obtained for the spoked wheel setup and compares them with those for the 1.5-stage turbine.

Experimental Setup and Aerodynamic Design

Figure 1(*a*) shows a schematic of the experimental facility. The flow enters the annular test rig after passing a settling chamber. The vertical test section consists of two stators (3, 6) and one wake generator (a real rotor or alternatively, a spoked wheel rotor)

Contributed by the Fluids Engineering Division of ASME for publication in the JOURNAL OF FLUIDS ENGINEERING. Manuscript received September 28, 2006; final manuscript received May 14, 2007. Review conducted by Philip M. Ligrani.

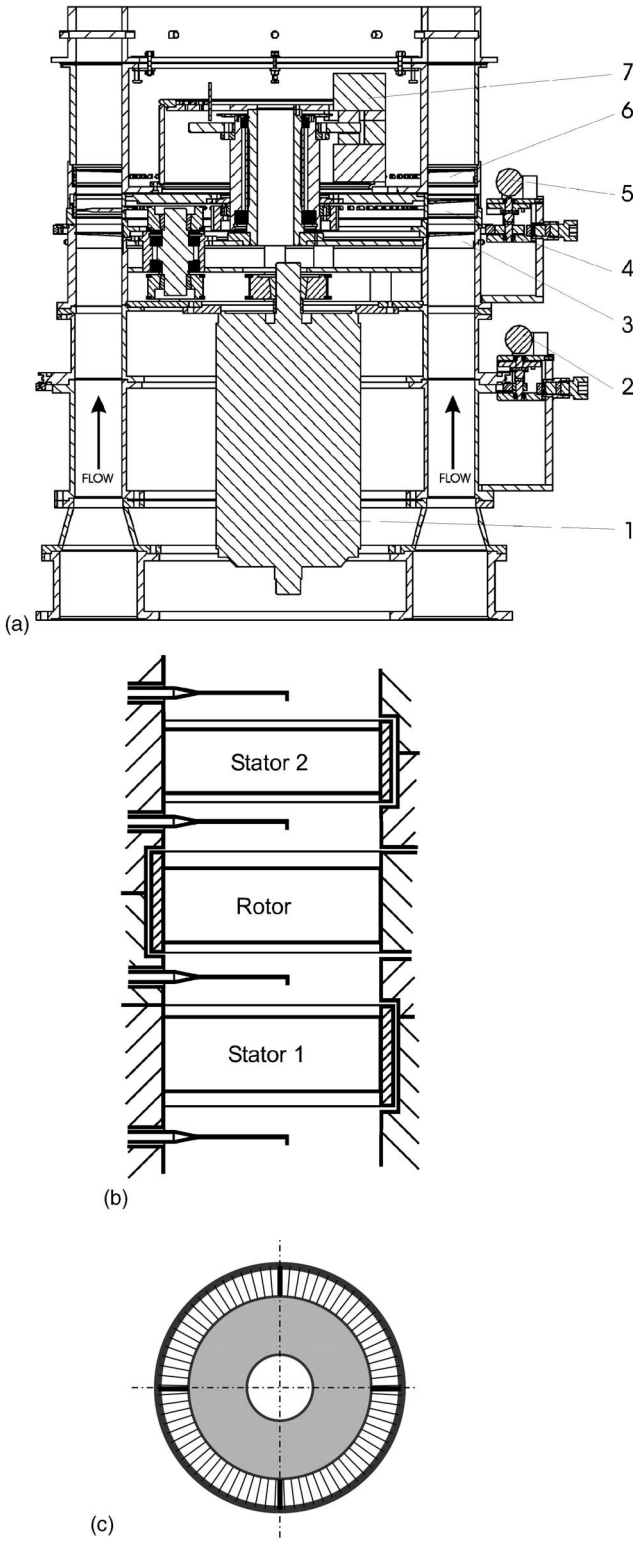

Fig. 1 TU Darmstadt clocking facility

(4). To adjust different clocking positions, stator 1 can be indexed circumferentially relative to stator 2 by the electric motor (2). Motor (5) allows wake traverses in circumferential direction. A 55 KW water cooled four quadrant electric generator (1) keeps the RPM of the rotor at a constant level and feeds the surplus power back to the supply system (1.5-stage turbine) or drives the spoked wheel rotor (spoked wheel setup). In case of unallowed mode of operation, the fail safe emergency break (7) causes a controlled shut down of the rotor.

A simplified expanded view of the blade rows for the 1.5-stage turbine (ROV) is given in Fig. 1(*b*) and the measuring planes are indicated by sketches of the probes. For simplification purposes, the felt seals are omitted and it has to be noted that only one probe at a time was applied during the measurements to avoid probe interference effects. The exact probe positions with the corresponding nomenclature are given in Fig. 2 for the two setups investigated in the present paper, the spoked-wheel setup (SRV) and the 1.5-stage turbine (ROV). The steady stator-stator setup that was investigated by Heinke [26] exhibits the same geometry as the spoked-wheel setup but without the wake generator. To adapt the different setups, exchangeable rings were designed that ensure a smooth flow channel and minimized leakage for each setup. As can be seen in Fig. 2, the spokes for the SRV rotate in the same plane as the trailing edges of the rotor blades for the ROV. In Fig. 1(*b*), the rotor blades would be substituted by cylindrical bars for the SRV. The orientation of Figs. 1(*a*) and 1(*b*) corresponds to the orientation of the test rig, whereas Fig. 2 is rotated by 90 deg to obtain the more usual orientation as used for CFD calculations.

For all three setups, stator 2 was identical and the time mean inflow angles and velocities had been adapted in order to obtain a similar aerodynamic loading for stator 2. Due to the negligible deflection caused by the cylindrical bars, the same stator 1 was used for the stator-stator and the spoked-wheel setup, whereas a different stator 1 had to be used for the turbine. The two different stators 1 were designed in such a way that their corresponding velocity deficits and turbulence intensities in the inlet plane of the wake generator showed similar distributions. To achieve approximate drag coefficients for both stators 1, a longer chord length for the stator 1 of the spoked-wheel setup was chosen to compensate for the reduced losses due to the smaller deflection angle. A detailed experimental investigation was carried out in a separate linear cascade wind tunnel to determine the diameter of the cylindrical bars and the axial distance between the blade rows (compare Heinke [25]). For the steady linear cascade tests, good agreement between the velocity deficits and turbulence distributions of the rotor blades and the cylindrical bars could be achieved in the stator 2 inlet plane. As will be discussed later in the paper, deviations from the linear cascade results were found for the annular clocking facility, and the corresponding unsteady wake profiles are given in Fig. 10 for different clocking positions in measuring plane E2.

To stabilize the spoked-wheel rotor, four support rods with a diameter of 10 mm were evenly spaced on the circumference, as can be seen in Fig. 1(*c*). The supports are necessary to hold the shroud, which was applied to minimize vibrations of the 77 spokes during the measurements. The support rods inevitably disturb the pneumatic measurements (five-hole probes, static pressure tappings), but their influence was eliminated for the time resolved measurements (*x*-wire probe, surface mounted hot-film gauges). The details about the experimental setup and the installed equipment are described in more detail by Heinke [25].

Table 1 gives an overview of the geometric and aerodynamic parameters. Stator 2 was designed at MTU Munich as a state-of-the-art high-lift LP turbine airfoil which, under design flow conditions, has a laminar separation bubble on the suction side. To study the behavior of the separation bubble in detail, the current design slightly differs from actual turbine blade design to increase the bubble size for the low Mach number flow. The Reynolds number, based on exit conditions and cord length of stator 2, is in the order of 217,000. For the design flow conditions, the flow can be considered incompressible. In the midspan region, secondary flows are negligible and felt seals are applied between rotating parts to minimize leakage flows.

On the stator 2 leading edge, a pressure tapping is used to

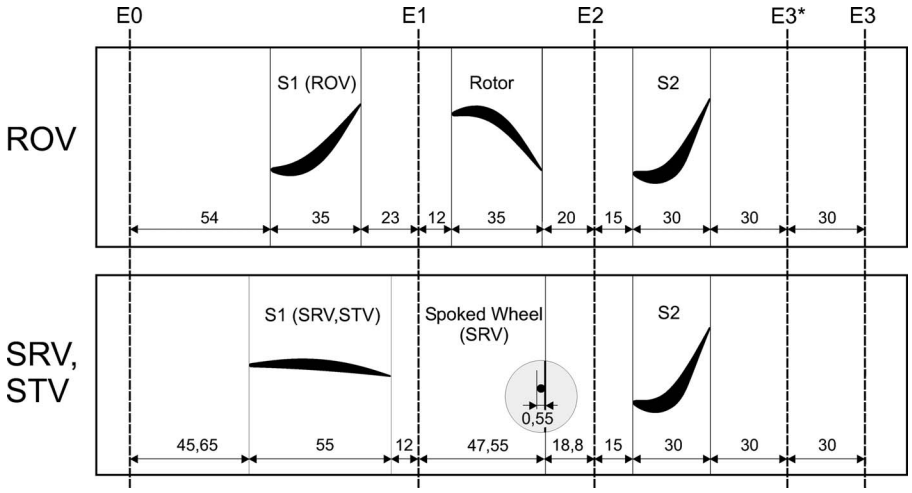

Fig. 2 Definition of the measuring planes

define the clocking position: The smallest measured total pressure on the leading edge indicates clp=0.0. Due to the distortion of the stator 1 wake within the rotor passage for the turbine, this position does not necessarily coincide with the impingement point of the stator 1 wake on the stator 2 leading edge. However, numerical calculations show that the two positions are very close. Based on these results, it is assumed that for clp=0.0, the stator 1 wake hits the leading edge of stator 2. The clocking positions cover one airfoil pitch at midspan and vary from −0.5 to 0.5. The magnitude of clp, given as the fraction of one stator pitch at midspan, is a measure of the circumferential distance between the streamline of the S1 wake core and the streamline leading to the leading edge of S2. Negative values indicate that the stator 1 wake impinges on the pressure side of S2 and positive values indicate impingement points on the suction side. For the spoked-wheel setup, no distortion of the stator 1 wakes due to the wake generator takes place.

Measurement Techniques

The pressure measurements along the stator 2 vane were performed using a ScaniValve equipment. The pressure sensor was a PDCR22 with a linearity of 0.04% and a pressure range of 70 mbar. A 12 bit A/D converter and a computer with a Pentium II processor were used to carry out the data acquisition.

A PSI9016 pressure scanner with a pressure range of 1 psi and an accuracy of 0.15% (full scale) was used for the five-hole probe

Table 1 Geometry and aerodynamic parameters

Parameter	Stator 1	Rotor	Stator 2
Geometry			
Tip diameter	881 mm	881 mm	881 mm
Hub diameter	677.5 mm	677.5 mm	677.5 mm
Blade count	66	77	66
Vane blade spacing	35 mm	—	35 mm
Chord length, C	42.79 mm	41.01 mm	38.67 mm
Axial chord length, C_{ax}	35 mm	35 mm	30 mm
Span, H	101.75 mm	101.75 mm	101.75 mm
Pitch at midspan, s	37.09 mm	31.79 mm	37.09 mm
Aspect ratio, H/s	2.74	3.2	2.74
Geometrical turning angle	51.7 deg	59.5 deg	69.3 deg
Measured flow parameters			
Mass flow		13 kg/s	
Inlet total temperature, T_{t_0}		331.6 K	
Inlet Mach number, Ma_{c_0}		0.133	
Inlet flow angle, α		0.2 deg	
Inlet turbulence intensity, Tu_0		2.2 %	
Rotational speed, n	-	−1247 rpm	-
Exit Mach number, Ma_c	0.217	0.135	0.287
Exit flow angle, α	−53.2 deg	11.6 deg	−60.6 deg
Stage pressure ratio, p_{t_1}/p_{t_3}		1.042	
Reduced frequency, $f_r=(f\bar{C}_{S2})/(c_{ax_2})$		1.28	
Flow coefficient, $\phi=(c_{ax_2})/(\lvert U\rvert)$		0.95	
Stage loading, $\psi=(c_{u_2}-c_{u1})/(U)$		−1.45	
Degree of reaction, $R=[(c_2^2-c_1^2)/(2)-U(c_{u_2}-c_{u_1})]/[(c_3^2-c_1^2)/(2)-U(c_{u_2}-c_{u_1})]$		0.3	
Reynolds number, $Re_{C_{S2}}=(c_3 C_{S2})/(\nu)$		217,000	

measurements. To account for Mach- and Reynolds number effects, the probes were calibrated at similar Ma and Re numbers as during the experiment. To assess the influence of unsteady wakes on the pneumatic measurements, a variation of the tube length and diameter, as well as an error estimation proposed by Kazimierski and Horodko [30], were carried out. It was found that no correction procedure was necessary to account for unsteady effects.

Hot-wire measurements were carried out using a Dantec 55P62 *x*-wire probe, and an external TC6 temperature probe was used to compensate for temperature variations. The voltage signal was converted using a 12-bit A/D converter. The frequency response of the wires was optimized by a square wave test. A once per revolution TTL trigger signal allowed ensemble averaging of the measured signal. One-hundred fifty samples were found to be sufficient to resolve the stator 1 and rotor wakes. The sampling frequency was set to 30 kHz and a low pass filter of 10 kHz was applied. Measurement inaccuracies were mainly due to probe contamination and temperature differences between calibration and experiment which, due to changes of the density, cannot be completely eliminated by the compensation probe.

From the surface mounted hot-film gauges, a measure for the real wall shear stress, the nondimensional quasi-wall shear stress (QWSS)

$$\tau_{\mathrm{qw}} = \left(\frac{E^2 - E_0^2}{E_0^2}\right)^3 \tag{1}$$

was computed, where τ_{qw} is the quasi-wall shear stress, E is the output voltage, and E_0 is the voltage under zero flow conditions. Since the gauges were operated at constant temperature rather than constant overheat, the zero voltage E_0 was measured at the same air temperature as the voltage E during the experiment. To double the spatial resolution of just one hot film array, two adjacent blades were equipped on the suction side and two on the pressure side, maintaining the same inflow condition for each clocking position because of the same stator blade counts. On the two corresponding blades, the arrays where mounted shifted by half of the array sensor distance, which leads to a spatial resolution of 1.25 mm. To make possible an investigation of the whole boundary layer, the sensors cover the whole blade surface on the suction side as well as the pressure side, beginning with the leading edge. For the data representation, the average of the curves of the two corresponding blades was calculated. To maintain the original blade geometry, the blade surface had to be adjusted and the arrays where glued on lower by their sensor thickness. The application of the four blades was carried out by MTU/Munich. A multiplexer was used to scan the output voltages of the 71 sensors sequentially and pass it to the CTA bridge. After switching on the bridge, a waiting period of 1 sec was applied before the beginning of the measurement to allow the bridge to settle. To achieve the same overheat temperature of 60 °C for all sensors, deviations in sensor resistances had to be accounted for and each sensor was allocated an individual reference resistance in the anemometer bridge. The frequency response of the hot films was optimized by a square wave test. A once per revolution TTL trigger signal allows ensemble averaging of the measured signal. The sampling frequency was set to 20 kHz. Test measurements were carried out to optimize the number of ensembles required, which led to the number of 100 ensembles.

To assess the repeatability of the results, at least three measurements were taken for each clocking position, indicated by means of error bars in the figures being presented. Five-hole probe measurements of four stator 2 blades were carried out to find one stator 2 pitch that represented best the average of the four blades concerning total pressure loss and deflection angle. To evaluate the influence of the axial probe position, two measurements were carried out in the measuring planes 30 mm and 60 mm downstream of S2. Despite the mixing processes, observable for the local flow variables, the characteristics of the integral curves did not show a dependency on the probe position.

The probe measurements were carried out in five different measuring planes of which the results for the measuring planes 15 mm upstream and 60 mm downstream of S2 are being presented in the paper. The probes were aligned in such a way that their position upstream of S2 for clp=0.0 and y/s=0.0 coincides with the streamline of the stator 1 wake. The indication for this position was the maximum velocity deficit for clp=0.0. Downstream of S2, using the same procedure, the probes were aligned with the stator 2 wake for clp=0.0 and y/s=0.0. In both measuring planes, around y/s=0.0, a symmetrical traverse of 33 measuring points was carried out in circumferential direction over one airfoil pitch at midspan. Negative values of y/s indicate probe positions shifted toward the pressure side of S2 and positive values probe positions shifted toward the suction side, respectively. The flow angle α is measured from the axial direction.

To determine the loading of stator 2, two adjacent blades were instrumented with static pressure tappings: One on the suction side and one on the pressure side. To avoid interaction between the tappings, they have not been aligned, but every other tapping was shifted by 2 mm to the right and left of midspan, maintaining a spacing of 2 mm along the blade surface.

Nine different clocking positions were evenly spaced over one airfoil pitch, and one additional clocking position was introduced for the case when the impingement point of the stator 1 wake is shifted 6.3% toward the suction side of stator 2 (clp=0.063), which showed to be the clocking position of minimum total pressure loss for the turbine (compare König et al. [24]). Mean quantities are given in terms of pitch averaged values defined by

$$\langle \xi \rangle = \frac{1}{s}\int_{-s/2}^{s/2} \xi(y)\mathrm{d}y \tag{2}$$

where ξ corresponds to the flow variable of interest and s to the stator pitch at midspan.

Data Processing

To get insight into the unsteady nature of the flow field, a separation of the periodic and stochastic fluctuations was carried out by means of the ensemble-averaging technique using the equation

$$\tilde{\xi}(t) = \frac{1}{N}\sum_{i=1}^{N} \xi_i(t) \tag{3}$$

The parameter $\xi_i(t)$ denotes the instantaneous value of ensemble i, and N corresponds to the total number of measured ensembles. The ensemble-averaged $\widetilde{\mathrm{RMS}}$-value reveals information about the stochastic fluctuations of a signal and is defined by

$$\widetilde{\mathrm{RMS}}[\xi(t)] = \sqrt{\frac{1}{N}\sum_{i=1}^{N} [\xi_i(t) - \tilde{\xi}(t)]^2} \tag{4}$$

For simplification purposes, the time average of the $\widetilde{\mathrm{RMS}}$-value is labeled $\mathrm{RMS} \equiv \overline{\widetilde{\mathrm{RMS}}(\xi(t))}$.

A measure of the strength of the periodic fluctuations is the $\mathrm{RMS_p}$-value of the ensemble-averaged signal given by

$$\mathrm{RMS_p}(\xi) = \sqrt{\frac{1}{M}\sum_{j=1}^{M} [\tilde{\xi}(t_j^*) - \overline{\tilde{\xi}(t)}]^2} \tag{5}$$

where M indicates the number of the discrete measuring times t_j^* and $\overline{\tilde{\xi}(t)}$ is the time-averaged value of the ensemble-averaged signal.

Results

A prerequisite to compare the results of the different setups is a similar loading of stator 2, since the boundary layer behavior of S2 constitutes the major parameter, with regard to efficiency

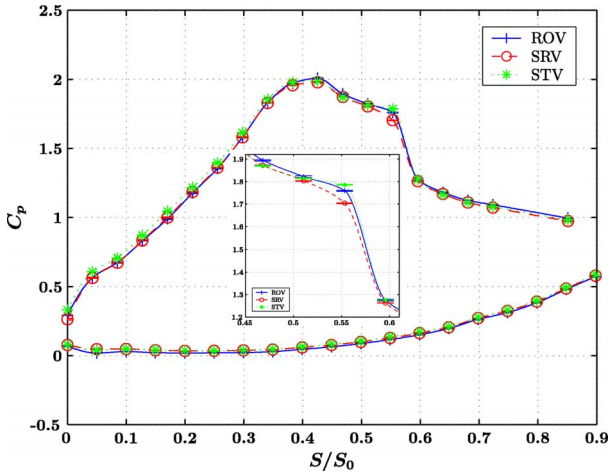

Fig. 3 Time-averaged static pressure distribution for different setups

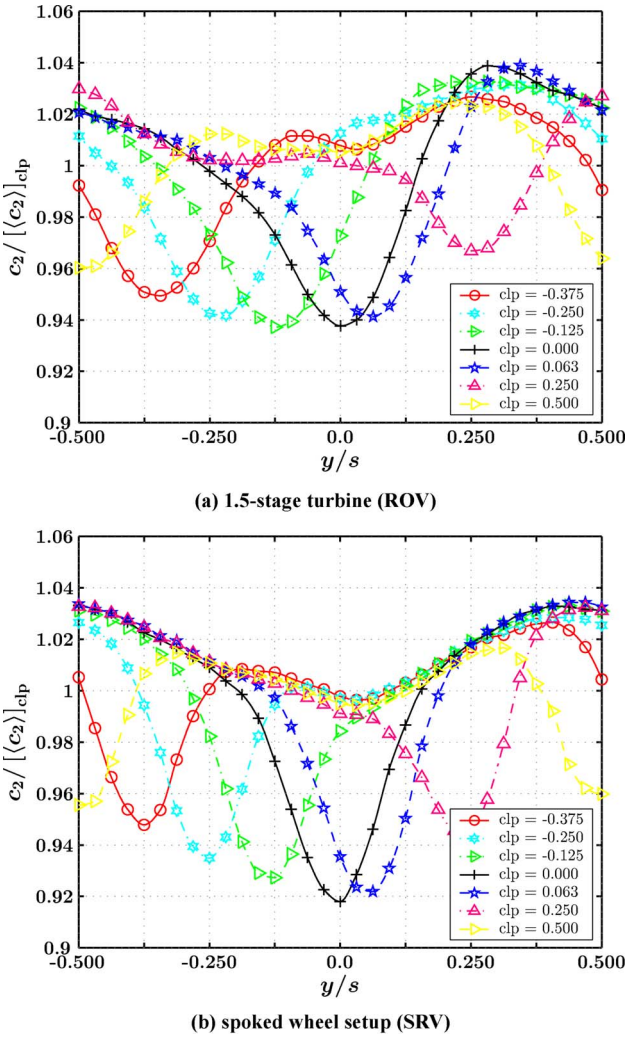

Fig. 4 Normalized absolute velocity upstream of S2

variations for different clocking positions. In Fig. 3, the static pressure distribution is shown for all three setups: The steady stator-stator setup (STV), the spoked-wheel setup (SRV), and the 1.5-stage turbine (ROV). Good agreement can be found between the three curves, but small deviations occur in the region of the separation bubble ($0.468 < S/S_0 < 0.6$). The stator-stator setup exhibits the steepest pressure rise downstream of the plateau-like region, which is an indication for the shortest separation bubble. As expected, the additional turbulence intensity introduced into the boundary layer due to the unsteady wakes for the SRV and the ROV leads to a shortening of the bubble. However, the separation bubble is even shorter for the SRV, although the wake characteristics of rotor blades and cylindrical bars were optimized with regard to similar velocity deficits and turbulence distributions. The reason for this behavior is the support rods mentioned earlier, that, due to their larger diameter, introduce additional turbulence into the boundary layer. In König et al. [24], it was shown that for the ROV, the shortest bubble occurs for clp=−0.125 and the longest bubble for clp=±0.5. For the SRV, the shortest bubble occurs for clp=0.0, whereas for $|\text{clp}| \geq 0.25$, the change of the static pressure distribution due to different clocking positions is negligible (not shown in the paper). This behavior is caused by the more confined S1 wakes upstream of S2 for the SRV, which can be seen in Fig. 6(*b*): For $|\text{clp}| \geq 0.25$, approximately the same intensity of the stochastic fluctuations takes place in proximity ($y/s=0.0$) of the stator 2 leading edge, which is known to be the major parameter with regard to the length of the separation bubble (compare König et al. [24]). As for the ROV, the maximum of the fluctuations in axial direction around $y/s=0.0$ leads to the shortest separation bubble, whereupon a change of the position of these maxima between SRV and ROV occurs. The dependency of the static pressure distribution on the clocking position is comparable for SRV and STV since for both setups, no interaction of the S1 wakes within the rotor passage takes place.

The velocity distribution normalized by its overall mean value upstream of stator 2 is shown in Fig. 4 for ROV and SRV. Since the probe traverse relative to stator 2 is identical for all clocking positions, the pronounced velocity deficit with changing clp is caused by the stator 1 wake flow. As the probe alignment was carried out for clp=0.0 in such a way that the minimum velocity was achieved for $y/s=0.0$ (probe on streamline of the stator 1 wake), a distinct velocity deficit can be seen at this position. For all other clp, the location of the maximum velocity deficit changes accordingly to the streamline of the stator 1 wake. The different intensity of the velocity deficit is caused by the superposition of the stator 1 wake and the stator 2 potential field. The influence of the latter can be seen in the region $c_2/[c_2]_{clp} \approx 1$ to 1.02 and $y/s \approx -0.25$ to 0.125 as a dent in the velocity distribution. For the SRV, this behavior is even more pronounced since no diffusion of the S1 wakes within the rotor passage takes place. This diffusion leads to a broadening of the velocity deficit for the ROV. Since the momentum losses of the two stators 1 are similar in the inlet plane of the wake generator, the broadening of the velocity dent for the ROV leads to smaller defect velocities.

In Fig. 5, the stator 2 inlet flow angle is plotted for six different clocking positions. The higher deflection angle in the region of $y/s \approx 0.125$ is caused by the stator 2 potential field, which yields to a deflection of the flow in this region towards the stator 2 suction side. For negative y/s, the potential field causes a flow turning towards the stator 2 pressure side, resulting in smaller deflection angles. For the ROV differences due to clocking are caused by the stator 1 wakes that, because of their velocity deficit, experience a reduced turning within the rotor passage in the absolute frame of reference. This behavior is obvious in Fig. 5(*a*) in the regions $y/s \approx -0.375$ (reduced turning angle for clp=−0.375) and $y/s \approx 0.125$ (reduced turning angle for clp=0.063). For the SRV, the dependency on the clocking position is due to another mechanism: Within the S1 wakes, lower deflection angles occur relative to the S1 pressure side and higher deflection angles relative to the S1 suction side (not shown in the paper). In Fig. 5(*b*), this behavior can be seen in proximity of the impingement position of the stator 1 wakes (e.g., $y/s=-0.375$ for clp=−0.375 or $y/s=0.25$ for clp=0.25): On the left-hand side (relative to the S1

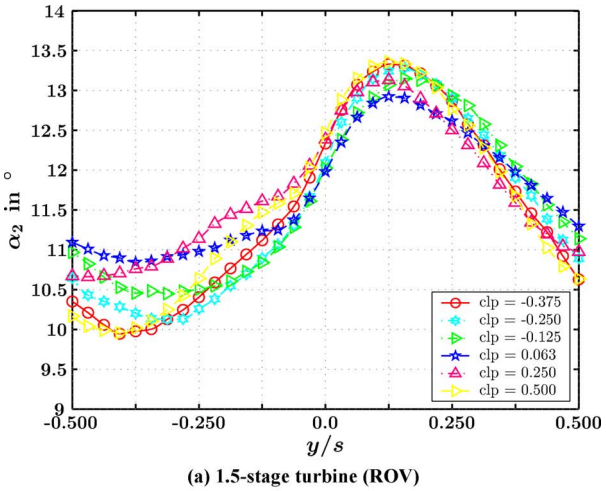

(a) 1.5-stage turbine (ROV)

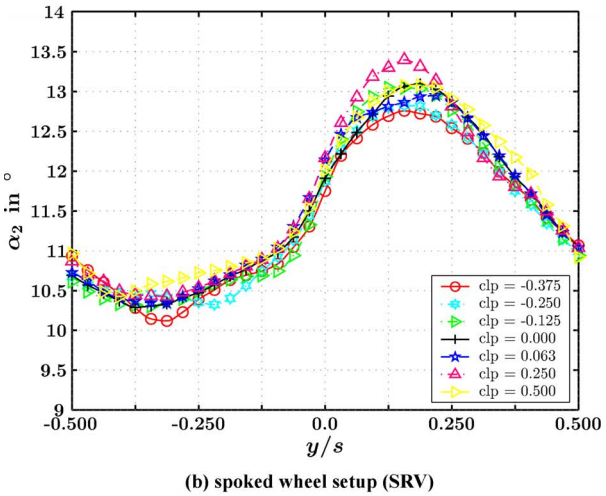

(b) spoked wheel setup (SRV)

Fig. 5 Flow angle upstream of S2

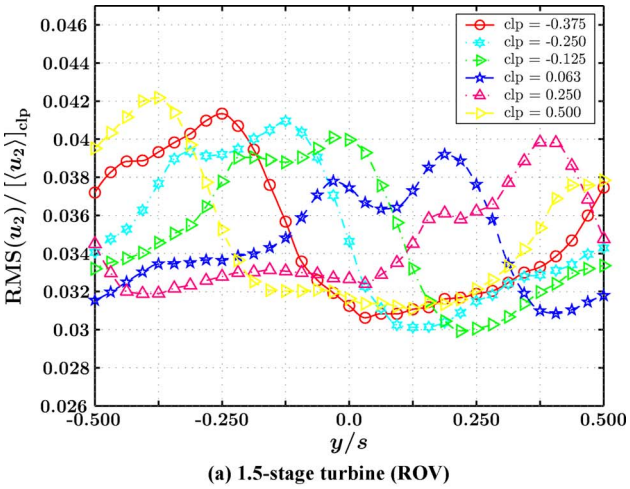

(a) 1.5-stage turbine (ROV)

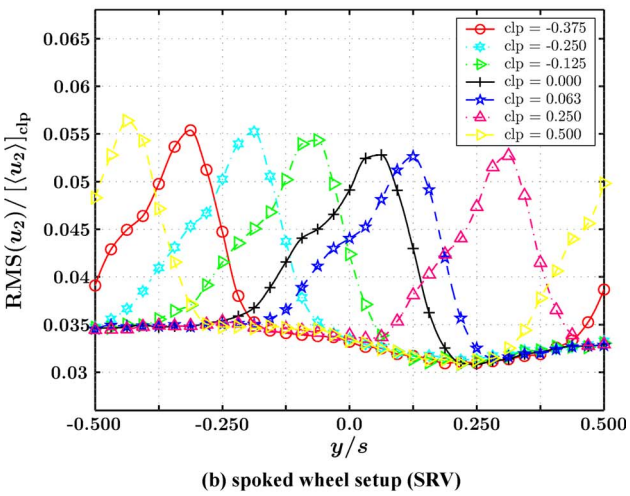

(b) spoked wheel setup (SRV)

Fig. 6 Normalized stochastic fluctuations in *x*-direction upstream of S2

suction side) of these positions, enhanced flow angles occur whereas reduced flow angles occur on the right-hand side (relative to the S1 pressure side).

In König et al. [24,29], it was shown that the stochastic unsteadiness upstream of S2 in axial direction dominates the unsteadiness on the S2 leading edge and hence the length of the separation bubble. This quantity is plotted in Fig. 6 for ROV and SRV. For the SRV, the range of the ordinate values is exactly twice the range for the ROV, to allow a better assessment of the change of the RMS value over the airfoil pitch for both setups. In both figures, the tendency of a double peak structure, which is typical for wake flows, can be seen in the S1 wake region. Outside the zone of influence of the S1 wakes, the fluctuation level remains almost constant for the SRV (compare Fig. 6(*b*)); the small variation is caused by the S2 potential field, which yields to a dampening of the fluctuations in the region of minimum static pressure ($y/s \approx 0.25$) upstream of S2. For the ROV in Fig. 6(*a*), the deformation of the S1 wakes within the rotor passage leads to a diffusion of the RMS maximum and a more pronounced double peak structure. Obviously the distortion of the S1 wakes for the ROV leads to a further separation of the fluid particles convecting from the suction and pressure sides of S1. Furthermore, the ROV interactions are also obvious outside of the S1 wake core. Although the turbulence intensities for SRV and ROV are similar in the stator 2 inlet plane for the steady case (compare Heinke [25]), a completely different behavior can be seen for the unsteady case: Due to the acceleration and longer distance of the S1 wakes traveling within the rotor passage for the ROV a stronger dissipation of the turbulence and the stochastic unsteadiness of the S1 wakes takes place, which leads to reduced RMS levels, especially in the S1 wake core region. Considering the stochastic unsteadiness (and the turbulence intensity, respectively) it becomes obvious that for ROV and SRV, the stator 2 inlet boundary conditions show distinct discrepancies.

For the ROV, it was shown that the strength of the periodic unsteadiness downstream of S2 constitutes the major loss parameter (compare König et al. [24,29]). It was pointed out that this behavior is caused by different amplification rates within the stator 2 suction side boundary layer for different clocking positions. In Fig. 7(*a*), the strength of the periodic unsteadiness within the suction side boundary layer is plotted for the ROV. A comparison with the corresponding curve for the SRV in Fig. 7(*b*) clearly indicates that different amplification processes take place with regard to the periodic unsteadiness for ROV and SRV. Therefore, the major loss parameter for the 1.5-stage turbine cannot be simulated by means of the simplified spoked-wheel setup.

With respect to efficiency variations, not only the profile loss of stator 2 is a relevant parameter, but also varying stator 2 inlet and exit flow angles. In König et al. [24,29], it was shown that for the ROV, the deflection angle of the rotor, as well as the deflection angle of stator 2, show a dependency on the clocking position. In Fig. 8, the behavior of the pitch averaged stator 2 exit flow angle is shown for ROV and SRV. It can be clearly seen that both curves show completely different characteristics. Quantitatively, the variation of the stator 2 exit angle accounts for 0.44 deg for the

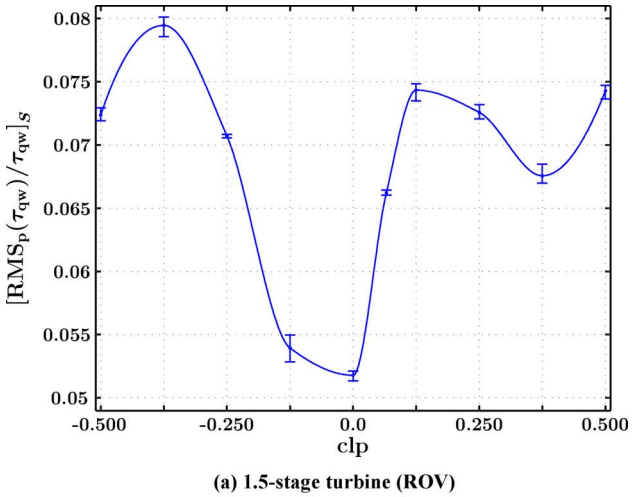

(a) 1.5-stage turbine (ROV)

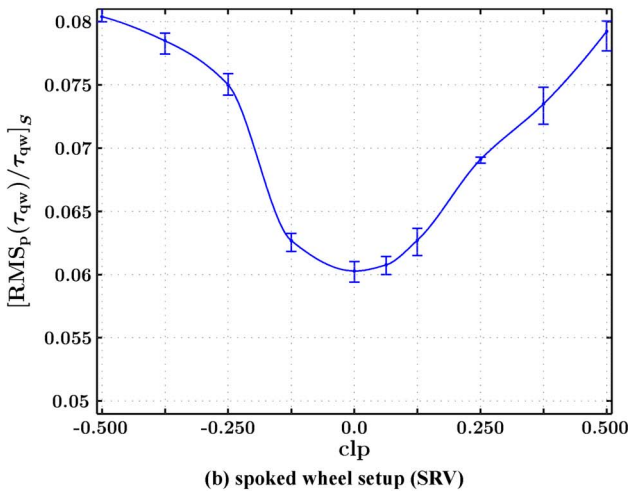

(b) spoked wheel setup (SRV)

Fig. 7 Time-averaged $\mathrm{RMS_p}$-value (periodic) along S2 suction side

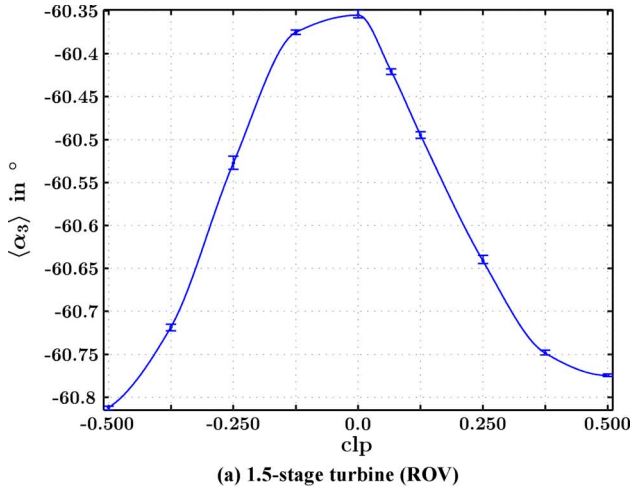

(a) 1.5-stage turbine (ROV)

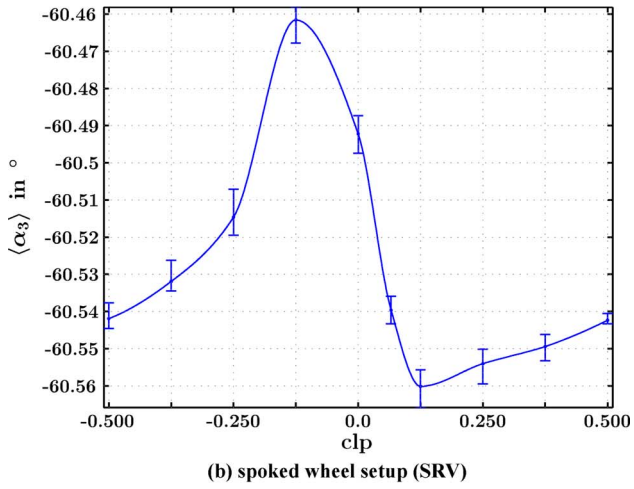

(b) spoked wheel setup (SRV)

Fig. 8 Pitch-averaged integral flow angle downstream of S2

ROV and 0.1 deg for the SRV, respectively. It is obvious that a spoked-wheel setup is not suited to simulate the dependency of the S2 deflection angle on the clocking position. Comparing the results of the steady stator-stator setup (Heinke [26]) and the spoked-wheel setup, a better correlation can be found: The clocking positions of maximum S2 deflection angle (clp=0.125 for the SRV and clp=0.063 for the STV) and the clocking positions of minimum S2 deflection angle (clp=−0.125 for the SRV and clp =−0.25 for the STV) show only a small deviation. In addition, the quantitative change of the pitch averaged S2 exit flow angle shows a better agreement for SRV and STV (0.1 deg and 0.17 deg, respectively) than for SRV and ROV. Obviously the different physical mechanisms that were discussed for the local values of the S2 inflow angle for ROV and SRV also affect the dependency of the S2 deflection angle. Therefore, the characteristics of the curve in Fig. 8(*a*) cannot be explained by the periodic unsteadiness alone, but the interaction of the stator 1 wakes within the rotor passage has to be taken into account.

In König et al. [24,29], it was shown that the turbulence production is one of the loss parameters that is responsible for efficiency variations due to clocking. In Fig. 9(*a*), the corresponding curve of the pitch averaged turbulent kinetic energy is plotted for the ROV. A comparison with the results of the SRV in Fig. 9(*b*) shows that both curves exhibit different characteristics, and that the mean value of the turbulence intensity is much higher for the SRV. The latter is caused by the higher S2 inlet turbulence intensity that was discussed previously and the resulting stronger stochastic unsteadiness within the stator 2 boundary layer. Comparing the STV (Heinke [26]) and the SRV, a better correlation between the trend of the two curves can be found: For both setups the TKE maximum occurs for clp=−0.125 and the position of the TKE minimum shows only a small deviation (clp=0.25 for the SRV and clp=0.125 for the STV). It is obvious that a spoked-wheel setup is not capable of resolving the physical mechanisms that lead to the dependency of the TKE production for different clocking positions in a real turbine.

So far, only time-averaged quantities have been discussed to compare the different setups. In Fig. 10, the ensemble-averaged time traces of the absolute velocity, the TKE, and the flow angle are given upstream of S2 for ROV and SRV. For both setups, the influence of the rotor wakes manifests as a dent in the velocity signal, enhanced TKE, and a higher deflection angle. For the ROV, the additional influence of the stator 1 wakes can be seen in a similar manner, e.g., as a dent in the velocity signal between two rotor wake passing events for clp=0.063. Furthermore, the stator 1 wakes lead to a time-dependent negative incidence angle of about 7.2 deg for clp=0.063. The resulting periodical movement of the stator 2 stagnation point yields to a phase shift of the ensemble-averaged QWSS signal in the front region of the S2 blade surface, as was discussed by König et al. [29]. For the SRV, the dependency of the ensemble-averaged flow angle on the clocking position is negligible, hence no phase shift occurs in the QWSS signal. As expected, lower velocities and enhanced turbulence intensities occur for the SRV when the measuring probe at position $y/s=0.0$ is affected by the chopped stator 1 wake seg-

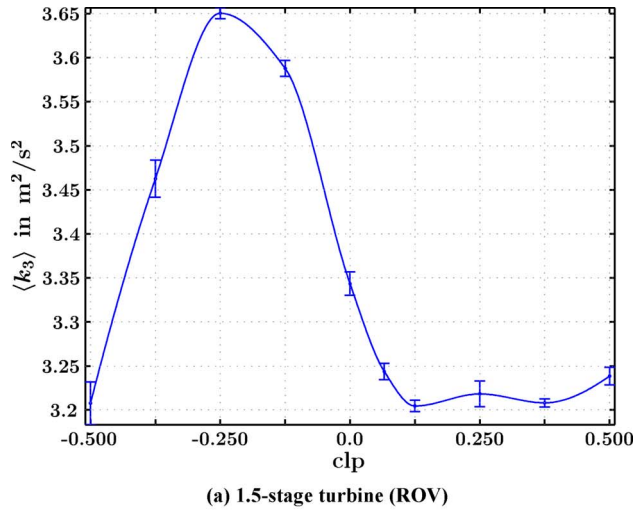

(a) 1.5-stage turbine (ROV)

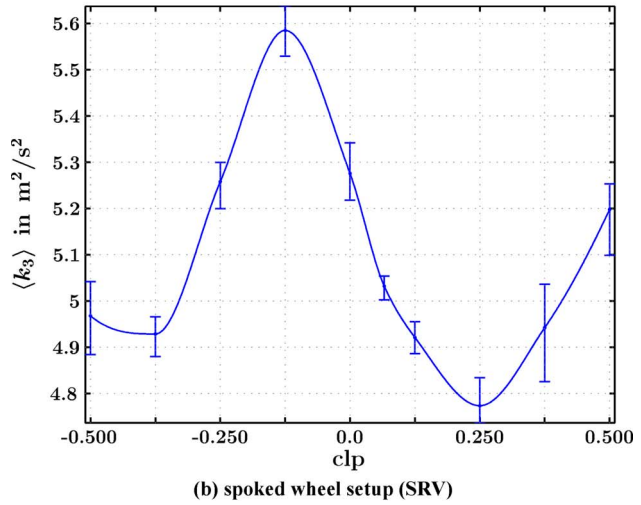

(b) spoked wheel setup (SRV)

Fig. 9 Pitch-averaged integral turbulent kinetic energy downstream of S2

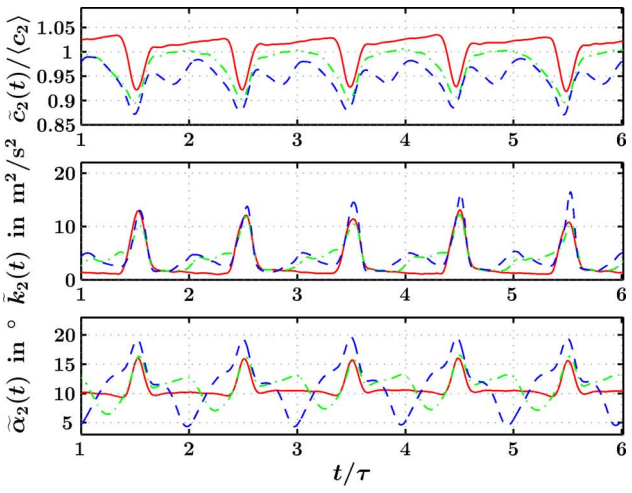

(a) 1.5-stage turbine (ROV)

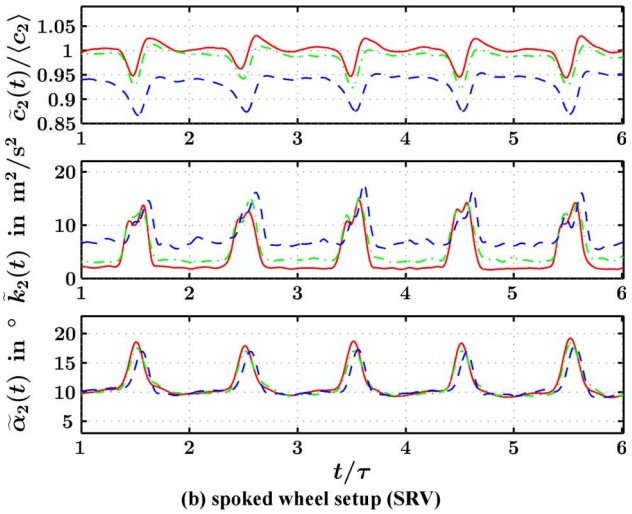

(b) spoked wheel setup (SRV)

Fig. 10 Ensemble-averaged absolute velocity, turbulent kinetic energy, and flow angle upstream of S2 for y/s=0.0 (blue/dashed line: clp=0.063, green/chain dotted line: clp=−0.125, red/solid line: clp=−0.375)

ments (e.g., clp=0.063). Due to the higher turbulence intensity for the SRV, stronger mixing processes take place compared to the ROV, which lead to a less pronounced velocity deficit in the ensemble-averaged signal for the SRV.

In Fig. 11, the response of the stator 2 boundary layer on the inflow conditions is plotted for ROV and SRV in terms of the ensemble-averaged QWSS. Characteristic propagation velocities within the stator 2 boundary layer were determined analyzing the ensemble-averaged traces of the QWSS, its RMS, and the total skewness (for a detailed discussion, compare König et al. [29]). The characteristic velocities were computed as a function of the local free-stream velocity as obtained from the static pressure distribution. Perturbations caused by the stator 1 wakes are indicated by the letter S and disturbances due to the rotor wakes by the letter R. The trajectory labelled FS shows the flow path of the local free-stream velocity. The vertical dashed line indicates the position where the acceleration parameter adopts the value 3×10^{-6}, which implicates that no generation of turbulent spots is possible upstream this point. The solid line in the region $S/S_0 \approx 0.5$ gives the time-dependent position of the transition point as obtained from the QWSS values. The black trajectories in Figs. 11(a) and 11(b) correspond to the characteristic velocities for the ROV and the white trajectories to the SRV. When the stator 1 wakes convect close to midway between two stator 2 vanes (clp $\approx \pm 0.5$), the interaction of the combined stator 1 and rotor vortical structures with the stator 2 boundary layer is negligible and the ST diagrams of the QWSS for ROV and SRV are very similar (not shown in the paper). In this case, the influence of the periodically incoming rotor wakes on the boundary layer behavior can be simulated by means of the spoked-wheel setup. However, distinct discrepancies occur when the stator 1 wakes impinge close to the leading edge of stator 2. This case is shown in Fig. 11 for clp =0.063. For the ROV, the interaction mechanisms of the stator 1 and rotor wakes manifest as a phase shift of the ensemble-averaged QWSS signal in the front region of the blade, whereas no phase shift occurs for the SRV. The resulting phase shift between ROV and SRV for clp=0.063 can be seen comparing the trajectories of the ROV (R1) and the SRV (R1*). Furthermore, a perturbation of the boundary layer due to the stator 1 wakes (S1) can be seen in the front region of the blade for the ROV, whereas no such influence occurs for the SRV. In the transitional region around $S/S_0 \approx 0.5$, the additional influence of the stator 1 wakes can be seen for the ROV as an upstream movement of the transition point in the regions of influence of the stator 1 wakes (S2). For the SRV, this influence is negligible and the propagation velocities adopt slightly higher values compared to the ROV, which results in a small phase shift between the propagation directions of ROV (R4, black line) and SRV (R4, white line). In accordance with the stator 2 inlet boundary conditions, it can be summarized

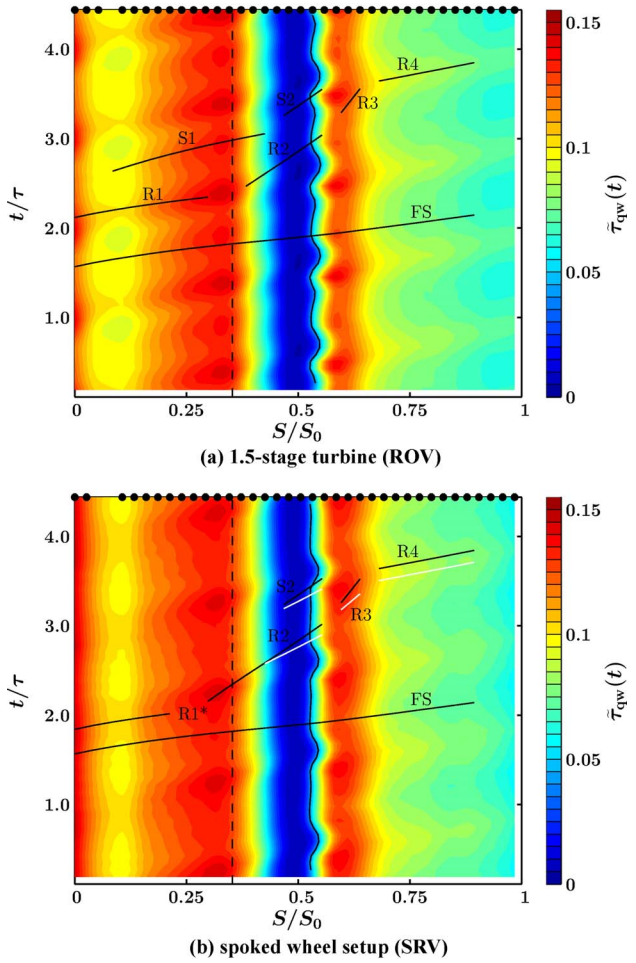

Fig. 11 ST diagrams of ensemble-averaged QWSS along stator 2 suction side, clp=0.063

that the stator 2 unsteady boundary layer behavior cannot be simulated by means of the spoked-wheel setup when the stator 1 wakes interact with the stator 2 boundary layer. The reason for this behavior is the skewing of the stator 1 wakes within the rotor passage for the ROV, which is caused by the different suction and pressure side velocities, due to the lift and bound vorticity of the rotor. The skewing is absent for the SRV case, where only a chopping of the stator 1 wakes takes place. This behavior becomes particularly clear in Fig. 11, where there are twice as many wake ripples in the ROV case as in the SRV case. A general discussion about the boundary layer behavior with details about the transition mechanisms can be found in König et al. [29].

Uncertainty Analysis. To assess the accuracy of the probe measurements, a detailed uncertainty analysis considering inaccuracies due to the measuring equipment, the calibration procedure, and slight fluctuations of the operation point was carried out (compare König [28]). The resulting maximum error bandwidths of the quantities that are being presented in the paper are summarized in Table 2. For derived quantities as the C_p-value, the Kline and McKlintock [31] method was applied to determine the corresponding uncertainty. Absolute values as given in Table 2 are of interest mainly for comparison reasons with numerical calculations. For the understanding of the clocking effect, the changes of the flow variables due to different clocking positions are of much more interest than their absolute values. The inaccuracy of those changes is at least one order of magnitude smaller than that of the absolute values.

Table 2 Uncertainty of selected flow variables

C_p	α	$\overline{c'^2}$	c
2.9%	0.75 deg	3%	2%

Conclusions

In the present paper, detailed experimental results are presented in order to get a better understanding of the flow physics and interaction mechanisms that take place if two adjacent stator rows with the same blade count are arranged in different circumferential positions (clocking). The experiments were carried out using two different experimental setups: A 1.5-stage axial turbine and a simplified model, a "spoked-wheel" setup with a wake generator consisting of cylindrical bars. Comparing the two setups presented in the paper with a third setup, a stationary stator-stator setup, the following conclusions can be drawn:

- Even when the wake parameters, such as turbulence intensity and velocity deficit, are similar for rotor blades and cylindrical bars for the steady case, a different behavior occurs for the unsteady case: Due to the acceleration and the longer distance of the stator 1 wakes traveling within the rotor passage for the 1.5-stage turbine, a reduction of the wake turbulence intensity and a broadening of the velocity deficit takes place.
- A spoked-wheel setup is well suited to simulate the influence of periodically incoming wakes on the transition behavior of stator 2 when the interaction of the stator 1 wakes with the stator 2 boundary layer is negligible.
- If the vortical structures of stator 1 and rotor wakes interact in proximity of the stator 2 blade surface, those effects cannot be simulated by means of a spoked-wheel setup (neither with regard to the formation of the interaction patterns, nor with regard to their influence on the stator 2 boundary layer). Particularly the influence of the stator 1 wakes on the ensemble-averaged stator 2 inflow angle and the resulting movement of the stagnation point cannot be resolved with the simplified setup.
- The last two statements alone clearly indicate that it is not possible to fully simulate the clocking effect by means of a spoked-wheel setup. Furthermore, the major loss parameter in the 1.5-stage turbine, the strength of the periodic unsteadiness, shows a completely different behavior if no interaction of the stator 1 wakes within the rotor passage takes place. However, a simplified spoked-wheel setup is well suited to separate some of the physical mechanisms concerning clocking.
- Considering time-mean flow quantities, such as the flow angle or the turbulence intensity downstream of stator 2, similar tendencies were found when comparing the unsteady spoked-wheel setup and the steady stator-stator setup. Since no wakes are present in the latter case, such a setup is not suited for realistic clocking investigations. However, it is useful to study the combined influence of an enhanced turbulence intensity and a velocity deficit on the boundary layer behavior of the stator located downstream.

Basically, a realistic simulation of a 1.5-stage turbine by means of a simplified spoked-wheel setup is not possible because the stator 1 wakes passing through a real rotor are both chopped and skewed by the different suction and pressure side velocities, due to the lift and bound vorticity of the rotor. Conversely, in the spoked-wheel case, the wakes are chopped but not skewed.

It has to be mentioned that great care was taken to obtain similar wake characteristics for rotor blades and cylindrical bars, whereas many investigations simply determine the diameter of the bars from the rotor trailing edge thickness. For the latter case, it is

assumed that the discrepancies between a setup with a wake generator consisting of cylindrical bars and a real turbine will be even larger when it comes to clocking investigations.

Acknowledgment

We would like to thank the German Science Foundation (DFG) who has generously granted this project.

Nomenclature

$[\ ]_S$ = average along the surface coordinate S
c = flow velocity in absolute frame of reference
c' = fluctuating velocity component
C = chord length
C_p = $([p_{t_{2,FS}}]_{clp}-p)/([p_{t_{2,FS}}]_{clp}-[\langle p_3\rangle]_{clp})$
clp = clocking position (fraction of stator pitch at midspan)
E = measuring plane (E0, E1, E2, E3)
E = measured voltage
E_0 = measured voltage at zero flow conditions
f = blade passing frequency
k = turbulent kinetic energy
p = static pressure
p_t = total pressure
RMS = root mean square
ROV = 1.5-stage turbine (rotor setup)
s = stator pitch at midspan
S = surface coordinate
S_0 = total length of the surface coordinate
S1, S2 = Stator 1, Stator 2
SRV = spoked-wheel setup
STV = stator-stator setup
QWSS = quasi-wall shear stress
t = time
u = velocity component in x-direction
U = circumferential velocity
x = coordinate in axial direction
y = coordinate in circumferential direction
α = flow angle in absolute frame of reference
ν = kinematic viscosity
$\bar{\xi}$ = time-averaged value of flow variable $\xi(t)$
$\langle\xi\rangle$ = pitch-averaged value of flow variable $\xi(y)$
$\tilde{\xi}(t)$ = ensemble-averaged value of flow variable $\xi(t)$
$[\xi]_{clp}$ = arithmetic mean value over all clp
τ = rotor periodic time
τ_{qw} = quasi-wall shear stress

Subscripts

0 = measuring plane E0 upstream of S1
1 = measuring plane E1 downstream of S1
2 = measuring plane E2 15 mm upstream of S2
3 = measuring plane E3 60 mm downstream of S2
ax = axial flow direction
FS = free stream
p = periodic fluctuations
u = circumferential direction

References

[1] Schlichting, H., 1930, "Über das ebene Windschattenproblem," Ing.-Arch., **1**, pp. 553–571.
[2] Townsend, A. A., 1947, "Measurements in the Turbulent Wake of a Cylinder," Proc. R. Soc. London, Ser. A, **190**, pp. 551–561.
[3] Ermshaus, R., 1956, "Eigentümlichkeiten turbulenter Nachlaufströmungen," Mitt. Max-Planck-Inst. für Strömungsforschung No. 46, Göttingen, Germany.
[4] Eifler, J., 1974, "Zur Frage der freien turbulenten Strömungen, insbesondere hinter ruhenden und bewegten Zylindern," Ph.D. thesis, TH Darmstadt, Germany.
[5] Pfeil, H., and Eifler, J., 1975, "Zur Frage der Schubspannungsverteilung für die ebenen freien turbulenten Strömungen," Forsch. Ingenieurwes., **41**(4), pp. 105–112.
[6] Pfeil, H., and Eifler, J., 1975, "Messungen im turbulenten Nachlauf des Einzelzylinders," Forsch. Ingenieurwes., **41**(5), pp. 137–145.
[7] Savill, A. M., 1983, "The Turbulent Structure of a Highly Curved Two-Dimensional Wake," *IUTAM Symposium on Complex Turbulent Flows*, Springer, pp. 185–197.
[8] Nakayama, A., 1987, "Curvature and Pressure-Gradient Effects on a Small-Defect Wake," J. Fluid Mech., **175**, pp. 215–246.
[9] Schobeiri, M. T., Pappu, K., and John, J. 1995, "Theoretical and Experimental Study of Development of Two-Dimensional Steady and Unsteady Wakes Within Curved Channels," ASME J. Fluids Eng., **117**, pp. 593–598.
[10] Schobeiri, M. T., John, J., and Pappu, K., 1996, "Development of Two-Dimensional Wakes Within Curved Channels: Theoretical Framework and Experimental Investigation," ASME J. Turbomach., **118**, pp. 506–518.
[11] Kiock, R., 1973, "Einfluß des Turbulenzgrads auf die aerodynamischen Eigenschaften von ebenen Verzögerungsgittern," Forsch. Ingenieurwes., **39**(1), 17–28.
[12] Trost, N., 1975, "Einfluß der Zuströmturbulenz auf die Strömung in Axialgittern," Ph.D. thesis, TU Darmstadt, Germany.
[13] Pfeil, H., and Schröder, T., 1981, "Decay of the Wake Behind a Cylinder Crossing Rapidly the Flow," AIAA Paper No. AIAA-81-0209.
[14] Schröder, T., 1985, "Entwicklung des instationären Nachlaufs hinter quer zur Strömungsrichtung bewegten Zylindern und dessen Einfluß auf das Umschlagsverhalten von ebenen Grenzschichten stromabwärts angeordneter Versuchskörper," Ph.D thesis, TH Darmstadt, Germany.
[15] O'Brien, J. E., and Capp, S. P. 1989, "Two-Component Phase-Averaged Turbulence Statistics Downstream of a Rotating Spoked-Wheel Wake Generator," ASME J. Turbomach., **111**, pp. 475–482.
[16] Stoffel, B., 1996, "Blade Wakes in Axial Turbomachines—Their Structure and Unsteady Downstream Effects," *Int. Symposium on Fluid Machinery and Fluid Engineering*, Beijing, China, Sept. 9–12.
[17] Schulte, V., and Hodson, H. P., 1998, "Prediction of the Becalmed Region for LP Turbine Profile Design," ASME J. Turbomach., **120**, pp. 839–846.
[18] Stadtmüller, P., Fottner, L., and Fiala, A., 2000, "Experimental and Numerical Investigation of Wake-Induced Transition on a Highly Loaded LP Turbine at Low Reynolds Numbers," ASME Paper No. 2000-GT-0269.
[19] Howell, R. J., Ramesh, O. N., Hodson, H. P., Harvey, N. W., and Schulte, V., 2001, "High Lift and Aft-Loaded Profiles for Low-Pressure Turbines," ASME J. Turbomach., **123**, pp. 181–188.
[20] Coton, T., Arts, T., Lefebvre, M., and Liamis, N., 2003, "Unsteady and Calming Effects Investigation on a Very High-Lift LP Turbine Blade—Part I: Experimental Analysis," ASME J. Turbomach., **125**, pp. 281–290.
[21] Schobeiri, M. T., Read, K., and Lewalle, J., 2003, "Effect of Unsteady Wake Passing Frequency on Boundary Layer Transition, Experimental Investigation, and Wavelet Analysis," ASME J. Turbomach., **125**, pp. 251–266.
[22] Schobeiri, M. T., and Öztürk, B., 2004, "Experimental Study of the Effect of Periodic Unsteady Wake Flow on Boundary Layer Development, Separation, and Reattachment along the Surface of a Low Pressure Turbine Blade," ASME J. Turbomach., **126**, pp. 663–676.
[23] Schobeiri, M. T., Öztürk, B., and Davis, D. E., 2005, "On the Physics of Flow Separation along a Low Pressure Turbine Blade under Unsteady Flow Conditions," ASME J. Fluids Eng., **127**, pp. 503–513.
[24] König, S., Stoffel, B., and Schobeiri, M. T., "Experimental Investigation of the Clocking Effect in a 1.5-Stage Axial Turbine—Part I: Time-Averaged Results," ASME J. Turbomach., accepted.
[25] Heinke, W., 2002, "Experimentelle Untersuchungen zum Clocking-Effekt an einer stationären Stator-Stator-Anordnung," Ph.D. thesis, TU Darmstadt, Germany.
[26] Heinke, W., König, S., Matyschok, B., Stoffel, B., Fiala, A., and Heinig, K. 2004, "Experimental Investigations on Steady Wake Effects in a High-Lift Turbine Cascade," Exp. Fluids, **37**, pp. 488–496.
[27] König, S., Heidecke, A., Stoffel, B., Fiala, A., and Engel, K., 2004, "Clocking Effects in a 1.5-Stage Axial Turbine—Boundary Layer Behaviour at Midspan," ASME Paper No. GT2004-54055.
[28] König, S., 2006, "Untersuchung des Einflusses überlagerter Stator- und Rotornachläufe auf den Clocking-Effekt an einer 1.5-stufigen axialen Gasturbine," Ph.D. thesis, TU Darmstadt, Germany.
[29] König, S., Stoffel, B., and Schobeiri, M. T., "Experimental Investigation of the Clocking Effect in a 1.5-Stage Axial Turbine—Part II: Unsteady Results and Boundary Layer Behavior," ASME J. Turbomach., accepted.
[30] Kazimierski, Z., and Horodko, L., 1990, "Total Pressure Averaging by Small-Diameter Tubes in Pulsating Flows," AIAA J., **28**(1), pp. 140–145.
[31] Kline, S. J., and McClintock, F. A., 1953, "Describing Uncertainties in Single-Sample Experiments," Mech. Eng. (Am. Soc. Mech. Eng.), **75**, pp. 3–8.